Design, synthesis and biological activity studies of 1-aryl-3-(4-methoxybenzyl)ureas as proposed irreversible GSK-3 inhibitors in Alzheimer's disease therapeutic development

by

Jana Venter

Thesis presented in fulfilment of the requirements for the degree of Master of Science in the Faculty of Science at Stellenbosch University

Supervisor: Dr. Margaret A. L. Blackie

Co-supervisor: Prof. Willem A. L. van Otterlo

Department of Chemistry and Polymer Science

Faculty of Natural Science

April 2019

The financial assistance of the National Research Foundation (NRF) towards this research is hereby acknowledged. Opinions expressed and conclusions arrived at are those of the author and are not necessarily to be attributed to the NRF.

Declaration

By submitting this thesis electronically, I declare that the entirety of the work contained therein is my own, original work, that I am the sole author thereof (save to the extent explicitly otherwise stated), that reproduction and publication thereof by Stellenbosch University will not infringe any third party rights and that I have not previously in its entirety or in part submitted it for obtaining any qualification.

March 2019

Abstract

Alzheimer's disease (AD) is a progressive neurodegenerative disease, characterised by memory loss and cognitive decline. No cure has been found for the disease yet, therefore the development of disease-modifying therapeutics (DMTs), which can target the underlying mechanisms of AD, is necessary. Glycogen synthase kinase 3 (GSK-3) has become a promising CNS target, since GSK-3 dysregulation has been shown to play a central role in the multifactorial neuropathogenesis of AD.

In this project, a proposed library of structurally-related, irreversible GSK-3β inhibitors was modelled, synthesised, characterised and biologically tested as potential AD drug candidates. The library contained two sets of 1-aryl-3-(4-methoxybenzyl)ureas wherein the incorporated aryl group was a benzothiazole or benzimidazole scaffold, respectively. Different electrophilic warheads were incorporated onto the scaffolds, with the potential to form a covalent, irreversible bond with nucleophilic Cys199 in the GSK-3 ATP pocket. Targeting of Cys199 was suggested to provide increased GSK-3 selectivity, since Cys199 is exchanged with other amino acids in structurally-related enzymes.

A library of 10 covalent inhibitors containing the nitrile, halomethylketone (HMK), vinyl ketone, ethynyl ketone and acrylamide electrophilic warheads was successfully synthesised, as well as the reference GSK-3 inhibitor, AR-A014418 (AstraZeneca). The synthetic route commenced with the preparation of the 6-substituted 2-aminobenzothiazoles and 6-substituted 2-aminobenzimidazoles in good yields. Thereafter, the scaffolds were coupled to 4-methoxybenzylamine through carbonyldiimidazole-mediated urea formation, which afforded excellent yields for the benzothiazoles and moderate yields for the benzimidazoles, proposedly due to tautomeric effects in the latter. These ureas were further modified in position 6 of the benzazole scaffolds, to incorporate the respective electrophilic warheads.

The GSK-3β inhibitory activity results were promising, with high activities measured for the nitrile-substituted ureas and the HMK-substituted benzimidazole urea. In comparison to the reference GSK-3 inhibitor, which displayed an IC_{50} value of 0.072 ± 0.043 µM in the assay, the best IC_{50} value obtained in the library was 0.086 ± 0.023 µM, observed for 1-(6-cyano-1*H*-benzo[*d*]imidazol-2-yl)-3-(4-methoxybenzyl)urea. In general, the benzimidazole series displayed better IC_{50} values than the equivalent inhibitors in the benzothiazole series. Although an initial assay was carried out to ascertain whether the newly synthesised inhibitors were in fact irreversible inhibitors, the results remain ambiguous and further study is required to confirm this hypothesis.

In conclusion, highly active GSK-3β inhibitors were successfully developed and may potentially contribute to future AD drug development.

Uittreksel

Alzheimersiekte (AD) is ‘n progressiewe neurodegenerasiesiekte, gekenmerk deur geheueverlies en kognitiewe kwyning. Daar is tans geen geneesmiddel beskikbaar vir die siekte nie, daarom is die ontwikkeling van siekte-wysigingsmiddels, wat instaat is om die onderliggende siekteverwekkende meganismes van AD te teiken, noodsaaklik. Die glikogeen sintase kinase 3 (GSK-3) ensiem is ‘n belowende teiken in die sentrale senuweestelsel, aangesien daar getoon is dat abnormale GSK-3 vlakke bydra tot veelvoudige faktore in die neuropatogenese van AD.

In hierdie projek is ‘n versameling van struktuurverwante, onomkeerbare GSK-3β inhibeerders voorgestel, waarna dit gemoduleer, gesintetiseer en biologies getoets is as potentiële AD geneesmiddelkandidate. Die versameling het bestaan uit twee stelle 1-ariel-3-(4-metoksibensiel)ureumverbindings, waarin die arielgroep onderskeidelik ‘n bensotiasool- of bensimidasool-struktuur verteenwoordig het. Hierdie sentrale strukture is elk aangepas met ‘n verskillende elektrofiliese reaktiewe groep, aangesien hierdie substituent potensieel ‘n kovalente, onomkeerbare binding met sisteïen 199 (Cys199) in die ATP bindingsetel van GSK-3 kan vorm. Cys199 word vervang met ander aminosure in struktuurverwante ensieme, daarom kan ‘n kovalente binding met Cys199 moontlik die selektiwiteit van die GSK-3 inhibeerders verbeter.

‘n Versameling van 10 kovalente inhibeerders, met onderskeidelik die nitriel, halometielketoon (HMK), vinielketoon, etenielketoon en akrielamied elektrofiliese reaktiewe groepe, is suksesvol gesintetiseer, asook die kontrole GSK-3 inhibeerder, AR-A014418 (AstraZeneca). Die sintesepad het ‘n aanvang geneem met bereiding van die 6-gesubstitueerde 2-aminobensotiasool- en 6-gesubstitueerde 2-aminobensimidasool-verbindings, met goeie opbrengste. Hierdie verbindings is daarna gekoppel aan 4-metoksibensielamien met behulp van karbonieldiimidasool, om die bensotiasool-ureumverbindings te vorm met puik opbrengste. Die opbrengste van die bensimidasool-ureumverbindings was gematig, moontlik a.g.v. toutomeriese effekte. Die ureumverbindings is verder aangepas by posisie 6 van die bensasool-basisstruktuur, om sodoende die relevante elektrofiliese reaktiewe groepe te koppel.

GSK-3β inhiberingsaktiwiteit resultate was belowend en die beste aktiwiteit is gemeet vir die nitriel-gesubstitueerde ureumverbindings en die HMK-gesubstitueerde bensimidasool-ureumverbinding. Die aktiefste inhibeerder was 1-(6-siano-1*H*-benso[*d*]imidasol-2-iel)-3-(4-metoksibensiel)ureum, met ‘n IC_{50} waarde van 0.086 ± 0.023 µM. Hierdie waarde het ook goed vergelyk met die aktiwiteit van die kontrole GSK-3 inhibeerder (IC_{50} waarde = 0.072 ± 0.043 µM). Die bensimidasool reeks het oor die algemeen better IC_{50} waardes vertoon as ooreenstemmende inhibeerders in die bensotiasool reeks.

Alhoewel ‘n aanvanklike ensiemtoets uitgevoer is om die onomkeerbare bindingsmeganisme van die nuut-gesintetiseerde inhibeerders te bevestig, was die resultate van die kontrole GSK-3 inhibeerder onverklaarbaar en word verdere navorsing benodig om hierdie hipotese te bevestig.

Ten slotte, hoogs aktiewe GSK-3β inhibeerders is suksevol ontwerp en kan potensieel bydra tot toekomstige AD geneesmiddel ontwikkeling.

Acknowledgements

The past two years have been a valuable learning experience, which I would not have been able to complete without advice and technical support. I would like to thank my supervisor, Dr. M. A. L. Blackie and co-supervisor, Prof. W. A. L. van Otterlo for their guidance, chemistry advice, synthesis help and enthusiasm. Thank you to Dr. G. E. Arnott, who was always willing to answer questions about synthesis and for the valuable recommendations after report-back meetings. I would like to express my gratitude to the rest of the academics in the Group of Organic and Medicinal Chemistry (GOMOC), as well as all my undergraduate and postgraduate lecturers who taught me valuable knowledge and scientific reasoning skills.

A big thank you to Anton Hamann, who first introduced me to the Organic lab as an Honours student and taught me all of the protocols and relevant techniques. Similarly, I am grateful to Jonny Hay and Alet van der Westhuyzen who taught me many more synthetic tricks, helped with equipment and were always willing to provide me with chemicals. A special thanks to Alet for her support and long lab conversations. Thank you for the help and motivation from all the students in the GOMOC group. A special thanks to Monica Clements, Khaya Gould (your enthusiasm is contagious), Charlotte Mamogobo, Luke Hodson, Trégen Snayer (for sacrificing your fume-hood every now and then) and Tanya Mabank.

I would like to express my gratitude for the single-crystal X-ray diffraction experiment and data analysis performed by Monica Clements. Thank you to Mrs. Elsa Malherbe and Dr. Jaco Brand at the Central Analytical Facilities (CAF) for assisting with NMR data generation, as well as their interest in my work. Thank you to Dr. Marietjie Stander and Mr. Malcolm Taylor at the Mass Spectrometry unit of CAF, for analysing my samples. I would like to thank our collaborator, Prof. Ana Martínez, at the Instituto de Química Medica-CSIC in Madrid, Spain for the biological GSK-3 enzyme assays and the reversibility studies. I would also like to acknowledge the technical staff of the De Beers building for a job well-done, and their kindness and willingness to assist with chemicals and equipment.

Lastly, a special thank you to my husband and dearest parents, family, and friends for their support and patience.

— You are never too old to set another goal or to dream a new dream —

C.S. Lewis

— Ek kyk op na die berge: Waarvandaan sal daar vir my hulp kom? My hulp kom van die Here —

Ps. 121, 1–2

Acknowledgements for funding

The financial assistance of the National Research Foundation (NRF) towards this research is acknowledged, and I would like to express my gratitude for the Innovation Master's Scholarship over the period 2017 – 2018.

I would also like to thank Stellenbosch University for their contribution to funding, in the form of a Postgraduate Merit Bursary.

Table of Contents

Chapter 1: The pathogenesis of Alzheimer's disease and the search for drug therapies

1.1 Introduction: Alzheimer's Disease

Alzheimer's disease (AD) is the most prevalent form of dementia and has been proposed to contribute to 60 – 70% of dementia cases.[1] Other forms of dementia include frontotemporal dementia, dementia with Lewy bodies, vascular dementia and dementia due to Parkinson's disease.[2] Dementia is a syndrome caused by chronic or progressive disease in the brain, which impairs memory, as well as one or more domains of cognitive functioning, such as comprehension, language, judgement, personality and orientation. These impairments are often accompanied by a decline in emotional and behavioural control. As a result, a patient's level of functioning and ability to perform daily activities are decreased.[2,3]

As the predominant form of dementia, AD is thus defined as a progressive neurodegenerative disease with clinical symptoms of memory loss and cognitive decline, which is characterised at the molecular level by deposits of intracellular neurofibrillary tangles (NFTs) and extracellular β-amyloid (Aβ) plaques (insoluble proteins) in the brain.[4] The pathogenesis of the disease results in a loss of neurons and neuronal processes in, primarily, the cortical regions of the brain, which results in a decreased brain volume.[5,6] Within only a few years, AD patients can no longer function independently, creating great challenges and suffering for the AD individuals, as well as their families.

AD is a global challenge in terms of health care and is associated with enormous societal costs. The global impact of dementia was analysed by Alzheimer's Disease International in the World Alzheimer Report of 2015.[7] In 2015, 46.8 million people were estimated to live with dementia globally, of which 4 million people were living in Africa. The total economic cost of dementia worldwide was estimated to amount to US $818 billion. Currently there is no cure for AD and other forms of dementia, and the number of dementia cases has been estimated to increase to 74.7 million by 2030.[7] Due to the global effect of dementia on patients, family members, care-givers, health systems and the economy, dementia has been declared a public health priority by the World Health Organisation.[1] As a result, research on dementia and AD has also been prioritised.

In order to develop potential drug therapies for AD – which can either prevent the onset of AD, delay the progression of the disease or act as curative treatment – the possible causes of AD have been explored, based on the associated molecular mechanisms and neuropathological hallmarks of the disease.

1.2 The main neuropathological hallmarks of the disease

The characteristic neuropathological hallmarks of AD have been well defined by histopathological examinations of the AD brain, at autopsy. On an anatomical level, cerebral atrophy as a result of neuronal loss, as well as the loss of synapses and dendritic spines (responsible for signal transduction), have been observed.[5] At the microscopic level, the main neuropathological hallmarks of AD are the deposits of intracellular neurofibrillary tangles (NFTs) and extracellular β-amyloid (Aβ) plaques.[4] It is the accumulation of these deposits which damages neurons, leads to synaptic dysfunctions, and in the case of Aβ plaques, also promotes local microglial- and astrocyte-mediated inflammation which can result in the further degeneration of neurons.[8,9]

1.2.1 Extracellular β-amyloid plaques

The extracellular β-amyloid plaques consist of aggregated Aβ peptides (38 – 43 amino acids), which are formed by the proteolytic cleavage of β-amyloid precursor protein (APP).[10] APP is a type-1 transmembrane glycoprotein expressed in many peripheral organs. In the brain, APP and its cleaved products have shown to contribute to neurogenesis, plasticity, synaptic function, lipid homeostasis and cellular stress response.[11]

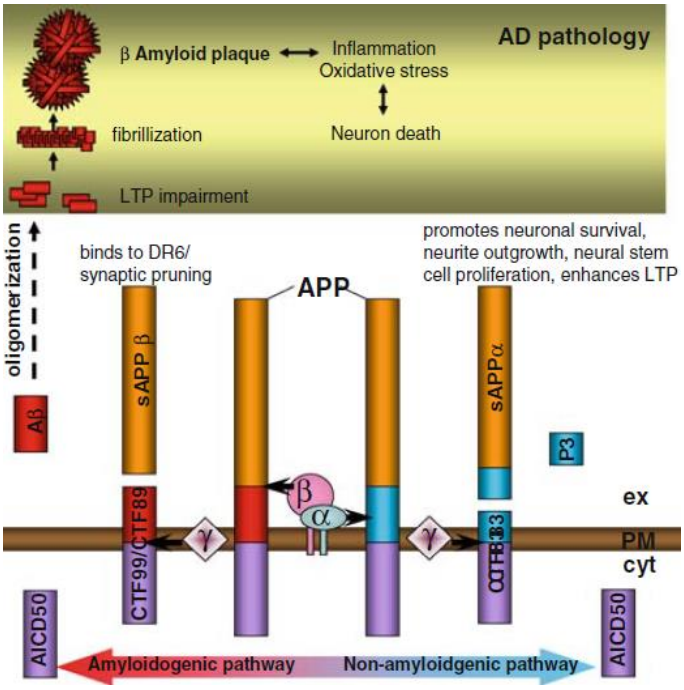

Figure 1.1: Aβ peptides are generated when APP is cleaved by β-secretases and y-secretases in the amyloidogenic pathway. Aβ peptides aggregate to form β amyloid plaques. In the non-amyloidogenic pathway, α-secretases cleave the Aβ sequence (figure obtained from Chow et al.[10]). PM: plasma membrane; ex: extracellular; cyt: cytosol; LTP: Long-term potentiation; CTF 83/p3/AICD50/CTF 99/CTF 89: C-terminal fragments; sAPPα/sAPPβ: N-terminal fragments.

APP processing can follow either the amyloidogenic or non-amyloidogenic pathway (Figure 1.1). The canonical amyloidogenic pathway (that is, β-amyloid plaque producing) leads to Aβ peptide formation and in this pathway, β-secretases and γ-secretases are responsible for proteolytic cleavage.[11] The nonamyloidogenic (non-Aβ-producing) pathway involves cleavage of APP by the α-secretase enzyme. The cleavage site of this enzyme is located within the Aβ sequence of the APP protein, and as a result cleavage by α-secretase will prevent the formation of Aβ peptides.[10]

β-site APP-cleaving enzyme 1 (BACE 1) is the prime enzyme responsible for β-secretase activity in the amyloidogenic pathway.[12] BACE 1 reaches the plasma membrane (where the transmembrane protein, APP, is located) by trafficking in endocytic pathways, but is recycled rapidly, thereby limiting BACE 1 activity with APP at the plasma membrane.[10] Of additional interest is that the activity of the BACE 1 enzyme is promoted by the low pH in endosomes and intracellular compartments.[12]

Thus, the amyloidogenic pathway commences primarily with the internalisation of the APP protein into an endosome. In early endosomes, APP is cleaved by β-secretases to release a soluble amino-terminal fragment, sAPPβ, and a C-terminal fragment (CTFβ), either CTF99 or CTF89, depending on the cleavage site.[10] sAPPβ can be reinserted into the plasma membrane by endosome recycling, whereas CTFβ is internalised further to late endosomes, lysosomes, the *trans*-Golgi network, endoplasmic reticulum (ER) and multivesicular bodies (MVBs). γ-Secretases are active in these compartments, with high activity in especially the *trans*-Golgi network and the mitochondria-associated endoplasmic reticulum membrane.[11] CTFβ is cleaved by γ-secretases *via* endoproteolytic ε-cuts, to form Aβ49 and Aβ48 peptides. These peptides are then sequentially trimmed by γ-secretases to generate Aβ peptides ranging from 38 to 43 residues in length (Figure 1.2).[13] Thereafter, the Aβ peptides are transported into the extracellular space by exocytosis, where accumulated Aβ peptides may aggregate to form Aβ oligomers and amyloid plaques.[11]

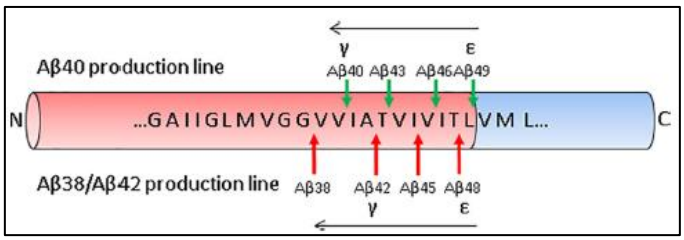

Figure 1.2: γ-Secretases initially cleave CTFβ at the ε-sites to form the Aβ49 and Aβ48 species. Sequential trimming by γ-secretase produces shorter Aβ peptides, such as Aβ40, Aβ38, and Aβ42 (figure obtained from Andrew et al.[14]).

Unfortunately, the understanding of APP processing pathways in neurodegeneration and β-amyloid plaque formation is complicated by the subcellular localization of enzyme processes, the activities of

APP metabolites and the alternative substrates of APP-cleaving enzymes.[10] Furthermore, Aβ peptides are subjected to post-translational modifications, which can change the toxicity, fibril-forming and oligomerisation properties of the Aβ peptide.[11] Also, the complexity of the accepted model of APP proteolytic cleavage has increased due to the discovery of novel noncanonical APP enzymes, δ-secretase, η-secretase, meprin-β and cathepsin B, which can also partake in proteolytic cleavage of APP to produce potentially toxic metabolites in the brain.[14]

1.2.1.1 The link between Aβ peptides and neurotoxic effects

The normal amyloidogenic APP pathway produces predominantly Aβ40 peptides (~ 90%), together with Aβ42 (~ 5 – 10%) and other minor Aβ species.[15] The Aβ40 peptides have been proposed to be less amyloidogenic than Aβ42, Aβ43, and longer Aβ peptides, which are more hydrophobic and highly self-aggregating.[13] Indeed, increased extracellular concentrations of Aβ42 have been shown to promote amyloid deposition, whereas high levels of Aβ40 have demonstrated to inhibit Aβ deposition.[15,16] Thus, increased ratios of Aβ42 and highly self-aggregating Aβ peptides relative to Aβ40, result in amyloid plaque formation and neurotoxicity.[13]

Several types of Aβ peptide assemblies have been identified in the human brain, referred to as amyloid plaques (aggregates of amyloid fibrils) and Aβ oligomers (e.g. dimers, trimers, dodecamers).[11] In the literature, Aβ oligomers have been described to be more neurotoxic than amyloid plaques.[17] Soluble Aβ oligomers that are not confined to amyloid plaque surfaces, are able to disperse into brain tissue, where it can exhibit high levels of neurotoxicity by impairment of synaptic functions and synaptic structures.[13,17]

In general, many studies have provided evidence that increased production of neurotoxic Aβ peptides or failure in Aβ peptide clearance mechanisms, can lead to oligomerisation and amyloid plaque formation.[13]

1.2.2 Intracellular neurofibrillary tangles

The presence of intracellular neurofibrillary tangles (NFTs) is the other major neuropathological hallmark associated with AD. NFTs are formed when tau proteins are hyperphosphorylated. Tau proteins are microtubule-associated proteins (MAP) and associate via certain sequence motifs to tubulin in order to stabilise cytoskeletal microtubules in central nervous system (CNS) nerve cells. When tau proteins are hyperphosphorylated, tau-microtubule associations are disrupted, which result in the detachment of tau proteins and microtubule degeneration. The tau proteins then pair up with other threads of tau protein to form paired helical filaments (PHFs) and straight filaments (SFs), which accumulate to form insoluble tangles inside the affected cell.[18,19]

Tau proteins are generally axonal proteins, i.e. proteins that stabilise microtubules in the axon of the neuron. However, the hyperphosphorylation of tau proteins results in the movement of detached tau proteins from the axon to the somatodendritic compartment of the neuron, where the tangles accumulate and deposit as insoluble aggregates (Figure 1.3).[11] These abnormal deposits in the somatodendritic compartment disrupt neuronal communication and vital physiological functions, by sequestering stabilising proteins and obstructing other proteins, such as kinesins and dynamins, which are responsible for neuronal transport.[11] General cytoskeletal dysfunction takes place, due to microtubule degeneration and microtubule transport inhibition, which impedes the transport of organelles and endocytic vesicles.[20]

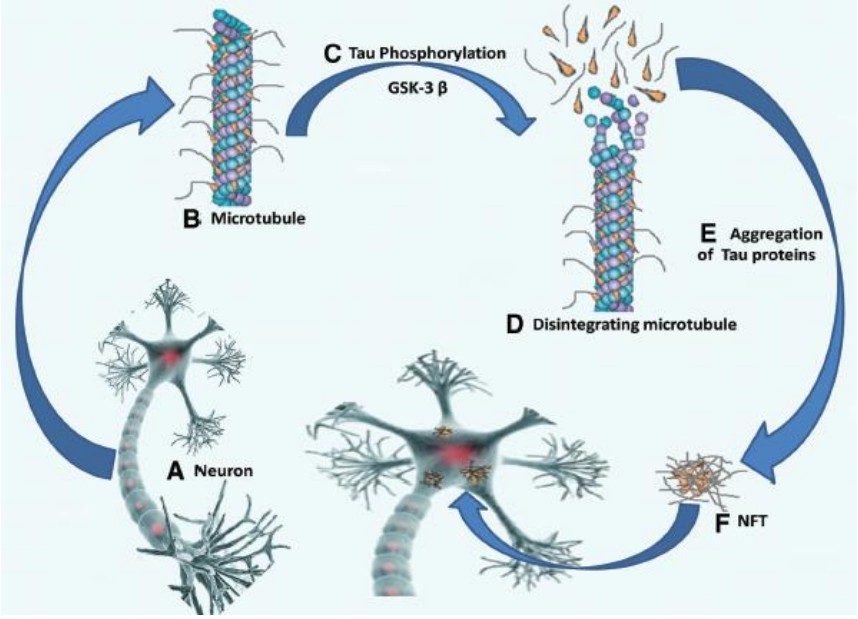

Figure 1.3: The hyperphosphorylation of tau proteins results in NFT assembly. A: CNS neuron, B: Tau proteins stabilise axonal microtubules, C: Hyperphosphorylation of tau protein by a protein kinase, e.g. GSK-3β., D: Hyperphosphorylated tau detaches from the microtubule, causing microtubule degeneration, E: Tau proteins pair-up, tangle together and aggregate, F: The insoluble NFTs accumulate in the somatodendritic compartment of the neuron (Figure is reproduced from Dubey et al.[21]).

In vivo studies have also suggested that soluble tau oligomers, which precede NFTs, are neurotoxic, and that they contribute to synaptic and mitochondrial dysfunction, as well as memory loss, before they aggregate into fibrils to form NFTs.[22] Fibril formation is characterised by an increase in β-sheet structure, in contrast to tau proteins which are soluble, natively unfolded proteins with limited secondary structure.[23]

Although tau is principally known to become dysfunctional by hyperphosphorylation, abnormal post-translational modifications such as acetylation, carboxy-terminal truncation by caspase 3, and *N*-glycosylation have also been reported to result in tau aggregation.[19,20] These post-translational events were identified by the comparison of tau proteins from the brains of AD patients and cognitively-healthy elderly persons.[20]

Tau phosphorylation is one of the earliest modifications that occur in the AD brain.[19,24] Braak and Braak performed a study in which the six well-defined stages of NFT and neuropil thread deposition were observed.[25] The deposits resulted in an increase in cortical destruction, which was mirrored by a worsening in clinical AD symptoms.[6] Stages I – II corresponded to pathological changes in the transentorhinal region of the brain, and these stages developed preferentially in the absence of Aβ deposits.[24] Stages III – IV entailed the distribution of the tangles into both the entorhinal and transentorhinal regions, whereas stages V – VI were characterised by isocortical destruction.[6] In contrast, a corresponding study on the stages of β-amyloid plaque deposition depicted an inconsistent relationship between the number of amyloid deposits and clinical severity.[6]

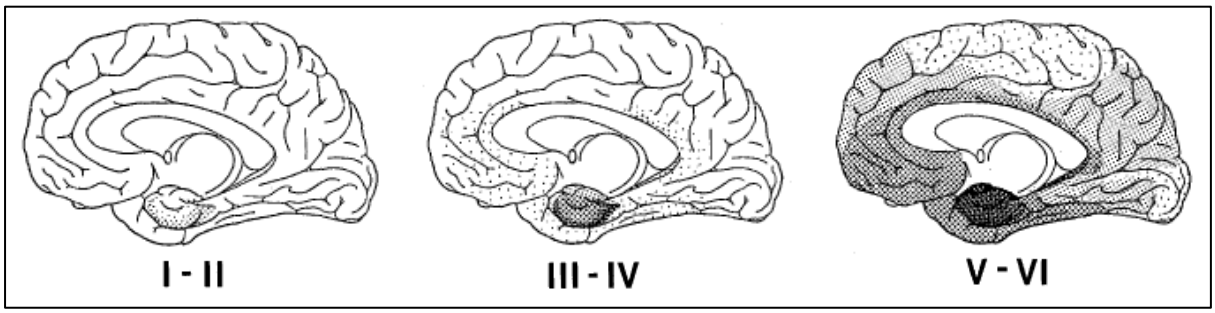

Figure 1.4: Tangle distribution during different stages of continual AD progression (image obtained from Braak and Braak.[25])

The characteristic pattern of tau pathology and its correlation with clinical symptoms in AD, have thus made NFTs an important hallmark of the disease.

1.2.3 Translating neuropathological hallmarks to the molecular mechanism of AD

The underlying mechanisms and factors which induce the accumulation of extracellular and intracellular fibrillary proteins in AD are not fully understood.[8] Multiple factors, including aging, genetic factors, chemical factors, infectious agents, vascular disturbances, pre-existing syndromes, immune system dysfunctions, mitochondrial dysfunctions, nerve growth factor disruptions and other environmental factors have been hypothesised to induce pathways leading to Aβ peptide production, amyloid deposits and NFT formation.[8,26]

1.3 Risk factors for AD

The cause of AD is multifactorial and has been proposed to be influenced by a complex combination of several genetic, epigenetic and environmental factors. Aging is the predominant risk factor for AD, while numerous environmental factors have also been proposed to contribute to late-onset AD, including head injury, diabetes, obesity, hyperlipidemia, hypertension and low education levels.[5]

Early-onset AD is found in only 1 – 5% of AD patients and refers to the clinically observable onset of AD disease in an adult before the age of 65.[27,28] This type of AD is often found in patients with a family history of AD, Down's syndrome or lymphoma, and the disease progress is relatively rapid. In contrast, AD with a late onset refers to the beginning of the disease after the age of 65. Usually, the disease only commences in the late 70s or thereafter, and deterioration usually takes place slower.[3] More than 95% of AD cases have a late onset and therefore support aging as a major risk factor.[27]

1.3.1 Genetic aspects in early-onset AD

92 – 100% of early-onset AD cases are inherited (familial AD), but only approximately 10% of these early-onset AD cases (that is <1% of all early- and late-onset cases) could be directly linked to autosomal dominant inheritance due to mutations in the APP, presenilin-1 (PS-1) and presenilin-2 (PS-2) genes.[28,29] AD-causative mutations in the APP gene, and the location of the APP gene on chromosome 21, furthermore explained the high incidence of AD-like brain pathology detected in aged Down syndrome patients with a trisomy 21.[28] The PS-1 gene located on chromosome 14 displays the highest mutation frequency, and more than 100 mutations have been identified in this gene.[27] The PS-2 gene is located on chromosome 1 and mutations in this gene are more rare. PS-1 and PS-2 mutations result in aberrant γ-secretase activity, which activates the amyloidogenic APP processing pathway, resulting in increased levels of neurotoxic Aβ42 peptides.[28] The rest of the early-onset AD cases are genetically unexplained and could potentially be connected to epigenetic dysregulations and undetected genetic alterations.[30]

1.3.2 Genetic and non-genetic aspects in late-onset AD

Late-onset AD (>95% of AD cases) has a complex etiology, which has been linked to genetic and non-genetic factors. Late-onset AD has been found to have a highly polygenic mechanism of inheritance, with a heritability of approximately 70%.[29] Wingo and co-workers[29] also found that heritability decreases with age of AD onset, implying that AD onset at older ages correlates more strongly to non-genetic environmental causes.[29]

Risks for sporadic forms of AD (i.e. with no family history) have been connected to aging, the presence of apolipoprotein E4 (apoE4), vascular disturbances and environmental/lifestyle factors.

ApoE is a polymorphic protein, with three common alleles—apoE2, apoE3 and apoE4—which can occupy the gene's locus. It has been estimated that individuals with two copies of the apoE4 allele (homozygotes) have a ~60% risk of developing AD by the age of 85, whereas the chance is reduced to ~30% for apoE4 heterozygotic individuals.[5] ApoE4 proteins decrease Aβ clearance, thereby increasing amyloid deposition. Furthermore, it has been suggested that brain stress responses and injuries can amplify neuronal apoE production, to induce repair and remodelling. The process also involves proteolytic cleavage; however, apoE4 species are more susceptible to truncation than apoE3. Thus, in individuals with apoE4, high levels of neurotoxic apoE4 fragments are produced. These apoE4 fragments have been connected to tau pathology and mitochondrial dysfunction.[5]

A third of AD cases worldwide can be related to vascular disturbances and environmental/lifestyle factors.[31] These factors often co-exist with genetic factors across the life-span, thereby increasing AD risk. Vascular disturbances and environmental/lifestyle factors are considered modifiable risk factors, which can be altered through lifestyle changes or pharmacological treatment.[32] Major protective factors which may reduce AD risk, include education, physical activity, improved socioeconomic factors, diet and medical care. Ultimately, the interplay of risk factors and protective factors impacts the overall risk for late-onset AD (Figure 1.5).[32]

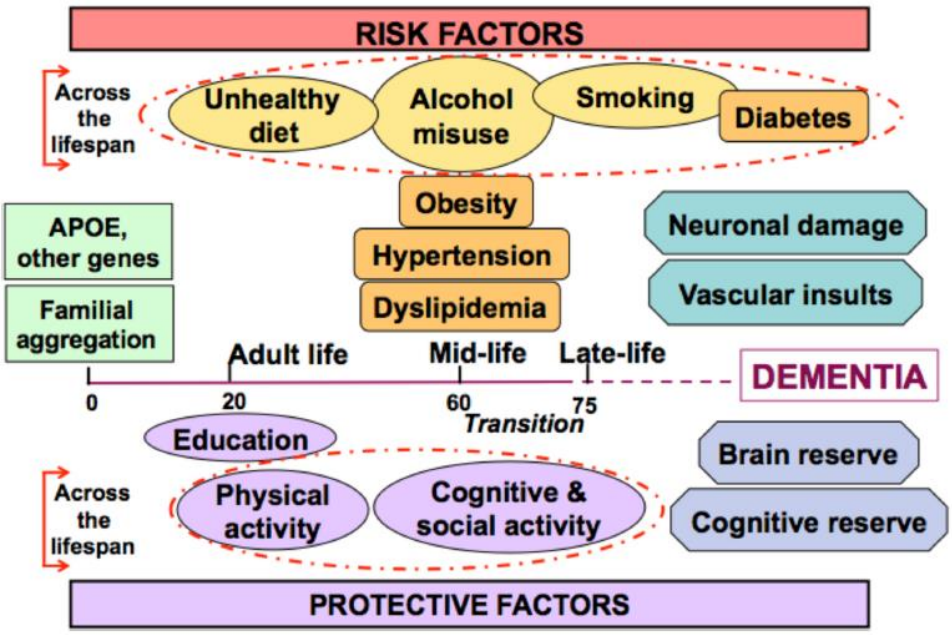

Figure 1.5: Major vascular and lifestyle-related risk factors, as well as protective factors across the lifespan, associated with late-onset AD (figure obtained from Sindi et al.[32]).

1.4 Therapeutic drug developments: Major strategies

The neuropathology of the AD brain and the links between risk factors and AD pathogenesis, had led to several hypotheses for the origin and mechanism of AD development, which have influenced the choice of drug targets and the design of novel drug candidates in therapeutic drug development. No curative treatment has been found for the disease yet and no new drugs have been approved for AD treatment since 2003, making drug development for AD a priority.[33] Next, the major areas for therapeutic development over the past years will be discussed.

1.4.1 Cholinergic drug therapies

From AD neuropathological findings, the cholinergic hypothesis was the first to emerge (1976) and was based on the early loss of cholinergic neurons in the basal forebrain of AD patients.[34,35] Cholinergic neurons use the neurotransmitter, acetylcholine, to transmit chemical signals. Thus, the loss of cholinergic neurons and the deficiency in acetylcholine decrease neurotransmittance and result in cognitive decline and memory impairment.[36] Drug development following the cholinergic hypothesis focused firstly on acetylcholinesterase (AChE) inhibitors, and secondly on the design of acetylcholine-receptor agonists. AChE inhibitors can reduce the normal levels of acetylcholine cleavage by AChE in the synaptic space, thereby resulting in enhanced acetylcholine response. Alternatively, acetylcholine-receptor agonists can enhance acetylcholine responses in postsynaptic neurons, thereby accounting for lowered levels of acetylcholine.[37]

1.4.1.1 AChE inhibitors

Four AChE inhibitors (Donepezil, Rivastigmine, Galantamine and Huperzine-A) have been successfully developed and clinically approved, but these cholinergic drugs are symptomatic therapeutics and result temporarily in slight cognitive and behavioural enhancement (Figure 1.6).[34] Initially, tacrine (1993) was the first AChE inhibitor to be FDA approved; however, the drug was soon withdrawn from the market due to liver toxicity. Apart from low organ specificity, the first generation AChE inhibitors lacked selectivity for acetylcholine — they also inhibited butyrylcholinesterase (BuChE). Therefore, the second generation AChE inhibitors (incl. Donepezil, Galantamine, Huperzine-A) were focused mainly on improving AChE selectivity.[8] Rivastigmine, notably, inhibits both AChE and BuChE, but specifically in brain tissue. The drug's slowly reversible (pseudo-irreversible) binding mode inactivates the enzymes for a prolonged time, which allowed Rivastigmine to have a low protein-binding profile (low risk).[38] Octohydroaminoacridine succinate is another example of an AChE inhibitor and is currently in phase III trials (Figure 1.6).[33,39]

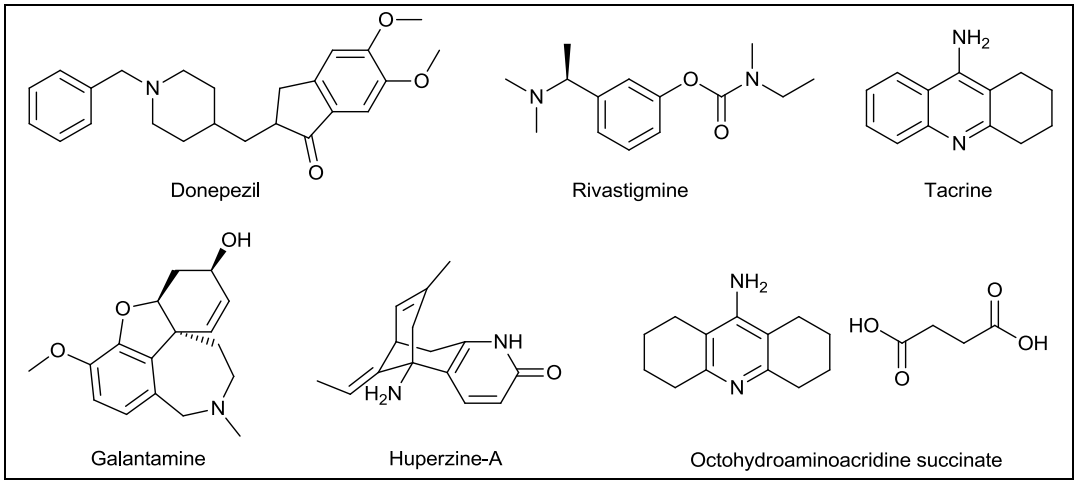

Figure 1.6: The structures of the discussed AChE inhibitors.[8,39] Donepezil, Rivastigmine, Galantamine and Huperzine-A are clinically approved symptomatic treatments.

Although the drugs following the cholinergic hypothesis are symptomatic therapeutics, drug development in this pipeline is still ongoing, in order to provide more effective symptomatic treatments to the more than 15 million people already affected by AD worldwide, especially for patients in the moderate to advanced stages of the disease.[33] As mentioned, drug development based on the loss of cholinergic neurotransmission has not only been focused on AChE inhibitors, but also the design of acetylcholine-receptor agonists (activators) and 5-HT6/H3 receptor antagonists (which block or reduce response).

1.4.1.2 Acetylcholine-receptor agonists

The activation of muscarinic and nicotinic acetylcholine-receptors has been proposed to enhance levels of acetylcholine response, which may temporarily improve cognition and memory. M1 muscarinic acetylcholine-receptor modulators in phase II and III clinical trials have displayed promising efficacy in cognition, but presented acute adverse effects including gastrointestinal symptoms, increased salivary flow, sweating and frequent urination, which generally limited the success of these compounds.[40] Nicotinic acetylcholine-receptor agonists also resulted in cognitive enhancement, but of even greater interest was that *in vivo* studies demonstrated that nicotinic acetylcholine-receptors were also involved in positive Aβ detoxification mechanisms, making it a more attractive pharmacological target. The nicotinic receptors act as carrier proteins in the binding of extracellular Aβ, to facilitate autophagic degradation and to reduce Aβ neurotoxicity.[41] Encenicline (EVP-6124) and Ispronicline (AZD-3480) are examples of nicotinic receptor agonists which had reached phase III and phase II trials, respectively (Figure 1.7).[8,42] However, trials on Encenicline were paused due to serious gastrointestinal side effects.[8] Ispronicline is also no longer in clinical trials, and the recent clinical results are not yet available.

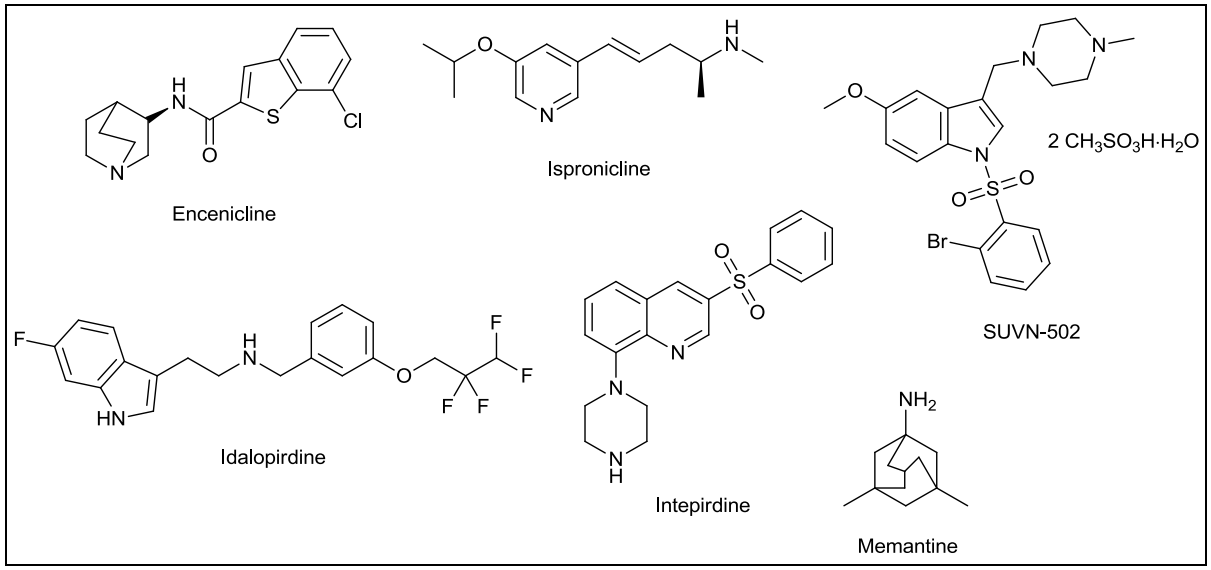

Figure 1.7: The structures of selected acetylcholine receptor agonists and 5-HT6/H3/NMDA receptor antagonists.[8,42–45]

1.4.1.3 5-HT6/H3 receptor antagonists

Serotonin (5-hydroxytryptamine, 5-HT) is involved in the regulation of multiple signalling pathways, with the serotonergic neuron network distributed throughout almost all the brain structures. Imbalanced serotonergic signalling has been related to AD, and the 5-HT6 receptor subtype is specifically involved in memory and cognition.[8] Furthermore, blockage of the 5-HT6 receptors enhances cholinergic transmission and several 5-HT6 receptor antagonists have been included in clinical trials.[37] In 2017, Idalopirdine (Lu AE58054) and Intepirdine (RVT-101) failed in phase III trials due to primary efficacy endpoints that were not met, despite the promising efficacy and safety results in phase II (Figure 1.7).[33,37,43,44] SUVN-502 is another potent, selective and orally active antagonist currently in phase II clinical trials.[8,33,45]

Histamine H3 receptors are expressed mainly in the CNS, and the blockage of these receptors enhances presynaptic release of histamine and other neurotransmitters such as acetylcholine.[37] Needless to say, H3 receptor antagonists were developed and included into clinical trials.

1.4.2 Glutamatergic neurotransmission

Aberrant stimulation of *N*-methyl-*D*-aspartate (NMDA) glutamate receptors, which are a major class of receptors in the mammalian brain, results in increased concentrations of intracellular Ca^{2+} which can be excitotoxic to neurons. The degeneration of glutamatergic pathways early in AD was confirmed by neuropathological and neurochemical studies, and follow a pattern that corresponds to the deposition of β-amyloid plaques and NFTs.[46] Memantine is the only NMDA antagonist on the market

and is the most recently (2003) FDA approved AD drug (Figure 1.7). Memantine provides temporary improvements in cognition, behaviour and functional state in AD patients with moderate to severe AD.[8,34]

1.4.3 Moving from symptomatic treatments to disease-modifying therapeutics

The palliative nature of drugs developed alongside the cholinergic hypothesis and glutamatergic neurotransmission theory necessitated a re-assessment of the hypothesis of AD pathogenesis. The development of disease-modifying therapeutics (DMTs) which can intervene in primary molecular mechanisms of AD is necessary to prevent or delay the onset/progression of the disease. In order to target primary molecular mechanisms, alternative AD hypotheses and drug development strategies were focused on the major neuropathological hallmarks of the disease, i.e. β-amyloid plaques and NFT formation.

1.4.4 Anti-amyloid drug therapies

The amyloid cascade hypothesis has dominated research in the AD therapeutic development pipeline and the choice of pharmacological targets since its proposal in 1991, by Hardy and Allsop.[47] The hypothesis was grounded on one of its major neuropathological hallmarks—extracellular β-amyloid plaque deposits—in the AD-affected brain, as well as the amyloidogenic pathway associated with the formation of Aβ peptides and β-amyloid plaques. The amyloid cascade hypothesis proposed that Aβ peptide overproduction occurs very early in the disease pathology and that it further drives β-amyloid plaque formation, tau hyperphosphorylation, NFT formation, inflammatory responses and neurotoxicity, leading to progressive neuronal death.[40]

Aβ peptides are produced mainly through the canonical amyloidogenic pathway, through sequential cleavage of APP by β- and y-secretases (as explained in Section 1.2.1, Figure 1.1). The amyloid cascade hypothesis has further been connected to an imbalance in Aβ42 peptide ratio relative to other Aβ species, which is proposed to induce Aβ accumulation and oligomerisation in AD pathology. Progression in Aβ accumulation was proposed to translate directly to increased clinical symptoms.[13]

Therapeutic strategies have focused mainly on the inhibition of Aβ peptide production or the removal of Aβ peptides, with the major strategies pertaining to β-secretase inhibitors, y-secretase inhibitors, α-secretase activators and anti-aggregants. Active and passive immune-mediated mechanisms have been explored to inhibit Aβ generation or to promote Aβ peptide clearance, which included the use of Aβ-binding antibodies or the phagocytosis of opsonised Aβ peptides.[34] In January 2018, clinical trial activities, based on the annual review by Cummings *et al.*,[33] comprised 14 (54%) anti-amyloid agents in phase III, 18 anti-amyloid agents in phase II, and 5 in phase I. These anti-amyloid agents included

mainly immunotherapies, BACE inhibitors (β-secretase 1 inhibitors) and anti-aggregation drug candidates.

1.4.4.1 β-secretase (BACE) inhibitors

β-secretase inhibitors have been developed to interfere in the Aβ producing amyloid cascade, in which APP is cleaved by β-secretase. β-site APP-cleaving enzyme 1 (BACE 1) is the prime enzyme responsible for β-secretase activity in the amyloidogenic pathway. The development of these inhibitors has proved to be challenging since the enzyme has several cellular substrates apart from APP, due to its role in other physiological processes required to maintain cognitive function.[48] Furthermore, BACE inhibitors must be able to penetrate the blood-brain barrier to modulate the enzyme's activity.[34] The first-generation BACE inhibitor, BI 1181181 (structure not yet disclosed), was orally administered, but was suspended in the third round of phase I trials due to side-effects (skin reaction).[49] The second-generation BACE inhibitors failed due to liver toxicity, whereas several third-generation BACE inhibitors (e.g. E2609, AZD3293, CNP520, JNJ-54861911) have now reached phase III clinical trials (Figure 1.8).[33,37,50,51] Verubecestat (MK-8931) is an orally active small-molecule BACE inhibitor which successfully reduced Aβ levels in the cerebrospinal fluid of AD patients in early clinical trials. However, Verubecestat resulted in much disappointment when the drug failed in phase III, due to overall futility (lack in the reduction of cognitive and functional decline 50 months after onset) and adverse side-effects.[52]

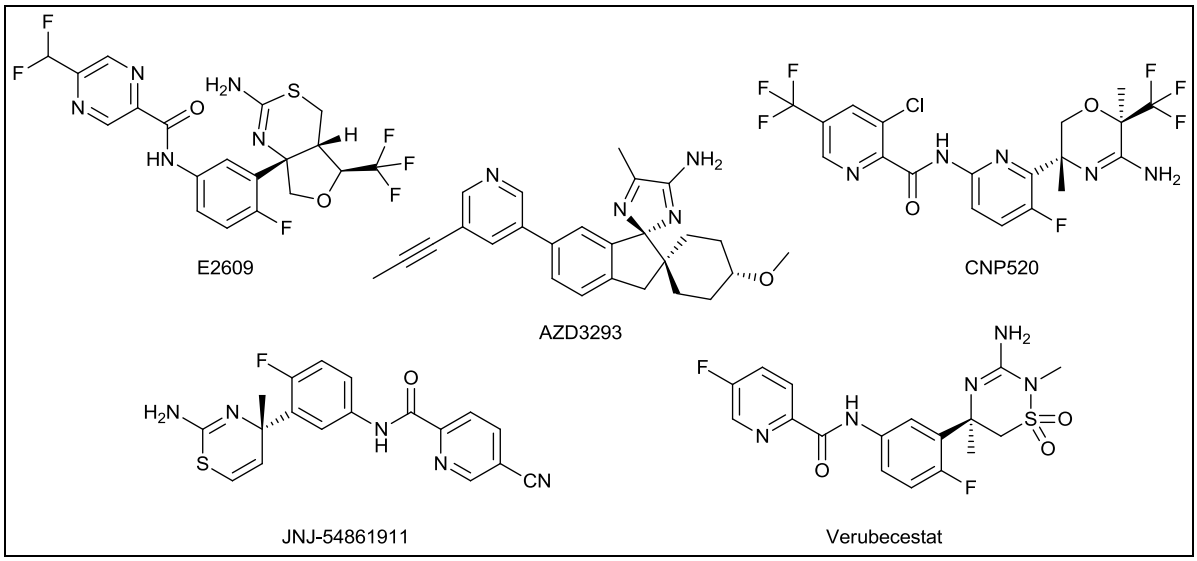

Figure 1.8: The structures of some third-generation BACE-inhibitors in clinical trials[8,50,51,53]

1.4.4.2 γ-Secretase inhibitors

After cleavage by BACE, γ-secretase participates in the final cleavage steps to generate Aβ from APP. However, γ-secretases also facilitate the intramembranous cleavage of the Notch protein and several other substrates, including ErbB4, p75NTR, neurotrophin receptor, N-cadherin and the β4 sodium channel subunit, which complicates γ-secretase inhibitor development.[34] Unselective γ-secretase inhibitors have been associated with hematological toxicity, gastrointestinal side-effects, hair-colour changes and skin reactions, mainly due to the concomitant inhibition of the Notch signalling pathways which further affects cell differentiation.[34] Several γ-secretase inhibitors with increased selectivity, have reached clinical trials and have successfully reduced Aβ levels in the plasma or cerebrospinal fluid of patients, but unfortunately, serious adverse events accompanied these studies. Semagacestat (Figure 1.9) is the only agent to have reached phase III trials thus far and was withdrawn in 2010 due to futility, dose-related worsening of functional ability and serious side-effects (e.g. skin cancer, weight loss, infections).[54,55] More concerning is that the amyloid-level reductions induced by Semagacestat did not result in any significant effects/changes in brain-imaging studies.

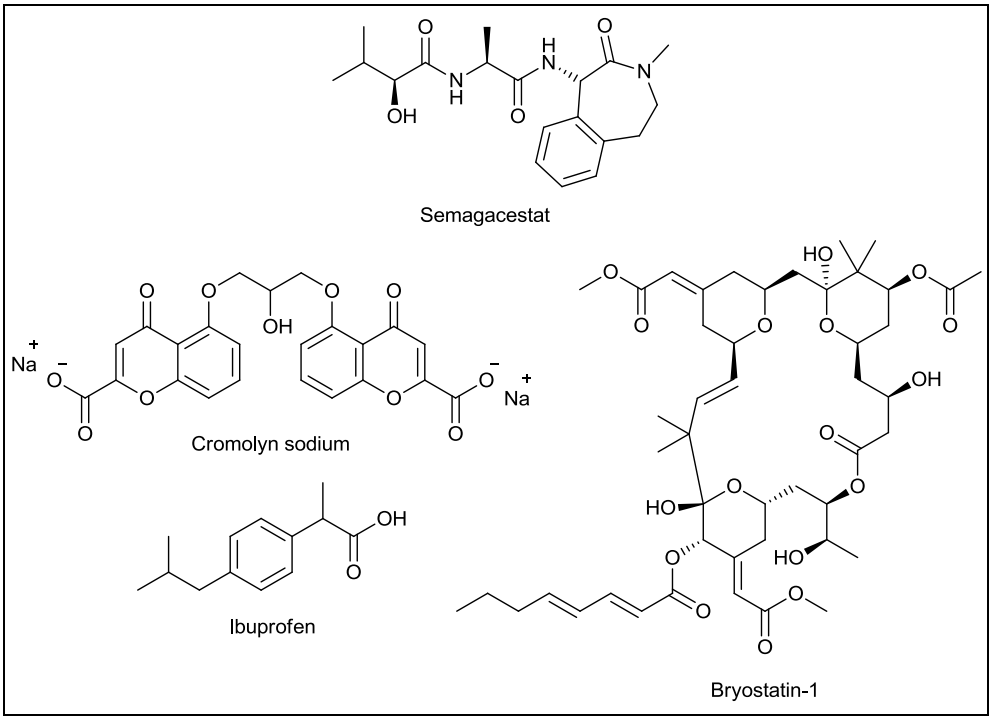

Figure 1.9: The structures of γ-secretase inhibitor, Semagacestat, protein kinase C activator, Bryostatin-1, and anti-aggregant ALZT-OP1 (Cromolyn sodium + Ibuprofen).[8,55,56]

1.4.4.3 α-Secretase activators

α-Secretase partakes in the non-amyloidogenic pathway of APP processing and cleaves APP within the Aβ sequence, as described in Section 1.2.1. Therefore, the upregulation of α-secretase activity is proposed to reduce the levels of Aβ peptide production. For example, Bryostatin-1 (Figure 1.9) activates protein kinase C and sAPPα excretion, which further stimulates α-secretase activity. This agent recently completed phase IIa clinical trials and was well tolerated in AD patients.[8,34,57]

1.4.4.4 Anti-aggregants

Anti-aggregants are focused on the development of drugs that will prevent Aβ peptide aggregation and plaque formation. The neurotoxicity of Aβ oligomers in synaptic function is well known, therefore anti-aggregants are also aimed at destabilising Aβ oligomeric species.[17,34] This strategy is mainly focused on the design of small-molecules or peptides that can bind and stabilise Aβ monomers, to prevent oligomerisation and rather accommodate natural Aβ clearance mechanisms. Other strategies are aimed at the neutralisation of toxic Aβ assemblies, by binding to them and promoting clearance mechanisms.[58] Challenges encountered in the design and clinical trials of anti-aggregants include limited knowledge on the molecular structure of the target, uncertain modes of action, selectivity challenges, modest potencies and brain-blood barrier permeability challenges.[58] ALZT-OP1 is currently in phase III clinical trials and is a combination drug therapy comprised of Cromolyn sodium and Ibuprofen (Figure 1.9). Cromolyn sodium, a small-molecule known for its anti-inflammatory effect in asthma treatment, was found to inhibit Aβ monomer aggregation *in vitro* and to reduce soluble Aβ levels in the brain *in vivo*.[56] Another promising candidate is the oligosaccharide drug, sodium oligo-mannurarate (GV-971), which recently completed phase III clinical trials. This orally active drug successfully reached its efficacy end points in phase III trials and works through a multi-targeting mechanism to inhibit Aβ fibril formation and decrease neuroinflammation.[59]

1.4.4.5 Immunotherapy

Immune-mediated mechanisms investigated in AD drug development include the use of antibodies to solubilise Aβ peptides through binding, the use of plasma antibodies to extract Aβ peptides from the brain, or to opsonise Aβ peptides to facilitate phagocytosis.[34] Solanezumab—a monoclonal antibody designed to bind soluble Aβ peptide and facilitate its removal—was a very promising passive immunotherapy developed by Eli Lilly and Company, but failed in three large phase III trials when no significant improvement in cognitive decline and function was observed.[60] The study further highlighted the improbability that the removal of free Aβ peptides from plasma will lead to increased Aβ clearance in the brain (peripheral sink hypothesis).[60] Plenty of research has been devoted to the

development of immunotherapies, with six anti-amyloid immunotherapies in phase III, six in phase II and five in phase I, as determined by Cummings *et al.* in January 2018.[33] These agents include monoclonal antibodies, polyclonal antibodies, amyloid vaccines and other active immunotherapies. CAD-106 (phase III) is an example of an amyloid vaccine. CAD-106 consists of a short $A\beta_{1-6}$ peptide (a specific B-cell epitope) connected to a virus-like QB particle, which elicits the production of Aβ-specific antibodies without uncontrolled T-cell responses (longer Aβ fragments induce uncontrolled immune responses). The Aβ-specific antibodies are proposed to further bind and clear Aβ peptides.[34,37]

1.4.4.6 Conclusion on anti-amyloid drug development

Several drug candidates following the amyloid hypothesis and targeting mild to moderate AD, have failed thus far or have shown controversial results.[19] As in the cases of Tramiprosate (first-generation anti-aggregant), Rosiglitazone (β-secretase inhibitor), Verubecestat (β-secretase inhibitor), Semagacestat (γ-secretase inhibitor), Bapineuzumab (monoclonal antibody) and Solanezumab (monoclonal antibody), the compounds have shown positive results in preclinical, phase I and phase II trials, but have failed in phase III, showing no efficacy or a worsening in cognition.[8,34] These failures have given rise to the reconsideration of the role of β-amyloid deposits in the pathogenesis of AD. As a result, interest has also grown in the tau-based hypothesis, which will be described next.

1.4.5 Tau-centric drug therapies

The tau hypothesis is more recent and focuses on intracellular NFTs as the major contributor to the pathogenesis of AD. The pathology of NFT formation was discussed in Section 1.2.2. The major protein kinases associated with the hyperphosphorylation of tau (>95% of *in vivo* phosphorylation) are glycogen synthase kinase 3 (GSK-3) and cyclin-dependent kinase 5 (CDK-5).[61]

Tau-based drug development has lagged behind Aβ-targeted drugs and the target is relatively unexploited.[19] Therapeutic approaches in this class focus on anti-aggregants, the inhibition of tau-phosphorylating kinases, tau clearance, increased microtubule stabilisation and immunotherapies. Few drug trials have involved tau-centric drugs and only two tau-directed drug candidates, Valproate (GSK-3 inhibitor) and TRx-0237 (aggregation inhibitor) have yet reached phase III clinical trials.[33,34]

1.4.5.1 Anti-aggregants

Based on tauopathies, hyperphosphorylated tau proteins assemble to form paired helical filaments (PHFs) which accumulate into insoluble tangles to form NFTs. Tau protein aggregation inhibitors aim to prevent the aggregation of tau that has been hyperphosphorylated or subjected to abnormal post-translational modifications.[37] Methylene blue (also known as Rember) is a first-generation tau anti-

aggregant which interferes in tau-tau binding, and further displays antioxidant activity and mitochondrial function enhancement (Figure 1.10).[19] In phase II trials, the drug displayed promise in slowing disease progression in patients with moderate AD within 24 weeks; however, bioavailability was low and side-effects included diarrhea, dizziness, painful urination and accidental falls.[37,62] The leuco-form of methylene blue, TRx-0237, replaced methylene blue in clinical trials, since the reduced form is better absorbed in the stomach (Figure 1.10). Although phase III clinical trials are still ongoing, TRx-0237 has completed three phase III clinical studies in which efficacy endpoints were unfortunately not met.[63]

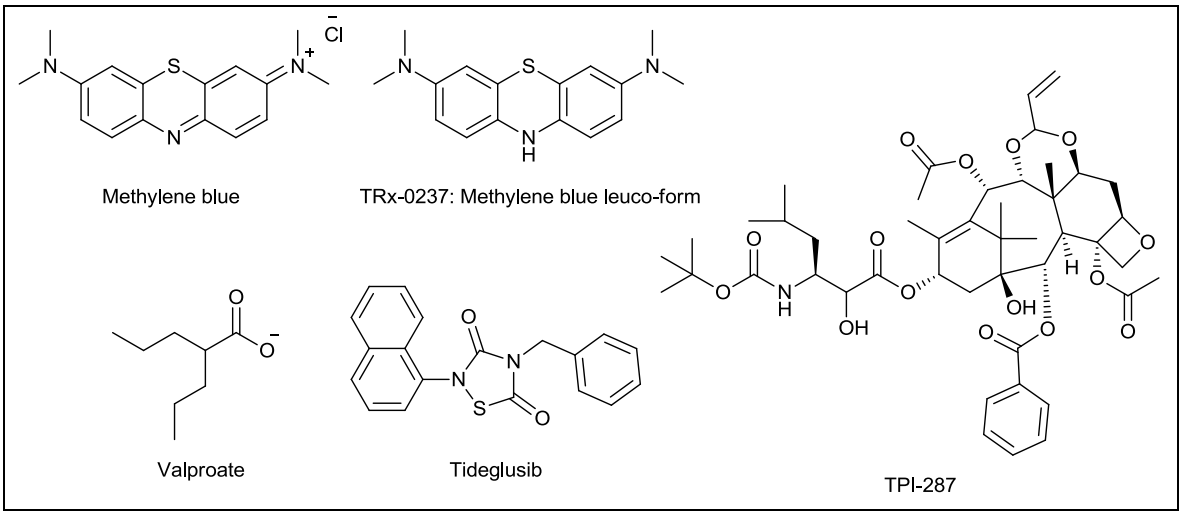

Figure 1.10: The structures of selected tau-centric drug therapies[8,55,64]

1.4.5.2 Kinase inhibitors

Tau-phosphorylating kinases, especially CDK-5 and GSK-3, are often over-expressed/over-activated in the brains of AD patients, resulting in the hyperphosphorylation of tau.[61] Tau-phosphorylating kinase inhibitors are proposed to counteract hyperphosphorylation and NFT formation. Recent years in tau-phosphorylating kinase inhibitor development were thus focused mainly on preclinical efforts to address issues involving toxicity and specificity. The most clinical advances have been made in the development of GSK-3 inhibitors.[65]

Valproate and lithium salts are well-known therapeutics for psychiatric disorders, and additionally, these drugs are also GSK-3 inhibitors known to reduce tau phosphorylation. Valproate reached phase III clinical trials on mild to moderate AD patients. However, results were disappointing with no significant improvements in cognition and function.[34] Preclinical studies with lithium chloride in mice, have shown decreased β-amyloid production due to the inhibition of GSK-3. An *in vivo* reduction of

tau phosphorylation was observed in different animal models. However, the results from AD clinical trials with lithium chloride were controversial due to clinical trial design flaws.[61]

The non-ATP competitive, irreversible GSK-3 inhibitor, Tideglusib (NP-12, Figure 1.10), has shown positive results in animal models, with reductions in tau phosphorylation, Aβ load, neuronal death, and astrogliosis.[20] In phase IIa studies orally administered doses were found to improve the cognitive levels of mild to moderate AD patients; however, efficacy endpoints were unfortunately not met in the phase IIb trials. Ultimately, the drug was well tolerated (safe), but did not result in any clinical benefits.[66]

Tau proteins are also subjected to other post-translational modifications, which can result in tau dysfunction. Therefore, other kinase inhibitors that can target for example tau acetylation, tau deglycosylation and tau truncation, have been explored as possible AD therapeutics.[20]

1.4.5.3 Microtubule stabilisers

Hyperphosphorylated tau proteins detach from microtubules, resulting in microtubule destabilisation. In 2007, Bahr and co-workers[67] conducted a study with a hippocampal slice model in which they firstly proved that a loss in microtubule integrity can contribute to synaptic decline in AD, and secondly that microtubule-stabilising drugs can counteract the synaptic deterioration. As a result, the therapeutic potential of microtubule stabilisers is under investigation. TPI-287, a taxane derivative, is an example of a microtubule protein modulator in phase I clinical trials (Figure 1.10).[33]

1.4.5.4 Immunotherapy

Similar to anti-amyloid strategies, anti-tau immunotherapy holds much potential in AD therapeutic development. Antibodies against phosphorylated, mutant, oligomeric or misfolded tau can reduce pathological tau levels.[20] AADvac-1 was the first tau-vaccine to enter phase I clinical trials (2013) and is currently in phase II.[33,68] The vaccine, AADvac-1, contains synthetic $tau_{294-305}$ peptides based on a regulatory sequence which is essential for oligomerisation in natural tau.[68] The peptides are conjugated to keyhole limpet hemocyanin (KLH) carriers and combined with aluminium hydroxide as an adjuvant. In animal studies, AADvac-1 produced antibodies capable of targeting brain tau, and reduced tau pathology and behavioural improvements were observed.[20]

The vaccine, ACI-35, follows an alternative approach wherein a tau epitope is selectively targeted. Phosphorylation at the Ser396 and Ser404 sites of tau was reported to be an early event in AD pathology.[69] ACI-35, therefore, contains synthetic $tau_{393-408}$ peptides which are phosphorylated at

Ser396 and Ser404, and as a result, antibodies targeting the phosphorylated epitope are produced. The vaccine is currently in phase 1b clinical trials.[37,65]

Developments in passive immunisation, pertaining to humanised antibodies, have yielded multiple new clinical candidates, including RG-7345, BMS-986168, ABBV-8E12, RO 7105705, LY3303560.[20]

1.4.6 Other therapeutic approaches

The etiology of AD remains complex and the adaptation of hypotheses to explain the etiology and pathogenesis of the disease, results in the frequent exploration of new therapeutic targets and therapeutic approaches. Herewith the main areas in alternative therapeutic strategies:

1.4.6.1 Drugs to target oxidative stress and mitochondrial dysfunction

Oxidative stress, due to an imbalanced system of oxidants and anti-oxidants, has been well-documented in the brains of AD patients and AD transgenic mice.[70] The oxidants, such as reactive oxygen species (ROS) and reactive nitrogen species (RNS), are capable of reacting with lipids, proteins, carbohydrates, DNA, RNA and other biomolecules in the brain. Oxidative modification damages the biomolecules and results in dysfunction.[71] The oxidative stress hypothesis suggests that the AD brain is under increased oxidative stress and that free radical species may influence neuronal degeneration and the pathogenesis of AD directly.[70] As a result, drugs with strong antioxidant activities (mostly multitargeted drugs), have been included in clinical trials to achieve neuroprotection.[8]

Several factors, including amyloid plaques, neurotoxic trace elements, mitochondrial dysfunction, tissue injury and aging have been associated with free radical production.[70] Mitochondrial disfunction occurs early in AD disease progression and has been connected to increased mitochondrial DNA mutations due to cytochrome oxidase dysfunction.[72] Latrepirdine is an example of a drug that was in clinical trials and was proposed to exert protective effects on mitochondrial structure and function (Figure 1.11).[34]

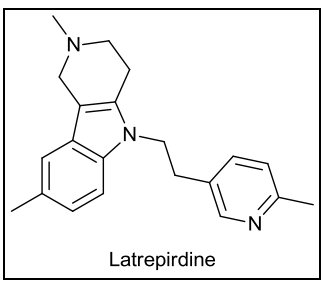

Figure 1.11: The structure of Latrepirdine[44]

1.4.6.2 Neurotrophic drugs

Neurogenesis (generation of new neurons) occurs continually in distinct regions of the adult brain. Nerve growth factor (NGF) is important for the survival and outgrowth of cholinergic neurons in the basal forebrain, and an imbalance in NGF has been linked to the activation of the amyloidogenic pathway and neuronal death. As a result, the increased delivery of NGF to the cholinergic neurons has been explored as a drug strategy to prevent neuron degeneration and to protect synapses.[34,73]

1.4.6.3 Drugs to target neuroinflammation

AD is associated with chronic inflammation in the AD brain, which further results in neuron degeneration. It was discovered that Aβ plaques promote local microglial- and astrocyte-mediated inflammation. Immune responses produce superoxide, complement components, complement receptors and cytokines, which can be neurotoxic to cells and contribute to AD progression in the cases of hyperactivation.[9] Microglia are the prime immune cells responsible for active immune response in the CNS.[9] As a result, some therapeutic strategies have entailed the design of microglial activation inhibitors, in order to inhibit neuroinflammation. The cognitive benefit of anti-inflammatory drugs is also being explored.[37]

1.4.6.4 Multitargeted approaches

The multifactorial nature of AD pathogenesis has been recognised and has influenced drug design to include multitargeted drug strategies. Multitargeted drugs in the context of AD were defined by Bachurin *et al.* to have "an integrated action on a number of biological targets involved in the pathogenesis of the disease".[8] The integrated action of a potential drug on multiple neurobiological targets—including the major neuropathological hallmarks, Aβ peptides and hyperphosphorylated tau— holds interesting potential.

1.5 The GSK-3 hypothesis

Glycogen synthase kinase 3, GSK-3, is a serine/threonine protein kinase that regulates signal transduction in several physiological pathways, including glycogen metabolism, gene transcription, apoptosis and microtubule stability.[4] GSK-3 overexpression contributes to the hyperphosphorylation of tau proteins, which results in NFT formation in AD. GSK-3 inhibitors were discussed in Section 1.4.5.2 as a kinase inhibitor strategy in tau-centric drug development for AD. The design of this project was based on the recently formulated GSK-3 hypothesis, in which GSK-3 is proposed to play a central role in the etiology and multifactorial pathogenesis of AD, an integrated role which stretches beyond

tau hyperphosphorylation.[4] The central role of GSK-3 in AD neuropathology is depicted in Figure 1.12.[74]

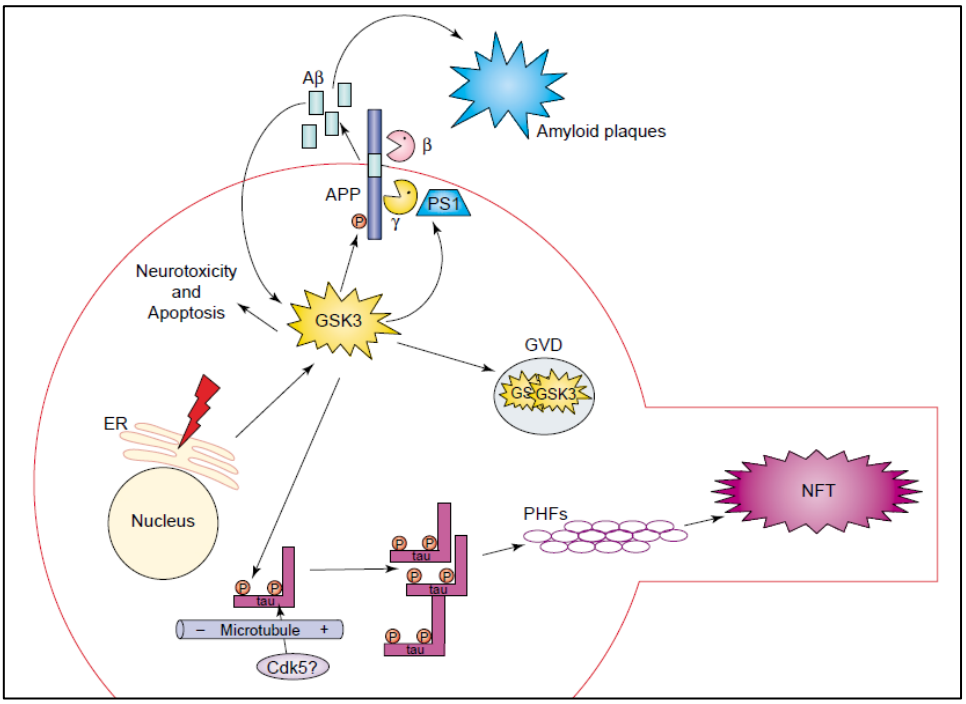

Figure 1.12: The central role of GSK-3 in the neuropathology of AD (figure reproduced from Jope and Johnson).[74] PHFs: paired helical filaments; GVD: Granulovacuolar degeneration.

Substantial evidence supports the GSK-3 hypothesis and has confirmed the role of GSK-3 dysregulation—most likely due to aberrant upstream wingless-type MMTV integration site family (Wnt) signalling or insulin signalling—in the pathogenesis of sporadic and familial forms of AD.[4] The GSK-3 hypothesis regards GSK-3 to be a critical link between tau hyperphosphorylation and β-amyloid plaques.[75]

As discussed in previous sections, the overexpression of GSK-3 results in the hyperphosphorylation of tau proteins, which destabilises tau-microtubule associations, give rise to the misfolding of tau proteins and results in insoluble tangles (NFTs) inside the affected neuron. However, GSK-3 overexpression also results in the elevated production of Aβ peptides from APP through GSK-3 activity on α-secretase. Three α-disintegrin and metalloproteases (ADAM), ADAM-10, ADAM-17, and ADAM-9, constitute the α-secretase complex. GSK-3 is suggested to down-regulate α-secretase activity through ADAM inhibition.[75] The down-regulation of α-secretase favours the amyloidogenic (β-amyloid producing) pathway. Furthermore, GSK-3 may also modify the function of PS-1, a protein which forms part of the APP processing enzyme, y-secretase.[75] The effect of GSK-3 on BACE1 (β-secretase which facilitates the amyloidogenic pathway) was observed through a GSK-3 inhibition study. GSK-3

inhibition was found to reduce BACE1 gene expression, reduce the activity of BACE1 on APP, and to reduce Aβ peptide production in AD model mice.[75,76] It should be further noted that Aβ peptides can increase GSK-3 activity, whereas studies have shown that GSK-3 inhibition can reduce Aβ-induced neurotoxic effects.[77]

Throughout numerous studies on the effects of GSK-3 on AD pathogenesis, it became clear that GSK-3 is not only involved in tau hyperphosphorylation and Aβ plaque production, but also in inflammatory responses, neurotoxicity, reduced acetylcholine synthesis, adult neurogenesis impairment, endoplasmic reticulum (ER) stress and apoptosis.[4,75]

GSK-3 levels are known to be up-regulated in the brains of AD patients and due to the multifactorial role of GSK-3 in AD pathogenesis, it has become a popular CNS target in the development of disease-modifying AD therapeutics.[36] It has also been postulated that GSK-3 inhibitors might exert therapeutic effects at several main stages of the disease.

1.6 Chapter conclusion

As the predominant form of dementia, AD is a progressive neurodegenerative disease associated with clinical symptoms of memory loss and cognitive decline, and major neuropathological hallmarks of intracellular NFTs, extracellular Aβ plaques and neuroinflammation in the brain. AD has a global effect on patients, family members, caregivers, health systems and the economy, therefore the development of potential drug therapies for AD is necessary.

AD drug discovery is challenging since the risk factors and molecular mechanisms of AD development are multifactorial and not fully understood. In the last decade, more than 50 potential AD therapeutics have reached phase II clinical trials, but none has successfully completed phase III.[8] In this chapter, the major trends in AD drug discovery were highlighted and included strategies pertaining to cholinergic, glutamatergic, anti-amyloid, tau-centric, antioxidant, neurotrophic and anti-inflammatory drug therapies. GSK-3 is also a promising CNS drug target, since dysregulated GSK-3 activity plays a central role in AD development and provides a link between β-amyloid plaques, tauopathy, inflammatory responses and reduced cholinergic transmission.

The next chapter will commence with a project problem statement, whereafter the formulation of our hypothesis will be discussed based on work previously performed in the literature. Chapter 2 will also highlight important aspects in the design of our proposed library of GSK-3 inhibitors.

1.7 References

1 World Health Organisation (WHO), *Dementia: A Public Health Priority*, WHO Press, Geneva, 2012.

2 A. Buffington, D. Lipski and E. Westfall, *J. Am. Osteopath. Assoc.*, 2013, **113**, 768–775.

3 World Health Organisation (WHO), *The ICD-10 Classification of Mental and Behavioural Disorders: Clinical Descriptions and Diagnostic Guidelines*, WHO Press, Geneva, 1992.

4 C. Hooper, R. Killick and S. Lovestone, *J. Neurochem.*, 2008, **104**, 1433–1439.

5 Y. Huang and L. Mucke, *Cell*, 2012, **148**, 1204–1222.

6 H. Braak and E. Braak, *Acta Neurol. Scand.*, 1996, **94**, 3–12.

7 M. Prince, A. Wimo, M. Guerchet, G.-C. Ali, Y.-T. Wu and M. Prina, *World Alzheimer Report 2015: The Global Impact of Dementia*, Alzheimer's Disease International, London, 2015.

8 S. O. Bachurin, E. V. Bovina and A. A. Ustyugov, *Med. Res. Rev.*, 2017, **37**, 1186–1225.

9 A. K. Vehmas, C. H. Kawas, W. F. Stewart and J. C. Troncoso, *Neurobiol. Aging*, 2003, **24**, 321–331.

10 V. W. Chow, M. P. Mattson, P. C. Wong and M. Gleichmann, *Neuromolecular Med.*, 2010, **12**, 1–12.

11 J. C. Polanco, C. Li, L. G. Bodea, R. Martinez-Marmol, F. A. Meunier and J. Götz, *Nat. Rev. Neurol.*, 2018, **14**, 22–39.

12 R. Vassar, D. M. Kovacs, R. Yan and P. C. Wong, *J. Neurosci.*, 2009, **29**, 12787–12794.

13 D. J. Selkoe and J. Hardy, *EMBO Mol. Med.*, 2016, **8**, 595–608.

14 R. J. Andrew, K. A. B. Kellett, G. Thinakaran and N. M. Hooper, *J. Biol. Chem.*, 2016, **291**, 19235–19244.

15 S. G. Younkin, *J. Physiol.*, 1998, **92**, 289–292.

16 J. Kim, L. Onstead, S. Randle, R. Price, L. Smithson, C. Zwizinski, D. W. Dickson, T. Golde and E. McGowan, *J. Neurosci.*, 2007, **27**, 627–633.

17 P. Liu, M. N. Reed, L. A. Kotilinek, M. K. O. Grant, C. L. Forster, W. Qiang, S. L. Shapiro, J. H. Reichl, A. C. A. Chiang, J. L. Jankowsky, C. M. Wilmot, J. P. Cleary, K. R. Zahs and K. H. Ashe, *Cell Rep.*, 2015, **11**, 1760–1771.

18 T. Kramer, B. Schmidt and F. Lo Monte, *Int. J. Alzheimers Dis.*, 2012, **2012**, 1–23.

19 F. Panza, V. Solfrizzi, D. Seripa, B. P. Imbimbo, M. Lozupone, A. Santamato, C. Zecca, M. R. Barulli, A. Bellomo, A. Pilotto, A. Daniele, A. Greco and G. Logroscino, *Biomed. Res. Int.*, 2016, **2016**, 1–15.

20 E. E. Congdon and E. M. Sigurdsson, *Nat. Rev. Neurol.*, 2018, **14**, 399–415.

21 H. Dubey, K. Gulati and A. Ray, *Rev. Neurosci.*, 2018, **29**, 241–260.

22 C. A. Lasagna-Reeves, D. L. Castillo-Carranza, U. Sengupta, A. L. Clos, G. R. Jackson and R. Kayed, *Mol. Neurodegener.*, 2011, **6**, 39–52.

23 M. Von Bergen, S. Barghorn, J. Biernat, E.-M. Mandelkow and E. Mandelkow, *Biochim. Biophys. Acta*, 2005, **1739**, 158–166.

24 H. Braak and E. Braak, *Neurobiol. Aging*, 1997, **18**, 351–357.

25 H. Braak and E. Braak, *Acta Neuropathol.*, 1991, **82**, 239–259.

26 R. A. Armstrong, *Folia Neuropathol.*, 2013, **51**, 169–188.

27 C. Zekanowski, D. Religa, C. Graff, S. Filipek and J. Kuznicki, *Acta Neurobiol. Exp.*, 2004, **64**, 19–31.

28 R. Rademakers, M. Cruts and C. van Broeckhoven, *Sci. World J.*, 2003, **3**, 497–519.

29 T. S. Wingo, J. J. Lah, A. I. Levey and D. J. Cutler, *Arch. Neurol.*, 2012, **69**, 59–64.

30 R. Cacace, K. Sleegers and C. Van Broeckhoven, *Alzheimer's Dement.*, 2016, **12**, 733–748.

31 S. Norton, F. E. Matthews, D. E. Barnes, K. Yaffe and C. Brayne, *Lancet Neurol.*, 2014, **13**, 788–794.

32 S. Sindi, F. Mangialasche and M. Kivipelto, *F1000Prime Rep.*, 2015, **7: 50**.

33 J. Cummings, G. Lee, A. Ritter and K. Zhong, *Alzheimer's Dement. Transl. Res. Clin. Interv.*, 2018, **4**, 195–214.

34 F. Mangialasche, A. Solomon, B. Winblad, P. Mecocci and M. Kivipelto, *Lancet Neurol.*, 2010, **9**, 702–716.

35 P. Davies and A. J. F. Maloney, *Lancet*, 1976, **2**, 1403.

36 A. Martinez, C. Gil and D. I. Perez, *Int. J. Alzheimer's Dis.*, 2011, **2011**, 1–7.

37 S.-Y. Hung and W.-M. Fu, *J. Biomed. Sci.*, 2017, **24**, 47.

38 M. L. Onor, M. Trevisiol and E. Aguglia, *Clin. Interv. Aging*, 2007, **2**, 17–32.

39 X. Zhao, Y. Liang, J. Xu, D. Zhang, D. Wang, J. Gu and Y. Cui, *Biol. Pharm. Bull.*, 2012, **35**, 1502–1508.

40 L. S. Schneider, F. Mangialasche, N. Andreasen, H. Feldman, E. Giacobini, R. Jones, V. Mantua, P. Mecocci, L. Pani, B. Winblad and M. Kivipelto, *J. Intern. Med.*, 2014, **275**, 251–283.

41 S. Y. Hung, W.-P. Huang, H.-C. Liou and W.-M. Fu, *Neuropharmacology*, 2015, **93**, 243–251.

42 Sandoz AG, WO2017060287 (A1), 2017.

43 J. Arnt, B. Bang-Andersen, B. Grayson, F. P. Bymaster, M. P. Cohen, N. W. DeLapp, B. Giethlen, M. Kreilgaard, D. L. McKinzie, J. C. Neill, D. L. Nelson, S. M. Nielsen, M. N. Poulsen, J. M. Schaus and L. M. Witten, *Int. J. Neuropsychopharmacol.*, 2010, **13**, 1021–1033.

44 H. Ferrero, M. Solas, P. T. Francis and M. J. Ramirez, *CNS Drugs*, 2017, **31**, 19–32.

45 R. Nirogi, A. Shinde, R. S. Kambhampati, A. R. Mohammed, S. K. Saraf, R. K. Badange, T. R.

Bandyala, V. Bhatt, K. Bojja, V. Reballi, R. Subramanian, V. Benade, R. C. Palacharla, G. Bhyrapuneni, P. Jayarajan, V. Goyal and V. Jasti, *J. Med. Chem.*, 2017, **60**, 1843–1859.

46 M. R. Hynd, H. L. Scott and P. R. Dodd, *Neurochem. Int.*, 2004, **45**, 583–595.

47 J. Hardy and D. Allsop, *Trends Pharmacol. Sci.*, 1991, **12**, 383–388.

48 J. R. M. Coimbra, D. F. F. Marques, S. J. Baptista, C. M. F. Pereira, P. I. Moreira, T. C. P. Dinis, A. E. Santos and J. A. R. Salvador, *Front. Chem.*, 2018, **6: 178**.

49 *BI 1181181*, 2015, https://www.alzforum.org/therapeutics/bi-1181181 [accessed: 05/11/2018].

50 Eisai Co. Ltd, *Phase II clinical study of elenbecestat demonstrates safety and tolerability in MCI and mild to moderate Alzheimer's disease at 18 months*, 2018, http://www.chemdiv.com/phase-ii-clinical-study-elenbecestat-demonstraytes-safety-tolerability-mci-mild-moderate-alzheimers-disease-18-months/ [accessed: 08/11/2018].

51 U. Neumann, M. Ufer, L. H. Jacobson, M. Rouzade-Dominguez, G. Huledal, C. Kolly, R. M. Lüönd, R. Machauer, S. J. Veenstra, K. Hurth, H. Rueeger, M. Tintelnot-Blomley, M. Staufenbiel, D. R. Shimshek, L. Perrot, W. Frieauff, V. Dubost, H. Schiller, B. Vogg, K. Beltz, A. Avrameas, S. Kretz, N. Pezous, J. Rondeau, N. Beckmann, A. Hartmann, S. Vormfelde, O. J. David, B. Galli, R. Ramos, A. Graf and C. L. Lopez, *EMBO Mol. Med.*, 2018, **10: e9316**.

52 M. F. Egan, J. Kost, P. N. Tariot, P. S. Aisen, J. L. Cummings, B. Vellas, C. Sur, Y. Mukai, T. Voss, C. Furtek, E. Mahoney, L. H. Mozley, R. Vandenberghe, Y. Mo and D. Michelson, *N. Engl. J. Med.*, 2018, **378**, 1691–1703.

53 T. Nguyen, *Drug structures made public in New Orleans*, 2018, https://cen.acs.org/articles/96/web/2018/03/Drug-structures-made-public-New-Orleans.html [accessed: 08/11/2018].

54 R. S. Doody, R. Raman, M. Farlow, T. Iwatsubo, B. Vellas, S. Joffe, K. Kieburtz, F. He, X. Sun, R. G. Thomas, P. S. Aisen, E. Siemers, G. Sethuraman and R. Mohs, *N. Engl. J. Med.*, 2013, **369**, 341–350.

55 A. Rauk, *Chem. Soc. Rev.*, 2009, **38**, 2698–2715.

56 Y. Hori, S. Takeda, H. Cho, S. Wegmann, T. M. Shoup, K. Takahashi, D. Irimia, D. R. Elmaleh, B. T. Hyman and E. Hudry, *J. Biol. Chem.*, 2015, **290**, 1966–1978.

57 T. J. Nelson, M.-K. Sun, C. Lim, A. Sen, T. Khan, F. V. Chirila and D. L. Alkon, *J. Alzheimer's Dis.*, 2017, **58**, 521–535.

58 H. Amijee and D. I. C. Scopes, *J. Alzheimer's Dis.*, 2009, **17**, 33–47.

59 B. M. Miller, *Novel Drug Treatment Shows Improved Cognition in a Phase 3 Clinical Trial in Persons with Mild-to-Moderate Alzheimer's Disease in China*, 2018,

https://www.prnewswire.com/news-releases/novel-drug-treatment-shows-improved-cognition-in-a-phase-3-clinical-trial-in-persons-with-mild-to-moderate-alzheimers-disease-in-china-300737649.html [accessed: 06/11/2018].

60 L. S. Honig, B. Vellas, M. Woodward, M. Boada, R. Bullock, M. Borrie, K. Hager, N. Andreasen, E. Scarpini, H. Liu-Seifert, M. Case, R. A. Dean, A. Hake, K. Sundell, V. Poole Hoffmann, C. Carlson, R. Khanna, M. Mintun, R. DeMattos, K. J. Selzler and E. Siemers, *N. Engl. J. Med.*, 2018, **378**, 321–330.

61 D. I. Perez, C. Gil and A. Martinez, in *Emerging Drugs and Targets for Alzheimer's Disease*, ed. A. Martinez, Royal Society of Chemistry, Cambridge, 2010, vol. 1, pp. 173–194.

62 C. M. Wischik, R. T. Staff, D. J. Wischik, P. Bentham, A. D. Murray, J. M. D. Storey, K. A. Kook and C. R. Harrington, *J. Alzheimer's Dis.*, 2015, **44**, 705–720.

63 *LMTM*, 2018, https://www.alzforum.org/therapeutics/lmtm [accessed: 07/11/2018].

64 A. Martinez, D. I. Perez and C. Gil, *Curr. Top. Med. Chem.*, 2013, **13**, 1808–1819.

65 M. Medina, *Int. J. Mol. Sci.*, 2018, **19**, 1160.

66 S. Lovestone, M. Boada, B. Dubois, M. Hüll, J. O. Rinne, H. J. Huppertz, M. Calero, M. V. Andrés, B. Gómez-Carrillo, T. León and T. Del Ser, *J. Alzheimer's Dis.*, 2015, **45**, 75–88.

67 D. Butler, J. Bendiske, M. L. Michaelis, D. A. Karanian and B. A. Bahr, *Eur. J. Pharmacol.*, 2007, **562**, 20–27.

68 E. Kontsekova, N. Zilka, B. Kovacech, P. Novak and M. Novak, *Alzheimer's Res. Ther.*, 2014, **6**, 44.

69 S. Mondragón-Rodríguez, G. Perry, J. Luna-Muñoz, M. C. Acevedo-Aquino and S. Williams, *Neuropathol. Appl. Neurobiol.*, 2014, **40**, 121–135.

70 W. R. Markesbery, *Free Radic. Biol. Med.*, 1997, **23**, 137–147.

71 R. Sultana and D. A. Butterfield, *J. Alzheimer's Dis.*, 2010, **19**, 341–353.

72 P. H. Reddy and M. F. Beal, *Trends Mol. Med.*, 2008, **14**, 45–53.

73 A. Cattaneo, S. Capsoni and F. Paoletti, *J. Alzheimer's Dis.*, 2008, **15**, 255–283.

74 R. S. Jope and G. V. W. Johnson, *Trends Biochem. Sci.*, 2004, **29**, 95–102.

75 M. Llorens-Martín, J. Jurado, F. Hernández and J. Ávila, *Front. Mol. Neurosci.*, 2014, **7**, 1–11.

76 P. T. T. Ly, Y. Wu, H. Zou, R. Wang, W. Zhou, A. Kinoshita, M. Zhang, Y. Yang, F. Cai, J. Woodgett and W. Song, *J. Clin. Invest.*, 2013, **123**, 224–235.

77 S. Koh, M. Y. Noh and S. H. Kim, *Brain Res.*, 2008, **1188**, 254–262.

Chapter 2: The Roots of our Hypothesis

2.1 Problem statement: The need for disease-modifying therapeutics

Therapeutic agents in the AD drug developing pipeline can be grouped according to their proposed mechanisms of action.[1] These mechanisms can be classified further as being either symptomatic or disease-modifying.[1] Symptomatic therapies generally target neurotransmitter mechanisms, to achieve cognitive enhancement or to treat neuropsychiatric symptoms.[2] Symptomatic treatments aim to improve the behaviour and memory of AD patients. Disease-modifying therapeutics (DMTs) in AD aim to prevent or delay the onset or progression of AD, and target the inherent pathophysiologic mechanisms of the disease.[2] Although AD drug development has been successful in terms of symptomatic treatments, attempts to develop DMTs have failed.[3]

The failures in DMT research and development in the AD field have accentuated the urgent need for DMT candidates in the AD drug development pipeline. An assessment of the DMT candidates in globally registered clinical drug trials for AD in January 2018, revealed only 17 DMT candidates to be in phase I, 36 DMTs in phase II and 17 DMTs in phase III trials.[4] This limited number of DMT candidates in trials is concerning, as it is restricting the advancement of AD drug development.[4]

In the past years, the DMT drug pipeline has been focused mainly on the amyloid hypothesis. Given the repeated failures of trials with anti-amyloid candidates targeting mild to moderate AD through different mechanisms of action, the interest in tau-based candidates has grown.[5] This is a natural step, since AD therapeutic approaches are influenced greatly by the disease's two major neuropathological hallmarks, extracellular β-amyloid plaques and intracellular NFTs (mainly consisting of hyperphosphorylated tau protein) in the brain.[5] It is noteworthy that when this project was initiated in 2017, the number of tau-related candidates in clinical trials amounted to nine,[2] and in 2018 the number of tau-related candidates have increased to 16.[4] Recent and past therapeutic approaches to tau-related therapies have included tau protein kinase inhibitors, active and passive immunotherapies, microtubule-stabilizing agents and tau aggregation inhibitors, and provide many more opportunities for exploration.[5]

The potential for tau-based therapies is supported by studies which indicate a significant relationship between NFT counts and neuronal loss.[6,7] Giannakopoulos *et al.*[7] reported that approximately 84% of patient neuronal loss in their studied areas (CA1 field in the hippocampus, entorhinal cortex and Brodmann area 9) could be accounted for by NFTs. This link between NFT topography and clinical phenotype promoted the interest in tau-based targets.[5] In contrast, amyloid deposition appears to

contribute to cognitive decline in AD, but only a weak correlation exists between the stages of deposition and the severity of clinical expression.[6,8]

With the hope of contributing to the AD drug pipeline and knowing that many opportunities are available in tau-based therapies, we undertook the task of exploring the development of new hit molecules which have the potential to generate a new DMT in the field of AD.

2.2 Our central nervous system target: GSK-3

Target-based drug discovery is largely dependent on the success of choosing a target that is critical to the disease process, i.e. a validated target.[4] The complex multifactorial nature of AD and the well-established connections between β-amyloid plaques and tau hyperphosphorylation,[7,9] have directed the interest of our group to the GSK-3 hypothesis (discussed in Chapter 1). The GSK-3 enzyme plays a central role in the multifactorial pathogenesis of sporadic and familial forms of AD, and GSK-3 inhibition has been shown to decrease Aβ peptide production, as well as tau hyperphosphorylation.[9,10] Building on earlier work done by Dr A.R. Hamann on inhibitors of this enzyme in our research group,[11] our aim was to develop a new GSK-3 protein kinase inhibitor. It should be noted that very few GSK-3 inhibitors have successfully reached clinical trials yet and that the 2018 AD drug development pipeline included only one GSK-3β inhibitor (phase II).[4]

Mammalian GSK-3 exists in two isoforms, known as GSK-3α (51 kDa) and GSK-3β (47 kDa). GSK-3β has a 85% amino acid sequence homology to GSK-3α and their kinase binding sites share 98% similarity.[12] Rodent and bovine models have shown that the GSK isoforms are expressed in various mammalian tissues, but that both isoforms are the most abundant in the brain tissue and contribute to AD.[12] The GSK-3β isoform exists almost primarily in the brain tissue of the adult rat, with very low concentrations in other tissues such as the testis, ovary, lung, heart and thymus.[13] GSK-3β has been identified as the key kinase responsible for abnormal tau hyperphosphorylation and was co-crystallised with ATP analogues ADP and AMPPNP in 2003 by Kohno, Sugio and co-workers.[14] Most of the research in the literature pertaining to this topic has been focused on the GSK-3β enzyme as therapeutic target, due to this enzyme's pivotal role in many cellular signalling processes in the brain.[15]

The homology of the GSK3α and GSK3β binding sites complicates the development of isoform-specific inhibitors. As a result, most of the GSK3 inhibitors in the literature are not isoform-specific and thus inhibit both isoforms with the same potency.[10]

2.3 Reversible GSK-3 inhibitors and their binding interactions

The development of reversible GSK-3 inhibitors has prospered in recent years. The majority of GSK-3 inhibitors explored were ATP competitive.[10] Major structural classes of known ATP competitive GSK-3 inhibitors include maleimides, indolyl-maleimides, staurosporine-related organometallic ruthenium complexes, indoles, indirubins, paullones, pyrazolamides, pyrimidine-/furopyrimidine derivatives, oxadiazoles, thiazoles, benzimidazoles, pyrazolones and pyridones.[10] Many of these inhibitors displayed good or excellent inhibition potencies, allowing the identification of key binding interactions in the ATP binding pocket.[10]

GSK-3 inhibitors can be tested against either the GSK-3β or the GSK-3α isoform. Due to the focus on GSK-3β and the availability of crystallographic structures of GSK-3β/ligand complexes, most inhibitors are tested specifically against GSK-3β. Table 2.1 was constructed in order to obtain an overview of important residues which contribute to the hinge region of the GSK-3β ATP binding pocket, for a number of popular inhibitor motifs. The available IC_{50} data are also reported. The overview is based on the comprehensive studies of Kramer *et al.*[10] in which several GSK-3 inhibitors were evaluated in order to obtain insight into the activity and selectivity profile of the GSK-3β ATP binding site.

The images in Table 2.1 were generated by Kramer *et al.*[10] and represent GSK-3β/inhibitor complexes extracted from the Protein Data Bank (PDB IDs: 1Q4L,[16] 1Q3D,[16] 1Q41,[16] 1Q3W,[16] 3F7Z,[17] 2O5K[18]). The interactions of the inhibitors with GSK-3β were illustrated by Kramer *et al.*[10]

Table 2.1: An overview to highlight hinge interactions in the GSK-3β ATP binding pocket

The inhibitor's binding mode to the ATP binding pocket of GSK-3β[10]	**Structural class example**
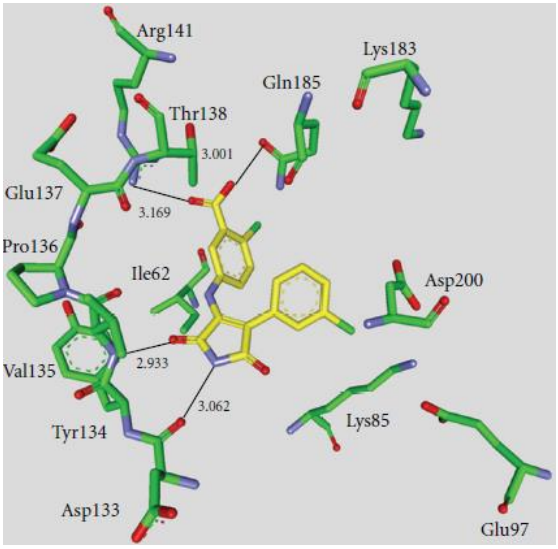	Maleimide derivative, named I-5 PDB ID: 1Q4L 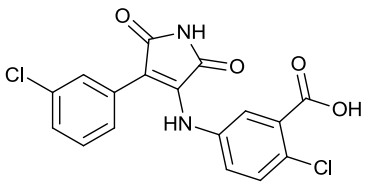 **IC_{50} (GSK-3β, GSK-3α)**[16]**:** 160 nm, 76 nm **Key interactions:**[16] Asp133 (carbonyl O), Val135 (backbone N), Arg141 & Gln185

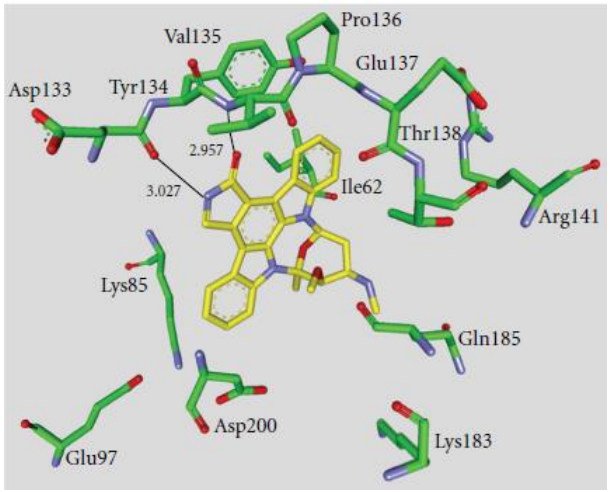

Staurosporine inhibitor

PDB ID: 1Q3D

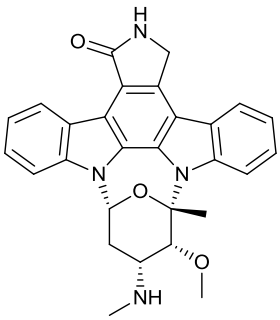

IC_{50} (GSK-3β):[16] 15 nm

Key interactions:[16] Val135 (backbone N), Asp133 (carbonyl O), water-mediated interaction with Gln185 (not shown).

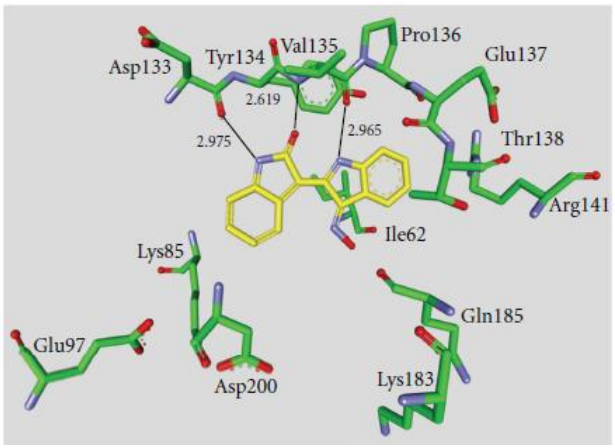

Indole derivative, indirubin-3'-monoxime

PDB ID: 1Q41

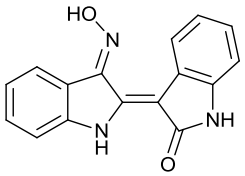

IC_{50} (GSK-3β):[16] 22 nm

Key interactions:[16] Val135 (backbone N, carbonyl O), Asp133 (carbonyl O), water-mediated interaction with Gln185 (not shown)

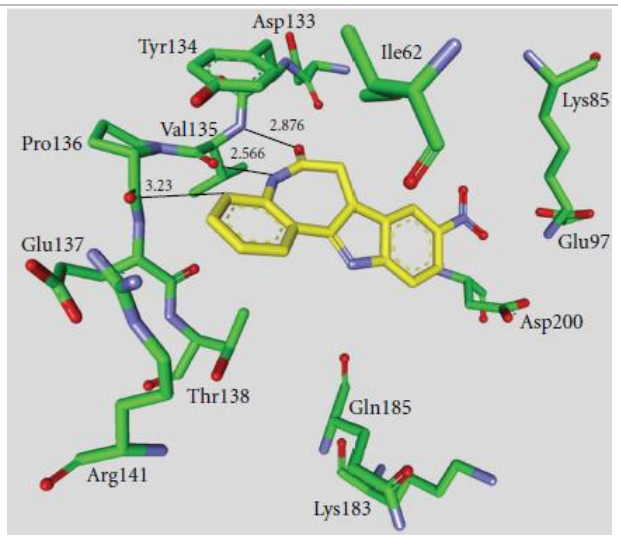

Paullone derivative, Alsterpaullone

PDB ID: 1Q3W

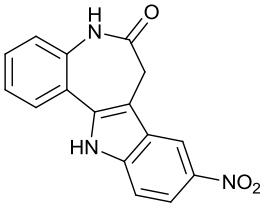

IC_{50} (GSK-3β):[16] 4 nm

Key interactions:[16] Val135 (backbone N, carbonyl O), water-mediated interaction with Asp133 and Gln185 (not shown)

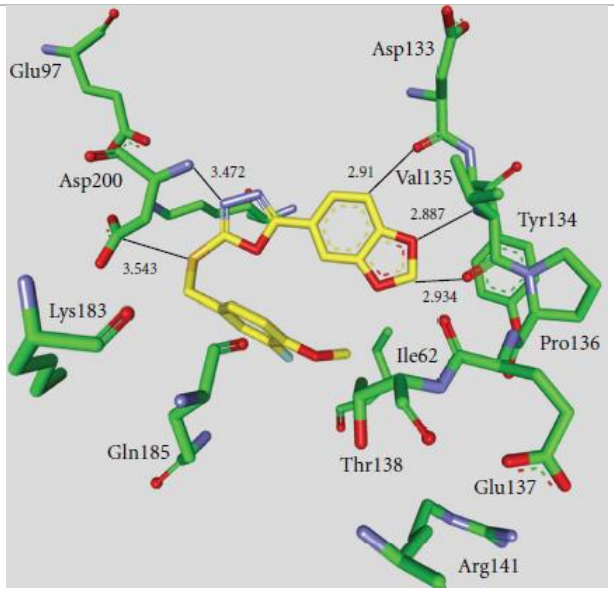

1,3,4-Oxadiazole derivative

PDB ID: 3F7Z

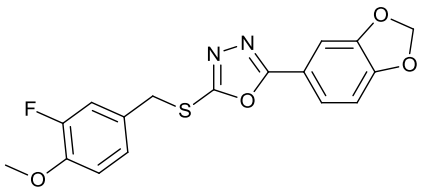

IC_{50} (GSK-3β):[17] 65 nm

Key interactions:[17] Val135 (backbone NH, carbonyl O), Asp133, water-mediated Lys85-Glu97-Asp200 hydrogen bond network

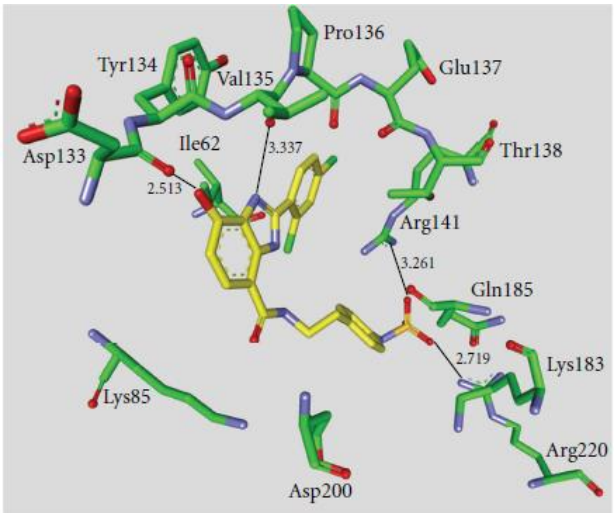

Benzimidazole derivative

PDB ID: 2O5K

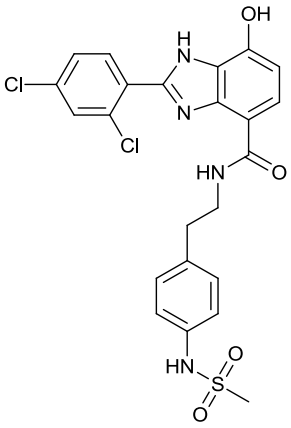

IC_{50} (GSK-3β):[18] 15 nm

Key interactions:[18] Asp133 (carbonyl O), Val135 (carbonyl O), Arg141 & Arg220 (with SO_2)

Through an inspection of different structural classes, by Kramer *et al.*,[10] it became apparent that all ATP competitive GSK-3 inhibitors bind the hinge region through one or more hydrogen bonds with Val135. In most cases, a hydrogen bond to the Asp133 backbone strengthened the inhibitor's interaction with the hinge region. These results were in accordance with the binding interactions which were observed in the crystal structure of GSK-3β with the non-hydrolysable ATP-analogue, adenylyl imidodiphosphate (AMPPNP, PDB ID: 1PYX[16]). AMPPNP's adenine ring forms hydrogen bonds with residues Val135 and Asp133 in the hinge binding region.[16]

Good interactions with the hinge region enhance an GSK-3 inhibitor's affinity for the GSK-3 ATP binding pocket, which promotes good inhibition activity. However, good selectivity requires additional binding interactions which will favour GSK-3 over other kinases. Figure 2.1 depicts a schematic outline of the different areas in the GSK-3β ATP binding pocket that may contribute to activity and selectivity.[10]

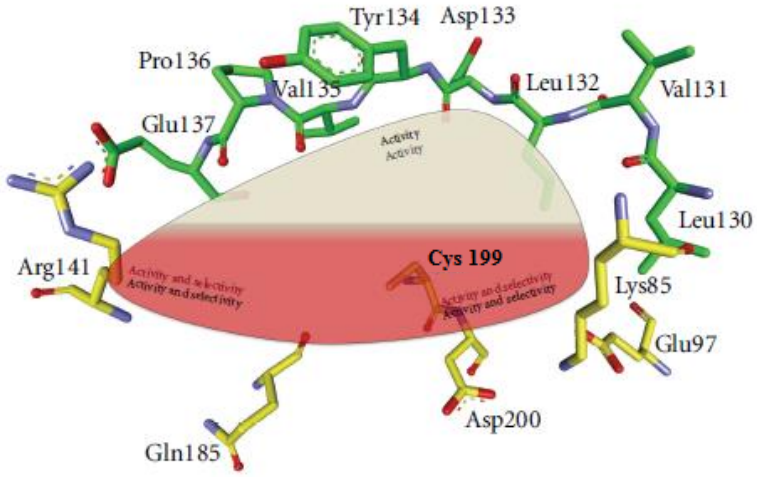

Figure 2.1: Important binding interaction regions of the GSK-3β ATP pocket and their potential to provide activity and selectivity[10]

The selectivity of reversible ATP-competitive inhibitors for GSK-3 over other kinases was improved through additional hydrogen bond contacts with residues in the selectivity areas. Interactions with the small hydrophobic pocket (Ile62, Gly63, Phe67, Val70), water-mediated bonds with Gln185 and water-mediated interactions with the Lys85-Glu97-Asp200 network, also contributed to improved degrees of selectivity.[10] However, selectivity remained a challenge with reversible ATP-competitive inhibitors.

The translation of potent small-molecule GSK-3 inhibitors into clinically approved therapeutics has posed difficulties over the past years, with the major obstacles pertaining to selectivity, blood-brain barrier penetration and chronic toxicity.[19]

2.4 The selectivity challenge

Protein kinases encoded by the human kinome are known to possess a more or less conserved binding site for ATP.[20] Many of the previously reported GSK-3 inhibitors have not achieved the required selectivity over kinase panels, due to high sequence conservation in the ATP binding site. This was especially the case with CDK-1, CDK-2 and CDK-5. CDK-2 displays the greatest structural homology with GSK-3β, by sharing 33% of its amino acid sequence over the core kinase domain (residues 55 –

345 of GSK-3β).[21,22] GSK-3's role in many different signalling pathways necessitates selective and moderate inhibition, in order to prevent adverse off-target- and side-effects.[10]

No time was spent in this project on the development of isoform-selective GSK-3 inhibitors, considering that both isoforms have been suggested to contribute to the pathogenesis of AD and since the catalytic domains of the GSK-3β and GSK-3α isoforms are 98% identical.[21,23] The acquirement of selectivity towards GSK-3 over the different protein kinases of the human kinome was regarded as first priority.

Non-ATP competitive GSK-3 inhibitors have been proposed as an alternative strategy towards selectivity and include allosteric modulators and substrate competitive inhibitors.[24] In the case of allosteric modulators, allosteric pockets on the GSK-3 enzyme surface have been discovered and provide the opportunity for modulation through conformational changes.[20] The uniqueness of the allosteric pocket promotes kinase selectivity and the inhibitor no longer competes with ATP.[24] In the case of substrate competitive inhibitors, the substrate site may offer enhanced selectivity, but the inhibitor will have to compete with the substrate.[24] The substrate is usually a pre-phosphorylated substrate to which GSK-3 introduces another phosphate group.

Irreversible protein kinase inhibitors provide another alternative towards selectivity by targeting a unique reactive residue in the ATP binding site of GSK-3 through covalent modification. Irreversible inhibitors have gained interest in cancer research, where they have been utilised to avoid resistance in protein kinase therapy.[20,25]

2.5 The covalent target residue: Cys199

Martínez and co-workers[26] were the first to describe irreversible GSK-3β inhibitors. They utilised the halomethylketone (HMK) moiety as electrophile and developed a library of thienylhalomethylketones, obtaining an IC_{50} of 0.5 μM after optimisation. The HMK moiety proved to be the key structural feature towards activity and their enzyme mapping, reversibility and kinetic studies further supported inhibition through the covalent modification of cysteine 199 in the ATP binding pocket of GSK-3β. Covalent bond formation between the Cys199 thiol and the HMK moiety would entail the formation of a new thioether carbon-sulfur bond (Figure 2.2). The HMK halide atom is situated close to a protonated Lys85 residue in the ATP pocket, which might stabilise the halide anion upon elimination.[26] The location of Cys199 in the GSK-3β ATP binding pocket can be seen in Figure 2.1.

This covalent strategy is very attractive in terms of selectivity, since the ATP binding pocket of GSK-3 uniquely contains this Cys199 residue, which is not conserved in structurally related kinases such as

CDK-1, CDK-2 and CDK-5.[26,27] Of importance is that this unique cysteine residue is present in the ATP binding site of GSK3α and GSK3β.[26]

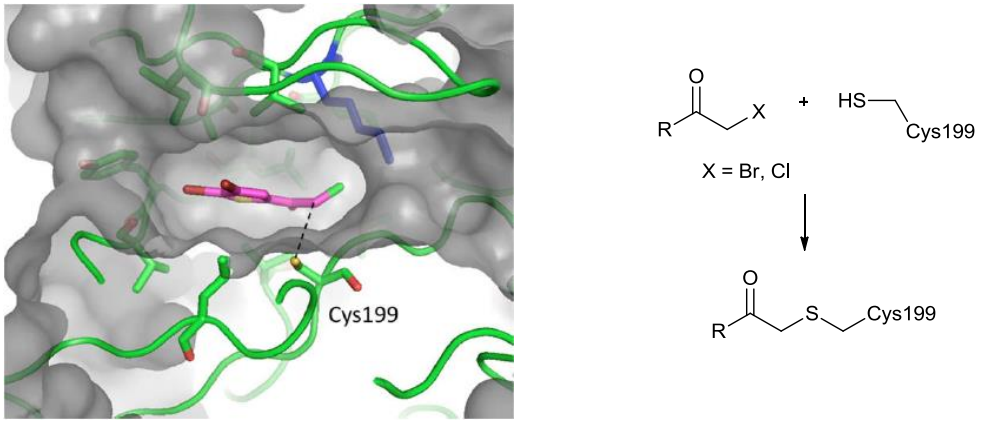

Figure 2.2: HMK GSK-3β inhibitors are postulated to target and covalently modify the Cys199 residue. The Lys85 residue is presented in dark blue.[26]

Martínez and co-workers[27] managed to successfully switch reversible maleimide-based inhibitors into potent irreversible GSK-3β inhibitors by incorporating an HMK moiety onto the scaffold in a position that would be suitable for Cys199 modification (Scheme 2.1). A time-dependent study of inhibition percentage versus preincubation time confirmed the irreversible binding mode of the new compounds. Of note is that for reversible inhibitors, the inhibition percentage remains constant for different preincubation times, while irreversible inhibitors show an increase in inhibitory activity when the enzyme and the ligand are preincubated for a longer time before measuring inhibition percentage.[27]

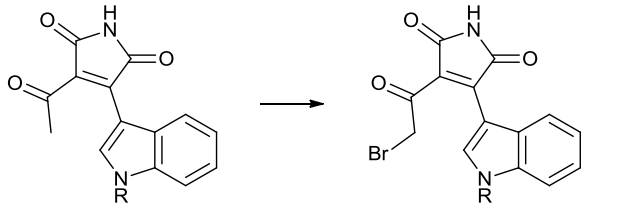

1a R = H (IC_{50} = 4.47 μM)
1b R = Me (IC_{50} = 0.89 μM)

2a R = H (IC_{50} = 0.047 μM)
2b R = Me (IC_{50} = 0.005 μM)

Scheme 2.1: Martínez and co-workers switched reversible inhibitors into potent irreversible HMK inhibitors of GSK-3[27]

Inspired by the success of this approach, herein we aim to design and synthesise covalent inhibitors of GSK-3 through a reaction with Cys199. Using molecular modelling to allow for further key interactions in the active site, we hope to increase selectivity through this approach.

2.6 Targeted covalent inhibitors: Considerations

A covalent inhibitor is designed to contain a mildly electrophilic moiety, which has an affinity for a molecular nucleophilic target.[28] Irreversible covalent modification will suppress a kinase's biological function through a covalent binding interaction which is irreversible on the biological timescale. The irreversible covalent approach potentially affords the advantages of high selectivity and potency, prolonged duration of action and low dosages.[28]

Historically, the pharmaceutical industry has been reluctant to follow covalent inhibition strategies, due to hepatotoxic risks exerted by these drugs.[28] Toxicological effects were related to protein haptenization, where the haptens were electrophilic metabolites generated by P-450 cytochrome catalysed oxidation reactions. These haptens covalently bind cellular proteins in an indiscriminate fashion, causing functional damage.[28,29]

Targeted covalent drug strategies have gained significant interest in the past decade, after several chemotherapeutic targeted covalent inhibitors were demonstrated to be safe and effective.[29] The approval of these drugs onto the market has created reassurance that targeted covalent inhibitors do not necessarily create hepatotoxicity. It was also discovered, retrospectively, that some well-known marketed drugs, such as aspirin, penicillins and cephalosporins, rely on covalent modification to exert their function. It was concluded that reactive metabolites from hepatotoxic drugs are highly electrophilic and react indiscriminately, in contrast to the ideal covalent inhibitor which should contain a weakly electrophilic warhead and selectively modify a unique protein target.[28]

Irreversible drug development strategies adopt several approaches in an attempt to reduce the risks of toxicity. Firstly, a high degree of target selectivity is essential. In the design of an inhibitor, good bioinformatics and proteomic tools are advantageous. A high-affinity reversible inhibitor is considered to be a good starting point in the design of a scaffold because the molecule must first associate reversibly in the ATP-binding pocket, before a covalent bond can form. In order to react irreversibly, an electrophilic moiety of suitable reactivity must be incorporated onto the scaffold at a position correctly orientated for interaction with the nucleophilic protein moiety. The nucleophilic residue in the protein pocket should be accessible and uncommon in other kinases.[28]

Secondly, low drug doses and less frequent administration decrease the risks of off-target effects and high burdens of reactive metabolites. Therefore, the drug molecule should have high potency and good oral bioavailability. Few drugs with dosages of less than 10 mg/day have been associated with liver injury.[28]

Lastly, candidate covalent inhibitors should be screened for their susceptibility towards metabolic activation at an early stage. Metabolic activation of the electrophilic warhead or another group on the molecule can increase the electrophilic nature of the inhibitor and result in off-target effects.[28]

In order to minimize toxicity risks, it is important to keep these various aspects of irreversible inhibitor design in mind when pursuing covalent inhibitor strategies.

2.7 The design of our scaffold: Incorporating aims of high selectivity and non-toxicity

In an attempt to obtain a high degree of selectivity, this project aims to design and synthesise covalent GSK-3 inhibitors which target Cys199 in the ATP-binding pocket. In accordance with Perez *et al.,*[27] we intend switching a known reversible inhibitor into an irreversible inhibitor, by connecting a reactive electrophilic warhead onto the scaffold. To reduce toxicity risks, as discussed in Section 2.6, we will utilise a highly selective, high affinity reversible GSK-3 inhibitor as a scaffold for the design of our targeted covalent inhibitor.

In 2003, AstraZeneca[21] reported the potent activity and high selectivity of the novel small-molecule GSK-3 inhibitor, AR-A014418 (**3**, Figure 2.3). This thiazole is a reversible ATP-competitor and inhibited GSK-3 (equal mix of α and β) with an IC_{50} value of 104 nm. It was shown to bind the hinge region of the GSK-3β ATP pocket through three hydrogen bond interactions (PDB ID: 1Q5K). In addition, the nitro group forms water-mediated polar interactions with Lys85-Glu97-Asp200 and the phenyl ring forms a stacking interaction with Arg141.[21]

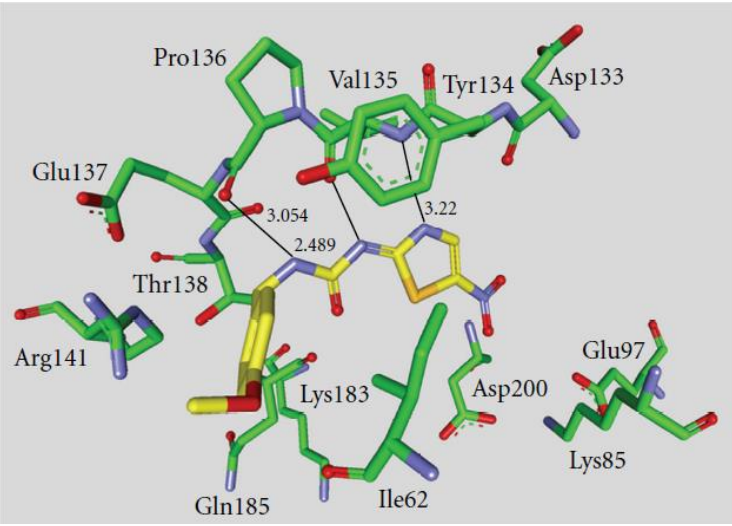

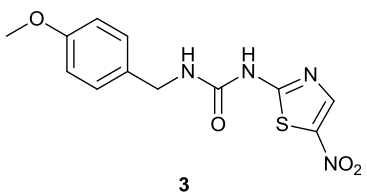

3

Figure 2.3: The binding site interactions of AR-A014418 with GSK-3β (The figure was prepared by Kramer et al.[10] from the enzyme/inhibitor complex structure with PDB ID: 1Q5K)

AR-A014418 was shown to be highly selective for GSK-3 and did not significantly inhibit CDK-2, CDK-5 or the rest of the 26 protein kinases which were assayed.[21] However, AR-A014418 was unfortunately found to be toxic.[30]

With the use of a zebrafish embryo phenotype assay, Lo Monte *et al.*[30] showed that when the thiazole ring of AR-A014418 was replaced with a pyridine or benzothiazole ring structure, the toxicity of the compound diminished. This benzothiazole derivative (**4**, Figure 2.4) had a GSK-3 inhibition potency comparative to AR-A014418 and was also suggested to have a kinase selectivity profile and docking mode similar to AR-A014418, based on brief biological activity and docking studies.[30] The calculated logP of benzothiazolyl urea **4** was 3.34, which is favourable according to Lipinski's general rule of 5 which predicts that: "poor absorption or permeation is more likely when there are more than 5 H-bond donors, 10 H-bond acceptors, the molecular weight is greater than 500 and the calculated Log P is greater than 5."[30,31]

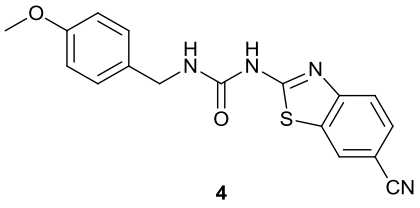

4

Figure 2.4: The potent and less toxic benzothiazole derivative of AR-A014418

In our study, we intend combining several desirable structural characteristics to establish our structural scaffold. Benzothiazolylurea GSK-3β inhibitor **4** (Figure 2.4) will be utilised as a scaffold in the design of our Cys199-targeted covalent inhibitors. Bearing in mind the proposed docking mode of **4**, we hypothesise that the electrophilic warhead should be incorporated onto the benzothiazole ring in order to position it in close proximity of the Cys199 target residue. This approach was also followed by Perez *et al.*[27] when they designed the Cys199-targeted benzimidazole-derived HMK GSK-3 inhibitor **5** (Figure 2.5, IC_{50} = 580 nM).

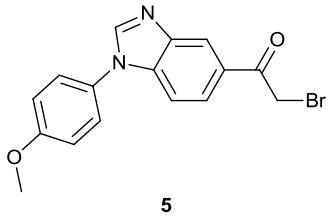

5

Figure 2.5: The irreversible benzimidazole-derived HMK GSK-3 inhibitor synthesised by Perez et al.[27]

We will attempt to introduce different reactive electrophilic warheads onto the structural scaffold. We will also explore the benzimidazole derivatives of the proposed compounds. In conclusion, the general benzazole urea scaffold of our proposed irreversible GSK-3 inhibitors is depicted in Figure 2.6.

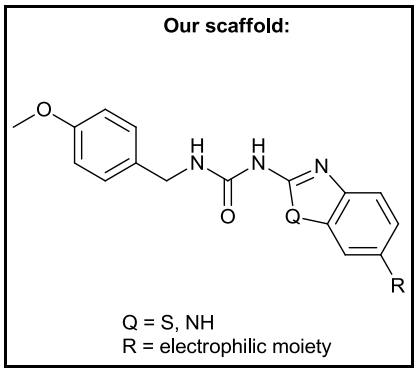

Figure 2.6: The 1-aryl-3-(4-methoxybenzyl)urea scaffold of our proposed irreversible GSK-3 inhibitors

2.8 Project aims

The aim of this project is to design, synthesise and biologically evaluate a small library of structurally-related, irreversible GSK-3 inhibitors as potential Alzheimer's disease drug candidates. Our library will include two sets of 1-aryl-3-(4-methoxybenzyl)ureas, wherein the incorporated aryl group will be a benzothiazole or benzimidazole scaffold, respectively. The benzothiazole scaffold has displayed potential in previous GSK-3 inhibitor design studies,[30] whereas the benzimidazole scaffold will be investigated as an alternative core structure to evaluate its possible effect on activity. Each molecule will contain an electrophilic warhead, with the potential to form a covalent (irreversible) bond with nucleophilic Cys199 in the GSK-3 ATP binding pocket. Typical electrophilic warheads capable of reacting with reactive cysteine residues will be explored, based on electrophilic moieties that have been widely utilised in reported irreversible inhibitors of the protein kinase cysteinome.[29]

Molecular modelling studies will be used to confirm the viability of our proposed covalent inhibitors and to design the final library for synthesis. Next, synthetic procedures will be developed to prepare the compound library. Several characterisation techniques will be employed to confirm the structures of the synthesised compounds.

Finally, we aim to send the library of synthesised compounds away for biological testing, to test their inhibitory activity against the GSK-3β enzyme. The biological activity scores will be compared to the molecular modelling results, in a structure-activity study. This structure-activity study will evaluate our understanding of the interactions of our proposed inhibitors with the active site of GSK-3β.

2.9 References

1 J. Cummings, T. Morstorf and G. Lee, *Alzheimer's Dement. Transl. Res. Clin. Interv.*, 2016, **2**, 222–232.

2 J. Cummings, G. Lee, T. Mortsdorf, A. Ritter and K. Zhong, *Alzheimer's Dement. Transl. Res. Clin. Interv.*, 2017, **3**, 367–384.

3 F. Mangialasche, A. Solomon, B. Winblad, P. Mecocci and M. Kivipelto, *Lancet Neurol.*, 2010, **9**, 702–716.

4 J. Cummings, G. Lee, A. Ritter and K. Zhong, *Alzheimer's Dement. Transl. Res. Clin. Interv.*, 2018, **4**, 195–214.

5 F. Panza, V. Solfrizzi, D. Seripa, B. P. Imbimbo, M. Lozupone, A. Santamato, C. Zecca, M. R. Barulli, A. Bellomo, A. Pilotto, A. Daniele, A. Greco and G. Logroscino, *Biomed. Res. Int.*, 2016, **2016**, 1–15.

6 G. Gold, E. Kovari, G. Corte, F. R. Herrmann, A. Canuto, T. Bussiere, P. R. Hof, C. Bouras and P. Giannakopoulos, *J. Neuropathol. Exp. Neurol.*, 2001, **60**, 946–952.

7 P. Giannakopoulos, F. R. Herrmann, T. Bussière, C. Bouras, E. Kövari, D. P. Perl, J. H. Morrison, G. Gold and P. R. Hof, *Neurology*, 2003, **60**, 1495–1500.

8 H. Braak and E. Braak, *Neurobiol. Aging*, 1997, **18**, 351–357.

9 C. Hooper, R. Killick and S. Lovestone, *J. Neurochem.*, 2008, **104**, 1433–1439.

10 T. Kramer, B. Schmidt and F. Lo Monte, *Int. J. Alzheimers Dis.*, 2012, **2012**, 1–23.

11 A. R. Hamann, PhD thesis: Design and development of novel irreversible GSK-3β inhibitors to address Alzheimer's disease, Stellenbosch University, 2018.

12 J. R. Woodgett, *EMBO J.*, 1990, **9**, 2431–2438.

13 M. Takahashi, K. Tomizawa, R. Kato, K. Sato, T. Uchida, S. C. Fujita and K. Imahori, *J. Neurochem.*, 1994, **63**, 245–55.

14 M. Aoki, T. Yokota, I. Sugiura, C. Sasaki, T. Hasegawa, C. Okumura, K. Ishiguro, T. Kohno, S. Sugio and T. Matsuzaki, *Acta Crystallogr., Sect. D*, 2004, **60**, 439–446.

15 M. Llorens-Martín, J. Jurado, F. Hernández and J. Ávila, *Front. Mol. Neurosci.*, 2014, **7**, 1–11.

16 J. A. Bertrand, S. Thieffine, A. Vulpetti, C. Cristiani, B. Valsasina, S. Knapp, H. M. Kalisz and M. Flocco, *J. Mol. Biol.*, 2003, **333**, 393–407.

17 M. Saitoh, J. Kunitomo, E. Kimura, Y. Hayase, H. Kobayashi, N. Uchiyama, T. Kawamoto, T. Tanaka, C. D. Mol, D. R. Dougan, G. S. Textor, G. P. Snell and F. Itoh, *Bioorg. Med. Chem.*, 2009, **17**, 2017–2029.

18 D. Shin, S. C. Lee, Y. S. Heo, W. Y. Lee, Y. S. Cho, Y. E. Kim, Y. L. Hyun, J. M. Cho, Y. S. Lee and S. Ro, *Bioorg. Med. Chem. Lett.*, 2007, **17**, 5686–5689.

19 S. H. Liang, J. M. Chen, M. D. Normandin, J. S. Chang, G. C. Chang, C. K. Taylor, P. Trapa, M. S. Plummer, K. S. Para, E. L. Conn, L. Lopresti-Morrow, L. F. Lanyon, J. M. Cook, K. E. G. Richter, C. E. Nolan, J. B. Schachter, F. Janat, Y. Che, V. Shanmugasundaram, B. A. Lefker, B. E. Enerson, E. Livni, L. Wang, N. J. Guehl, D. Patnaik, F. F. Wagner, R. Perlis, E. B. Holson, S. J. Haggarty, G. El Fakhri, R. G. Kurumbail and N. Vasdev, *Angew. Chem., Int. Ed.*, 2016, **55**, 9601–9605.

20 A. Martinez, D. I. Perez and C. Gil, *Curr. Top. Med. Chem.*, 2013, **13**, 1808–1819.

21 R. Bhat, Y. Xue, S. Berg, S. Hellberg, M. Ormö, Y. Nilsson, A. C. Radesäter, E. Jerning, P. O. Markgren, T. Borgegård, M. Nylöf, A. Giménez-Cassina, F. Hernández, J. J. Lucas, J. Díaz-Nido and J. Avila, *J. Biol. Chem.*, 2003, **278**, 45937–45945.

22 B. Bax, P. S. Carter, C. Lewis, A. R. Guy, A. Bridges, R. Tanner, G. Pettman, C. Mannix, A. A. Culbert, M. J. B. Brown, D. G. Smith and A. D. Reith, *Structure*, 2001, **9**, 1143–1152.

23 D. E. Hurtado, L. Molina-Porcel, J. C. Carroll, C. MacDonald, A. K. Aboagye, J. Q. Trojanowski and V. M.-Y. Lee, *J. Neurosci.*, 2012, **32**, 7392–7402.

24 A. Martinez, C. Gil and D. I. Perez, *Int. J. Alzheimer's Dis.*, 2011, **2011**, 1–7.

25 C. P. Belani, *Cancer Invest.*, 2010, **28**, 413–423.

26 D. I. Perez, S. Conde, C. Pérez, C. Gil, D. Simon, F. Wandosell, F. J. Moreno, J. L. Gelpí, F. J. Luque and A. Martínez, *Bioorg. Med. Chem.*, 2009, **17**, 6914–6925.

27 D. I. Perez, V. Palomo, C. Pérez, C. Gil, P. D. Dans, F. J. Luque, S. Conde and A. Martínez, *J. Med. Chem.*, 2011, **54**, 4042–4056.

28 T. A. Baillie, *Angew. Chem., Int. Ed.*, 2016, **55**, 13408–13421.

29 Q. Liu, Y. Sabnis, Z. Zhao, T. Zhang, S. J. Buhrlage, L. H. Jones and N. S. Gray, *Chem. Biol.*, 2013, **20**, 146–159.

30 F. Lo Monte, T. Kramer, A. Boländer, B. Plotkin, H. Eldar-Finkelman, A. Fuertes, J. Dominguez and B. Schmidt, *Bioorg. Med. Chem. Lett.*, 2011, **21**, 5610–5615.

31 C. A. Lipinski, F. Lombardo, B. W. Dominy and P. J. Feeney, *Adv. Drug Deliv. Rev.*, 1997, **23**, 3–25.

Chapter 3: Molecular modelling studies

3.1 The structure of GSK-3β: Brief overview

The first binary complex structure of GSK-3β was solved from the X-ray crystallographic structures of GSK-3β with the ATP analogues, ADP (PDB ID: 1J1C) and AMPPNP (PDB ID: 1J1B).[1] Since then, several ATP-competitive inhibitors have been co-crystallised with GSK-3β and studied by X-ray diffraction (see for example PDB files: 1Q5K,[2] 1Q4L,[3] 1Q3D,[3] 1Q41,[3] 1Q3W,[3] 3F7Z,[4] and 2O5K[5]). GSK-3β forms a dimeric complex in its asymmetric unit, which consists out of two molecules of GSK-3β (protein chain A and B). Each GSK-3β protein chain has an independent ATP-binding site as shown in Figure 3.1.[1]

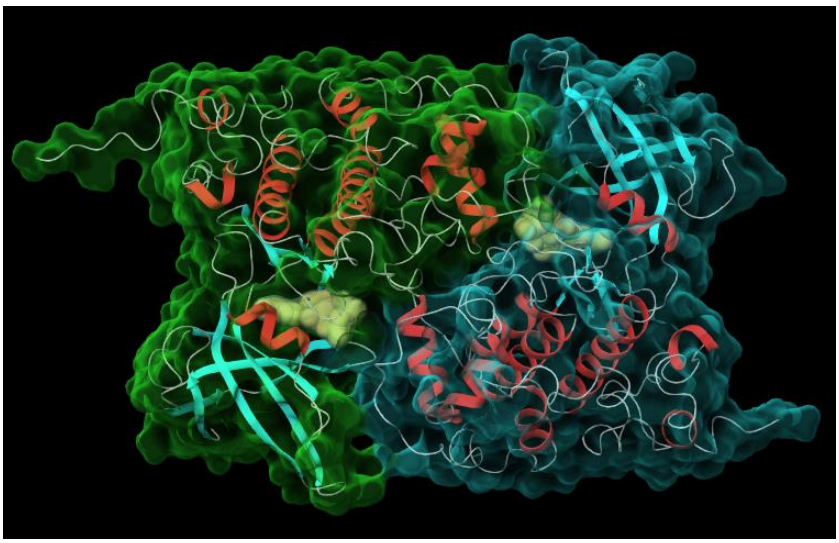

Figure 3.1: The dimeric complex of GSK-3β with AMPPNP (PDB ID: 1J1B).[1] The green and cyan surfaces each represent a GSK-3β protein chain. The AMPPNP ligands are represented by yellow spheres in the two independent ATP-binding pockets. (Figure prepared with Maestro v11.1 Schrödinger Drug Discovery Suite[6])

A surface representation of the GSK-3β protein is depicted in Figure 3.2.[7] The GSK-3β protein chain has two major domains, known as the N-terminal and the C-terminal domains. The N-terminal domain comprises antiparallel β-strands and a short helix denoted as 'helix αC'. The C-terminal domain of the GSK-3β protein chain is α-helical. The inhibitor or ATP analogue binds in a deep cleft which is situated between the C- and N-terminal lobes. The hinge region, which is crucial for effective ATP binding site interactions, forms a loop which connects the C- and N- terminal domains.[1]

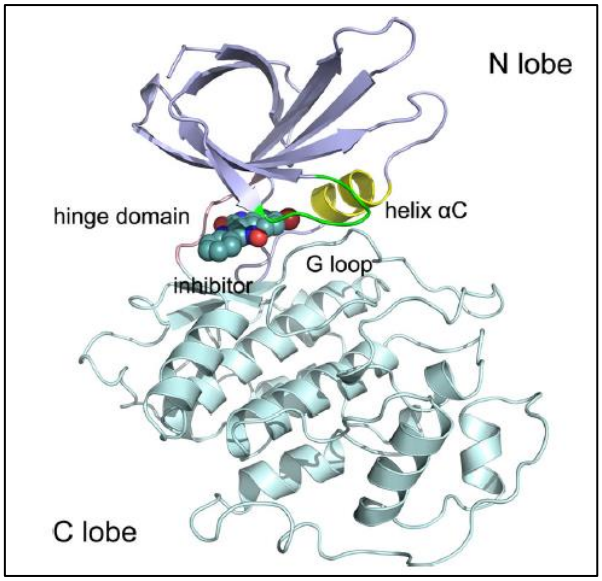

Figure 3.2: A surface representation of the GSK-3β protein monomer in complex with an inhibitor (PDB ID: 1UV5).[8] The inhibitor atoms are depicted by spheres. (Figure reproduced from Li et al.[7])

3.2 Molecular Modelling

The molecular modelling docking studies were performed using the Maestro v11.1 Schrödinger Drug Discovery Suite.[6] Maestro v11.1 is the graphical user interface, from which Glide v7.4[9–11] was run to perform high accuracy docking studies. Glide (Grid-based ligand docking with energetics) is a docking methodology that uses hierarchical filters to search the positional, orientational and conformational space around a docked ligand, in order to optimise its interactions with the receptor active-site.[9] The receptor's shape and properties are defined in a receptor grid. In the final steps of the hierarchy, the best docking poses are energy minimised and scored.[12]

Energy minimisation in the Maestro v11.1 suite was performed with the molecular mechanics force field, OPLS3.[13] The basic characteristics of the OPLS potential energy function include that it is based on a fixed charge electrostatic model. Non-bonded interactions are described by Coulomb and van der Waals terms. At the heart of the OPLS model is the non-bonded parameter set which was produced when the parameters were optimised to simulate liquid state thermodynamics. Bonding interactions include bond-stretching and angle-bending interactions which are described by harmonic terms. Torsion is described by a condensed Fourier transform term. The parameters required in bonded terms were fitted to quantum chemical data in the design of the OPLS3 force field model.[13]

The X-ray crystallographic structure of the reference compound, AR-A014418 (**3**),[2] in complex with GSK-3β was utilised to perform our docking studies (PDB ID: 1Q5K). Docking studies performed by Lo Monte *et al.*[14] suggested that their reversible benzothiazole urea inhibitors had a similar docking

mode to AR-A014418. Therefore, we were operating from the reasonable presumption that the proposed benzothiazole- and benzimidazole ureas would display a docking mode similar to AR-A014418. Considering that an irreversible inhibitor first binds the ATP-binding pocket in a reversible fashion, whereafter the covalent bonding step takes place, the modelling studies were commenced with reversible docking studies. The best reversible ligand poses would then be subjected to covalent modelling studies.

3.2.1 Protein preparation

The typical protein structure obtained from the Protein Data Bank requires preparation before it can be utilised for molecular modelling purposes. These protein files consist solely out of heavy atoms (hydrogen atoms are omitted) and may contain water molecules, co-crystallised ligands, co-factors and metal ions. Connectivity information, such as bond orders and formal charges are generally omitted. Several other issues, such as ionisation- and tautomeric state assignments and side chain orientations were thus addressed during protein preparation in order to obtain a chemically correct structure.[12]

To this end, the GSK-3β/AR-A014418 co-crystallised structure (resolution: 1.94 Å) was imported into Maestro from the Protein Data Bank (PDB ID: 1Q5K).[2] The multimeric protein was next reduced to a single ligand-receptor unit by deleting protein chain B, in order to reduce computational cost. All Glide computations were thus performed on protein chain A.

The GSK-3β protein was prepared with the 'Protein Preparation Wizard'.[6] The structure was pre-processed to assign bond orders, add missing hydrogen atoms, fill in missing side chains and loops, delete water molecules beyond 5 Å of the ligand and to return the most favourable protonation state for the ligand at pH 7 ± 2. The protein structure was further refined by optimising the hydrogen bond network at pH 7, which included the sampling of asparagine, glutamine and histidine residue orientations.[12] After hydrogen bond optimisation, water molecules with fewer than 3 hydrogen bond interactions to non-water molecules were removed. In the final step, the refined structure was energy minimised, using the OPLS3 force field and an RMSD tolerance of 0.30 Å to restrain heavy-atom displacement.

3.2.2 Receptor grid generation

Before a ligand can be docked to a receptor molecule, the receptor molecule's physical properties, and more specifically the active site, must be defined and represented on a receptor grid. The receptor grid is rigid and only allows for side-chain hydroxylated carbon rotations. However, Glide incorporates a degree of protein flexibility by decreasing the van der Waals radii of non-polar atoms in the active

site, with a constant factor. Smaller penalties for close contacts allow for more flexible docking since proteins can adjust their active-site slightly to accommodate ligands.[10]

The receptor grid of the GSK-3β protein was generated using the 'Receptor Grid Generation' panel. The co-crystallised ligand in the active site was used to define the size of the receptor grid box, whereafter the ligand was excluded from the receptor grid. The centre of the active site grid box was set to the following coordinates: x = 24.91 Å, y = 22.48 Å, z = 9.30 Å, based on the centroid of the co-crystallised ligand.

3.2.3 Our selection of electrophilic warheads and subsequent ligand preparation

Several electrophilic moieties capable of targeting nucleophilic residues, such as cysteine, have been identified and employed in the development of irreversible covalent inhibitors. These warheads include electrophilic moieties such as α-halomethylketones, acrylamides, alkynes, vinyl sulfonates sulfonyl fluorides and epoxides.[15,16] These electrophilic warheads achieve irreversible bond formation most commonly through Michael addition, nucleophilic substitution or nucleophilic addition mechanisms.[16]

The α-halomethylketone-, acryloyl-, propioloyl- and acrylamide warheads were explored in this project. In the case where our hypothesis and small library of irreversible inhibitors yield positive results, additional electrophilic warheads could be investigated in the future. Since our work is based on the irreversible halomethylketone inhibitors developed by Perez *et al.*[17] (see Chapter 2), we began with exploration of the α-halomethylketone moiety. As a matter of intellectual and scientific curiosity, the C-Br bond of the α-halomethylketone group was also replaced with a double or triple bond to form the acryloyl- and propioloyl moieties, which are proposed to react through a Michael addition reaction. Furthermore, the acrylamide moiety was explored, due to its predominant employment in covalent inhibitor development.[15] Acrylamide warheads are favoured, since they display weak electrophilic properties and require close proximity to their targets, in order to interact.[15] This variation in electrophilic warhead could prove useful as we develop knowledge and capability in the broader field of developing new irreversible inhibitors for kinases involved in a variety of disease processes. In the context of this project we hoped it would give variation in the biological efficacy of the inhibitors, which could be useful.

The modelling studies were focused mainly on the set of ligands depicted in Scheme 3.1. The proposed set is based on the chosen scaffold, 1-(6-cyanobenzo[*d*]thiazol-2-yl)-3-(4-methoxybenzyl)urea (**4**), as discussed in Chapter 2. Therefore the cyano-substituted ureas were also included in the modelling and synthetic studies. It should be noted that nitrile warheads have been proposed to act as reversible

targeted covalent inhibitors in their reactions with cysteine.[18,19] A reversible targeted covalent inhibitor binds the target residue through a covalent interaction, to form a covalent protein-inhibitor complex, but its reversible mechanism of bond formation enables the inhibitor to dissociate from the protein on the biological timescale.[15]

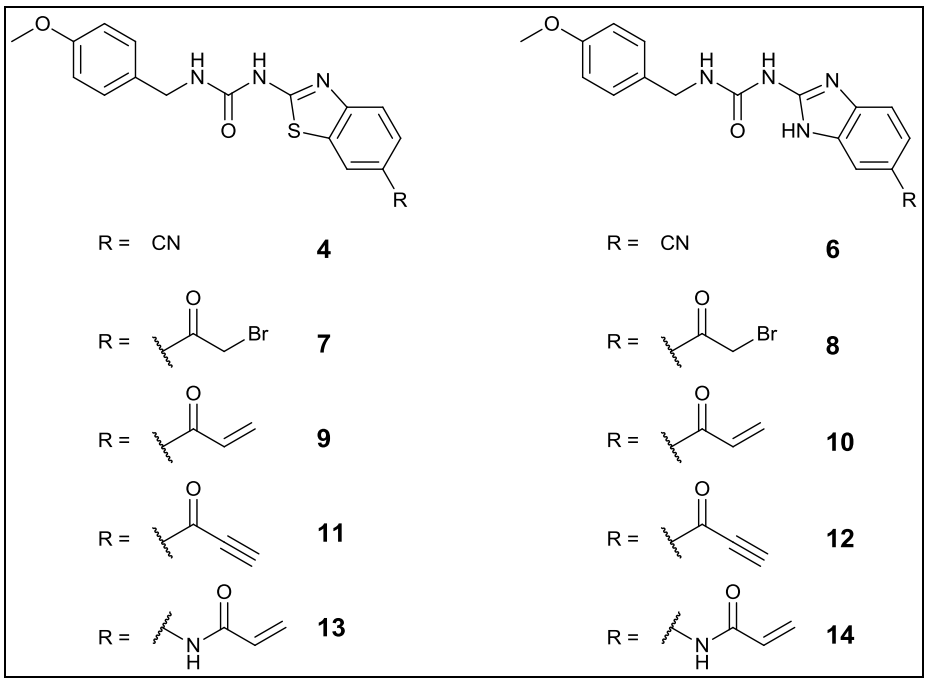

Scheme 3.1: The main set of ligands that was used in the molecular docking studies

It is worth mentioning that an additional brief modelling study was performed, where ligands with a one carbon atom linker between the electrophilic warhead and the benzothiazole/benzimidazole ring were docked (Figure 3.3). The linker-type ligands delivered poor results for the benzothiazole series during the reversible docking stage – it pushed the ligands slightly towards the outside of the pocket – therefore the linker-type ligands were not further explored.

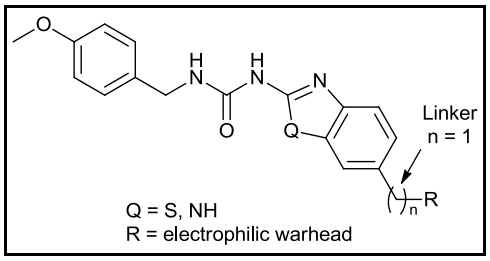

Figure 3.3: Ligands with a one carbon atom linker

Reference ligand, AR-A014418 (**3**), and the ligands in Scheme 3.1 required ligand preparation before they could be utilised in the docking studies. The 'LigPrep' function was used to convert the 2D ligand structures into chemically correct 3D structures. The correct protonation state of the ligands at

pH 7 ± 2, as well as tautomeric structures, were generated. The final step of 'LigPrep' entailed geometry optimisation to generate low-energy structures.

Theoretically, the benzimidazole ligands have three tautomeric state structures (Scheme 3.2). The tautomeric states of the benzimidazole ring undergo rapid exchange, thereby rendering substitution positions 5 and 6 equivalent in an unsubstituted aromatic ring.[20] After ligand preparation, we chose to dock both the tautomeric structures **a** and **b** for all benzimidazole ligands.

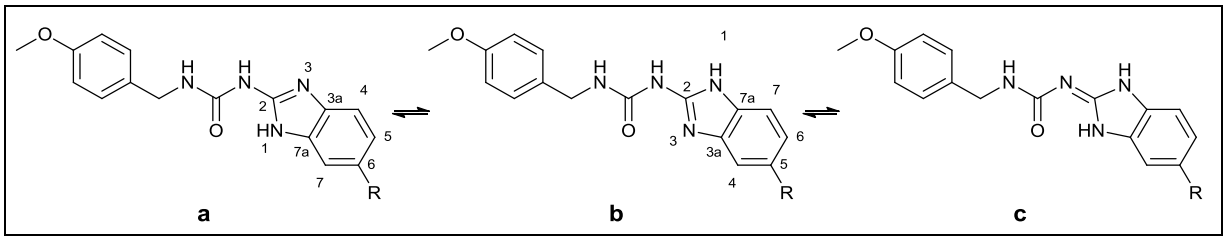

Scheme 3.2: The tautomeric states of the benzimidazole urea

Throughout this thesis, all benzimidazole ureas were drawn in the tautomeric form **a**, as defined in Scheme 3.2. We hypothesised that tautomer **a** might be more favoured, due to the intramolecular hydrogen bond that is able to form between N_1 and the urea carbonyl oxygen, to form an intramolecular 6-membered ring. Tautomeric form **a** was also supported by crystal structure analysis, which will be discussed further in Chapter 5, Section 5.3.1.1.

3.2.4 Reversible docking of our proposed GSK-3β inhibitors

The Glide ligand docking calculations were next performed using the extra-precision (XP) sampling mode. This is a more extensive sampling and scoring method that applies strict penalties to docking poses that do not comply with established physical chemistry concepts. The improved scoring function includes concepts such as adequate solvation, hydrophobic pocket occupancy and the differentiation of hydrogen bond types, with the aim of removing false positives.[11]

Ligands were docked flexibly, by the sampling of ligand conformations in the receptor site. Following the default settings, ligand conformations were restricted to the sampling of pyramidal nitrogen inversion and ring conformations. We chose to restrict amide bonds to *trans* conformations within an angle range of 20°. No additional constraints were applied during the docking stage and final post-dock minimisation was performed using the OPLS3 force field.

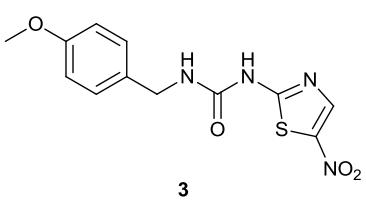

3

Overall, the described method resulted in good reversible docking results. In the initial stages, the docking model was validated by docking the co-crystallised ligand of the parent PDB file (**3**, AR-A014418, also known as the *reference ligand*), into the modelled protein structure (Figure 3.4). The pose of docked ligand **3** was used to calculate an RMSD (root-mean-square deviation) value relative to its core position in the crystal structure. The RMSD value was 0.800 Å and this low deviation value confirmed the accuracy of the docking model. AR-A014418 (**3**) had an XP docking score of -7.005 kcal/mol and this value was used as a reference in the comparative docking studies of the proposed inhibitors.

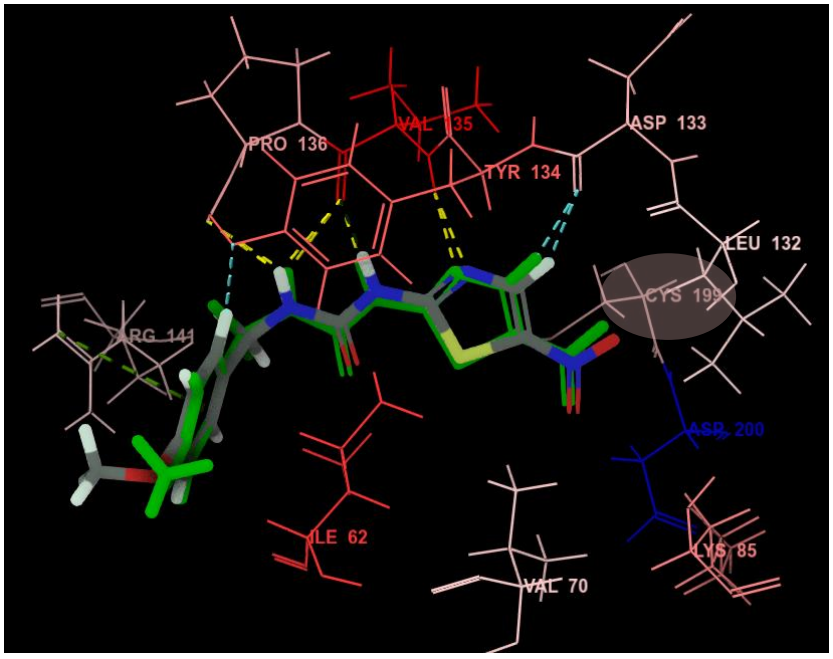

Figure 3.4: An overlay of reference ligand AR-A014418 (3) in its co-crystallised conformation (PDB ID: 1Q5K; coloured by element) and docked conformation (green); RMSD = 0.800 Å. The position of the Cys199 residue relative to the ligand is highlighted. Binding interactions are displayed in dotted lines: yellow – hydrogen bonds; blue – aromatic hydrogen bonds; green – pi-pi stacking interaction.

3.2.4.1 Evaluating the position of the electrophilic warhead relative to Cys199 in the reversible docking pose

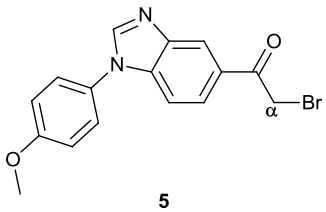

5

We also docked Perez *et al.*'s[17] irreversible halomethylketone inhibitor **5** (IC_{50} = 580 nM) in the modelled protein to investigate the position of its electrophilic warhead relative to Cys199, in the reversible docking stage (Figure 3.5). There is no X-ray crystallographic structure available in the literature for this compound, so the modelled docking pose could

not be compared to the binding mode of a co-crystallised ligand. In this docking model, the distance from the C_α atom of the HMK moiety to the sulfur of Cys199 was 4.82 Å.

We had to decide on a suitable distance criteria which would guide the selection of non-covalently docked ligands for subsequent covalent docking studies. Herein, the distance refers to the distance between the sulfur atom of Cys199 and the reactive atom of the electrophilic moiety. For **5**, the modelled distance was 4.82 Å**.** In essence, if this distance was too large, the electrophilic warhead would not be in close enough proximity of Cys199 during the reversible docking stage to allow for covalent modification. A maximum distance – which would be used in the visual inspection of reversible docking poses – had to be defined, in order to select favourable ligands for further covalent docking studies.

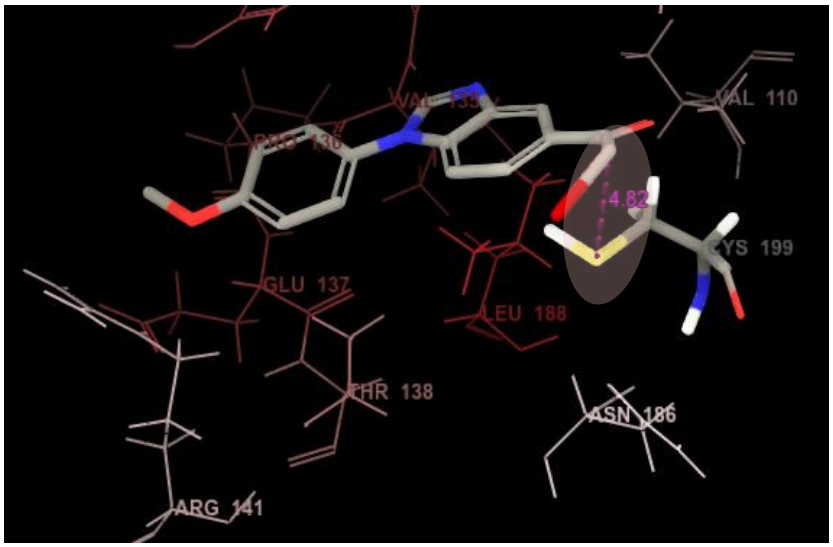

Figure 3.5: Our docking model of Perez et al.'s[17] irreversible HMK GSK-3β inhibitor. The measured distance between the sulfur atom of Cys199 and the C_α carbon of the halomethylketone moiety is highlighted (4.82 Å).

In the covalent docking protocol of Maestro Schrödinger, the Cys199 side chain conformation is sampled with respect to different conformations of the ligand's electrophilic moiety. Poses must satisfy a distance of ≤ 5 Å between the two atoms which will constitute the new covalent bond. This distance is unrealistic for a covalent bond, but is tolerated due to optimisation steps that follow downstream in the modelling process.[21] In our case, we investigated the covalent feasibility of our non-covalently docked ligands, before subjecting them to the covalent docking protocol (which have high computational cost). At this stage, the configuration of the electrophilic moiety had not yet been optimised with respect to the Cys199 side chain conformations, therefore we would generally accept a distance close to 5 Å (or less).

3.2.4.2 Reversible docking results

The proposed set of GSK-3 inhibitors displayed good reversible docking results and similar binding modes to reference ligand, AR-A014418 (**3**). The docking results of the proposed halomethylketone inhibitors (**7**, **8a**, **8b**) will be used to demonstrate the general docking modes observed for the benzothiazole and benzimidazole series, respectively.

Figure 3.6 represents the surface binding site of the receptor and the orientation of benzothiazole urea **7** in the pocket. Both the benzothiazole and the benzimidazole series fit inside the pocket in this manner. The electrophilic warhead is positioned in the deepest end of the pocket, the urea functionality acquires hydrogen bonds to the hinge binding region and the 4-methoxybenzyl group is situated towards the outside of the pocket. The L-shape of the binding pocket is noteworthy. The pocket is elongated along the hinge region, which facilitates the planarity of the core regions of our inhibitors. The benzylic carbon of the 4-methoxybenzyl group, allows out-of-plane bending to facilitate the entrance region of the pocket.

Figure 3.7 depicts the binding interactions of HMK benzothiazole urea **7**. In this modelling outcome, both NH protons of the urea functionality formed hydrogen bonds with hinge residue Val135. A weaker aromatic hydrogen bond was visible between one of the benzothiazole aromatic hydrogens and the backbone carbonyl oxygen of hinge residue Asp133. In addition, the HMK carbonyl oxygen formed a hydrogen bond with Asp200. The distance between the C_α carbon of the HMK group and the sulfur atom of Cys199 was 4.45 Å, which is a promising target distance (based on our parameters) for further covalent studies. The rest of the benzothiazole series (**4, 9, 11, 13**) displayed the same binding modes. The binding interactions of the acrylamide benzothiazole urea **13** differed slightly. The larger electrophilic moiety pushed the molecule slightly towards the outside of the pocket. Instead of forming two hydrogen bonds with Val135, the two NH protons formed bonds with Pro136 and Val135 respectively.

The binding modes and binding interactions of HMK benzimidazole urea **8a** and its tautomer, **8b**, are represented in Figure 3.8 and Figure 3.9. Both benzimidazole urea tautomers have similar docking modes, therefore tautomerism was not expected to hinder successful docking. The benzimidazole series accommodated the formation of one additional hydrogen bond in the hinge region. Hydrogen bond interactions are established with hinge residues Val135 and Pro136, and an aromatic hydrogen bond with Asp133 is present in most cases. The imidazole moiety allows rotation of the benzimidazole ring while maintaining the additional hydrogen bond in the hinge region, thereby allowing the electrophilic moiety to manoeuvre itself into the most favourable docking position.

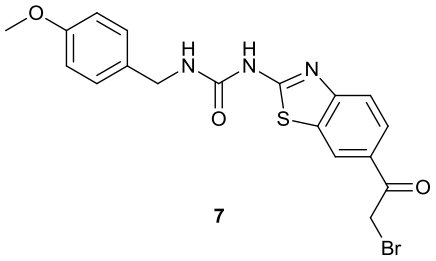

7

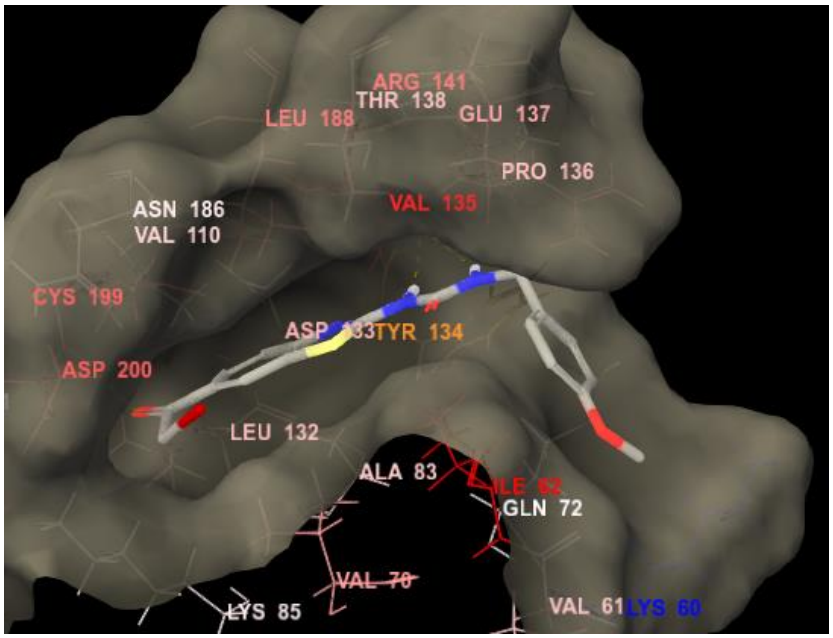

Figure 3.6: The positioning of proposed HMK inhibitor 7 in the GSK-3β binding pocket

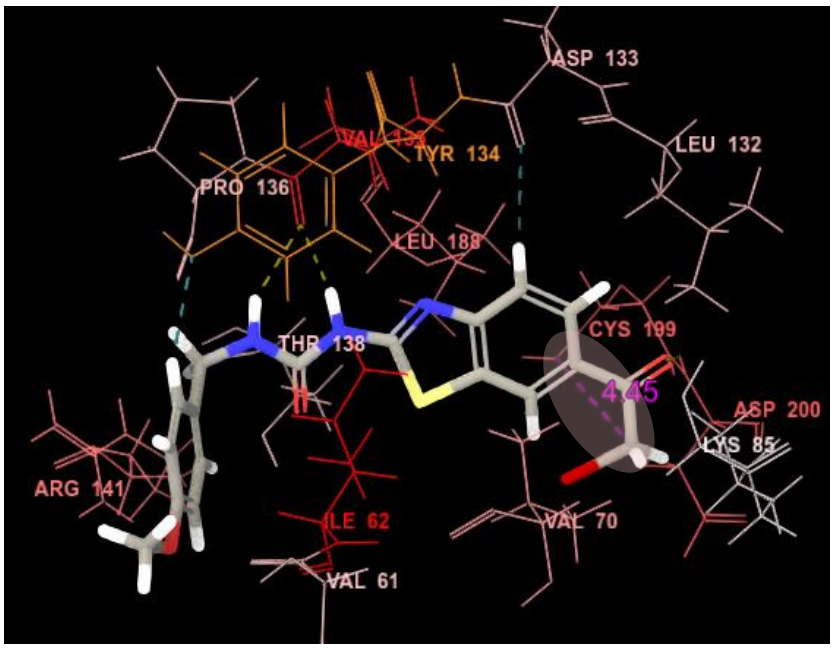

Figure 3.7: Ligand-receptor interactions of HMK ligand 7 with the binding site residues. Dotted lines: yellow – hydrogen bonds; blue – aromatic hydrogen bonds. The measured distance between the sulfur atom (Cys199) and the C_α atom (HMK) is highlighted (4.45 Å).

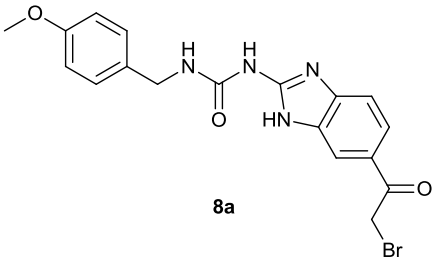

8a

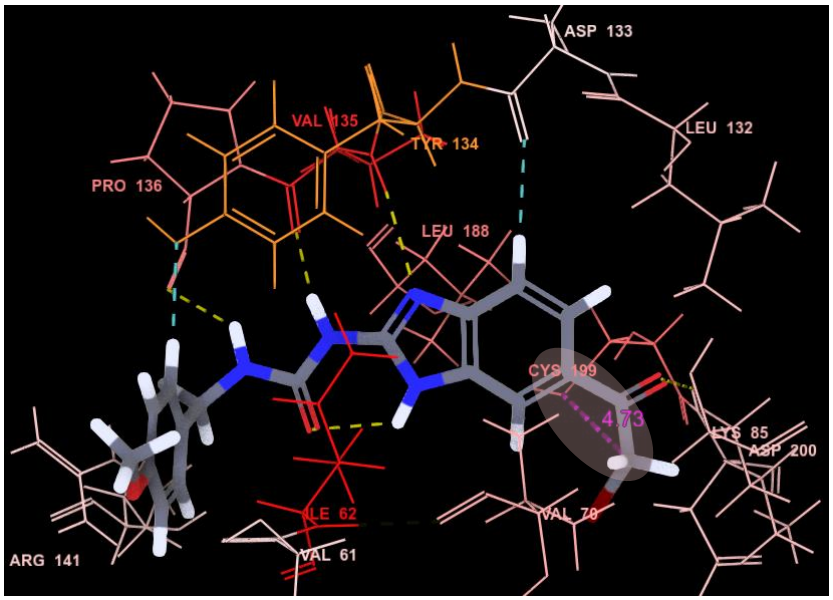

Figure 3.8: Ligand-receptor interactions of HMK ligand 8a with the GSK-3β binding site residues. Dotted lines: yellow – hydrogen bonds; blue – aromatic hydrogen bond. The measured distance between the sulfur atom (Cys199) and the C_α atom (HMK) is highlighted (4.73 Å).

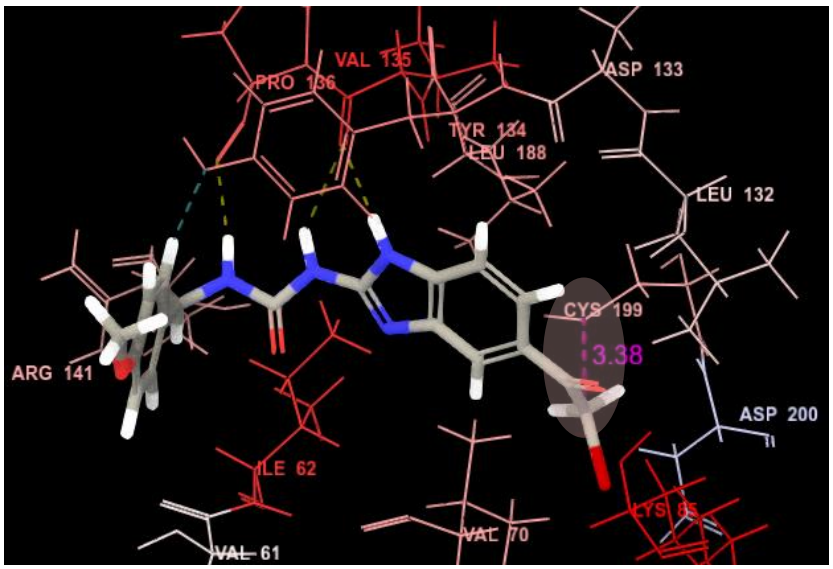

Figure 3.9: Tautomer 8b of the HMK ligand and its ligand-receptor interactions with the GSK-3β binding site residues. The measured distance between the sulfur atom (Cys199) and the C_α atom (HMK) is highlighted (3.38 Å).

The benzimidazole scaffold's ability to form one additional hydrogen bond can be ascribed to the donating ability of the lone pair on the unprotonated nitrogen in the imidazole ring. The lone pair nitrogen of unsubstituted benzimidazole is a weak base in nature, due to the strong acidic properties of its conjugate acid (pKa [BH^+] = 5.59).[22] If the benzimidazole ring is rotated towards the hinge region, the weak base can form a hydrogen bond interaction with the backbone amide hydrogen of Val135. However, the lone pair nitrogen of unsubstituted benzothiazole is a much weaker base (the conjugate acid is much stronger, pKa [BH^+] = 1.2)[23] and does not seem to facilitate this hydrogen bond.

The reversible docking results are summarised in Table 3.1. All of the proposed inhibitors displayed more favourable (lower energy) docking scores than reference ligand **3** (AR-A014418)'s docking score of -7.005 kcal/mol. The benzimidazole series yielded the best docking scores, with scores ranging from -9.338 kcal/mol to -8.469 kcal/mol. This is most likely due to the benzimidazole urea's ability to accommodate an additional hydrogen bond to the hinge region of the ATP binding site. The benzothiazole series also yielded good docking scores in the range of -7.651 kcal/mol to -7.206 kcal/mol.

Tautomeric structures of the benzimidazole-derived ureas were originally docked to ensure that tautomerism does not cause major shifts in the docking poses of ligands. Generally, the tautomeric structures docked similarly in the binding site. The different tautomers resulted in changes in the distances of the electrophilic warheads from the Cys199 target residue and may also provide improved stereoelectronic effects, i.e. in the orientation of the electrophilic warhead. No favourable docking poses were obtained for ligands **10b** and **12b**, although good docking scores were obtained for their tautomers **10a** and **12a**, respectively. In these two cases, the existence of a tautomeric equilibrium might result in lower activity scores.

When the proposed ligands were compared, the propioloyl-substituted ureas (**11**, **12**) displayed the least favourable docking scores and gave relatively long target distances in the non-covalent docking stage. The linearity of the propioloyl group, together with the planarity of the core structure, are proposed to disadvantage this type of ligand.

Overall, the distances measured between electrophilic warhead reactive atoms and the sulfur of Cys199 were deemed feasible for further covalent docking studies and optimisation.

Table 3.1: A summary of the reversible docking results (Glide v7.4, Schrödinger Drug Discovery Suite).

Reversible and irreversible reference ligands								
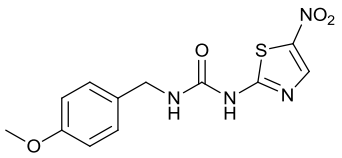			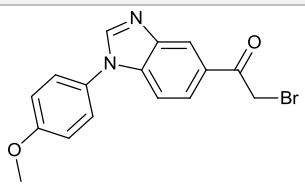					
	XP docking Gscore (kcal/mol)			**XP docking Gscore (kcal/mol)**	**Distance from the reactive atom to Cys199 (Å)**			
3	-7.005		**5**	-5.939	4.82			
Proposed ligands								
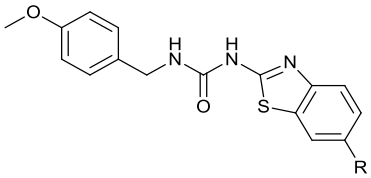			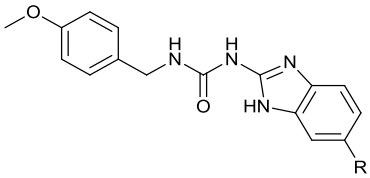			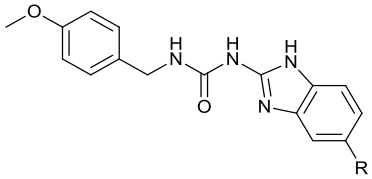		
R	**XP docking Gscore (kcal/mol)**	**Distance from the reactive atom to Cys199 (Å)**	**R**	**XP docking Gscore (kcal/mol)**	**Distance from the reactive atom to Cys199 (Å)**	**R**	**XP docking Gscore (kcal/mol)**	**Distance from the reactive atom to Cys199 (Å)**
4	-7.651	4.01	**6a**	-9.089	3.95	**6b**	-8.469	3.97
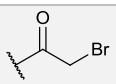 **7**	-7.278	4.45	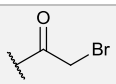 **8a**	-8.859	4.73	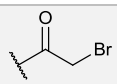 **8b**	-8.994	3.38
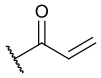 **9**	-7.305	5.53	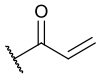 **10a**	-9.338	3.84	 **10b**	No result	–
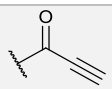 **11**	-7.206	5.16	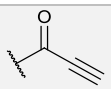 **12a**	-8.596	5.15	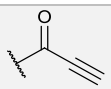 **12b**	No result	–
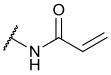 **13**	-7.562	5.08	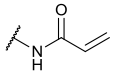 **14a**	-9.180	5.20	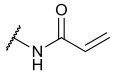 **14b**	-8.963	4.86

3.2.5 Covalent docking studies of the proposed GSK-3β inhibitors

The reversible docking poses associated with the results in Table 3.1, were used as the input ligands for the covalent studies. The covalent docking study was performed using the Glide 'Covalent Docking' function.[21] This function commences with a reversible docking step wherein non-covalent ligand poses of the input ligand are sampled in order to obtain poses which are stabilised by non-covalent interactions and in which the reactive warhead is in close proximity of the target residue. Then the receptor side chain conformation is sampled relative to these poses. Subsequently, the receptor and ligand are linked by a covalent bond and the protein-ligand complex is optimised by OPLS3 and VSGB2.0.[24] VSGB2.0 is an energy model used in protein structure modelling.

Due to the formation of a covalent protein-ligand complexes, a different scoring method is used to score covalent ligand poses. A binding affinity score is used to compare the ligands. The affinity score combines the non-covalent Glide docking score with a Glide docking score obtained from a 'non-covalent' version of the final covalent docking pose.[21]

The covalent binding modes and binding interactions of HMK ligands **7** and **8** are stacked on their non-covalent binding modes in Figure 3.10 and Figure 3.11, respectively. These covalent binding modes are also representative of the covalent poses observed for the rest of the benzothiazole- and benzimidazole urea series. From the docking results, it appeared that covalent bond formation was tolerated well inside the binding site, with only minor shifts in ligand orientation being observed. The covalent bond tended to shift the ligand slightly towards the outside of the pocket. Therefore it was observed that instead of forming two hydrogen bonds with Val135 in the hinge region, the ligands tended to form one hydrogen bond with Val135 and one hydrogen bond with either Pro136 or Tyr134. The rest of the ligand-receptor interactions (hydrogen bonds and aromatic hydrogen bonds) were maintained throughout covalent docking.

The tautomeric structures of the benzimidazole-based ligands docked similarly during the non-covalent studies, therefore the best covalent affinity score that was obtained for a ligand regardless of its tautomeric state, was reported (Table 3.2). An affinity score of -7.359 kcal/mol was calculated for covalent reference ligand **5**. The nitrile ligands, **4** and **6**, displayed good covalent affinity scores of -7.670 kcal/mol and -8.447 kcal/mol, respectively. It should be noted that the nitrile ligands are aimed to provide selectivity through a covalent attack on Cys199, but may also provide decreased toxicity risks due to the potential reversible nature of the bond. The rest of the proposed set of ligands obtained positive covalent docking results, with affinity scores ranging between -9.457 kcal/mol and -7.548 kcal/mol. These promising covalent results supported our aim of designing and synthesising targeted covalent inhibitors for the GSK-3 enzyme.

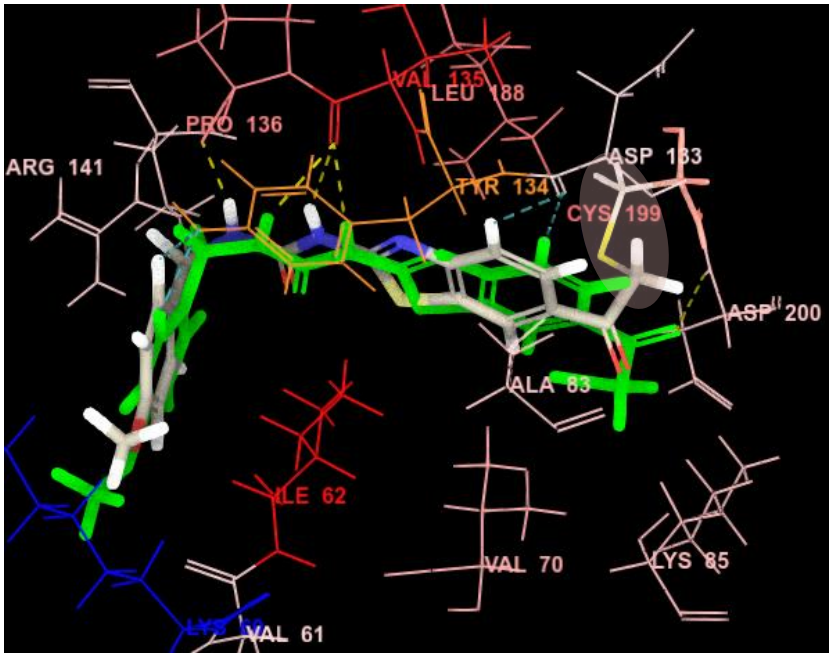

Figure 3.10: An overlay of HMK ligand 7 (benzothiazole-derived) in its covalent docking pose (coloured by element) and in its non-covalent docking pose (green); Dotted lines: yellow – hydrogen bonds; blue – aromatic hydrogen bonds. The covalent bond with Cys199 is highlighted.

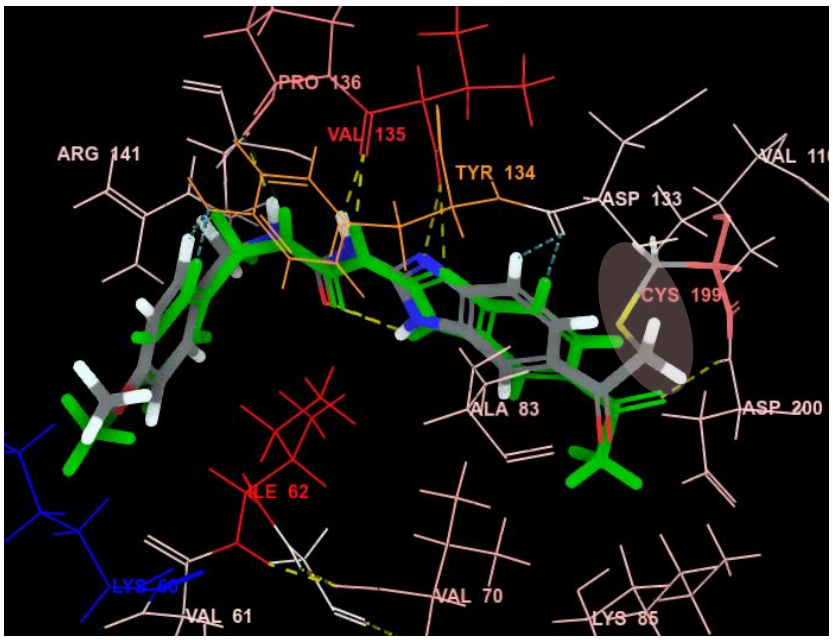

Figure 3.11: An overlay of HMK ligand 8 (benzimidazole-derived) in its covalent docking pose (coloured by element) and in its non-covalent docking pose (green); Dotted lines: yellow – hydrogen bonds; blue – aromatic hydrogen bonds. The covalent bond with Cys199 is highlighted.

Table 3.2: A summary of the irreversible docking results (Covalent Docking, Schrödinger Drug Discovery Suite)

Irreversible reference ligand			
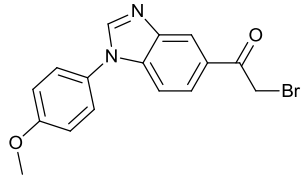			
	Affinity score (kcal/mol)		
5	-7.359		
Proposed ligands			
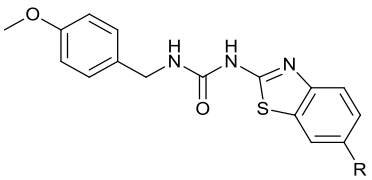		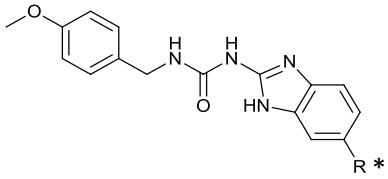	
R	**Affinity score (kcal/mol)**	**R**	**Affinity score (kcal/mol)**
CN **4**	-7.670	CN **6**	-8.447
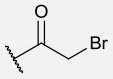 **7**	-7.837	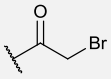 **8**	-8.520
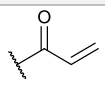 **9**	-7.548	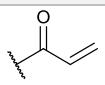 **10**	-8.652
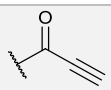 **11**	-8.190	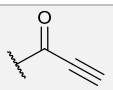 **12**	-9.457
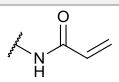 **13**	-8.524	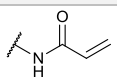 **14**	-8.980

* Henceforth we do not distinguish between tautomeric structures, the best docking score was reported.

3.3 Concluding remarks

The modelled binding modes, target distances and docking scores in both the non-covalent and covalent stages were very promising for the proposed 1-benzazole-3-(4-methoxybenzyl)urea series. Therefore, it was decided that the whole series, as was depicted in Scheme 3.1, would be synthesised. If the variations in ligand binding modes correlate to variations in biological efficacy, it could provide good evidence that this molecular modelling approach can be used to develop and refine potential lead molecules. The synthesis of the proposed compound library will be discussed next.

3.4 References

1 M. Aoki, T. Yokota, I. Sugiura, C. Sasaki, T. Hasegawa, C. Okumura, K. Ishiguro, T. Kohno, S. Sugio and T. Matsuzaki, *Acta Crystallogr., Sect. D*, 2004, **60**, 439–446.

2 R. Bhat, Y. Xue, S. Berg, S. Hellberg, M. Ormö, Y. Nilsson, A. C. Radesäter, E. Jerning, P. O. Markgren, T. Borgegård, M. Nylöf, A. Giménez-Cassina, F. Hernández, J. J. Lucas, J. Díaz-Nido and J. Avila, *J. Biol. Chem.*, 2003, **278**, 45937–45945.

3 J. A. Bertrand, S. Thieffine, A. Vulpetti, C. Cristiani, B. Valsasina, S. Knapp, H. M. Kalisz and M. Flocco, *J. Mol. Biol.*, 2003, **333**, 393–407.

4 M. Saitoh, J. Kunitomo, E. Kimura, Y. Hayase, H. Kobayashi, N. Uchiyama, T. Kawamoto, T. Tanaka, C. D. Mol, D. R. Dougan, G. S. Textor, G. P. Snell and F. Itoh, *Bioorg. Med. Chem.*, 2009, **17**, 2017–2029.

5 D. Shin, S. C. Lee, Y. S. Heo, W. Y. Lee, Y. S. Cho, Y. E. Kim, Y. L. Hyun, J. M. Cho, Y. S. Lee and S. Ro, *Bioorg. Med. Chem. Lett.*, 2007, **17**, 5686–5689.

6 *Maestro*, version 11.1, Schrödinger, LLC, New York, NY, 2017.

7 X. Li, X. Wang, Z. Tian, H. Zhao, D. Liang, W. Li, Y. Qiu and S. Lu, *J. Mol. Model.*, 2014, **20**, 1–11.

8 L. Meijer, A.-L. Skaltsounis, P. Magiatis, P. Polychronopoulos, M. Knockaert, M. Leost, L. Pearl, X. P. Ryan, C. A. Vonica, A. Brivanlou, R. Dajani, C. Crovace, C. Tarricone, A. Musacchio, S. M. Roe and P. Greengard, *Chem. Biol.*, 2003, **10**, 1255–1266.

9 R. A. Friesner, J. L. Banks, R. B. Murphy, T. A. Halgren, J. J. Klicic, D. T. Mainz, M. P. Repasky, E. H. Knoll, M. Shelley, J. K. Perry, D. E. Shaw, P. Francis and P. S. Shenkin, *J. Med. Chem.*, 2004, **47**, 1739–1749.

10 T. A. Halgren, R. B. Murphy, R. A. Friesner, H. S. Beard, L. L. Frye, W. T. Pollard and J. L. Banks, *J. Med. Chem.*, 2004, **47**, 1750–1759.

11 R. A. Friesner, R. B. Murphy, M. P. Repasky, L. L. Frye, J. R. Greenwood, T. A. Halgren, P. C. Sanschagrin and D. T. Mainz, *J. Med. Chem.*, 2006, **49**, 6177–6196.

12 *Glide 7.4 User Manual*, Schrödinger, LLC, New York, NY, 2017.

13 E. Harder, W. Damm, J. Maple, C. Wu, M. Reboul, J. Y. Xiang, L. Wang, D. Lupyan, M. K. Dahlgren, J. L. Knight, J. W. Kaus, D. S. Cerutti, G. Krilov, W. L. Jorgensen, R. Abel and R. A. Friesner, *J. Chem. Theory Comput.*, 2016, **12**, 281–296.

14 F. Lo Monte, T. Kramer, A. Boländer, B. Plotkin, H. Eldar-Finkelman, A. Fuertes, J. Dominguez and B. Schmidt, *Bioorg. Med. Chem. Lett.*, 2011, **21**, 5610–5615.

15 T. A. Baillie, *Angew. Chem., Int. Ed.*, 2016, **55**, 13408–13421.

16 Q. Liu, Y. Sabnis, Z. Zhao, T. Zhang, S. J. Buhrlage, L. H. Jones and N. S. Gray, *Chem. Biol.*, 2013, **20**, 146–159.

17 D. I. Perez, V. Palomo, C. Pérez, C. Gil, P. D. Dans, F. J. Luque, S. Conde and A. Martínez, *J. Med. Chem.*, 2011, **54**, 4042–4056.

18 J. T. Palmer, C. Bryant, D.-X. Wang, D. E. Davis, E. L. Setti, R. M. Rydzewski, S. Venkatraman, Z.-Q. Tian, L. C. Burrill, R. V. Mendonca, E. Springman, J. McCarter, T. Chung, H. Cheung, J. W. Janc, M. McGrath, J. R. Somoza, P. Enriquez, Z. W. Yu, R. M. Strickley, L. Liu, M. C. Venuti, M. D. Percival, J.-P. Falgueyret, P. Prasit, R. Oballa, D. Riendeau, R. N. Young, G. Wesolowski, S. B. Rodan, C. Johnson, D. B. Kimmel and G. Rodan, *J. Med. Chem.*, 2005, **48**, 7520–7534.

19 J. J. M. Wiener, S. Sun and R. L. Thurmond, *Curr. Top. Med. Chem.*, 2010, **10**, 717–732.

20 L. B. Townsend and D. S. Wise, *Parasitol. Today*, 1990, **6**, 107–112.

21 K. Zhu, K. W. Borrelli, J. R. Greenwood, T. Day, R. Abel, R. S. Farid and E. Harder, *J. Chem. Inf. Model.*, 2014, **54**, 1932–1940.

22 H. Sari and A. K. Covington, *J. Chem. Eng. Data*, 2005, **50**, 1425–1429.

23 M. H. Abraham, P. P. Duce, D. V Prior, D. G. Barratt, J. J. Morris and P. J. Taylor, *J. Chem. Soc., Perkin Trans. 2*, 1989, **25**, 1355–1375.

24 J. Li, R. Abel, K. Zhu, Y. Cao, S. Zhao and R. A. Friesner, *Proteins*, 2011, **79**, 2794–2812.

Chapter 4: The synthesis of functionalised benzothiazole- and benzimidazole urea scaffolds

4.1 Key retrosynthetic steps

The retrosynthetic analysis in Scheme 4.1 highlights the major steps that we envisioned would constitute the synthetic route to the 1-benzazole-3-(4-methoxybenzyl)urea series. The urea functionality of the proposed inhibitors would be constructed from a nucleophilic 2-aminobenzazole ring and an electrophilic equivalent of 4-methoxybenzylamine (**15**). To this end, the synthesis of appropriately functionalised, bicyclic benzothiazole/benzimidazole ring scaffolds was commenced. Due to the electrophilicity of the reactive warheads, we aimed to incorporate the warheads after urea formation, through modification of the substituent R- group.

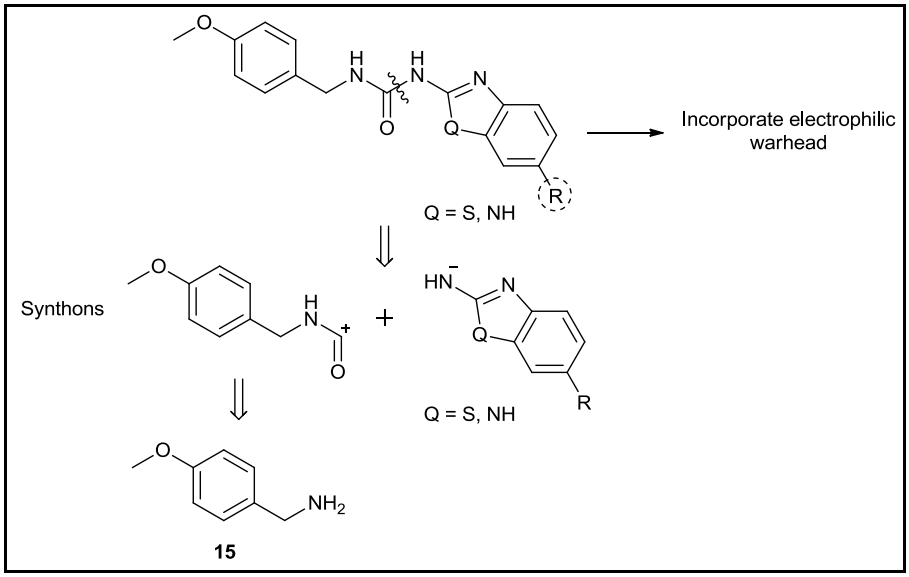

Scheme 4.1: Important retrosynthetic steps that would form part of the synthetic approach

The first priority was to synthesise the benzothiazole and benzimidazole heterocycles that would serve as scaffolds in the proposed inhibitors.

4.2 Privileged structures: Benzothiazoles and benzimidazoles

Privileged structures are extremely useful in drug discovery strategies, especially in the rational design and/or optimisation of new lead compounds.[1] IUPAC (International Union of Pure and Applied Chemistry) defined a 'privileged structure' as a "substructural feature which confers desirable (often drug-like) properties on compounds containing that feature. [A privileged structure] often consists of a semi-rigid scaffold which is able to present multiple hydrophobic residues without undergoing

hydrophobic collapse."[2] A privileged structure provides a core structure with highly favourable characteristics to a drug design process and this core structure can then be functionalised to improve potency and selectivity.[1]

Benzothiazoles are privileged bicyclic compounds which are present in marine and terrestrial natural products of medicinal use. Benzothiazole-derived therapeutics have shown a broad range of biological activities including antitubercular, antimicrobial, antimalarial, anticonvulsant, anthelmintic, analgesic, anti-inflammatory, antidiabetic and anticancer properties.[3] The benzothiazole heterocycle is stabilised by its aromatic structure and contains reactive sites which permit functionalisation.[4,5]

The benzimidazole heterocyclic structure attracted attention in the 1950s when it was found to form a characteristic part of the structure of Vitamin B12 (Figure 4.1).[6] Benzimidazole derivatives are also bioisosteres of the purine nucleotides, which promote their interactions with biomolecules in living organisms.[7] Benzimidazole-derived therapeutics have been associated with a broad range of biological activities including anthelmintic, antitubercular, antimicrobial, antimalarial, anticonvulsant, analgesic, anti-inflammatory, antidiabetic, anticancer, antifungal, antiviral and antioxidant properties.[7]

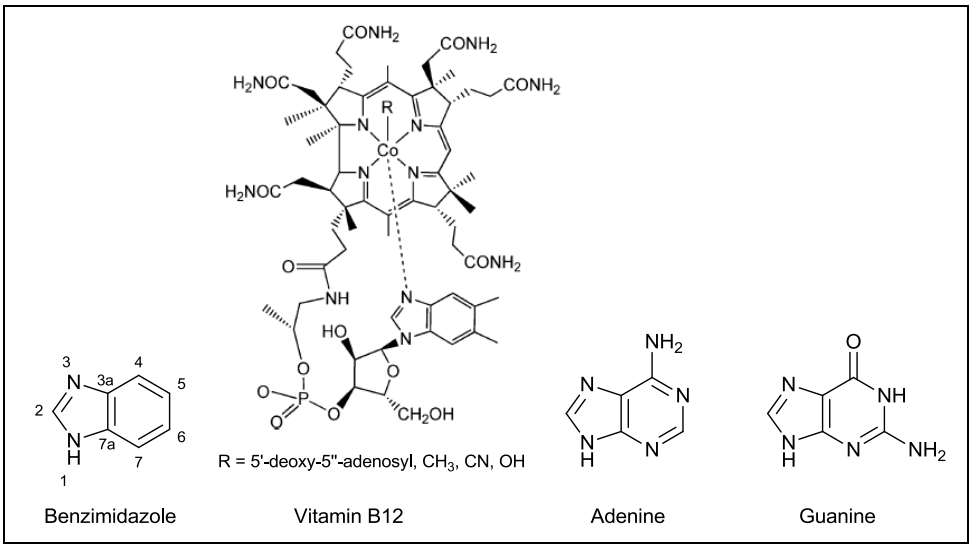

Figure 4.1: The structure of vitamin B12 and the purine nucleotides, adenine and guanine. (Image of Vitamin B12 reproduced from Pan et al.[8])

4.3 The synthesis of the 6-substituted 2-aminobenzothiazoles

There are several reported methods for 2-aminobenzothiazole synthesis. After a literature survey on 2-aminobenzothiazole synthesis,[3,9] it could be concluded that substituted anilines and arylthioureas are the most commonly used starting materials. Synthetic methods toward *N*-substituted 2-aminobenzothiazoles were also present in the literature and could provide an alternative synthetic

route to our target compounds in the case of synthetic complications. Typical examples of the reported methods for the synthesis of 2-aminobenzothiazoles are described below and displayed in Scheme 4.2. These include:

1. Anilines and substituted anilines in glacial acetic acid have been reacted with alkali thiocyanates in the presence of an oxidising agent such as bromine, at low temperatures, to yield the 2-aminobenzothiazole ring.[9,10]
2. In the Hugerschoff reaction, arylthioureas are treated with bromine in chloroform to promote cyclisation.[11,12]
3. The condensation reaction of 2-aminothiophenols with substituted aldehydes, carboxylic acids, alcohols, amines, nitriles and isocyanates are widely utilised in the synthesis of 2-substituted benzothiazoles.[3,13]
4. Various transition metals, including palladium, copper and iron, have been involved in the catalytic synthesis of *N*-substituted 2-aminobenzothiazoles, through the promotion of C-S bond formation/C-H functionalisation.[3,14]

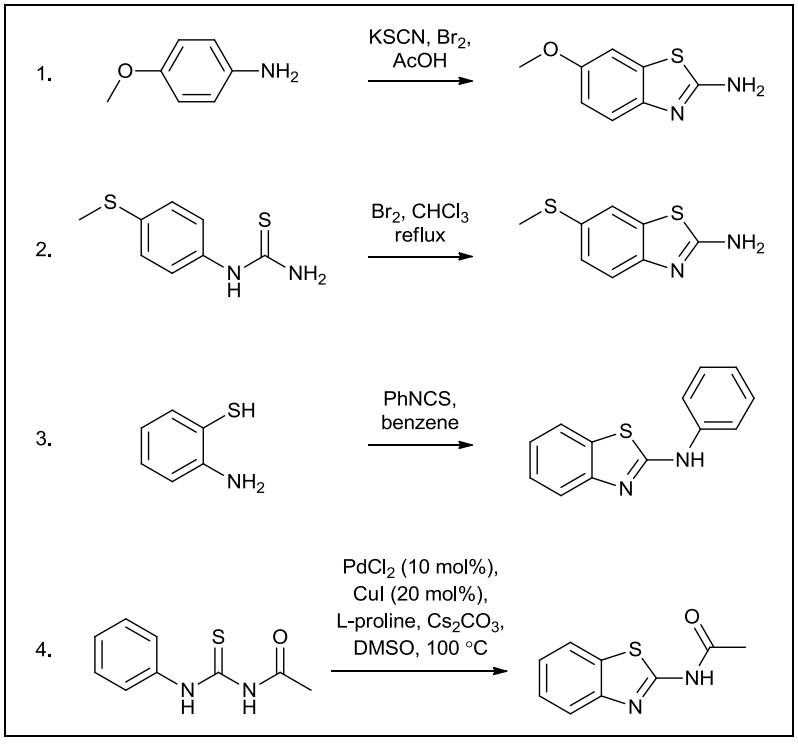

Scheme 4.2: Examples of synthetic procedures towards 2-aminobenzothiazoles

The first-mentioned procedure was followed, given that the substituted anilines were available as starting material and since the success of the method had been well-documented. This type of system, where a thiocyanation agent (KSCN, NaSCN or NH_4SCN) is combined with an oxidant, is regarded as the general procedure for the thiocyanation of aromatic amines.[15] Several different oxidants have

been used successfully in thiocyanation reactions in the literature, including Br_2, Cl_2, I_2, dichlorourea, $FeCl_3$, HIO_3, I_2O_5 and NBS.[15]

Thiocyanation refers to the substitution of a hydrogen atom with a thiocyano group and is mediated by thiocyanogen $(SCN)_2$.[16] Thiocyanogen acts as the electrophile in an electrophilic aromatic substitution reaction (eq. 4.1). It is therefore expected to favour substitution at the *para* and the *ortho* positions when it is reacted with an aromatic compound, containing an electron-donating group.[16]

$$ArH + (SCN)_2 \rightarrow ArSCN + HSCN \quad (eq.\ 4.1)$$

Thiocyanogen is unstable in solution, with a tendency to polymerise and hydrolyse. Therefore thiocyanogen is commonly generated *in situ* when it is employed in reactions.[16] The oxidant is responsible for the liberation of thiocyanogen from the alkali thiocyanate salts (eq. 4.2).[17]

$$2KSCN + Br_2 \rightarrow (SCN)_2 + 2KBr \quad (eq.\ 4.2)$$

After the *ortho* thiocyanation of our *para* substituted anilines (starting materials **16 – 19**), cyclisation was required to form the 2-aminobenzothiazoles (**20 – 23**)**.** The ease of cyclisation was influenced by the substituents located on the thiocyanated ring, and could occur either spontaneously or require heating under acidic conditions.[16]

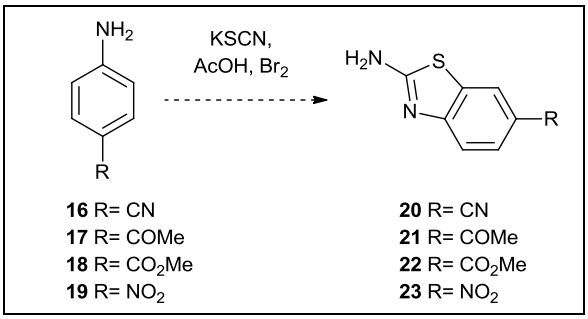

Scheme 4.3: The initial strategy towards 2-aminobenzothiazole synthesis

The R-groups (R= CN, COMe, CO_2Me, NO_2) in Scheme 4.3 were selected in accordance with the proposed strategy to modify these precursor groups into electrophilic warheads after urea synthesis.

4.3.1 The synthesis of 2-aminobenzo[*d*]thiazole-6-carbonitrile (20)

As a first attempt to synthesise 2-aminobenzo[*d*]thiazole-6-carbonitirile (**20**), a two-step literature procedure described by Sawhney and Boykin was followed (Scheme 4.4).[18] To this end, 4-aminobenzonitrile (**16**) and KSCN were dissolved in glacial acetic acid and treated dropwise with a solution of Br_2 in glacial acetic acid, at 5 °C. From Sawhney and Boykin's procedure, it was deduced

that the thiocyanated intermediate (**24**) can be isolated, whereafter a 2 h reflux in HCl would promote cyclisation to afford **20**. The reaction was carried out following their KSCN/Br_2 procedure and the intermediate (**24**) was isolated, but in only a low yield of 36%.

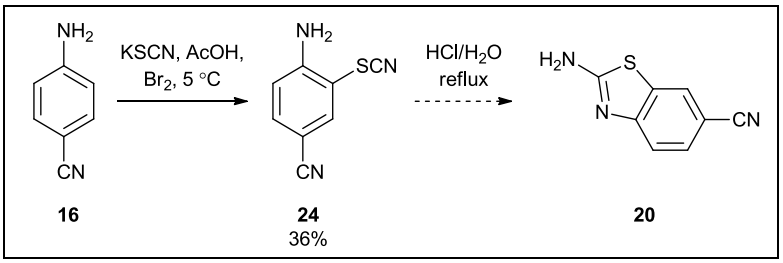

Scheme 4.4: A two-step procedure to synthesise 2-aminobenzo[d]thiazole-6-carbonitrile (20)

Several by-products were visible on TLC during the synthesis of the thiocyanated intermediate (**24**), which explained the low yield. Firstly, the molecular bromine (Br_2) present in the solution is highly reactive and difficulties in controlling the stoichiometric amount of Br_2 could result in brominated side products.[19] Secondly, the nascent thiocyanogen generated in the reaction solution is unstable and could participate in side reactions.[17] Optimisation studies were performed to increase the yield of the thiocyanation reaction. The results of the optimisation studies are concluded in Table 4.1, which will follow after the discussion of the results. The following optimisation strategies were thus explored:

4.3.1.1 Avoiding bromination side-products

Jordan and co-workers prepared a series of 2-aminobenzothiazoles using the Hugerschoff reaction and managed to improve the stoichiometric control over their bromine source by substituting Br_2 with the organic ammonium tribromide, benzyltrimethylammonium tribromide ($PhCH_2NMe_3Br_3$).[19] The high molecular weight and crystallinity of the organic ammonium tribromide allowed for better control over stoichiometry. Jordan and co-workers[19] extended their studies to explore the use of $PhCH_2NMe_3Br_3$ in the synthesis of 2-aminobenzothiazoles from substituted anilines. They successfully combined $PhCH_2NMe_3Br_3$ with NH_4SCN in acetonitrile to synthesise their 2-alkylaminobenzothiazoles.[19] Based on their studies, Br_2 in the thiocyanation reaction (**16** to **24**, Scheme 4.4) was replaced with an organic ammonium tribromide. Phenyltrimethylammonium tribromide ($PhNMe_3Br_3$/ PTAB) was available, and increased the yield of the thiocyanation step to 62%. Phenyltrimethylammonium tribromide served as a bromine source (eq. 4.3).

$$PhNMe_3Br_3 \rightleftarrows Br_2 + PhNMe_3Br \quad (eq.\ 4.3)$$

4.3.1.2 Considering a neutral solvent

DCM was explored as a neutral reaction solvent in the thiocyanation reaction with PTAB and KSCN, to determine whether solvent acidity affects the thiocyanation substitution reaction. The described conditions led to a much lower yield of 16%, therefore no other neutral solvents were explored.

4.3.1.3 Avoiding side-reactions due to nascent thiocyanogen

Side-reactions in the thiocyanation step due to freshly generated, reactive thiocyanogen, can be limited through the optimisation of various variables, including reagent equivalents, addition times, temperature and water content.[17] An optimisation study performed by Pilyugin *et al.*,[17] on the efficient preparation of 2-nitro-4-thiocyanoaniline in acetic acid with bromine and a thiocyanate salt, provided insight into the influence of these variables on thiocyanation. Based on their findings, the thiocyanogen equivalents generated *in situ* were optimised, which resulted in an increased yield of 75% for compound **24**. PTAB (the oxidant) was added in slight excess (1.4 equiv) to ensure that an excess of thiocyanogen was generated, in order to thiocyanate all of the starting material (**16**, 1.0 equiv). However, to limit the formation of bromination by-products, potassium thiocyanate was used in excess (3.2 equiv) relative to PTAB. The results of the discussed optimisation strategies are summarised in Table 4.1.

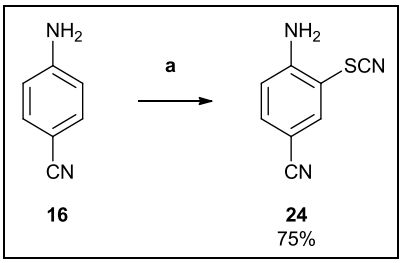

Scheme 4.5: The thiocyanation of 4-aminobenzonitrile (16)

Table 4.1: Summary of attempted thiocyanation reactions, step a (Scheme 4.5)

Step **a**		
Entry	**Reagents and reaction conditions**	**% yield**
1	1) KSCN *(2 equiv)*, glacial AcOH 2) Br_2 *(1 equiv)*, glacial AcOH, 5 °C to r.t., 2 h	36
2	1) KSCN *(2 equiv)*, glacial AcOH 2) PTAB *(1 equiv)*, 10 °C to r.t., 5.5 h	62
3	1) KSCN *(2 equiv)*, DCM 2) PTAB *(1.1 equiv)*, r.t., 20 h	16
4	1) KSCN *(3.2 equiv)*, glacial AcOH 2) PTAB *(1.4 equiv)*, 5 °C to r.t., 5 h	**75**

In the literature,[18] the thiocyanation reaction is quenched with water, whereafter the yellow precipitate is filtered and then recrystallised from EtOH. This procedure was followed for entries 1 and 2 in Table 4.1. However the dense yellow precipitate was difficult to work with, therefore a work-up step was incorporated into entries 3 and 4 which involved the extraction of the yellow precipitate with EtOAc and then purifying with silica column chromatography.

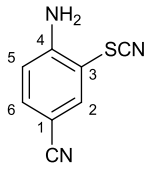

24

The presence of the thiocyanate group was confirmed by IR spectroscopy (Figure 4.2), to ensure that it is the thiocyanated product (**24**) and not the cyclised product (**20**). The C≡N stretch of the nitrile group was visible at 2220 cm^{-1}. A strong peak at 2158 cm^{-1} represented the stretch of the thiocyanate group. It should be noted that the isomeric *iso*thiocyanates (R-NCS) usually display a broad, strong characteristic peak in the region 2105 – 2060 cm^{-1}.[20] The absence of such a peak confirmed the successful attachment of a thiocyanate group to the ring and not a rearranged *iso*thiocyanate group.

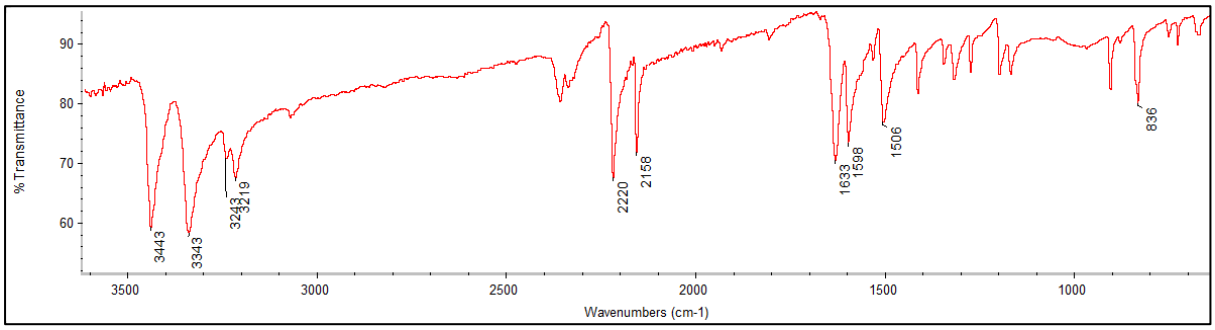

Figure 4.2: The IR spectrum of 4-amino-3-thiocyanatobenzonitrile (24)

In the ^{1}H NMR spectrum of **24**, the doublet of ArH_2 resonated at 7.95 ppm with a *meta J*-coupling constant of 2.0 Hz, ArH_6 resonated at 7.57 ppm as a doublet of doublets with *J*-coupling constants of 8.6 Hz and 2.0 Hz, and ArH_5 resonated as a doublet at 6.87 ppm with an *ortho J*-coupling constant of 8.6 Hz. The amine protons were represented by a broadened singlet at 6.93 ppm integrating for 2H. In the ^{13}C NMR spectrum, the expected number of eight carbon resonances were clearly visible. The ^{1}H NMR spectrum of **24** correlated well with the literature,[21] whereas the ^{13}C NMR spectrum has not yet been recorded in the literature.

Next, the cyclisation of 4-amino-3-thiocyanatobenzonitrile **24** (step **b**, Scheme 4.6) was approached. Following a literature procedure,[18] intermediate **24** was heated under reflux in 3.5 M HCl/H_2O for 2 h, which unfortunately did not afford the desired product. With the use of 3.5 M anhydrous HCl in 1,4-dioxane, water was excluded from the reagents and the product was obtained in a yield of 58% (entry 2, Table 4.2). The best yield (85%) was afforded when **24** was cyclised under anhydrous basic conditions, when heated under reflux with sodium hydride in THF (entry 4, Table 4.2).

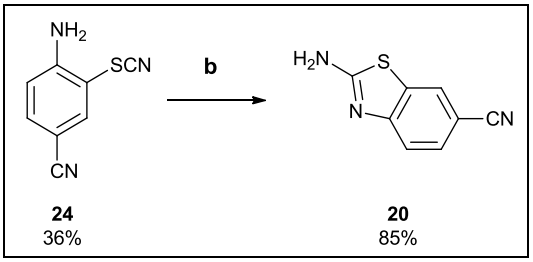

Scheme 4.6: The cyclisation of 4-amino-3-thiocyanatobenzonitrile (24)

Table 4.2: Ring-closing reactions for Step b

Step **b**		
Entry	**Reagents and reaction conditions**	**% yield**
1	3.5 M HCl in H_2O, reflux, 2h	–
2	3.5 M HCl in 1,4-dioxane, reflux, 1.5 h	58
3	2 M HCl in 1,4-dioxane, reflux, 4.6 h	31
4	NaH *(1.4 equiv)*, THF, reflux, 2 h	**85**

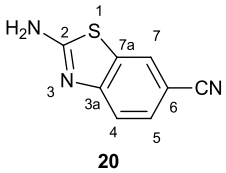

20

The success of the cyclisation reaction was confirmed by IR and NMR spectroscopy, as well as HRMS. Compound **20** displayed the C≡N stretch of the nitrile group at 2215 cm^{-1} in the IR spectrum. The thiocyanate stretch, previously observed at 2158 cm^{-1}, was absent and indicated the possible formation of the benzothiazole heterocycle. Ring formation was confirmed by the characteristic signal of the C_2 carbon at 170 ppm in the ^{13}C NMR spectrum of **20** (Figure 4.3). Sawhney and Boykin[18] have performed a ^{13}C NMR spectroscopic study on 2-aminobenzothiazoles, in which the signal of the C_2 carbon was consistently the furthest downfield, in a range of 162 – 172 ppm, and could be identified easily. The ^{13}C NMR spectroscopic resonance signals of **20** corresponded very well with the literature.[18] Sawhney and Boykin's study allowed the assignment of all the carbon chemical shifts. The ^{1}H NMR spectrum accounted for the amine as a broad singlet at 8.03 ppm, integrating for 2H. The signal of the ArH_7 aromatic proton appeared as a doublet (J = 1.7 Hz) at 8.17 ppm, the ArH_4 doublet (J = 8.4 Hz) resonated at 7.41 ppm and ArH_5 resonated as a doublet of doublets (J = 8.4, 1.7 Hz) at 7.60 ppm, again confirming the presence of a 1,2,4-trisubstituted aromatic ring.

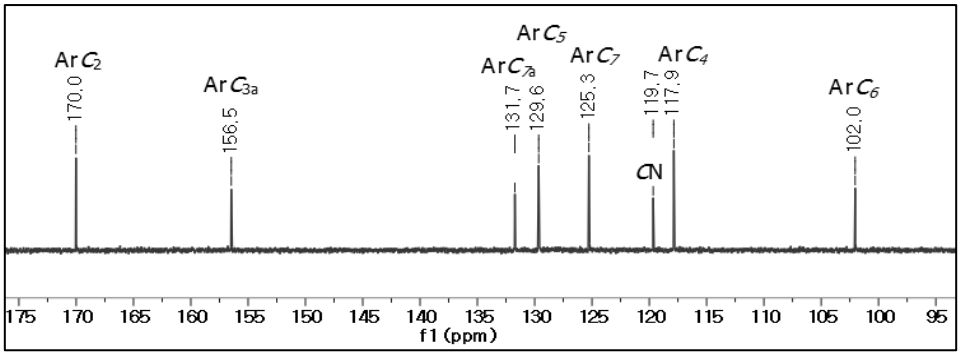

Figure 4.3: The ^{13}C NMR spectrum (DMSO-d_6) of 2-aminobenzo[d]thiazole-6-carbonitrile (20)

4.3.2 Completing the synthesis of the 2-aminobenzothiazole compound set

The syntheses of the rest of the 2-aminobenzothiazoles were approached with the hope of utilising the same synthetic strategy as was developed for 2-aminobenzo[*d*]thiazole-6-carbonitrile (**20**). The method would once again entail thiocyanation in the *ortho* position relative to the amine, isolation of the intermediate and subsequent reflux in a NaH/THF mixture to promote cyclisation. In the first thiocyanation step the 4-substituted anilines (**17**, **18**,[†] **19**, Scheme 4.7) and KSCN were dissolved in glacial acetic acid, treated with PTAB and stirred at room temperature for 5 h. When these reaction mixtures were analysed by TLC after 5 h, two major products were visible. With the help of NMR spectroscopy of the isolated major products in the reaction with **17**, it could be reasonably concluded that spontaneous ring-closing was taking place alongside thiocyanation. These reactions did not reach completion overnight, leaving a mixture of uncyclised and cyclised products. Luckily, when the reaction mixtures were heated under reflux for 10 minutes after the 5 h thiocyanation period, cyclisation was pushed towards completion to yield 2-aminobenzothiazoles **21**, **22** and **23** in one-pot reactions in good to acceptable yields.

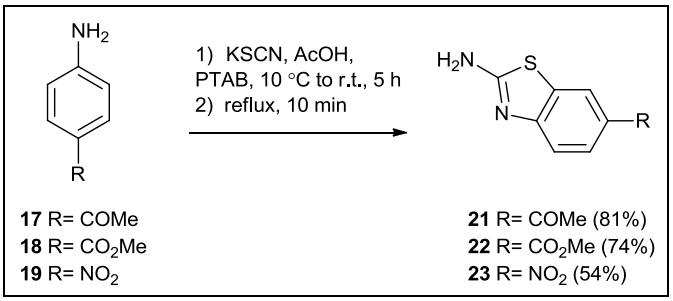

Scheme 4.7: The synthesis of 1-(2-aminobenzo[d]thiazol-6-yl)ethanone (21), methyl 2-aminobenzo[d]thiazole-6-carboxylate (22) and 6-nitrobenzo[d]thiazole-2-amine (23)

[†] The preparation of **18** is described on p. 68

It is noteworthy that when 4-aminobenzonitrile (**16**, Scheme 4.5) was thiocyanated, many more by-products were observed on TLC than with the thiocyanation of **17**, **18** and **19**. These by-products resulted in the failure of utilising a one-pot reaction for the synthesis of 2-aminobenzo[*d*]thiazole-6-carbonitrile (**20**). Therefore, isolation of intermediate **24** was necessary before cyclisation.

1-(2-Aminobenzo[*d*]thiazol-6-yl)ethanone (**21**) was afforded in an 81% yield and 6-nitrobenzo[*d*]thiazole-2-amine (**23**) was synthesised and isolated with a yield of 54%. The yield of **23** was lowered as a result of multiple purification attempts, in order to remove a smaller impurity of similar polarity. Compounds **21** and **23** displayed NMR spectroscopic data in accordance with the literature.[18,22,23] In both cases, cyclisation was confirmed by the signal of the C_2 carbon in the ^{13}C NMR spectra. The C_2 carbon resonance was visible at 169.8 ppm for **21**, and at 171.8 ppm for **23**.

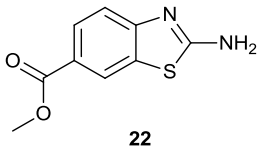

22

Methyl 2-aminobenzo[*d*]thiazole-6-carboxylate (**22**) was afforded in a yield of 74%. The spectroscopic data of **22** was inaccessible in our literature sources, and therefore the spectrum of compound **22** will be discussed. The amine protons were visible in the ^1H NMR spectrum at 7.90 ppm as a broad singlet integrating for 2H. The characteristic resonance pattern of the aromatic ring protons, entailing a doublet (J = 1.8 Hz), doublet of doublets (J = 8.4, 1.8 Hz) and a doublet (J = 8.4 Hz) each integrating for one proton, were clearly visible in the aromatic region. The methoxy hydrogens were accounted for by a singlet at 3.82 ppm, integrating for 3H. The important carbonyl signal of the methyl ester was present at 166.1 ppm in the ^{13}C NMR spectrum and the C_2 signal displayed at 169.8 ppm. The chemical shifts in the ^{13}C NMR spectrum of **22** were assigned by analogy, through a comparison with ethyl 2-aminobenzo[*d*]thiazole-6-carboxylate.[18] The shifts correlated very well and the ethyl carbon signals (14.2, 60.9 ppm) were substituted with a methyl carbon signal at 51.8 ppm. In the IR spectrum of **22**, the carbonyl stretching vibration was present at 1691 cm^{-1}. The structure was lastly confirmed by the presence of the $[M+H]^+$ ion peak in the HRMS spectrum at 209.0386 (*m/z* calculated: 209.0385).

4.3.3 The synthesis of methyl 4-aminobenzoate (18)

In Scheme 4.7, methyl 4-aminobenzoate (**18**) was used as starting material to synthesise methyl 2-aminobenzo[*d*]thiazole-6-carboxylate (**22**). Compound **18** was prepared from 4-aminobenzoic acid (**25**) according to a conventional procedure (Scheme 4.8).[24,25] To this end, a solution of 4-aminobenzoic acid (**25**) in an excess of methanol was cooled to 0 °C, whereafter thionyl chloride was added dropwise. The solution was heated under reflux overnight, followed by neutralisation, extraction and purification of the product (**18**) resulting in it being obtained in an excellent yield of 97%. In this procedure, thionyl chloride reacted with methanol to form anhydrous HCl, which catalysed the Fischer esterification of the carboxylic acid with methanol.[26]

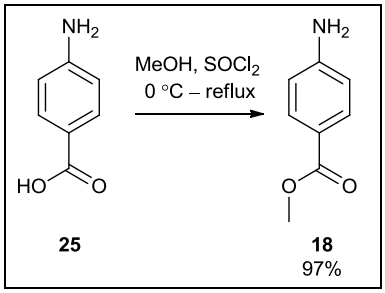

Scheme 4.8: The esterification of 4-aminobenzoic acid (25)

4.4 The synthesis of the 6-substituted 2-aminobenzimidazoles

Different methods have been developed in the literature to synthesise 2-aminobenzimidazoles.[27] Our literature search focused on ring-formation and more specifically the preparation of 2-aminobenzimidazoles which are unsubstituted at position 1 and contain a primary amine in position 2. It should be noted that o*rtho*-phenylenediamines are the most common starting materials utilized in benzimidazole heterocyclisation.[7,27] Typical examples of the reported methods are described below and displayed in Scheme 4.9:

1. The condensation of *o*-phenylenediamines with cyanogen bromide, cyanogen chloride, *in situ* generated cyanogen bromide or cyanamide afford high yields of 2-aminobenzimidazoles.[27]
2. *ortho*-Substituted nitrobenzenes have been utilised in reductive cyclisation approaches, in which the compound cyclises when the nitro group is hydrogenated. Schulze and co-workers[28] heated a mixture of *N*-(2,4-dinitrophenyl)cyanamide, elemental iron and glacial acetic acid under reflux, which resulted in a partial reduction and subsequent benzimidazole formation.
3. *N*-(*o*-aminophenyl)thioureas have been cyclised in ethanol with the help of oxidants, such as mercury(II) oxide and mercury(II) chloride to afford the desired 2-aminobenzimidazoles.[27]

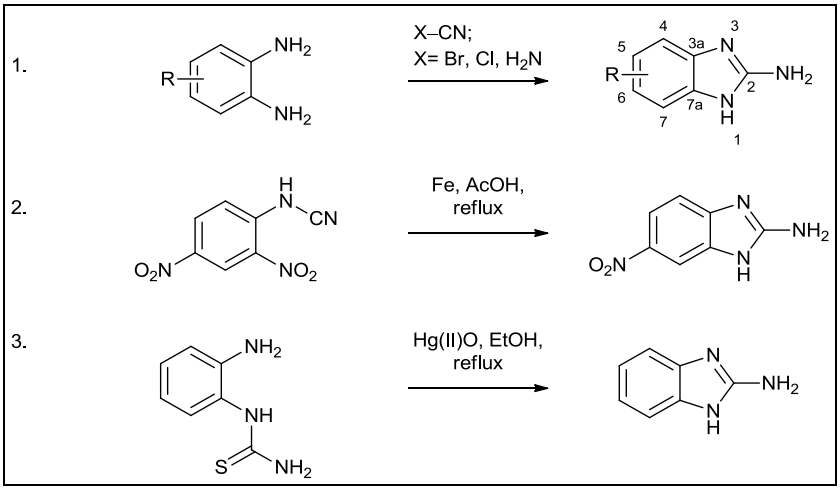

Scheme 4.9: Examples of synthetic procedures towards 2-aminobenzimidazoles

In this project, the first procedure utilising cyanogen bromide was followed, since the reaction method has been well described in the literature[29] and the *o*-phenylenediamine starting materials could be synthesised from the same substituted anilines (**16 – 18**) that were used as starting materials for the benzothiazole synthesis. A proposed synthetic plan towards the set of required 6-substituted 2-aminobenzimidazole rings is displayed in Scheme 4.10.

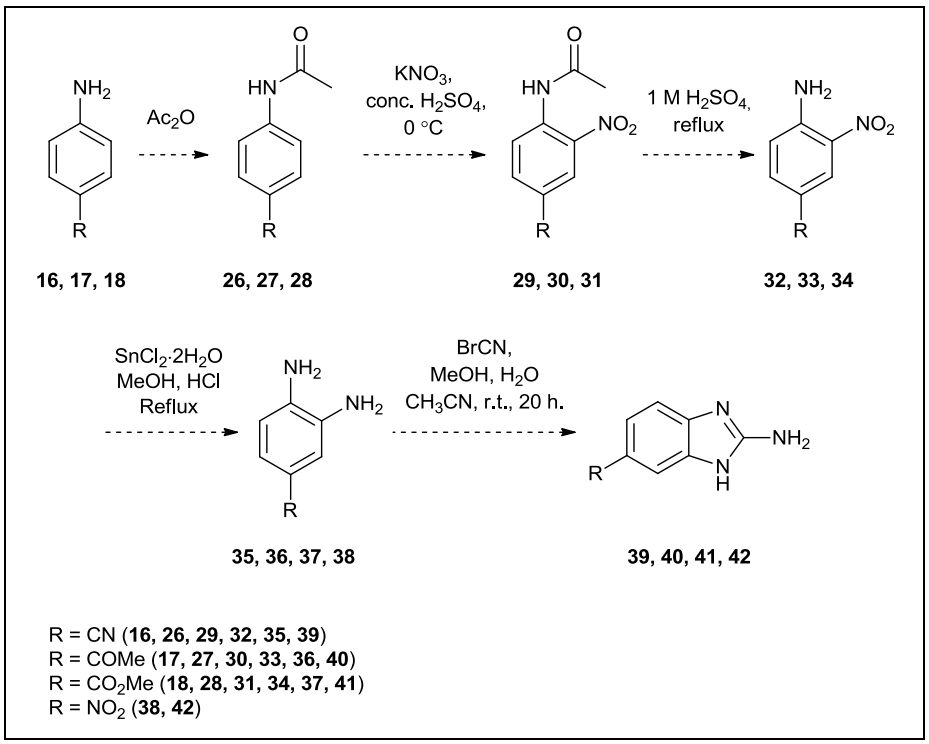

Scheme 4.10: A proposed synthetic route towards 2-aminobenzimidazoles 39 – 42

The synthetic plan was deduced from the available literature on the synthesis of 2-amino-1*H*-benzo[*d*]imidazole-6-carbonitrile (**39**) from 4-aminobenzonitrile (**16**).[29–31] This synthetic route would also be followed in the preparation of the rest of the 6-substituted 2-aminobenzimidazoles **40 – 42**, with the hope of utilising the same or similar reaction conditions. Selectivity issues were anticipated in the reduction step ($SnCl_2 \cdot 2H_2O$) in the synthesis of 6-nitro-1*H*-benzo[*d*]imidazol-2-amine (**42**) from 4-nitroaniline (R = NO_2). Therefore 4-nitrobenzene-1,2-diamine (**38**) was purchased, which was expected to be readily cyclised to form **42**.

The first three steps entailed a protection-nitration-deprotection procedure that is commonly seen in the literature when generating *ortho*-nitro anilines in strong acids. This is as a result of nitration studies on aniline in concentrated sulfuric acid, which resulted in mixtures of *meta*- and *para*-substituted products, with traces of *ortho*-substituted products.[32] The strongly acidic media is able to protonate the free amine to form the anilinium ion which is *meta*-directing. The equilibrium between aniline

(*para-/ortho*-directing) and the anilinium ion results in mixtures of mainly the *ortho* and *meta* products.[32] This mixture of products can be avoided by acylation of the amine. The resultant acetanilide is much less basic and acts as a *para-/ortho*-director. Acylation also decreases the reactivity of the aniline by delocalisation of the lone pair into the carbonyl group, which reduces the risk of over-nitration. To this end, the substituted anilines **16 – 18** would be acylated before nitration.

After the three-step sequence, the new nitro group would be reduced to form the *o*-phenylenediamine, which could subsequently be cyclised with cyanogen bromide to form the 6-substituted 2-aminobenzimidazoles.

4.4.1 The acetylation reactions

The acetylation of compounds **16**, **17** and **18** (Scheme 4.10) was readily accomplished with an excess of acetic anhydride, resulting in yields of 83%, 97% and 94% respectively. 4-Aminobenzonitrile (**16**) was acetylated according to the literature procedure of Fairley *et al.,*[31] in which acetic anhydride served as reagent and solvent. To this end, 4-aminobenzonitrile (**16**) was added portion-wise to an excess of acetic anhydride over 1 hour. Iced water was then added to the white suspension, whereafter the precipitated product was collected, washed and dried. The acetylation reactions of **17** and **18** were carried out in mixtures of acetic anhydride and DCM to allow for efficient stirring. The NMR spectra of synthesised compounds **26**, **27** and **28** compared well to the literature.[33–36]

4.4.2 Nitration of the acetamides

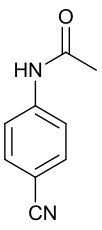

26

The nitration of *N*-(4-cyanophenyl)acetamide (**26**) was conducted in accordance with the nitration procedure described by Fairley *et al.*[31] Following their procedure, the acetamide (**26**) was added portion-wise to a cooled solution of potassium nitrate in concentrated sulfuric acid. In this procedure, concentrated nitric acid was generated *in situ* from the mixture of potassium nitrate and concentrated sulfuric acid. Nitric acid reacted further with concentrated sulfuric acid to yield nitronium ions (NO_2^+).[37] This mechanism is displayed in Figure 4.4.[38] It is well-known that the nitronium ion is the active nitrating agent that participates as the electrophile in the electrophilic substitution reaction on the aromatic ring.[37]

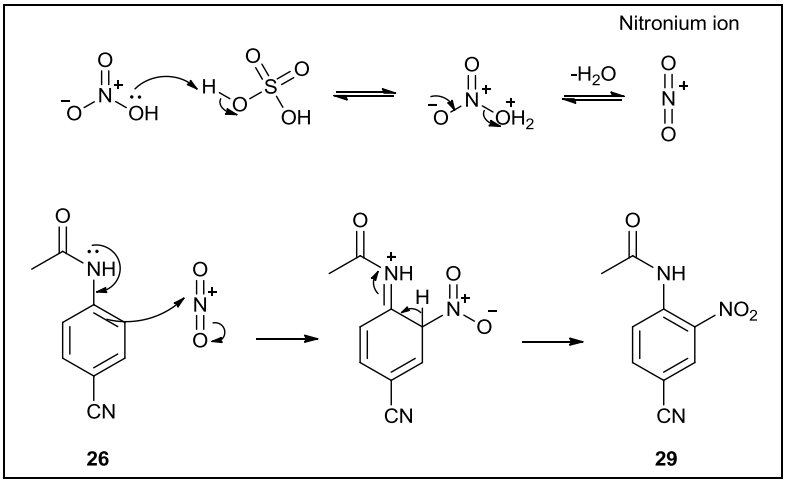

Figure 4.4: The formation of the nitronium (NO_2^+) ion and its electrophilic role in the nitration of acetamide 26.[38]

In our hands it was found that the nitration reaction was very sensitive to temperature. Fairly *et al.*[31] reported a yield of 88% (**29**) when they maintained the reaction temperature below 0 °C. In order to minimise overnitration, it was found necessary to conduct the reaction at −15 °C, to quench the reaction after 3.5 h and to utilise less than 2 equivalents of potassium nitrate. The optimisation studies for this reaction are summarised in Table 4.3, with the best reaction combination highlighted.

Table 4.3: Optimisation of the nitration of N-(4-cyanophenyl)acetamide (26)

Entry	Reagents and reaction conditions			% yield
	Reagents	Temperature (°C)	Time (h)	
1	KNO_3 *(2 equiv)*, 96 % H_2SO_4	0 to 5	3	20
2	KNO_3 *(1.5 equiv)*, conc. H_2SO_4	−15 to −10	3.5	**69**
3	KNO_3 *(1.5 equiv)*, conc. H_2SO_4	−15 to −10	5.5	43
4	KNO_3 *(2.1 equiv)*, conc. H_2SO_4	−15 to −10	3.5	67
5	KNO_3 *(3 equiv)*, conc. H_2SO_4	−15 to −10	2.5	51

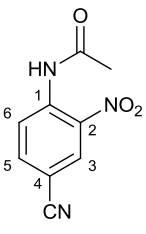

29

From the optimisation experiment, *N*-(4-cyano-2-nitrophenyl)acetamide (**29**) was isolated in a yield of 69%. In terms of spectroscopic characterisation, the amide NH proton appeared as a broad singlet at 10.54 ppm in the ^{1}H NMR spectrum and the acetyl methyl protons integrated for 3H at 2.34 ppm. The aromatic protons appeared as a doublet (J = 8.9 Hz, ArH_6) integrating for 1H at 9.02 ppm, a doublet (J = 2.0 Hz, ArH_3) integrating for 1H at 8.55 ppm and a doublet of doublets (J = 2.0, 8.9 Hz, ArH_5)

integrating for 1H at 7.87 ppm. This aromatic substitution pattern confirmed the presence of the mononitrated product. In the IR spectrum, the nitrile stretching vibration was visible at 2231 cm^{-1} and according to the bands of nitro compounds in the literature,[39] it is suggested that the bands at 1499 cm^{-1} and 1345 cm^{-1} represent the N=O asymmetric and symmetric stretches of the nitro group. All in all, the NMR spectroscopic results compared well to the literature.[40]

Succeeding in the development of a nitration strategy, the optimised KNO_3/conc. H_2SO_4 nitration procedure (entry 2, Table 4.3) was applied to *N*-(4-acetylphenyl)acetamide (**27**). Surprisingly, a very low yield of 10% was obtained and TLC analysis represented a mixture of starting material, mononitrated product and dinitrated product. Lowering of the reaction temperature to −25 °C did not improve the results. It was postulated that a milder nitrating agent would be required to nitrate **27**. The KNO_3/conc. H_2SO_4 system is known to be very reactive, since the *in situ* generated nitric acid is ionised completely into nitronium ions, resulting in a high concentration of nitronium ions, which can cause overnitration.[37]

A mixture of aqueous nitric acid and concentrated sulfuric acid (mixed acid) proved to be an effective and well-known alternative for nitration. The presence of water lowers the concentration of nitronium ions, resulting in milder nitrating action.[37] From Figure 4.4 it can be deduced that the equilibrium leading to nitronium ion formation is pushed backwards by the addition of water, whereas an increase in sulfuric acid concentration pushes the nitration reaction forward.

A very convenient nitration procedure was developed to nitrate acetamides **27** and **28** (Scheme 4.11). The *N*-(4-substituted phenyl)acetamide (**27**/**28**) and 65% nitric acid were combined and cooled to 0 °C. An equal volume of concentrated sulfuric acid (1:1 v/v; 65% HNO_3/conc. H_2SO_4) was then added dropwise, whereafter the mixture was left to stir for 1 hour at 0 °C. The reaction was quenched with water, basified to pH = 8 with conc. NH_4OH, extracted with EtOAc and then purified further by silica column chromatography. Very good selectivity for the mononitrated product was obtained using this procedure.

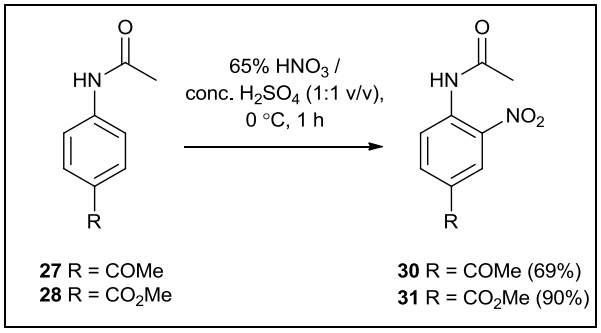

Scheme 4.11: The nitration of acetamides 27 and 28 with mixed acid

Using this approach, *N*-(4-acetyl-2-nitrophenyl)acetamide (**30**) was obtained in a yield of 69% and in terms of characterisation the NMR spectroscopic results of **30** compared well to the literature.[41] Methyl 4-acetamido-3-nitrobenzoate (**31**) was also obtained in an excellent yield of 90%. The ^{1}H NMR spectroscopic data of **31** displayed the amide NH proton signal at 10.55 ppm, the methoxy protons at 3.88 ppm and the amide methyl protons at 2.12 ppm, both integrating for 3H. The three aromatic proton signals observed, each integrating for 1H, confirmed mononitration.

4.4.3 The deacetylation and hydrogenation procedures

The next deacetylation step proceeded without any difficulty. Compounds **29**, **30** and **31** were individually heated under reflux in 1 M H_2SO_4 for 2 hours to afford compounds **32, 33** and **34** in excellent yields of 95%, 96% and 82% respectively (Scheme 4.12).[30] The nitrile group of compound **29** and the methyl ester group of compound **31** were stable against hydrolysis under these conditions. Again, the NMR spectroscopic results of all the compounds corresponded well to that available in the literature.[30,40,42–44]

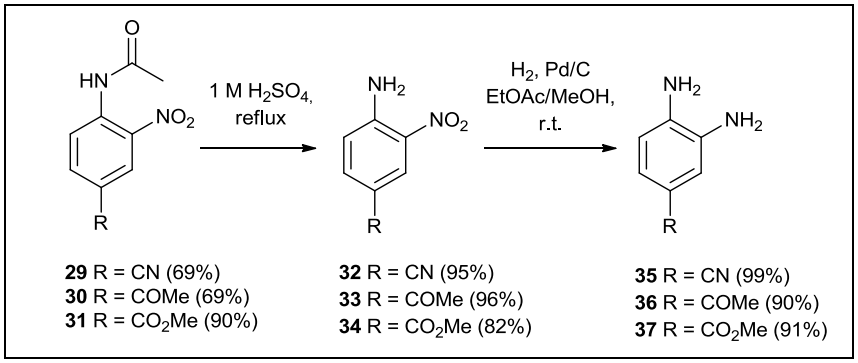

Scheme 4.12: The deacetylation and subsequent hydrogenation of compounds 29 – 31

The reduction of 4-amino-3-nitrobenzonitrile (**32**) was first attempted under reflux with tin(II) chloride dihydrate, concentrated HCl and methanol.[29] This reaction produced the desired product, but subsequent failure to separate the product from a by-product of similar polarity necessitated an alternative method. The diamines **35**, **36** and **37** were therefore obtained by hydrogenation with a H_2-balloon over 10% Pd/C at room temperature, in very clean reactions following the procedure of Tawar *et al.*[45] The solvent ratio was adjusted from 4:1 (EtOAc: MeOH) to 2:1 (EtOAc: MeOH) in the hydrogenations of **33** and **34** to allow for dissolution of the starting material. The hydrogenation reactions could be monitored through reaction colour and were found to be complete when the reaction mixtures had changed colour from bright yellow to a transparent orange or red.

Diamines **35**, **36** and **37** were obtained in excellent yields of 99%, 90% and 91% respectively. In terms of spectroscopic analysis, the two amine signals were observed in the ^{1}H NMR spectrum of each

compound. The amine signals appeared at 3.81 ppm and 3.39 ppm for **35**, at 5.36 ppm and 4.63 ppm for **36** and at 5.27 ppm and 4.65 ppm for **37**.

In the hydrogenation of **32** the mild reaction conditions provided chemoselectivity to reduce the nitro group, which is highly reactive towards catalytic hydrogenation, in the presence of a nitrile functionality.

4.4.4 Cyclisation to form the 6-substituted 2-aminobenzimidazoles

Diamines **35** – **38** were cyclised according to the method of Starcevic *et al.,*[29] in which the diamines were treated with 1.3 equivalents of cyanogen bromide in a mixture of methanol, water and acetonitrile (Scheme 4.13). The reaction was stirred at room temperature overnight and then basified with ammonium hydroxide. No precipitate formed, as suggested in the literature, and therefore a work-up procedure followed by silica column chromatography was required to isolate products **39** – **42** in excellent yields.

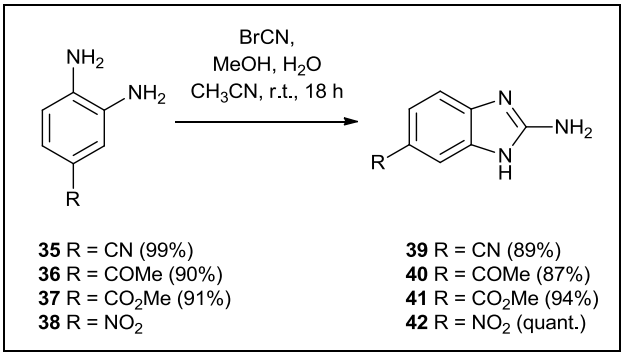

Scheme 4.13: The cyclisation of diamines 35 – 38 to form 6-substituted 2-aminobenzimidazoles

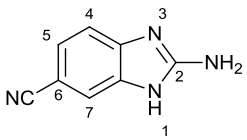

39

The ring cyclisation step afforded 2-amino-1*H*-benzo[*d*]imidazole-6-carbonitrile (**39**) in a yield of 89%. The ^{1}H NMR spectroscopic data correlated with the literature data,[29] however small differences in the chemical shift values were seen since the literature values were internally referenced to tetramethylsilane. Our values were referenced to the residual solvent signal in DMSO-d_6 (δ 2.50 ppm in ^{1}H NMR). In terms of key structural features, the primary amine integrated for 2H at 6.65 ppm and the imidazole NH_1 was present as a single broad signal at 11.14 ppm. The aromatic protons were visible as a doublet at 7.46 ppm (J = 1.6 Hz, 1H) representing ArH_7, a doublet of doublets at 7.26 ppm (J = 1.6 Hz, 8.1 Hz, 1H) representing ArH_5 and a doublet at 7.20 ppm (J = 8.1 Hz, 1H) representing ArH_4. The nitrile band was visible at 2213 cm^{-1} in the IR spectrum of **39**. The structure was lastly confirmed by the $[M+H]^+$ ion in the HRMS spectrum (*m/z* calculated 159.0671, found 159.0666).

To our knowledge, the ^{13}C NMR spectrum of **39** has not been reported in the literature before. The ^{13}C NMR spectrum of **39** displayed eight carbon signals, as expected, but four of these carbon signals appeared very weak and broad (Figure 4.5, broadened signals: δ = 144.0, 138.0, 114.4 and 112.4 ppm). In general, the acquisition of the ^{13}C NMR spectra of the benzimidazoles was challenging. Even after running the sample overnight and increasing the concentration of the sample in the NMR spectroscopy tube, several of the signals were not visible or appeared as very weak, broad signals. Increasing the relaxation delay of the ^{13}C NMR spectroscopic pulse sequence from 1s to 3s also did not improve the signal shapes. These problems were not observed in the equivalent 2-aminobenzothiazole set, since 1,3-tautomerism in the benzothiazole ring was not possible. In previous studies on 2-substituted benzimidazoles, the tautomerism in the benzimidazole ring has been reported to result in the broadening of the C_{3a}/C_{7a}, C_4/C_7 and C_5/C_6 signal sets in the ^{13}C NMR spectra.[46] Therefore the tautomeric effect is also suggested to result in the broadening of carbon signals in the ^{13}C NMR spectrum of **39**. From the data of an NMR spectroscopic study by Lopyrev *et al.*[47] on 2-substituted 5(6)-nitrobenzimidazoles, it is suggested that the four broadened signals of **39** correspond to C_{3a}, C_{7a}, C_4 and C_7, which further supports the involvement of tautomeric effects.

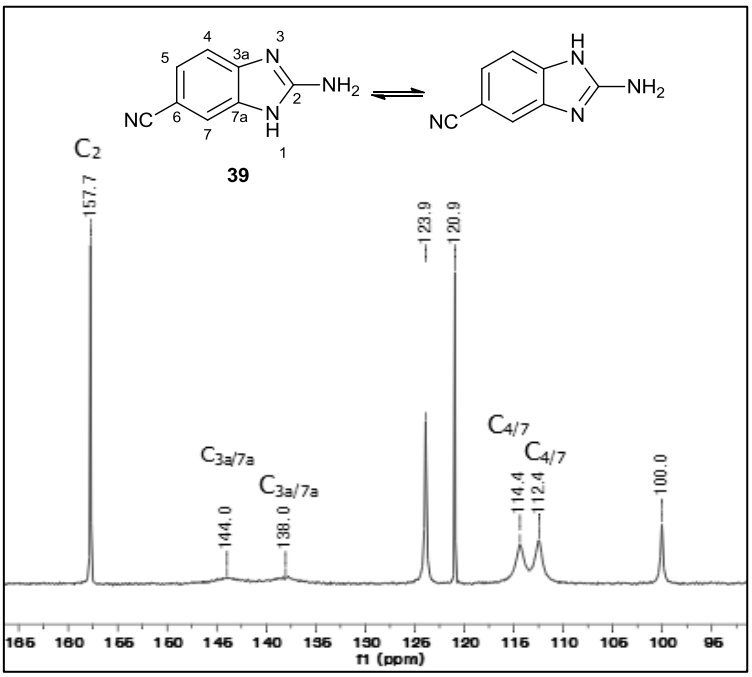

Figure 4.5: Tautomerism in the benzimidazole ring resulted in the broadening of signals in the ^{13}C NMR spectrum (DMSO-d_6) of 39.[46]

To assist in resolving the ^{13}C NMR spectra of the 6-substituted 2-aminobenzimidazoles synthesised in this project, two-dimensional NMR spectroscopic studies were performed on methyl 2-amino-1*H*-benzo[*d*]imidazole-6-carboxylate (**41**). No ^{13}C NMR spectroscopic data has been reported in the

literature for compound **41**. The ^{13}C NMR spectrum of **41** displayed eight carbon shift signals instead of the expected number of nine signals (Figure 4.6). In an attempt to explain the ^{13}C NMR spectrum of **41**, the gHSQC and gHMBC spectra were acquired and thus allowed for the assignment of the ^{13}C NMR signals. As seen in the spectra of both compounds **39** and **41** (Figure 4.5 and Figure 4.6), the ArC_{3a} and ArC_{7a} carbons are associated with very weak, broad signals. The missing carbon signal in the ^{13}C NMR spectrum of **41** was accounted for by the equivalent chemical shifts of the ArC_4 and ArC_7 signals at 111.7 ppm.

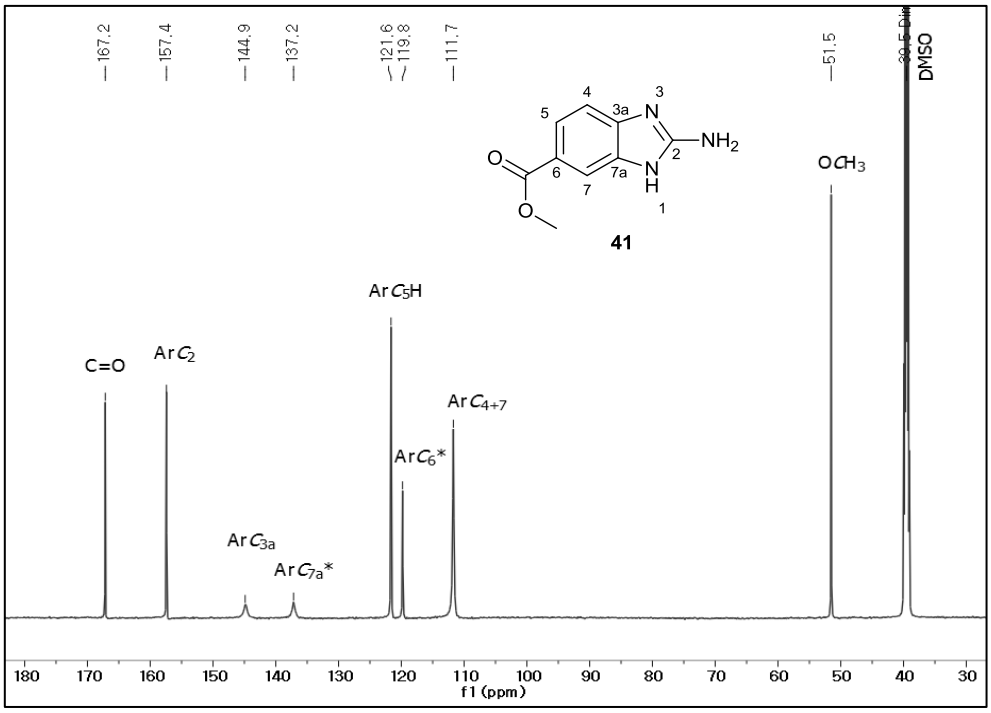

Figure 4.6: The ^{13}C NMR spectrum (DMSO-d_6) of methyl 2-amino-1H-benzo[d]imidazole-6-carboxylate (41). Signals were assigned with the help of two-dimensional NMR spectroscopy (gHSQC, gHMBC). *: An asterix represents a tentative assignment.

The 2D NMR spectroscopic data, correlations and assignments are available in tabular form in the experimental chapter (Chapter 9). The key correlations in the 2D NMR spectroscopic data, which allowed for the assignment of carbon signals, will be discussed next. The signals at 167.2 ppm and 51.5 ppm in the ^{13}C NMR spectrum of **41** represented the methyl ester's carbonyl carbon and methoxy carbon respectively. The position of the 167.2 ppm shift of the ester carbonyl carbon was confirmed by 3-bond couplings to H_5, H_7 and OCH_3 in the gHMBC spectrum (summarised in Figure 4.7). In the gHSQC spectrum of **41**, two benzimidazole aromatic ring protons, H_4 and H_7, correlated to the signal at 111.7 ppm, representing the ^{1}H$_4$ – ^{13}C$_4$ and ^{1}H$_7$ – ^{13}C$_7$ one-bond connectivities. The signal at 121.6 ppm arose from the carbon's one-bond connectivity with H_5.

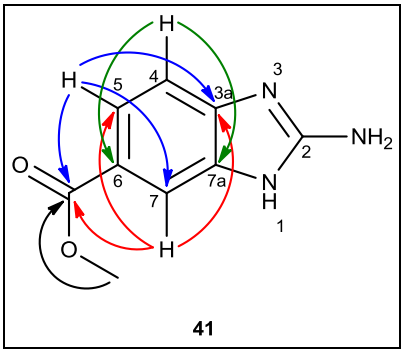

Figure 4.7: Long range ^{1}H – ^{13}C correlations in the gHMBC spectrum of compound 41

The gHMBC spectrum of **41** assisted in the assignment of the remaining carbon signals of ArC_2, ArC_{3a}, ArC_6 and ArC_{7a}. The carbon signal at 157.4 ppm had no correlations in the gHSQC and gHMBC spectra and was assigned as ArC_2. H_5 and H_7 correlated with ArC_{3a} through 3-bond couplings, therefore the signal at 144.9 ppm was assigned ArC_{3a}. The carbon atoms resonating at 119.8 ppm and 137.2 ppm each coupled to only H_4 in the gHMBC spectrum, which was best explained by the 3-bond couplings of ArC_6 and ArC_{7a} with H_4. Unfortunately, ArC_6 and ArC_{7a} could not be assigned unambiguously. The signals were thus tentatively assigned based on previously reported data on benzimidazoles,[47] and the assumption that the quaternary carbons, ArC_{7a} and ArC_{3a}, would have similar chemical environments and signal intensities. Therefore 137.2 ppm was assigned ArC_{7a} and 119.8 ppm was assigned ArC_6.

The ^{1}H NMR spectroscopic data collected for compound **41** corresponded well to the literature (no ^{13}C NMR spectroscopic data was available).[48] The imidazole NH_1 proton was not visible in the ^{1}H NMR spectrum due to tautomerism. Finally, the structure of methyl 2-amino-1*H*-benzo[*d*]imidazole-6-carboxylate (**41**) was confirmed by the $[M+H]^+$ ion in the HRMS spectrum (*m/z* calculated 192.0773, found 192.0779).

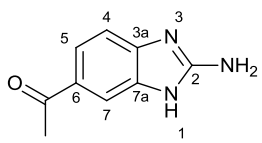

40

1-(2-Amino-1*H*-benzo[*d*]imidazol-6-yl)ethanone (**40**) was afforded in a yield of 87%. The compound's structure was confirmed with the help of ^{1}H NMR, ^{13}C NMR, FT-IR and HRMS. Again, the imidazole NH_1 proton was not visible in the ^{1}H NMR spectrum due to tautomerism. Again, the resonances of the ArC_{3a} and ArC_{7a} signals appeared as broadened signals at 145.1 and 137.1 ppm in the ^{13}C NMR spectrum of **40**.

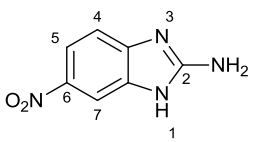

42

6-Nitro-1*H*-benzo[*d*]imidazol-2-amine (**42**) was synthesised in a quantitative yield. Of significance was that the rate of the reaction was slower and required an additional day of stirring. The ^{1}H NMR spectroscopy data collected for this

compound fitted the literature.[49] In the ^{13}C NMR spectrum, the carbon signals of ArC_{3a}, ArC_4, ArC_5, ArC_6, ArC_7 and ArC_{7a} were broadened.

Upon the investigation of the ^{13}C NMR spectra of the synthesised 6-substituted 2-aminobenzimidazole set, it was concluded that the signals of carbons affected by tautomerisation often appeared weak and broad, which complicated interpretation. The largest extent of signal broadening was observed for the ArC_{3a} and ArC_{7a} carbons, but the tautomeric effects often influenced more carbons in the benzimidazole ring.

The required 6-substituted 2-aminobenzothiazoles and the 6-substituted 2-aminobenzimidazoles were thus successfully prepared. The developed procedures have the potential to be extended to the synthesis of a broader range of 6-substituted- 2-aminobenzothiazoles and 2-aminobenzimidazoles. Proceeding from these successes, the prepared set of 2-aminobenzazoles was utilised as nucleophiles in the upcoming urea formation step.

4.5 The formation of the ureas

The objective for the urea formation step was to establish a synthetic procedure which could be applied to both the benzothiazole and the benzimidazole scaffolds. From the retrosynthetic analysis in Scheme 4.14, we envisaged transforming 4-methoxybenzylamine (**15**) into an equivalent electrophilic carbamoylating reagent ($R_1R_2NC=O$). This reagent could then be reacted with the nucleophilic 2-aminobenzazoles (**20** – **23**, **39** – **42**) to produce the corresponding ureas. Effectively, the aim was to couple two primary amines, resulting in the formation of the urea functionality.

4.5.1 Carbamoyl transfer agents

Four electrophilic carbamoyl cation equivalents (**43** – **46**) were proposed in Scheme 4.14. Carbamoyl transfer reagents can be monosubstituted ($R_1HNC=O$) or disubstituted ($R_1R_2NC=O$). The carbamoyl derivative of the primary amine, 4-methoxybenzylamine (**15**), would be monosubstituted, therefore the synthesis of *N*-monosubstituted carbamoylating reagents was explored.

Compound **43** represents the isocyanate carbamoylating equivalent and it is known that isocyanates are able to transfer monosubstituted carbamoyl groups ($R_1HNC=O$) onto nucleophiles.[50] Unfortunately, the most common preparations of isocyanates from primary amines require the use of toxic phosgene.[51] The reaction with phosgene yields the carbamoyl chloride equivalent from which hydrogen chloride can be eliminated, either thermally or with a tertiary base, to form the isocyanate equivalent.[52] Since *N*-monosubstituted carbamoyl chlorides can be unstable, the isocyanate equivalents are preferred.[53] But still, the general characteristics of isocyanates include toxicity, high

reactivity and instability.[54,55] In addition, in the presence of moisture, many isocyanates will decompose rapidly.[54] These characteristics are associated with handling difficulties when isocyanates are utilised in reactions, as well as storage difficulties.[55]

The high reactivity and instability of isocyanates can result in lowered yields during urea synthesis. In the synthesis of several 1-aryl-3-benzylureas by Lo Monte *et al.*,[56] isocyanate carbamoyl equivalents were generated *in situ* from benzylamines and triphosgene. These isocyanates were then reacted with unactivated or *n*-BuLi-preactivated aryl amines. The overall yields of the reactions ranged between 11% and 75%, with only a third of the yields reading above 50%.[56]

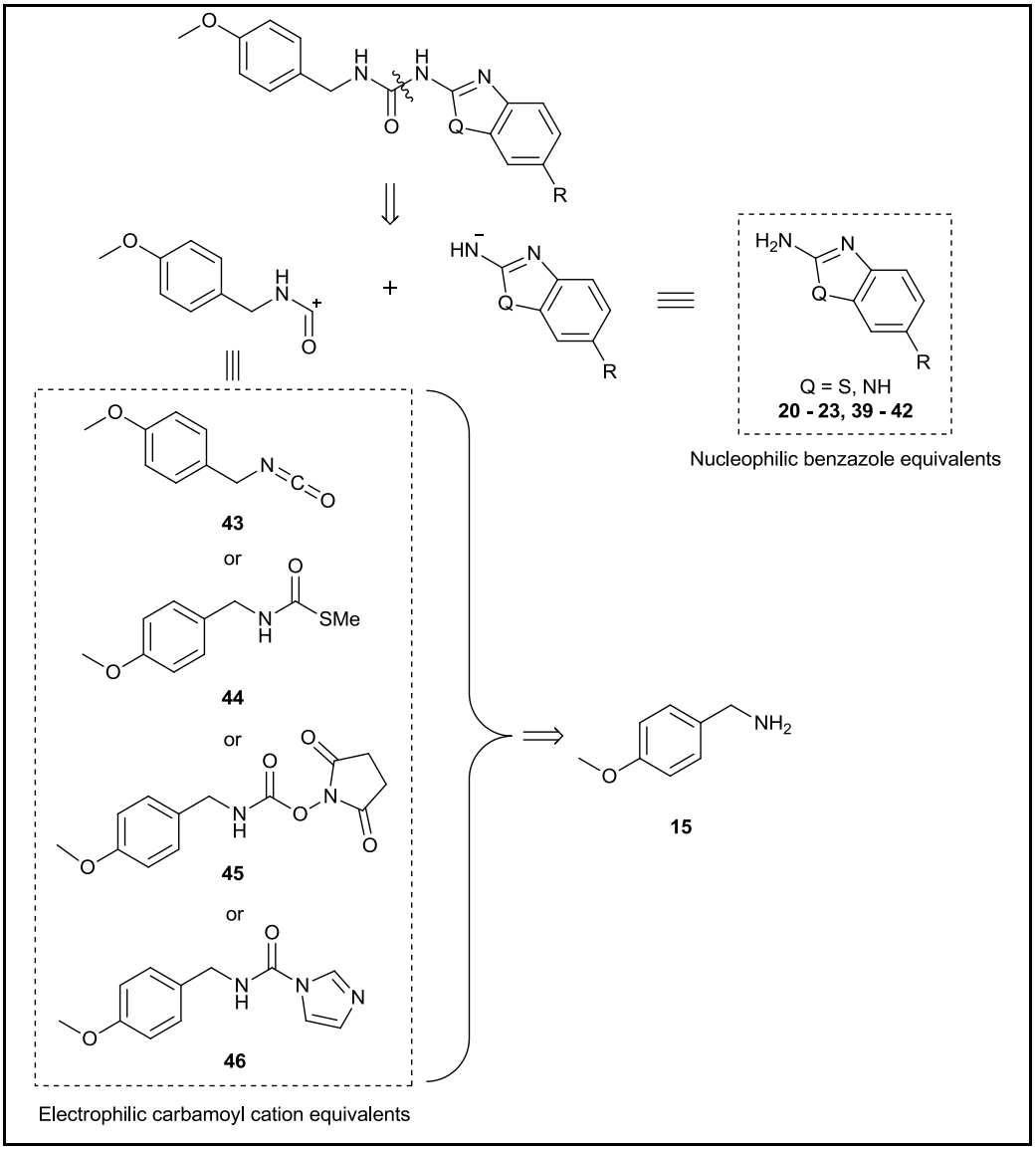

Scheme 4.14: A retrosynthetic analysis towards urea formation

Research has been aimed at the development of more stable, safe and storable carbamoylating reagents which can be obtained from greener, non-toxic synthetic procedures.[50,57] These procedures utilise non-toxic phosgene substitutes, such as *S,S'*-dimethyl dithiocarbonate (DMDTC), *N,N'*-disuccinimidyl carbonate (DSC) and *N,N'*-carbonyldiimidazole (CDI) (Figure 4.8), to synthesise alternative carbamoyl transfer agents.

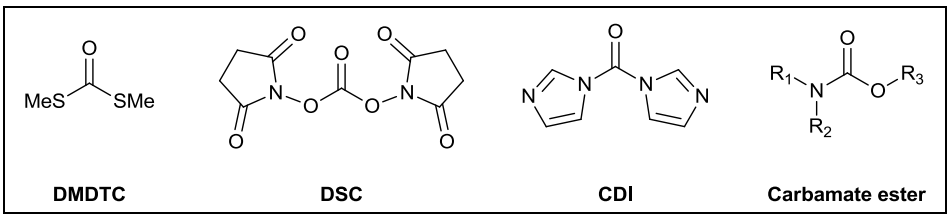

Figure 4.8: The structures of S,S'-dimethyl dithiocarbonate (DMDTC), N,N'- disuccinimidyl carbonate (DSC) and N,N'-carbonyldiimidazole (CDI) and a general carbamate ester

Possible carbamoyl cation derivatives which can be synthesised with use of DMDTC, DSC and CDI were displayed in Scheme 4.14, **44** – **46**. Compound **44** represents a proposed *S*-methyl *N*-alkylcarbamothioate carbamoylating equivalent. Fochi and co-workers[57] have published research on the synthesis of the *S*-methyl *N*-alkylcarbamothioates utilising the non-toxic reagent, DMDTC. In their work, the methylthiocarbonylating step with DMDTC required an excess of primary amine. Thereafter, the *S*-methyl *N*-alkylcarbamothioate equivalents were reacted with primary aliphatic amines to afford the ureas in high yields (>94%). The efficiency of urea formation with aromatic amines was not discussed.[57]

The carbamate esters (Figure 4.8) of primary and secondary amines have been widely used to accommodate urea formation. Several carbamate protecting groups, e.g. *t*-butyl, Bn, Cl_3CCH_2 (Troc), have produced ureas in high yields.[58] The *N*-hydroxysuccinimide (NHS) esters are popular carbamate esters in urea syntheses since the succinimidyl group withdraws electrons from the ester carbonyl carbon which promotes nucleophilic attack on the carbonyl group.[54,59] Compound **45** in Scheme 4.14 represents a proposed *N*-hydroxysuccinimide (NHS) ester equivalent of the carbamoyl cation synthon. Ogura and co-workers[59] have developed a method in which NHS esters were prepared from primary or secondary amines with DSC (Figure 4.8), in acetonitrile and triethylamine at room temperature, to afford the NHS esters in yields of 50% – 90%. Unfortunately, the subsequent reactions of the NHS esters with primary amines yielded low to moderate quantities of urea [59]

Batey and co-workers have performed a substantial amount of research (from 1998 – 2012)[50,60–64] on the use of CDI to prepare *N,N*-disubstituted carbamoyl cation synthon equivalents which can be applied to the synthesis of ureas, thioureas, carbamates, thiocarbamates and amides.[50] Their results

on these *N,N*-disubstituted carbamoylating reagents were outlined in a 'full study' in 2005[50] and were successfully concluded in 2008[64] with the establishment of common reaction- and purification conditions.

CDI is commercially available, crystalline and readily handled.[50] In the work of Batey and co-workers (Scheme 4.15), secondary amines were reacted with CDI in THF under reflux for 16 h, to form stable carbamoylimidazoles (**47**) in high yields.[50] These *N,N*-disubstituted carbamoylimidazoles (**47**) displayed low reactivity towards nucleophilic attack and where therefore activated by *N*-alkylation with methyl iodide to form the resonance-stabilised carbamoylimidazolium salts (**48**).[60] The carbamoylimidazolium salts (**48**) were more susceptible to nucleophilic attack.

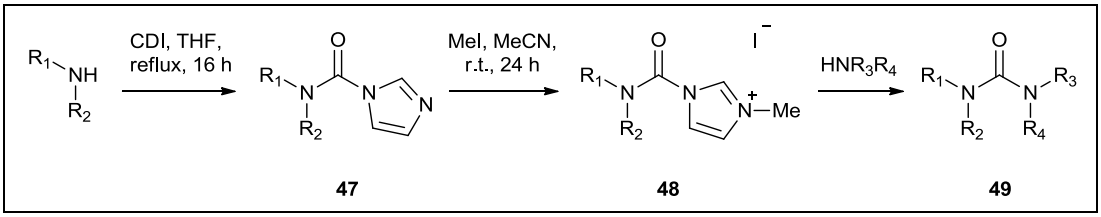

Scheme 4.15: The preparation of carbamoylimidazolium salts (48) from secondary amines in a two-step procedure utilising CDI and iodomethane. The reaction of the salts (48) with primary and secondary amines yield tri- and tetrasubstituted ureas (49).[50]

In most cases, these salts (**48**) were readily synthesised in high to quantitative yields, stable and storable for long periods of time.[50] The carbamoylimidazolium salts (**48**) act as *N,N*-disubstituted carbamoylating reagents and form unsymmetrical tri- or tetrasubstituted ureas (**49**) in high to quantitative yields upon reaction with primary or secondary amines.[50,64]

The use of CDI in urea synthesis attracted our attention due to the advantages that are offered with regard to reaction yields, non-toxicity and the stability of the carbamoylimidazoles. In order to use CDI in our synthetic procedures, we would have to synthesise *N*-monosubstituted carbamoylimidazole equivalents. Although most of Batey and co-workers' research were focused on *N,N*-disubstituted carbamoylating reagents, they expanded their work to monosubstituted *N*-alkyl carbamoylimidazoles in 2012.[65]

4.5.2 CDI coupling with primary amines: The synthesis of monosubstituted *N*-alkyl carbamoylimidazoles

Batey and co-workers[65] attempted to synthesise the monosubstituted *N*-alkyl carbamoylimidazole, *N*-methyl carbamoylimidazole **50**, by reacting methylamine ($MeNH_2$) with CDI (Scheme 4.16). As previously discussed, when secondary amines were reacted with CDI, stable *N,N*-disubstituted

carbamoylimidazoles formed, which required alkylation to react further. However, when this primary amine, $MeNH_2$, was reacted with CDI, a mixture of carbamoylimidazole **50** and the symmetrical urea product **51** formed. This implied that the *N*-monosubstituted carbamoylimidazole **50** was sufficiently reactive to react with a second $MeNH_2$ molecule to form the symmetrical urea product. Additionally, the reactivity of the unhindered amine, $MeNH_2$, could also promote the symmetrical urea formation.

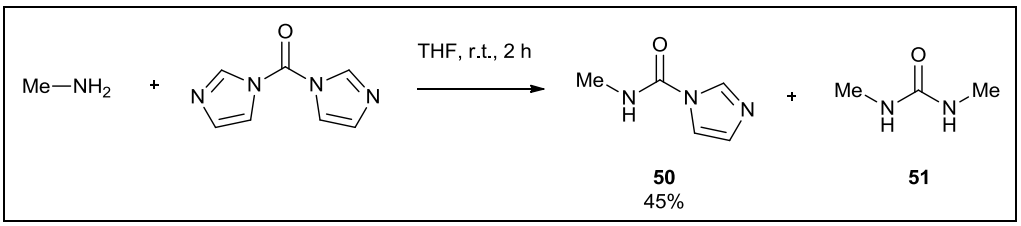

Scheme 4.16: The reaction of methyl amine with CDI by Batey and co-workers[65]

Batey and co-workers[65] solved this problem of symmetrical urea formation, by using the protonated methyl amine salt, methylammonium chloride ($MeNH_3Cl$) as starting material and reacting it with CDI in the absence of a base. A proposed mechanism of the reaction is displayed in Figure 4.9 below.[65] It is proposed that a $MeNH_3Cl$ molecule in close proximity to CDI in solution will activate the CDI by protonation. This protonation step will also provide a local concentration of $MeNH_2$ molecules which can attack at the CDI electrophilic centre. The nucleophilic substitution reaction releases imidazole and a subsequent deprotonation step affords the carbamoylimidazole **50**.[65] This method thus afforded **50** in a quantitative yield.

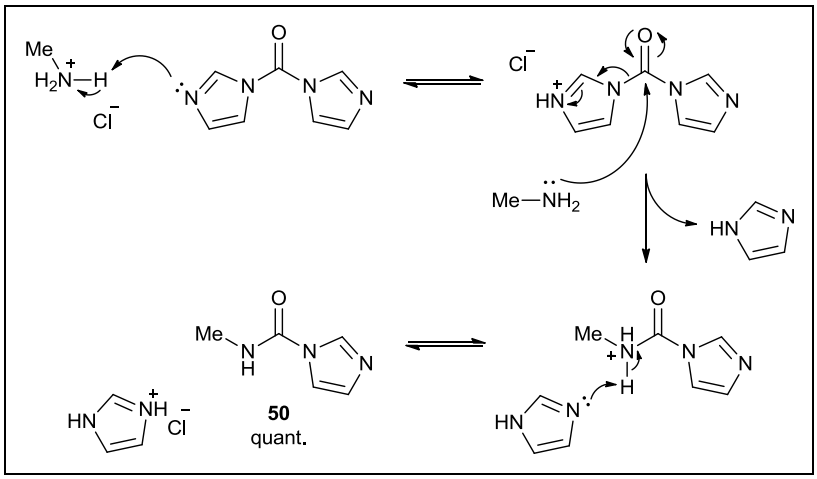

Figure 4.9: The proposed mechanism of N-Alkyl carbamoylimidazole formation from the ammonium hydrochloride salt, $MeNH_3Cl$.

N-methyl carbamoylimidazole (**50**) proved reactive enough to serve as a carbamoylating agent – the synthesis of the carbamoylimidazolium salt was not necessary – and was successfully reacted with primary and secondary amines in the presence of base (EtN_3 or NaH) to form ureas in high yields.[65]

Batey and co-workers[65] briefly expanded their studies to the synthesis of alternative *N*-alkyl carbamoylimidazoles. A high yielding procedure to synthesise GSK-3 inhibitor, AR-A014418 (**3**), was developed and is displayed in Scheme 4.17. The ammonium hydrochloride salt of 4-methoxybenzylamine (**15**) was generated *in situ* using 4 M HCl in dioxane in DCM, whereafter CDI and DMF were added to the mixture to form the carbamoylimidazole **46** in 98% yield. Carbamoylimidazole **46** was utilised as carbamoylating agent with 2-amino-5-nitrothiazole (**52**) to construct urea **3** in 97% yield. We envisaged utilising this procedure in the synthesis of our 1-benzazole-3-(4-methoxybenzyl)ureas.

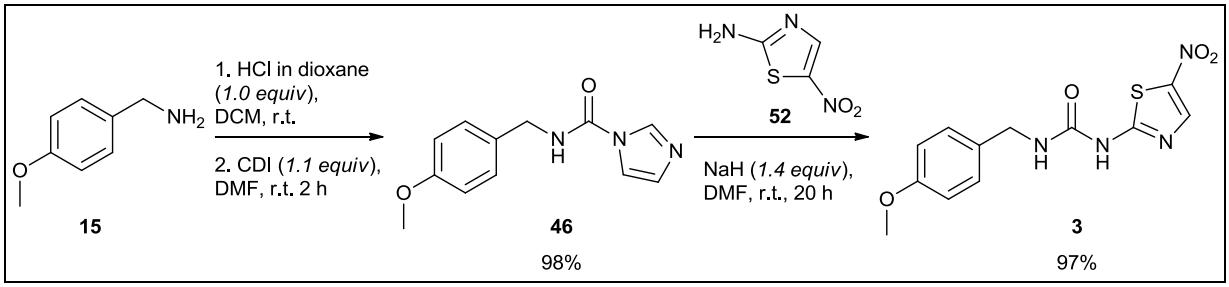

Scheme 4.17: The synthesis of AR-A014418 (3) by Batey and co-workers[65]

To explain the mechanistic aspects of urea formation with *N*-monosubstituted carbamoylimidazoles, the dissociation properties of the *N*-monosubstituted carbamoylimidazoles had to be considered. In contrast to the well-known stability of *N,N*-disubstituted carbamoylimidazoles, Staab[66] reported that *N*-monosubstituted carbamoylimidazoles (**53**) tend to dissociate into isocyanates (**55**) and imidazole when in solution (Scheme 4.18). Therefore in the urea formation mechanism, it has been proposed that the carbamoylimidazole (**53**) dissociates into its isocyanate first, whereupon the isocyanate (**55**) reacts with an amine nucleophile to form the urea (**54**).[67] This was established for aryl *N*-monosubstituted carbamoylimidazoles, wherein the aryl substituent can resonance-stabilise the zwitterionic intermediate which forms during dissociation.[67] In contrast, *N*-benzyl carbamoylimidazole and *N*-methyl carbamoylimidazole did not dissociate in solution, supposedly due to their inability to provide resonance stabilisation.[65,67] These results suggested that alkyl *N*-monosubstituted carbamoylimidazoles are attacked directly by nucleophiles to form ureas.

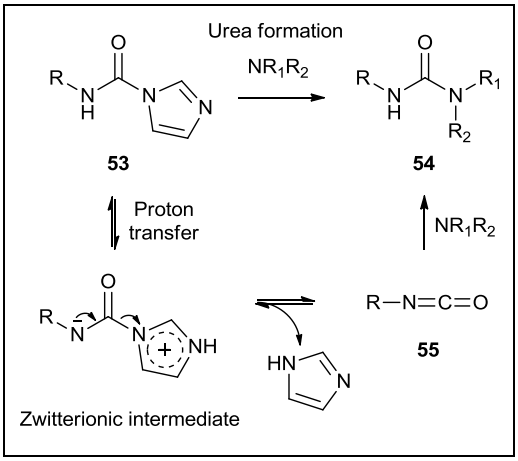

Scheme 4.18: Aryl N-monosubstituted carbamoylimidazoles dissociate in solution to form isocyanate equivalents that participate in urea formation[67]

Based on these results, we hypothesised that *N*-(4-methoxybenzyl) carbamoylimidazole (**46**) would not dissociate in solution, since the zwitterionic intermediate cannot be resonance-stabilised. Following the hypothesis, we proposed a mechanism in Scheme 4.19 for urea formation with *N*-(4-methoxybenzyl) carbamoylimidazole (**46**). In this mechanism, the deprotonated nucleophile reacts with carbamoylimidazole in a nucleophilic substitution reaction.

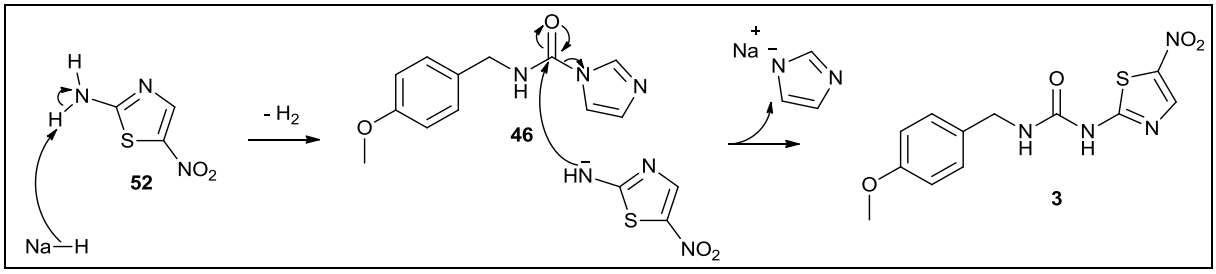

Scheme 4.19: A possible reaction mechanism for urea formation with N-(4-methoxybenzyl) carbamoylimidazole (46)

4.5.3 Our synthetic strategy towards urea formation

Having studied the literature, our synthetic strategy would entail the installation of the urea moiety by CDI-mediated coupling. CDI would be reacted with the ammonium hydrochloride salt of 4-methoxybenzylamine (**15**) to form the *N*-(4-methoxybenzyl) carbamoylimidazole (**46**), as displayed in Scheme 4.20. Carbamoylimidazole **46** would be reacted with the 6-substituted 2-aminobenzazoles to afford the 1-benzazolyl-3-(4-methoxybenzyl)ureas. The reagents were chosen to react with CDI in this order, as this would allow the bulk synthesis of *N*-(4-methoxybenzyl) carbamoylimidazole (**46**) for subsequent reactions with various 2-aminobenzazole scaffolds.

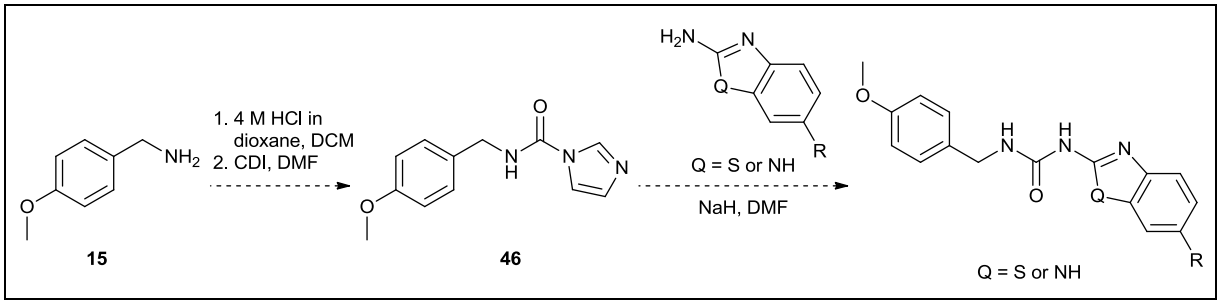

Scheme 4.20: Our synthetic strategy to afford a series of 1-benzazolyl-3-(4-methoxybenzyl)ureas

4.5.4 The synthesis of *N*-(4-methoxybenzyl) carbamoylimidazole (46)

A mixture of 4-methoxybenzylamine (**15**) in DCM was treated with 4 M HCl in 1,4-dioxane while stirring at room temperature. The mixture changed colour from colourless to white, indicating the *in situ* formation of the ammonium hydrochloride salt. After 10 minutes of stirring, DMF and CDI were added to the mixture at 0 °C. The reaction reached completion within 7 minutes of stirring, as indicated by the solution's end-point colour change from white to colourless. This short reaction time was found to be crucial to the success of the reaction and was in contrast with the 2 h reaction time reported in the literature.[65] When the reaction mixture was left to stir for longer, additional by-product formation took place.

A work-up procedure was carried out after the 7 minute reaction, in which the colourless solution was immediately concentrated *in vacuo* at 30 °C, diluted with EtOAc and washed four times with a saturated aqueous solution of NH_4Cl to achieve DMF removal. The product was further purified by column chromatography to afford *N*-(4-methoxybenzyl) carbamoylimidazole (**46**) as a crystalline white solid in quantitative yield.

The reaction method was readily scaled up from 0.14 g to 1.1 g (80% yield). The crystalline nature and stability of *N*-(4-methoxybenzyl) carbamoylimidazole (**46**) overcame the handling difficulties often associated with carbamoylating agents such as isocyanate. In addition, carbamoylimidazole **46** was storable in a sealed vial at room temperature for several months.

In the proposed reaction mechanism (Scheme 4.21), 4-methoxybenzylamine hydrochloride increases the electrophilicity of CDI by protonation. This step also releases a local concentration of free 4-methoxybenzylamine molecules which can participate in nucleophilic attack. A tetrahedral intermediate forms, from which imidazole (pK_a [BH^+] = 6.94 in DMSO, 25 °C)[68] is expelled, due to its better leaving group ability in comparison to 4-methoxybenzylamine (pK_a [BH^+] = 10.32 in DMSO, 25 °C).[69]

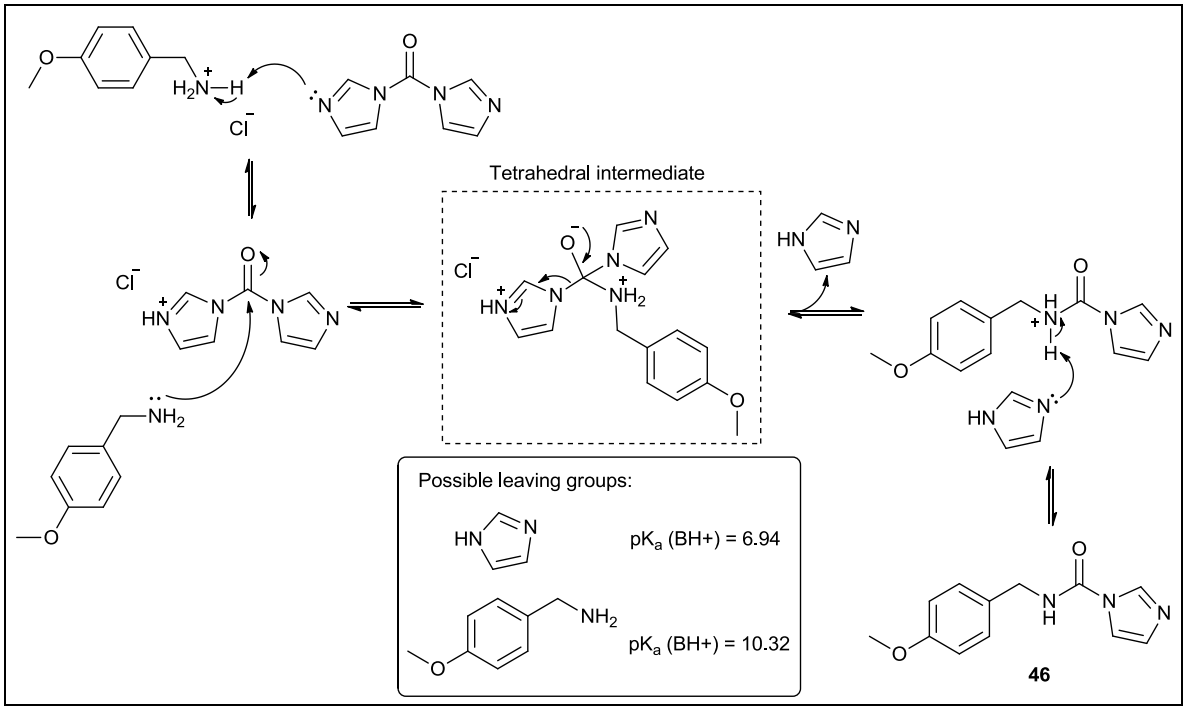

Scheme 4.21: The reaction mechanism of the synthesis of N-(4-methoxybenzyl) carbamoylimidazole

The ^{1}H NMR spectrum of *N*-(4-methoxybenzyl) carbamoylimidazole **46** is depicted in Figure 4.10. The three imidazole ring protons were accounted for at 8.06 ppm, 7.41 ppm and 6.89 ppm, respectively. The *para*-methoxybenzyl protons resonated as doublets at 7.23 ppm and 6.85 ppm.

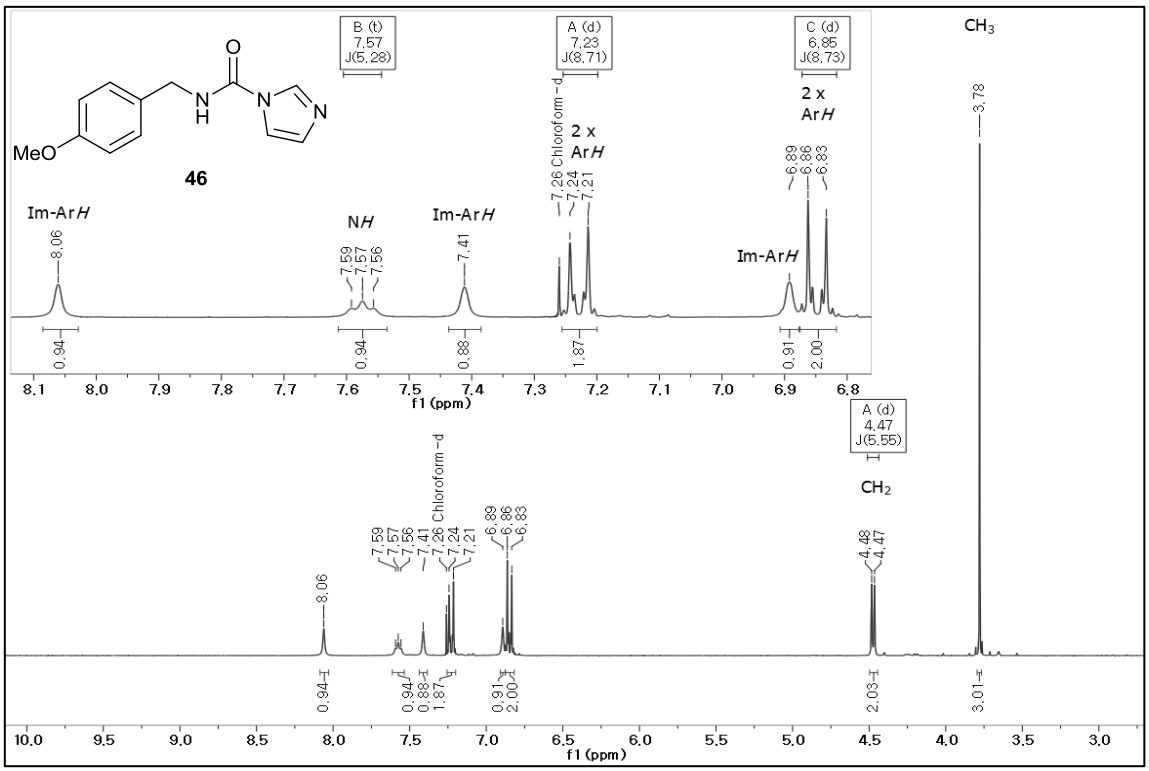

Figure 4.10: The ^{1}H NMR spectrum ($CDCl_3$) of N-(4-methoxybenzyl) carbamoylimidazole (46)

It should be noted that the amide proton (N*H*) and the benzylic CH_2 protons couple with one another. Therefore the amide proton was observed as a broad triplet at 7.57 ppm (J = 5.3 Hz) and the methylene protons were observed as a doublet integrating for 2H at 4.47 ppm (J = 5.6 Hz). The J-coupling values measured for these multiplets were not constant and this phenomenon was best accounted for by the broadness of the triplet signal. The broadened signal decreased the precision with which J-coupling values could be measured from the ^{1}H NMR spectrum. Therefore the J-coupling value of the sharper methylene proton signal was reported in the experimental data of compounds displaying this phenomenon. The ^{1}H NMR spectroscopic values of **46** deviated slightly from the values of Batey and co-workers,[65] but the ^{13}C NMR spectroscopic values corresponded very well. In addition, the structure was validated by the $[M+H]^+$ ion in the HRMS spectrum (*m/z* calculated 232.1086, found 232.1092).

The absence of additional sets of proton resonances[67] in the ^{1}H NMR spectrum — due to dissociated imidazole and isocyanate molecules — reinforced the hypothesis that *N*-(4-methoxybenzyl) carbamoylimidazole (**46**) do not dissociate spontaneously into its isocyanate equivalent in solution. The corresponding isocyanate $[M+H]^+$ ion was also not present in the HRMS spectrum of **46**.

N-(4-methoxybenzyl) carbamoylimidazole (**46**) was successfully synthesised in a quantitative yield and allowed for subsequent urea formation reactions with the prepared 2-aminobenzazole heterocycles.

4.5.5 Urea synthesis: Utilising the prepared 6-substituted-2-aminobenzothiazoles

The *N*-(4-methoxybenzyl)-*N*'-(6-substituted benzothiazolyl)ureas (**4**, **56** – **58**) were prepared in high yields, in a procedure that commenced with the dissolution of 2-aminobenzothiazole (**20** – **23**) and *N*-(4-methoxybenzyl) carbamoylimidazole (**46**) in DMF (Scheme 4.22). The mixture was treated portion-wise with 60% NaH in mineral oil and was left to stir at room temperature for 22 h. A work-up procedure involving multiple washes with a saturated aqueous solution of NH_4Cl was conducted to accomplish DMF removal.

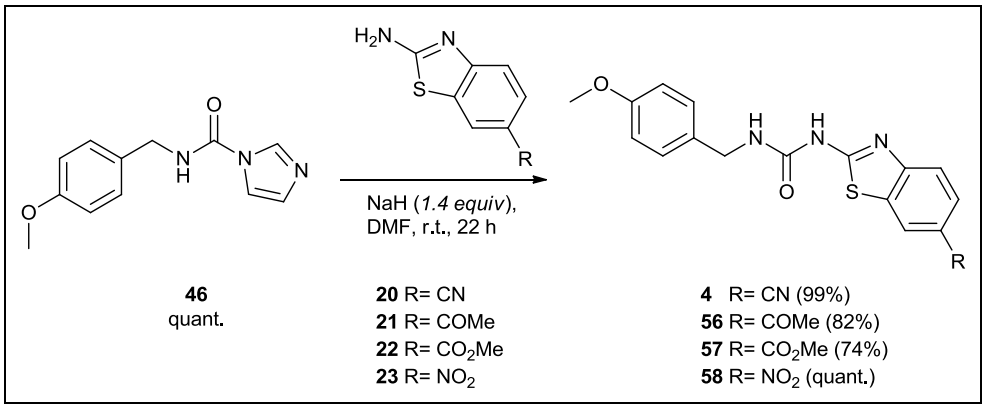

Scheme 4.22: The synthesis of N-(4-methoxybenzyl)-N'-(6-substituted benzothiazolyl)ureas

These urea formation reactions proceeded fairly cleanly; however small quantities of excess *N*-(4-methoxybenzyl) carbamoylimidazole (**46**) had to be removed by column chromatography. This purification step was not simple, since the polarity of carboxamide **46** was close to the polarity of the urea products. Purification was achieved when a mixed mobile phase, which consisted of MeOH, EtOAc and DCM, was used during silica column chromatography.

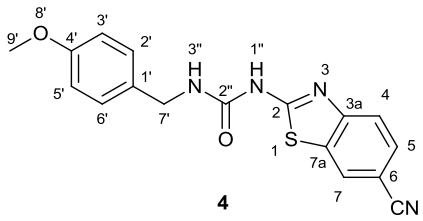

4

1-(6-Cyanobenzo[*d*]thiazol-2-yl)-3-(4-methoxybenzyl)urea (**4**) was synthesised in 99% yield. This proposed inhibitor has been synthesised before by Lo Monte *et al.*[56] in 70% yield, with the use of an isocyanate equivalent. It was concluded that we significantly improved the yield of **4**, with the use of *N*-(4-methoxybenzyl) carbamoylimidazole (**46**) as carbamoylating agent. The ^{1}H NMR and ^{13}C NMR spectroscopic results of **4** compared well to the literature.[56] Again, the resonance signal of the N$H_{3''}$ proton was split by the methylene protons of benzylic carbon ($C_{7'}$) to form a broad triplet at 7.20 ppm. The other urea proton, N$H_{1''}$, was visible as a broad singlet at 11.11 ppm.

The following general trends were seen in the ^{1}H NMR spectra of compounds **4**, **56** – **58**. The methoxy protons resonated at 3.73 ppm, the singlet integrating for 3H. The three benzothiazole proton signals (Ar$H_{4,5,7}$) coupled with one another and integrated for 1H each. The N$H_{3''}$ proton was generally observed as a broad triplet, whereas N$H_{1''}$ was observed in the range 11.02 – 11.25 ppm. The CH_2 proton resonance was split with a *J*-coupling constant of 5.8 Hz. Two doublets, each integrating for 2H, appeared in the aromatic region due to the benzylic ring protons. In the ^{13}C NMR spectra of compounds **4**, **56** – **58**, all expected carbon resonances were visible.

56 and **57** are newly synthesised compounds and the structures were confirmed by ^{1}H NMR, ^{13}C NMR and FT-IR spectroscopy, as well as HRMS. Compound **58** is known and the spectroscopic data compared well to the literature data.[56] Our synthetic procedure afforded **58** in a quantitative yield and improved greatly on the 26% yield reported by Lo Monte *et al.*[56]

4.5.6 Urea synthesis: Reference ligand, AR-A014418

Following the high yielding (97%) synthetic procedure of Batey and co-workers,[65] **3** was synthesised from the reaction of 2-amino-5-nitrothiazole (**52**) with *N*-(4-methoxybenzyl) carbamoylimidazole **46** in the presence of sodium hydride (Scheme 4.23). Several by-products were visible on TLC when the reaction was monitored and after a work-up procedure and column chromatography, the product was still impure. Trituration with DCM successfully afforded the pure product in >95% purity by LCMS, but

unfortunately in a low yield of 26%. The spectroscopic data of 1-(4-methoxybenzyl)-3-(5-nitrothiazol-2-yl)urea (**3**) compared very well to the literature.[65]

The reason for our low yield might be explained by the fact that the 2-amino-5-nitrothiazole (**52**) starting material was old and might have decomposed slightly over several years (the powder was brown instead of yellow). The nature of the by-products present in the reaction mixture and the crude product thus necessitated purification by trituration.

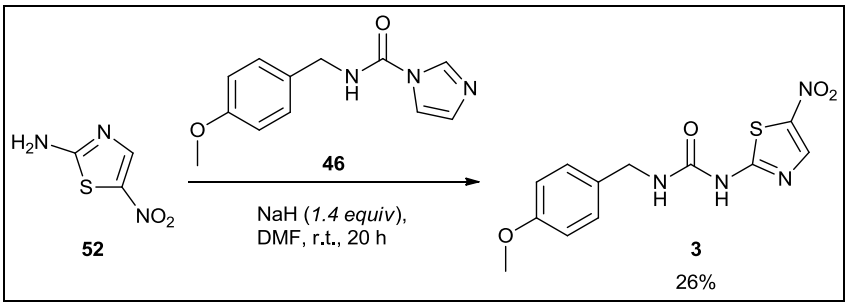

Scheme 4.23: The urea synthesis of AR-A014418 (3)

4.5.7 Urea synthesis: Utilising the prepared 6-substituted-2-aminobenzimidazoles

It was envisaged that the *N*-(4-methoxybenzyl)-*N*'-(6-substituted benzimidazolyl)ureas would be constructed from the 6-substituted-2-aminobenzimidazoles (**39** – **42**) via the same urea formation procedure.

In the initial reaction, 2-amino-1*H*-benzo[*d*]imidazole-6-carbonitrile (**39**) was treated with carbamoylimidazole **46** and NaH in DMF (Scheme 4.24). However this experimental procedure proved to be more challenging than expected. Firstly, a substantial amount of starting material (**39**) was left unreacted in solution. Secondly, any carbamoylimidazole **46** that remained in solution could not be separated from the product by column chromatography, due to the small polarity difference. This problem was solved with the use of an excess amount of base (NaH), to ensure that all carbamoylimidazole **46** reacted. Thirdly, the product was slightly unstable in solution. The decomposed by-product displayed similar polarity and was successfully removed by column chromatography with a mobile phase mixture of MeOH, EtOAc and DCM. To limit the quantity of decomposed product, the urea product had to be purified immediately after reaction completion.

It should be noted that no starting material remained in solution after the reaction was completed, when a 2-aminobenzothiazoles heterocycle (e.g. **20**) was used as nucleophile. However, with the 2-aminobenzimidazole heterocycles (e.g. **39**) as nucleophiles, starting material always remained in solution (see the yield comparison in Scheme 4.24). It is suggested that this might be due to

2-aminobenzimidazole's weaker nucleophilic nature. A lone pair or negative charge on the primary amine's nitrogen atom experiences greater delocalisation into the benzimidazole ring since the electrons can delocalise over three nitrogen atoms.

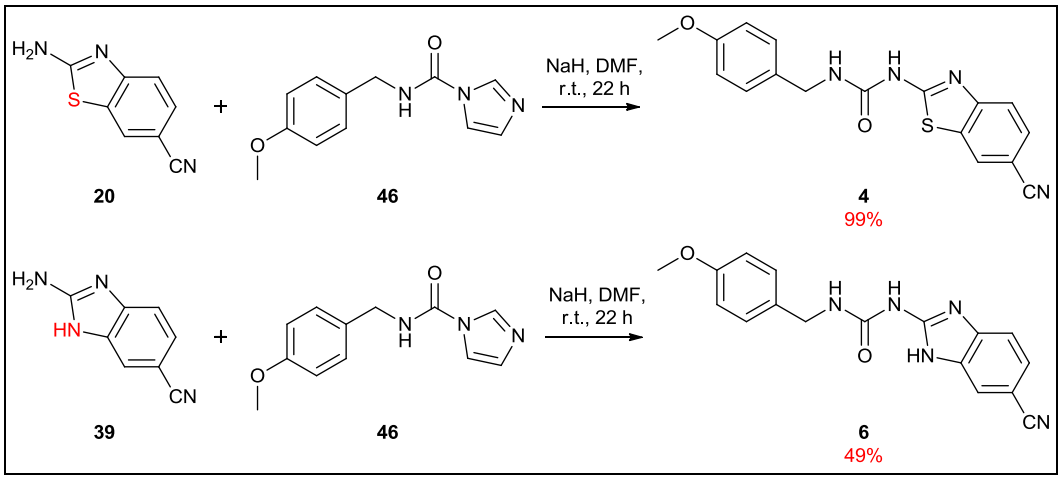

Scheme 4.24: A comparison of urea formation with 2-aminobenzothiazoles and 2-aminobenzimidazoles

Heating the reaction mixture to 80 °C did not push the reaction forward. It was then noted that although a substantial amount of 2-amino-1*H*-benzo[*d*]imidazole-6-carbonitrile (**39**) remained in solution, nearly none of the carbamoylimidazole **46** was left. Due to **39** not being a good nucleophile, **46** was consumed in more favourable side reactions.

To increase the nucleophilicity of the starting material, the reaction was attempted in THF with a stronger base, *n*-BuLi; however, more by-products formed. The by-products were later explained by the observation that the starting material (**39**) did not dissolve well in less polar solvents, THF and DCM, thereby hindering the reaction and promoting by-product formation. Therefore, the initial reaction conditions employing NaH and the polar solvent, DMF, were retained. Remaining starting material (**39**) could be removed readily as water-soluble salt in the work-up procedure, by washing with 1 M HCl.

In future optimisation studies, an increase in the electrophilicity of the carbamoylimidazole could be explored as an alternative to push the reaction forward. Methylation of the distal nitrogen in the imidazole ring of carbamoylimidazole **46** will form the resonance-stabilised carbamoylimidazolium salt and may activate **46** to make it more susceptible to nucleophilic attack by **39**.

1-(6-Cyano-1*H*-benzo[*d*]imidazol-2-yl)-3-(4-methoxybenzyl)urea (**6**) was obtained in a yield of 49% and the developed procedure was applied to afford the rest of the *N*-(4-methoxybenzyl)-*N*'-(6-substituted

benzimidazolyl)ureas in moderate yields (Scheme 4.25). To the best of our knowledge, ureas **6** and **59 – 61** have not been reported before in the literature. The structures of these compounds were thus confirmed by ^{1}H NMR, ^{13}C NMR and FT-IR spectroscopy and HRMS.

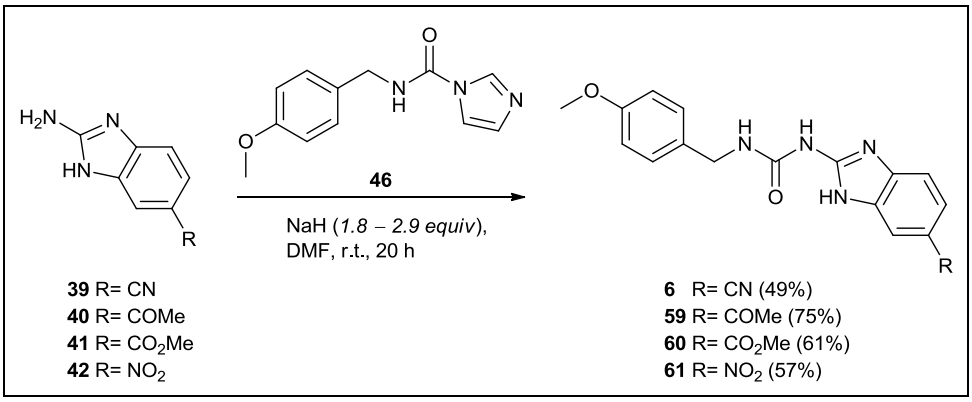

Scheme 4.25: The synthesis of N-(4-methoxybenzyl)-N'-(6-substituted benzimidazolyl)ureas

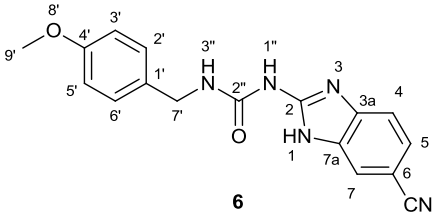

The three amine protons of 1-(6-cyano-1*H*-benzo[*d*]imidazol-2-yl)-3-(4-methoxybenzyl)urea (**6**) were distinguishable in its ^{1}H NMR spectrum and resonated at 12.09 ppm, 10.21 ppm and 7.48 ppm, respectively. The amine signal at 7.48 ppm was broadened and resembled the broad triplet expected for $NH_{3''}$. The benzimidazole ring protons resonated at 7.76 ppm as a singlet integrating for 1H (ArH_7) and at 7.44–7.41 ppm as a multiplet integrating for 2H (ArH_4, ArH_5). The CH_2 proton signal appeared as a doublet (J = 5.8 Hz) at 4.32 ppm integrating for 2H and the OCH_3 proton signal appeared at 3.73 ppm integrating for 3H. Two doublets, each integrating for 2H and with a J-coupling constant of 8.7 Hz represented the benzyl ring protons Ar$H_{2'}$, Ar$H_{3'}$, Ar$H_{5'}$ and Ar$H_{6'}$.

Similar trends were seen in the ^{1}H NMR spectra of compounds **59 – 61**. However, the benzimidazole ring proton signals observed for ArH_4, ArH_5 and ArH_7 appeared broadened in especially the ^{1}H NMR spectra of ester-derivative **60** and nitro-derivative **61**. The broadened signals are highlighted in the ^{1}H NMR spectrum of **60** (Figure 4.11). Signal broadening can be explained by the tautomerism in the benzimidazole ring. As experienced with the 6-substituted 2-aminobenzimidazoles (**39 – 42**) in Section 4.4.4, it was also challenging to obtain the ^{13}C NMR spectra of the benzimidazole ureas **6**, **59 – 61**, due to tautomeric effects. In general, the ^{13}C NMR spectra of ureas **6**, **59 – 61** were relatively inconclusive, due to missing carbon signals and the presence of weak, broadened signals. Only the signals in the far downfield and far upfield regions could be assigned; nonetheless, these signals corresponded well to the proposed structures. The structures were confirmed further with HRMS.

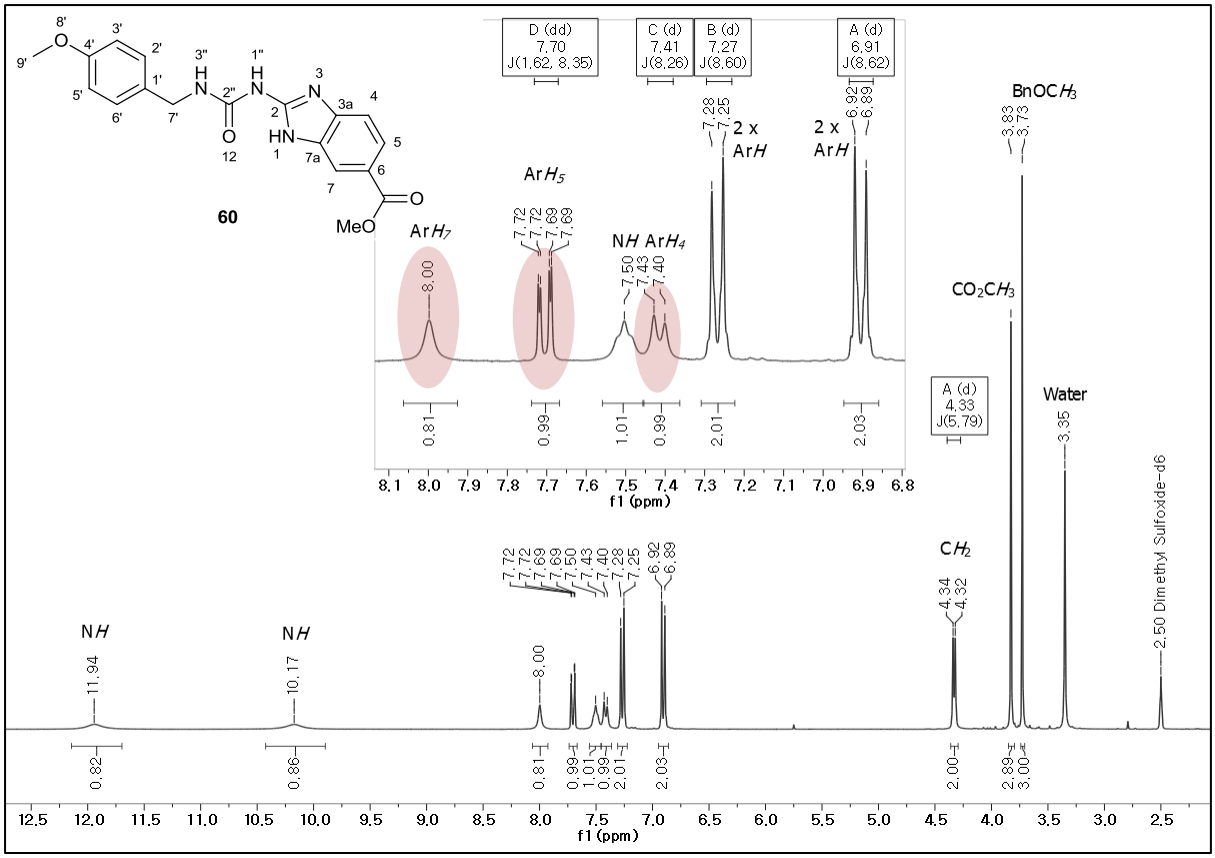

Figure 4.11: The ^{1}H NMR spectrum (DMSO-d_6) of methyl 2-[3-(4-methoxybenzyl)ureido]-1H-benzo[d]imidazole-6-carboxylate (60). The broadened signals of ArH$_4$, ArH$_5$ and ArH$_7$ are highlighted in red.

4.6 Chapter conclusion

This chapter commenced with the synthesis of appropriately functionalised benzothiazole and benzimidazole heterocycles which would constitute the scaffolds of our proposed 1-benzazole-3-(4-methoxybenzyl)urea GSK-3β inhibitors. Synthetic procedures towards these heterocycles were successfully developed and afforded the 6-substituted 2-aminobenzothiazoles and 6-substituted 2-aminobenzimidazoles in good yields. The final section of this chapter addressed urea synthesis, which required the development of an electrophilic carbamoylating reagent which would facilitate the coupling of two primary amines to form unsymmetrical disubstituted ureas. The *N*-(4-methoxybenzyl)-*N*'-(6-substituted benzothiazolyl)ureas were developed in excellent yields, whereas the synthesis of *N*-(4-methoxybenzyl)-*N*'-(6-substituted benzimidazolyl)ureas proved more challenging and afforded moderate yields. The nitrile-derivatised ureas (**4** and **6**) and the reference ligand AR-A014418 (**3**) were obtained from these syntheses and were sent for biological testing. The rest of the prepared ureas were precursors to proposed GSK-3β inhibitor molecules and their further modification will be discussed in the next chapter.

4.7 References

1 L. Yet, *Privileged Structures in Drug Discovery: Medicinal Chemistry and Synthesis*, John Wiley and Sons, Inc., Hoboken, 1st edn., 2018.

2 D. Maclean, J. J. Baldwin, V. T. Ivanov, Y. Kato, A. Shaw, P. Schneider and E. M. Gordon, *J. Comb. Chem.*, 2000, **2**, 562–578.

3 R. K. Gill, R. K. Rawal and J. Bariwal, *Arch. Pharm. Chem. Life Sci.*, 2015, **348**, 155–178.

4 R. Ali and N. Siddiqui, *J. Chem.*, 2013, **2013**, 1–12.

5 P. S. Yadav and S. G. P. Devprakash, *Int. J. Pharm. Sci. Drug Res.*, 2011, **3**, 1–7.

6 L. B. Townsend and D. S. Wise, *Parasitol. Today*, 1990, **6**, 107–112.

7 O. O. Ajani, D. V. Aderohunmu, C. O. Ikpo, A. E. Adedapo and I. O. Olanrewaju, *Arch. Pharm. Chem. Life Sci.*, 2016, **349**, 475–506.

8 L. Pan, H. Shimakoshi, T. Masuko and Y. Hisaeda, *Dalt. Trans.*, 2009, 9898–9905.

9 A. Gupta and S. Rawat, *J. Curr. Pharm. Res.*, 2010, **3**, 13–23.

10 C. G. Stuckwisch, *J. Am. Chem. Soc.*, 1949, **71**, 3417–3417.

11 F. E. Johnson and C. S. Hamilton, *J. Am. Chem. Soc.*, 1949, **71**, 74–76.

12 H. Hugerschoff, *Chem. Ber.*, 1901, **34**, 3130–3135.

13 Robert C. Tweit, *J. Heterocycl. Chem.*, 1970, **7**, 687–688.

14 J. K. Wang, Y. X. Zong, X. C. Wang, Y. L. Hu and G. R. Yue, *Chinese Chem. Lett.*, 2015, **26**, 1376–1380.

15 K. Nikoofar, *Chem. Sci. Trans.*, 2013, **2**, 691–700.

16 J. L. Wood, in *Organic Reactions*, ed. R. Adams, John Wiley and Sons, Inc., New York, 3rd edn., 1946, pp. 240–266.

17 V. S. Pilyugin, Y. E. Sapozhnikov, E. V. Klimakova, G. V. Kiseleva, S. L. Kuznetsova, T. P. Vorob'eva, G. E. Chikisheva and L. V. Yakovleva, *Russ. J. Appl. Chem.*, 2008, **81**, 459–464.

18 S. N. Sawhney and D. W. Boykin, *J. Org. Chem.*, 1979, **44**, 1136–1142.

19 A. D. Jordan, C. Luo and A. B. Reitz, *J. Org. Chem.*, 2003, **68**, 8693–8696.

20 E. Lieber, C. N. R. Rao and J. Ramachandran, *Spectrochim. Acta*, 1959, **13**, 296–299.

21 Institute Of Pharmacology And Toxicology, Academy Of Military Medical Sciences, EP2354136 (A1), 2011.

22 Takeda Pharmaceuticals Company Limited, EP3225618 (A1), 2017.

23 W. Hirose, K. Sato and A. Matsuda, *Eur. J. Org. Chem.*, 2011, **2011**, 6206–6217.

24 S. Hinsberger, J. C. De Jong, M. Groh, J. Haupenthal and R. W. Hartmann, *Eur. J. Med. Chem.*, 2014, **76**, 343–351.

25 B. D. Hosangadi and R. H. Dave, *Tetrahedron Lett.*, 1996, **37**, 6375–6378.

26 S. Caron, *Practical Synthetic Organic Chemistry: Reactions, Principles, and Techniques*, John Wiley and Sons, Inc., Hoboken, 1st edn., 2011.

27 R. Rastogi and S. Sharma, *Synthesis*, 1983, **1983**, 861–882.

28 J. Schulze, H. Tanneberg and H. Matschiner, *Z. Chem.*, 1980, **20**, 436–437.

29 K. Starcevic, I. Caleta, D. Cincic, B. Kaitner, M. Kralj, K. Ester and G. M. Karminski-Zamola, *Heterocycles*, 2006, **68**, 2285–2299.

30 B. Maji, K. Kumar, M. Kaulage, K. Muniyappa and S. Bhattacharya, *J. Med. Chem.*, 2014, **57**, 6973–6988.

31 T. Fairley, R. Tidwell, I. Donkor, N. Naiman, K. Ohemeng, R. Lombardy, J. Bentley and M. Cory, *J. Med. Chem.*, 1993, **36**, 1746–1753.

32 M. Brickman and J. H. Ridd, *J. Chem. Soc.*, 1965, 6845–6851.

33 W. Yin, C. Wang and Y. Huang, *Org. Lett.*, 2013, **15**, 1850–1853.

34 C.-H. Park and R. S. Givens, *J. Am. Chem. Soc.*, 1997, **119**, 2453–2463.

35 H. Sharghi, M. Jokar, M. M. Doroodmand and R. Khalifeh, *Adv. Synth. Catal.*, 2010, **352**, 3031–3044.

36 S. S. Thakkar, P. Thakor, H. Doshi and A. Ray, *Bioorg. Med. Chem.*, 2017, **25**, 4064–4075.

37 J. G. Hoggett, R. B. Moodie, J. R. Penton and K. Schofield, *Nitration and aromatic reactivity*, Cambridge University Press, London, 1971.

38 J. Clayden, N. Greeves and S. Warren, *Organic Chemistry*, Oxford University Press, Oxford, 2nd edn., 2001.

39 G. M. Lampman, D. L. Pavia, G. S. Kriz and J. R. Vyvyan, *Spectroscopy*, Brooks/Cole, Belmont, 4th edn., 2010.

40 D. Kelly, S. Bateman, R. Martin, M. Reum, M. Rose and A. Whittaker, *Aust. J. Chem.*, 1994, **47**, 247–262.

41 Y. Lu, Y. Li, R. Zhang, K. Jin and C. Duan, *Tetrahedron*, 2013, **69**, 9422–9427.

42 C. J. Reinhardt, E. Y. Zhou, M. D. Jorgensen, G. Partipilo and J. Chan, *J. Am. Chem. Soc.*, 2018, **140**, 1011–1018.

43 N. Charrier, E. Demont, R. Dunsdon, G. Maile, A. Naylor, A. O'Brien, S. Redshaw, P. Theobald, D. Vesey and D. Walter, *Synthesis*, 2006, **2006**, 3467–3477.

44 Y. Zhu, M. Zhao, W. Lu, L. Li and Z. Shen, *Org. Lett.*, 2015, **17**, 2602–2605.

45 U. Tawar, A. K. Jain, B. S. Dwarakanath, R. Chandra, Y. Singh, N. K. Chaudhury, D. Khaitan and V. Tandon, *J. Med. Chem.*, 2003, **46**, 3785–3792.

46 E. P. Papadopoulos and U. Hollstein, *Org. Magn. Reson.*, 1982, **19**, 188–191.

47 V. A. Lopyrev, L. I. Larina, T. I. Vakul'skaya, M. F. Larin, E. F. Shibanova, I. A. Titova, M. G.

Voronkov and E. E. Liepin'sh, *Magn. Reson. Chem.*, 1985, **23**, 301–304.

48 K. Sagi, K. Fujita, M. Sugiki, M. Takahashi, S. Takehana, K. Tashiro, T. Kayahara, M. Yamanashi, Y. Fukuda, S. Oono, A. Okajima, S. Iwata, M. Shoji and K. Sakurai, *Bioorg. Med. Chem.*, 2005, **13**, 1487–1496.

49 K. Kikuchi, R. B. Hannak, M. J. Guo, A. J. Kirby and D. Hilvert, *Bioorg. Med. Chem.*, 2006, **14**, 6189–6196.

50 J. A. Grzyb, M. Shen, C. Yoshina-Ishii, W. Chi, R. S. Brown and R. A. Batey, *Tetrahedron*, 2005, **61**, 7153–7175.

51 J. H. Saunders and H. J. Slocombe, *Chem. Rev.*, 1948, **43**, 203–218.

52 H. Babad and A. G. Zeiler, *Chem. Rev.*, 1973, **73**, 75–91.

53 A. R. Katritzky, O. Meth-Cohn, C. W. Rees and T. L. Gilchrist, *Comprehensive Organic Functional Group Transformations, Volume 6: Synthesis: Carbon with three or four attached heteroatoms*, Pergamon, Oxford, 1st edn., 1995.

54 G. T. Hermanson, *The Reactions of Bioconjugation*, Academic Press, London, 3rd edn., 2013.

55 J. Bansagi, MSc thesis: Development of Water Soluble ACP1 Analogues and Application of N-Alkyl Carbamoylimidazoles as Isocyanate Equivalents, University of Toronto, 2014.

56 F. Lo Monte, T. Kramer, A. Boländer, B. Plotkin, H. Eldar-Finkelman, A. Fuertes, J. Dominguez and B. Schmidt, *Bioorg. Med. Chem. Lett.*, 2011, **21**, 5610–5615.

57 E. Artuso, I. Degani, R. Fochi and C. Magistris, *Synthesis*, 2007, **2007**, 3497–3506.

58 S.-H. Lee, H. Matsushita, B. Clapham and K. D. Janda, *Tetrahedron*, 2004, **60**, 3439–3443.

59 K. Takeda, Y. Akagi, A. Saiki, T. Tsukahara and H. Ogura, *Tetrahedron Lett.*, 1983, **24**, 4569–4572.

60 R. A. Batey, V. Santhakumar, C. Yoshina-Ishii and S. D. Taylor, *Tetrahedron Lett.*, 1998, **39**, 6267–6270.

61 R. A. Batey, C. Yoshina-Ishii, S. D. Taylor and V. Santhakumar, *Tetrahedron Lett.*, 1999, **40**, 2669–2672.

62 R. A. Batey, M. Shen, V. Santhakumar and C. Yoshina-ishii, *Comb. Chem. High Throughput Screen.*, 2002, **5**, 219–232.

63 J. A. Grzyb and R. A. Batey, *Tetrahedron Lett.*, 2003, **44**, 7485–7488.

64 J. A. Grzyb and R. A. Batey, *Tetrahedron Lett.*, 2008, **49**, 5279–5282.

65 P. A. Duspara, M. Sadequl Islam, A. J. Lough and R. A. Batey, *J. Org. Chem.*, 2012, **77**, 10362–10368.

66 H. A. Staab, *Angew. Chem., Int. Ed.*, 1962, **1**, 351–367.

67 T. Rawling, A. M. McDonagh, B. Tattam and M. Murray, *Tetrahedron*, 2012, **68**, 6065–6070.

68 A. Kozak, M. Czaja and L. Chmurzyński, *J. Chem. Thermodyn.*, 2006, **38**, 599–605.

69 K. Bowden and S. I. J. Hirani, *J. Chem. Soc., Perkin Trans. 2*, 1990, 1889–1891.

Chapter 5: Incorporating the electrophilic warheads of the proposed irreversible targeted covalent inhibitors

This chapter addresses the incorporation of electrophilic warheads onto the prepared 1-benzazole-3-(4-methoxybenzyl)ureas to complete the synthesis of the Cys199-targeted covalent inhibitors which were designed to react with GSK-3 through an irreversible mechanism. To this end, the *N*-(6-substituted benzothiazolyl)-*N'*-(4-methoxybenzyl)ureas (**56** – **58**) and the *N*-(6-substituted benzimidazolyl)-*N*'-(4-methoxybenzyl)ureas (**59** – **61**) were synthesised with substituents in the sixth position, which can be modified to afford the desirable electrophilic warheads onto the scaffold. The modification objectives can be grouped into three sections as depicted in Scheme 5.1. The first modifications will focus on the alpha-bromination of acetyl derivatives **56** and **59** in order to obtain the halomethylketone derivatives. The second section of modifications is aimed at the synthesis of the acryloyl- and propioloyl-substituted products **9** – **12** from the ester-functionalised precursors, and the last modifications will pertain to the synthesis of the acrylamide inhibitors, **13** and **14**.

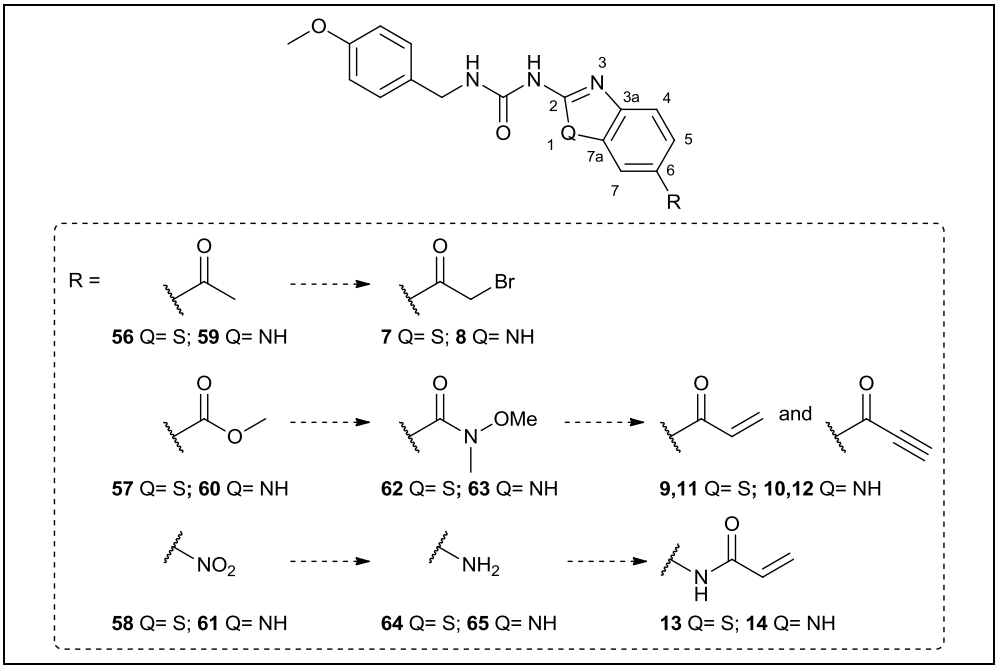

Scheme 5.1: The introduction of electrophilic warheads onto the synthesised 1-benzazole-3-(4-methoxybenzyl)ureas 56 – 58 and 59 – 61.

5.1 Alpha-monobromination to yield the halomethylketones

As discussed in the review of Vekariya and Patel,[1] a plethora of α-monobromination methods has been developed in the literature to address the bromination of aryl substituted ketones and other carbonyl compounds.[1] Several synthetic challenges, including over-bromination, low regioselectivity, the use of toxic reagents and long reaction times have motivated the development of a variety of procedures.[1] Different bromine sources have been utilised together with various catalysts, additives, solvents and temperatures in α-monobromination procedures.[1] Examples of bromine sources include reactions with *N*-bromosuccinimide (NBS),[2–6] molecular bromine,[7–9] hydrobromic acid,[10,11] copper(II) bromide,[12] bromo ionic liquids,[13] bromotrimethylsilane,[14] ammonium bromide[15,16] and organic ammonium tribromides, such as tetrabutylammonium tribromide[17] and phenyltrimethylammonium tribromide.[18]

Aryl substituted ketones often have more than one electron-rich donor site, which necessitates regioselective control to promote ketone halogenation over electrophilic aromatic substitution. Furthermore, α-bromination is often complicated by over-bromination in which more than one α-hydrogen are substituted to form the α,α-dibromoketone or even the α,α,α-tribromoketone. Selectivity for the monosubstituted product can be optimised with the use of suitable reagents and reaction conditions. However, a small amount of disubstituted product almost always accompanies the monosubstituted product in the equimolar reaction of a ketone with a bromine source, due to the occurrence of a disproportionation reaction (eq. 5.1).[19,20] This disproportionation reaction can increase the amount of dibrominated product as well as the amount of unbrominated product (starting material) in the reaction mixture.

$$2RCOCH_2Br \rightleftharpoons RCOCH_3 + RCOCHBr_2 \qquad (eq.\ 5.1)$$

5.1.1 α-Bromination of 1-(6-acetylbenzo[*d*]thiazol-2-yl)-3-(4-methoxybenzyl)urea (56)

In order to minimise disubstitution on the α-carbon of the acetyl group, careful stoichiometric control was required in the α-bromination reaction. The crystallinity and high molecular weight of the organic ammonium tribromide, trimethylphenylammonium tribromide (PTAB, $PhNMe_3Br_3$), facilitated satisfactory control over the equivalents of bromine source that entered the reaction. The utility of PTAB in α-brominations was discovered by Marquet and Jacques in 1959.[21] Apart from the advantages in stoichiometric control, PTAB is a much weaker electrophile than molecular bromine and provides more selectivity in reactions.[18] It has been suggested that α-bromination with PTAB, commences with enolization of the ketone in the rate-determining step, whereafter fast-stage bromination takes place.[17]

In our studies, the α-bromination of 1-(6-acetylbenzo[*d*]thiazol-2-yl)-3-(4-methoxybenzyl)urea (**56**) was unfortunately not selective for the monobrominated product when the reaction was treated with PTAB in a MeOH-DCM (1:1) solvent system.[22] After five hours of stirring at 20 °C, substantial amounts of both mono- and dibrominated products had formed, while starting material also remained in solution. The first option was to investigate an alternative solvent system, since the solvent is known to influence the degree of disproportionation (eq. 5.1), and the regioselectivity of the reaction.[19]

Anhydrous THF is a very popular solvent in α-bromination reactions with PTAB. THF not only serves as a solvent, but also as a base to react with HBr liberated in the reaction, thereby driving the reaction forward and preventing side-reactions due to free HBr in the reaction mixture (eq. 5.2).[18,19]

$$RCOCH_3 + Br_2 \rightleftharpoons RCOCH_2Br + HBr \qquad \textit{(eq. 5.2)}$$

Utilising this solvent, 1-[6-(2-bromoacetyl)benzo[*d*]thiazol-2-yl]-3-(4-methoxybenzyl)urea (**7**) was successfully synthesised by reacting 1.1 equivalents of PTAB with aryl acetyl **56** in THF as solvent (Scheme 5.2). The reaction was stirred at 30 °C for 64 h whereafter the solvent was removed *in vacuo* at 30 °C. The crude reaction mixture constituted mainly of α-monobrominated product; however, small quantities of starting material and α,α-dibrominated product were visible on TLC. After a work-up procedure with ethyl acetate and saturated aqueous sodium bicarbonate, the α-monobrominated product was isolated by column chromatography with a mobile phase mixture of EtOAc and DCM, to afford **7** in a yield of 35%.

In the described procedure, it was important to maintain the reaction temperature at 30 °C, since a higher reaction temperature of 40 °C visibly increased the formation of α,α-dibromoketone as a by-product on TLC. Unfortunately, the lower reaction temperature required a longer reaction time of 64 h. Excess PTAB also promoted α,α-dibromination, therefore the PTAB equivalents were limited to a range of 1.05 to 1.10 equivalents.

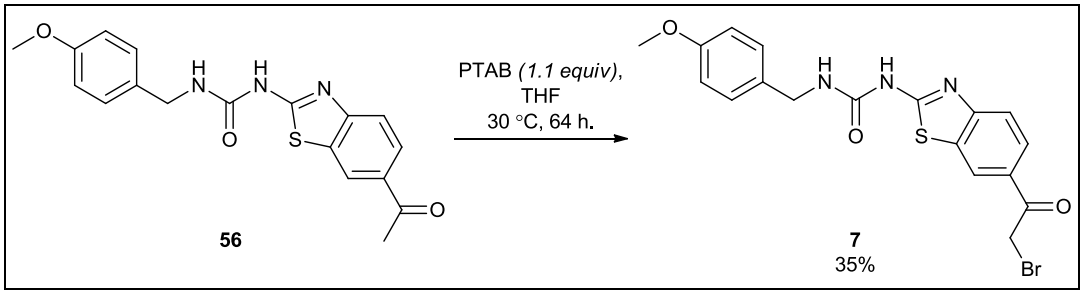

Scheme 5.2: α-Bromination of acetyl derivative 56 to yield halomethylketone 7

It was extremely difficult to separate the main α-monobrominated product **7** from the starting material and α,α-dibrominated product using column chromatography, due to the compounds' similarities in polarity. Apart from the disproportionation by-products, these purification difficulties contributed to the relatively low yield of the reaction (35%). Recrystallisation from EtOH was explored as an alternative purification technique, but the α,α-dibromoketone product was not successfully excluded from the crystals. It is proposed that an improved purification method will result in an increased isolated yield.

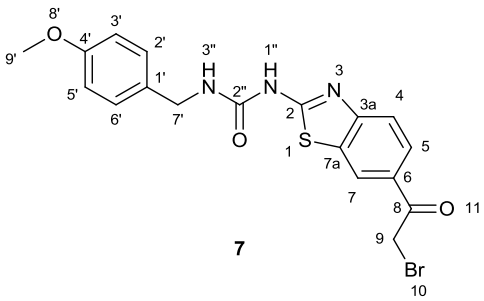

7

Halomethylketone **7** was obtained in >95% purity (determined by UPLC-MS) and was sent for biological testing. The structure of compound **7** was established by ^{1}H NMR, ^{13}C NMR and FT-IR spectroscopy, as well as HRMS. In the ^{1}H NMR spectrum, the presence of the halomethylketone moiety was confirmed by a singlet at 4.93 ppm integrating for 2H, which represented the CH_2-Br (H_9) protons. The signal of the H_9 protons was more downfield than expected for CH_2 protons, due to their connectivity to a carbon which is attached to an electronegative bromine atom. A broad singlet at 11.08 ppm represented the urea proton N$H_{1''}$. A broad signal at 7.21 ppm accounted for the urea proton N$H_{3''}$. The CH_2 ($H_{7'}$) proton signal appeared as a doublet at 4.31 ppm integrating for 2H, and was split by the proton of N$H_{3''}$ with a *J*-coupling constant of 5.8 Hz. The benzylic ring protons, Ar$H_{2'+6'}$ and Ar$H_{3'+5'}$ resonated as two doublets integrating for 2H each, with a *J*-coupling constant of 8.7 Hz. The methoxy protons were visible as a singlet integrating for 3H at 3.73 ppm. The three aromatic protons of the benzothiazole ring appeared as a doublet at 8.62 ppm (*J* = 1.7 Hz) representing ArH_7, a doublet of doublets at 7.99 ppm (*J* = 8.5, 1.7 Hz) representing ArH_5 and a doublet at 7.70 (*J* = 8.5 Hz) representing ArH_4. The ^{13}C NMR spectrum of compound **7** displayed a total of 16 carbon signals, as expected. The signal at 190.5 ppm validated the carbonyl carbon of the halomethylketone group, and the *C*H_2-Br (C_9) signal was visible at 34.0 ppm. With the installation of the α-bromine atom, the acetyl CH_3 proton- and carbon signals disappeared, which were previously visible at 2.60 ppm and 26.7 ppm in the ^{1}H NMR and ^{13}C NMR spectra of **56**, respectively. In the HRMS spectrum of halomethylketone **7**, the $[M+H]^+$ molecular ion was represented by two characteristic signals, since the bromine atom has two stable isotopes, ^{79}Br and ^{81}Br, which have 50.7% and 49.3% natural abundance, respectively.[23] The $[M+H]^+$ molecular ion, $C_{18}H_{17}N_3O_3S^{79}Br$, was found at 434.0178 (*m/z* calcd = 434.0174), and $C_{18}H_{17}N_3O_3S^{81}Br$ was found at 436.0162 (*m/z* calcd = 436.0174).

5.1.2 α-Bromination of 1-(6-acetyl-1*H*-benzo[*d*]imidazol-2-yl)-3-(4-methoxybenzyl)urea (59)

We were hoping to apply the α-bromination procedure described in the previous section to the benzimidazole derivative of acetyl **56**, to obtain the benzimidazole version (**8**) of halomethylketone **7**. Thus, 1-(6-acetyl-1*H*-benzo[*d*]imidazol-2-yl)-3-(4-methoxybenzyl)urea (**59**) was treated with PTAB in THF, whereafter the mixture was left to stir for 64 h at 30 °C. Unfortunately, the reaction was not selective for the α-monobrominated product. TLC revealed the major products in the reaction mixture to be starting material and a new product of similar, but lower polarity. Upon staining with *p*-anisaldehyde, this new product did not display the same colour properties as were observed for the α-monobrominated, α,α-dibrominated and even the α,α,α-tribrominated products, despite displaying similar polarity properties. Unfortunately, no products could be isolated from the crude mixture, due to the close polarities of all the by-products in such a non-selective type of reaction.

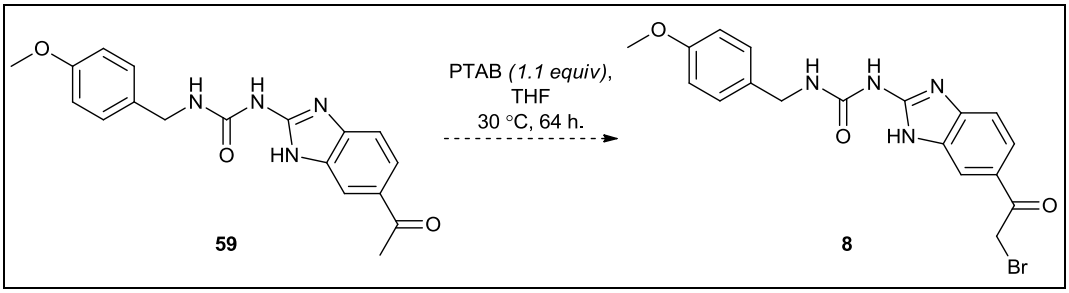

Scheme 5.3: The proposed α-bromination of acetyl derivative 59 to form halomethylketone 8

It is, however, possible that the imidazole ring amine (N_1H) activates the 6-membered ring of the benzimidazole core to promote electrophilic substitution in the *para (*or *ortho)* position (Figure 5.1). Activation increases the nucleophilicity of the benzimidazole core, making it a better nucleophile than the enol tautomer of the acetyl group. The reactivity of the enol is restricted by the rate of acetyl enolization in a neutral solvent. Compound **59** could also have been brominated on both the benzimidazole ring and the acetyl group. Previously, when the PTAB and THF method was performed on the benzothiazole derivative **56**, this type of by-product was not produced, which strengthened the argument that the electronics of the benzimidazole core altered the regioselectivity of the reaction.

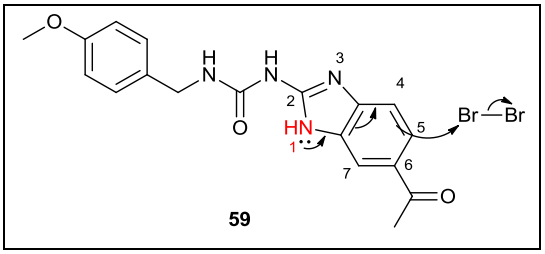

Figure 5.1: Activation of the benzimidazole core is suggested to compromise regioselectivity

At lower reaction temperature, 0 °C, the regioselectivity for the α-monobrominated product in the PTAB/THF reaction did not improve, affording a mixture of at least 4 products.

NBS is a popular and selective α-brominating agent with a milder electrophilic character than molecular bromine.[1] Furthermore, NBS employs an ionic mechanism when the reaction is catalysed by acid.[6] 1-(6-Acetyl-1*H*-benzo[*d*]imidazol-2-yl)-3-(4-methoxybenzyl)urea (**59**) was treated with 1.1 equivalents of NBS in a mixture of DCM and *p*-toluenesulfonic acid (0.1 equiv) at a temperature of 0 °C, whereafter the mixture was allowed to reach room temperature. After stirring for 2 h, the reaction mixture constituted of substantial amounts of starting material, monobrominated product and dibrominated product, as concluded from TLC analysis. These reaction conditions thus lacked control over the bromination reaction at the α-position of the acetyl.

At this point, a dual bromination challenge had to be addressed. Firstly, the regioselectivity of the reaction had to be directed towards the formation of the halomethylketone product instead of the benzimidazole electrophilic substitution product. Secondly, controlled bromination at the acetyl α-carbon was necessary to avoid over-bromination. It was envisaged that strongly acidic conditions would catalyse the rate of enolization at the acetyl group, thereby increasing the reactivity of the acetyl group. It is also well-known that α-bromination is more controlled under acid-catalysed conditions, in contrast to base-promoted conditions. In base-promoted conditions, bromination on the α-atom will continue until all hydrogen atoms have been replaced, since each additional bromine atom increases the acidity of the remaining α-hydrogens.[24]

Utilising strongly acidic conditions, 1-(6-acetyl-1*H*-benzo[*d*]imidazol-2-yl)-3-(4-methoxybenzyl)urea (**59**) was thus dissolved in an 8:3 mixture of glacial acetic acid and 48% HBr, whereupon it was treated dropwise with a mixture of molecular bromine in glacial acetic acid over 3 hours at 10 °C. The mixture was left to stir overnight at room temperature. This procedure appeared to be very selective for the α-monobrominated product, by TLC analysis. The α-monobrominated product was isolated using column chromatography, and the product displayed as a single spot on TLC. Unfortunately, ^{1}H NMR spectroscopy revealed the presence of a by-product, which displayed exactly the same R_f value on TLC as the product. This reaction was repeated in acetic acid and HBr, but with the less electrophilic bromine source, PTAB. Unfortunately, the by-product was still visible in ^{1}H NMR the spectrum, but this time in a smaller quantity (approx. 1:3 ratio of by-product to product). The by-product could not be removed successfully from the product, despite further purification attempts. The ^{1}H NMR spectra of the impure α-monobrominated products were used to investigate the nature of the by-product (Figure 5.2).

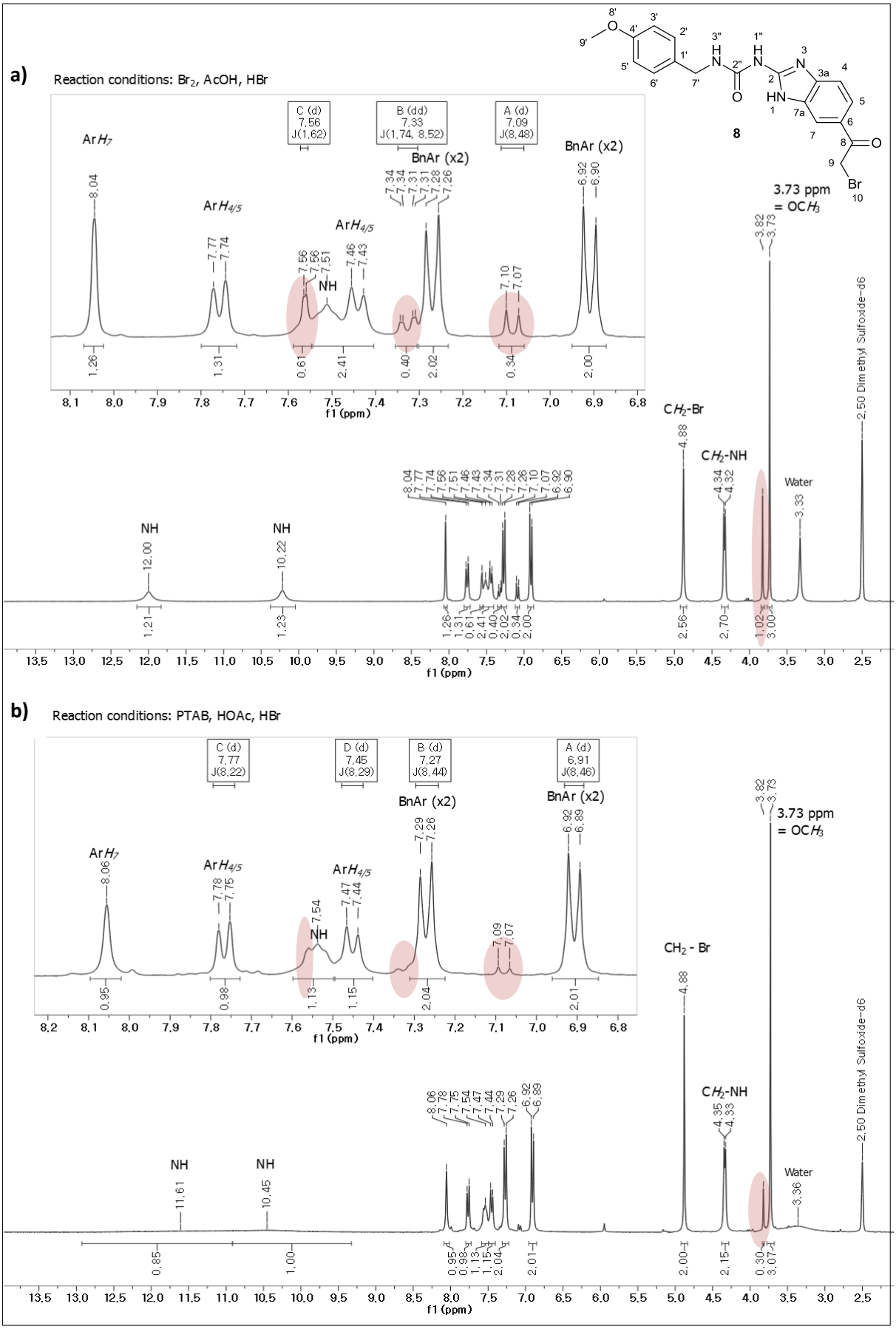

Figure 5.2: The ^{1}H NMR spectra of compound 8 (impure), isolated from the reactions with a) Br_2, AcOH, HBr, b) PTAB, AcOH, HBr. The signals of the predominant by-product are highlighted in red.

In the ^{1}H NMR spectra, it appeared that the chemical shift of the methoxy-signal (OCH_3) had shifted from 3.73 ppm to 3.82 ppm in the by-product. After careful interpretation of integration, peak patterns and coupling constants in the ^{1}H NMR spectra, it was proposed that the acidic conditions had also catalysed monobromination on the *para*-methoxybenzyl ring of **8**. The large doublets of the benzyl aromatic hydrogens were absent in the predominant signals of the by-product. Mono-bromination on the benzyl ring would result in a trisubstituted ring, with an aromatic substitution pattern appearing as two doublets and a doublet of doublets signal. This substitution pattern was visible (Figure 5.2) at 7.56 ppm (J = 1.6 Hz) as a doublet, 7.33 ppm (J = 1.7, 8.5 Hz) as a doublet of doublets and 7.09 ppm (J = 8.5 Hz) as a doublet. The J-coupling constant, 8.5 Hz, of the trisubstituted ring, agreed with the J-coupling constant of 8.5 Hz previously observed in the coupling pattern of the unsubstituted benzyl ring. Electrophilic aromatic bromination on the *para*-methoxybenzyl ring also explained the new chemical shift value of the methoxy group. No other chemical shift differences were visible in the spectra, which implied that aromatic bromination on the benzyl did not influence the chemical shift of distant hydrogens on the scaffold.

Returning to neutral conditions to avoid the new-found regioselectivity issues, copper(II) bromide was utilised as last resort for α-bromination. According to the literature, copper(II) bromide has displayed excellent α-bromination ability when refluxing in mixtures of EtOAc and/or chloroform.[12] Due to the low solubility of the starting material (**59**) in EtOAc, the reaction only commenced once ethanol was added to the mixture to dissolve the starting material.[25] Compound **59** was reacted with copper(II) bromide in a 5:1.2 mixture of EtOAc and ethanol, and the reaction was heated under reflux (80 °C) for 3 h. This reaction was also attempted at a lower reaction temperature of 55 – 65 °C. In both cases, the crude product mixture contained starting material, α-monobrominated product, as well as α,α-dibrominated product. Unfortunately, the α-bromoproduct could not be separated successfully from the α,α-dibromoproduct using column chromatography, as indicated by the presence of a signal at 5.16 ppm (C*H*-Br_2) and a signal at 4.88 ppm (CH_2-Br) in the ^{1}H NMR spectrum.

Table 5.1 below summarises the reagents and reaction conditions which were employed in the attempted α-brominations of benzimidazole urea **59**. Disappointingly, the exploration of different brominating reagents did not provide a successful and reliable method to synthesise halomethylketone **8**. It did not appear feasible to explore more alternative brominating agents. Due to the high degree of regioselectivity and halogenation control required in this bromination reaction, it was concluded that an alternative synthetic strategy was necessary.

Table 5.1: Failed attempts towards α-monobromination of benzimidazole derivative 59 (Scheme 5.3)

Entry	Reagents and reaction conditions	Outcomes
1	PTAB *(1.1 equiv)*, THF, 30 °C, 64 h	Non-selective. Major products: starting material and unknown product (possible electrophilic substitution on benzimidazole core).
2	PTAB *(1.1 equiv)*, THF, 0 °C, 2 h	Non-selective, despite lower temperature.
3	NBS *(1.1 equiv)*, PTSA *(0.1 equiv)*, DCM, 0 °C – r.t., 2 h	Over-bromination at α-position.
4	Br_2 *(1.0 equiv)*, HBr, HOAc, 10 °C, 3 h, then r.t., 18 h	Selective for α-monobromination, but an inseparable by-product was present in low quantity (possible monobromination on the *para*-methoxybenzyl ring).
5	PTAB *(1.0 equiv)*, HBr, HOAc, 10 °C, 30 min, then r.t., 18 h	Selective for α-monobromination, but the same inseparable by-product was present in low quantity.
6	Cu(II)Br, EtOAc/EtOH, reflux (80 °C), 3 h	Mixture of α-mono- and α,α-dibrominated products.
7	Cu(II)Br, EtOAc/EtOH, reflux (55 – 65 °C), 3 d	Mixture of α-mono- and α,α-dibrominated products.

*5.1.2.1 Synthesising halomethylketone **8** via a silyl enol ether intermediate*

In 1974, Reuss and Hassner[26] described the utility of silyl enol ethers (enolate equivalents) in a two-step procedure to halogenate carbonyl compounds. In the first step, trimethylsilyl enol ethers were prepared in order to eliminate the rate-determining enolization step which often complicates α-bromination. In the second step, Reuss and Hassner found that silyl enol ethers react instantaneously with bromine (1.0 equiv) to form α-monobrominated products, under careful temperature control.[26]

Conde-Ceide and co-workers[27] successful applied this silyl enol ether-mediated procedure to an acetyl group situated on an imidazo[1,2-*a*]-pyrazine scaffold (**66**), as seen in Scheme 5.4.

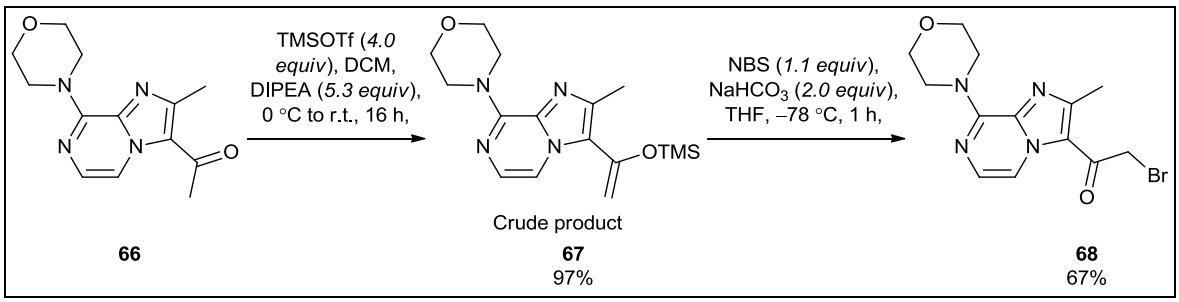

Scheme 5.4: Conde-Ceide and co-workers[27] converted ketone 66 into trimethylsilyl enol ether 67 to synthesise the α-monobrominated product, 68, in a good yield.

The crude silyl enol ether intermediate (**67**) was isolated in a work-up procedure with cold sat. $NaHCO_3$ and DCM, whereafter the organic layer was dried, filtered and concentrated *in vacuo*. The resultant crude oil (**67**) was used in the second bromination step with NBS at −78 °C, to afford the α-monobromination product (**68**) in a 67% yield.[27]

In accordance with the procedure of Conde-Ceide and co-workers,[27] halomethylketone **8** was successfully prepared in a 48% overall yield (over two steps) as seen in Scheme 5.5. Trimethylsilyl trifluoromethanesulfonate (TMSOTf, 3.9 equiv) and the base, *N,N*-diisopropylethylamine (DIPEA, 5.2 equiv), were initially used to generate the trimethylsilyl enol ether intermediate at 0 °C. The reaction mixture was left to stir overnight at room temperature, whereafter the reaction was found to be incomplete, as monitored by TLC. In contrast, Conde-Ceide and co-workers[27] reported a yield of 97% for the crude silyl enol ether **67** utilising this method. Thus, an increased reaction temperature (30 °C) was explored, and the reagent equivalents were increased (TMSOTf, 7.8 equiv; DIPEA, 10.4 equiv), but the reaction remained incomplete as judged by the presence of starting material on the TLC plate. In future studies, it is suggested that the reaction should be repeated utilising a stronger base, to drive the enolization equilibrium forward.

Nonetheless, a significant amount of silyl enol ether did form in the reaction mixture and the crude mixture was utilised to perform the subsequent bromination step. The crude mixture was used without any further purification, since silica column chromatography resulted in decomposition of the trimethylsilyl enol ether and regeneration of the starting material, regardless of using 0.5% Et_3N as a buffer in the mobile phase solvent system. In the bromination step, the crude mixture was treated with NBS (0.76 equiv) in a mixture of THF and $NaHCO_3$ powder (1.5 equiv) at −78 °C. After 1.5 h of stirring at −78 °C, the reaction was complete. The reaction was very selective for α-monobromination and the product was readily isolated *via* a work-up procedure with sat. $NaHCO_3$ and EtOAc, followed by silica column chromatography, to afford the final product **8** in an overall yield of 48% and a purity of 98% for biological testing. The high purity achieved in this reaction was satisfying, following all the previous attempts which required tedious separation procedures to remove bromination by-products.

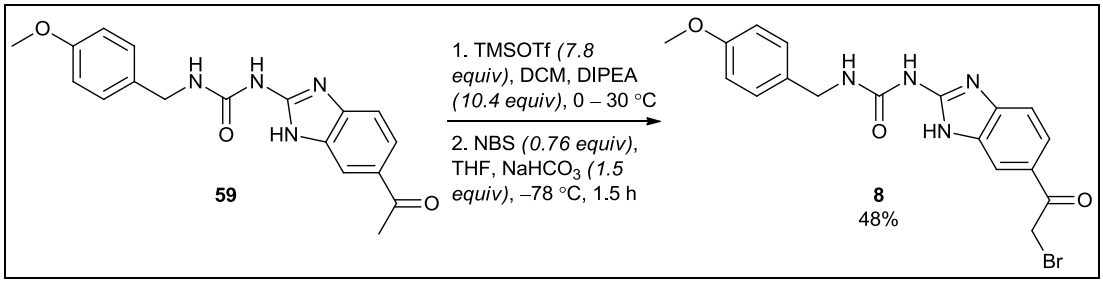

Scheme 5.5: The successful synthesis of halomethylketone 8 via a silyl enol ether intermediate

In the ^{1}H NMR spectrum of compound **8**, the characteristic signal at 4.88 ppm integrating for 2H, confirmed the presence of the two BrCH_2 protons. In the ^{13}C NMR spectrum, the HMK carbonyl carbon signal shifted from 197.1 ppm (**59**) to 191.0 ppm (**8**). In the HRMS spectrum of **8**, the $[M+H]^+$ molecular ion, $C_{18}H_{18}N_4O_3{}^{79}Br$, was found at 417.0565 (*m/z* calcd = 417.0562), and $C_{18}H_{18}N_4O_3{}^{81}Br$ was found at 419.0545 (*m/z* calcd = 419.0562).

5.2 The synthesis of the vinyl- and ethynyl ketones

The direct functional group conversion of esters to ketones, with the use of Grignard or organolithium reagents, has been a challenging task in the past. In this method, the organometallic reagent would react with the ester to form the ketone product; however the high reactivity of the ketone product would result in a high propensity of over-addition of organometallic reagent to the carbonyl centre, to produce the tertiary alcohol.[28] *N*-Methoxy-*N*-methylamides, also known as Weinreb amides,[28] are very popularly used intermediates which facilitate the synthesis of ketones from esters, without any over-addition of organometallic reagent.[29] When a Weinreb amide (**69**, Scheme 5.6) is treated with an organometallic reagent, a stable, metal-chelated, tetrahedral intermediate (**70**, **71**) forms upon addition of one molecule of organometallic reagent to the electrophilic carbonyl centre.[28] The metal-chelated intermediate is stable under the reaction conditions and prevents collapse to a ketone, thereby avoiding the reaction of the ketone with a second molecule of organometallic reagent. Upon aqueous acidic work-up, the stable intermediate transforms to the ketone product and any remaining organometallic reagent is quenched concomitantly.[30]

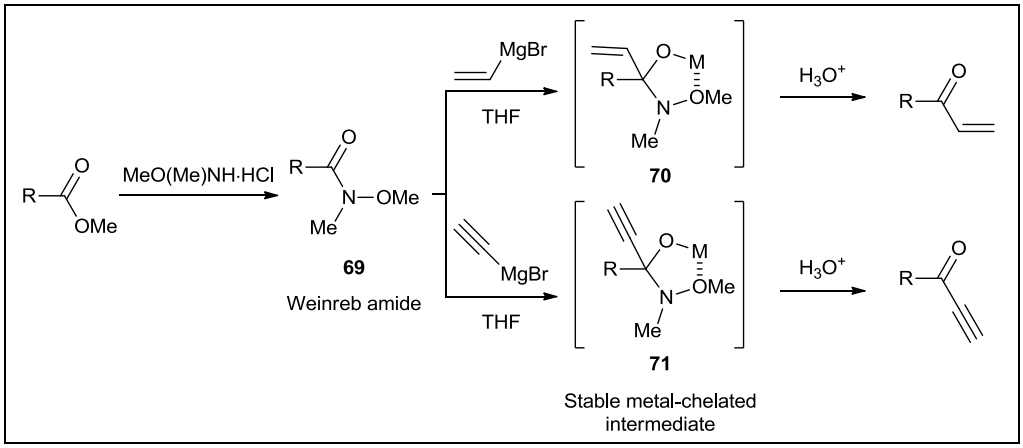

Scheme 5.6: The conversion of esters to ketones with Grignard reagent is well facilitated by Weinreb amides. Stable metal-chelated intermediates prevent the formation of over-addition products.

Scheme 5.6 depicts the planned conversion of ester precursors **57** and **60** (Scheme 5.1) into their acryloyl- and propioloyl-derivatives, using vinylmagnesium bromide and ethynylmagnesium bromide.

5.2.1 The preparation of Weinreb amides

Weinreb amides can be prepared from various compounds in the carboxylic acid oxidation state, including carboxylic acids, esters, lactones and acyl halides.[30] Two methods pertaining to the preparation of Weinreb amides from esters have been utilised predominantly in the literature and will be discussed. These methods were developed to address the challenges associated with the aminolysis of esters to form amides. These challenges included high reaction temperatures and/or prolonged reaction times.[31,32] Furthermore, strong alkali metal catalysts applied in aminolysis often did not accommodate sensitive functional groups.[33]

The amine, *N,O*-dimethylhydroxylamine, required in the preparation of Weinreb amides, is commercially available in its hydrochloride salt form, *N,O*-dimethylhydroxylamine hydrochloride [MeO(Me)NH·HCl]. The first convenient method for the preparation of Weinreb amides was based on the ester to amide conversion procedures developed by Weinreb and co-workers[33,34] In this method, a cooled solution of hydrochloride salt [MeO(Me)NH·HCl] in benzene, toluene or DCM was treated with trimethylaluminium (Me_3Al) to form an active aluminium species, supposedly the methylchloroaluminum amide (eq. 5.3).[34] The reaction of the active aluminium species with an ester produced the Weinreb amide.[35]

$$MeO(Me)NH{\cdot}HCl + Me_3Al \rightarrow MeO(Me)NAl(Cl)Me + 2CH_4 \qquad (eq.\ 5.3)$$

In 1997, Nakata and co-workers[36] found that dimethylaluminium chloride (Me_2AlCl) can also be used to generate active aluminium species. The active species, $MeO(Me)NAlCl_2$, generated the amides in shorter reaction times and in higher yields. These species also accommodated reactions with sterically hindered esters and lactones, which previously delivered poor results with Me_3Al.[36] It should be noted that these aminolysis reactions with Me_2AlCl and Me_3Al, generally required two to five equivalents of the active species to form the amide, as well as strictly inert reaction conditions.[29]

In 1995, Williams and co-workers[37] developed a new general method for the conversion of esters to Weinreb amides, using the hydrochloride salt [MeO(Me)NH·HCl] and isopropylmagnesium chloride as a base. In this method the magnesium amide, MeO(Me)NMgCl, was generated as active species and was reacted with the ester. Similarly to Nakata and co-workers,[36] this method was developed in an attempt to synthesise Weinreb amides from hindered esters.[37]

The method developed by Williams and co-workers[37] was optimised to ensure minimal by-product formation. In their initial optimisation studies, EtMgBr was used as organomagnesium reagent. EtMgBr and MeO(Me)NH·HCl were slurried in THF at 0 °C in the first step, whereafter the ester was treated immediately with the slurry in the second step. This reaction displayed low yields and Williams

and co-workers[37] hypothesised that the generated reactive species [MeO(Me)NMgCl] was either decomposing or reacting with more EtMgBr, before it could react with the ester in the second step. Therefore Williams and co-workers[37] developed a procedure in which the ester was present from the start of the reaction, and they achieved the formation of reactive species in the presence of the ester. When they created a slurry of the ester and MeO(Me)NH·HCl in THF at 0 °C and treated it with EtMgBr, the amide was isolated in 91% yield. The rapid reaction of the active species with the ester, outcompeted decomposition and the side-reactions due to EtMgBr.[37]

The preparation of reactive species from organomagnesium reagents in the presence of the ester, most importantly required that the organomagnesium reagent does not attack the carbonyl centre of the newly generated ketone product in solution. This problem was not completely avoided with nucleophilic bases MeMgCl and EtMgBr; however, the hindered nature of the base, isopropylmagnesium chloride (*i*-PrMgCl), completely solved this problem. Williams and co-workers[37] have also demonstrated the successful use of the non-nucleophilic bases, mesityl magnesium bromide and lithium hexamethyldisilazide (LHMDS). Nonetheless, *i*-PrMgCl provided the cleanest reactions (and similar yields) and was selected as the organomagnesium reagent of choice.

The efficient methods of both Nakata and co-workers[36] and Williams and co-workers[37] appeared promising for the preparation of the Weinreb amides required in this project.

*5.2.1.1 The synthesis of Weinreb amides **62** and **63***

The procedure of Williams and co-workers[37] was followed in the synthesis of Weinreb amides **62** and **63** (Scheme 5.7). However, *i*-PrMgCl was not available in our chemical store, therefore 2-bromopropane was used in accordance with the Weinreb preparation methods of Suto *et al.*,[38] to first prepare isopropylmagnesium bromide (*i*-PrMgBr) as base. The organomagnesium reagent was titrated and then applied to the ester and MeO(Me)NH·HCl in the Weinreb preparation reaction.

These reactions required inert conditions and were performed under argon. 2-Bromopropane was distilled from calcium hydride prior to the preparation of the organomagnesium reagent. Then, at room temperature, a small portion of 2-bromopropane was added to a flask with dry magnesium turnings and THF. While stirring vigorously, the mixture was warmed by hand, until the reaction mixture started to dissipate heat. The rest of the 2-bromopropane was then added by slow dropwise addition. The end of the reaction was indicated by the cooling of the reaction mixture.

The concentration of the prepared Grignard reagent was determined by the titration method of Lin and Paquette.[39] In this method, *i*-PrMgBr in THF was added dropwise to a solution of menthol in THF, with 1,10-phenanthroline as an indicator. An end-point colour change from colourless to pink was

observed. In the preparation of Weinreb amide **62**, the concentration of *i*-PrMgBr was 1.3 M in THF, and for **63**, the concentration of *i*-PrMgBr was 1.4 M in THF. These Grignard reagents were used immediately after titration.

A suspension of the ester (**57**/**60**, Scheme 5.7) and MeO(Me)NH·HCl were prepared in THF. The hygroscopic hydrochloride salt, MeO(Me)NH·HCl, was pre-dried overnight, under vacuum in a 40 °C oil bath. The suspension was then treated dropwise with *i*-PrMgBr at −20 °C. The reaction was allowed to reach −5 °C over one hour, whereafter it was quenched with sat. aq. NH_4Cl. The Weinreb amide was isolated by a work-up procedure and column chromatography.

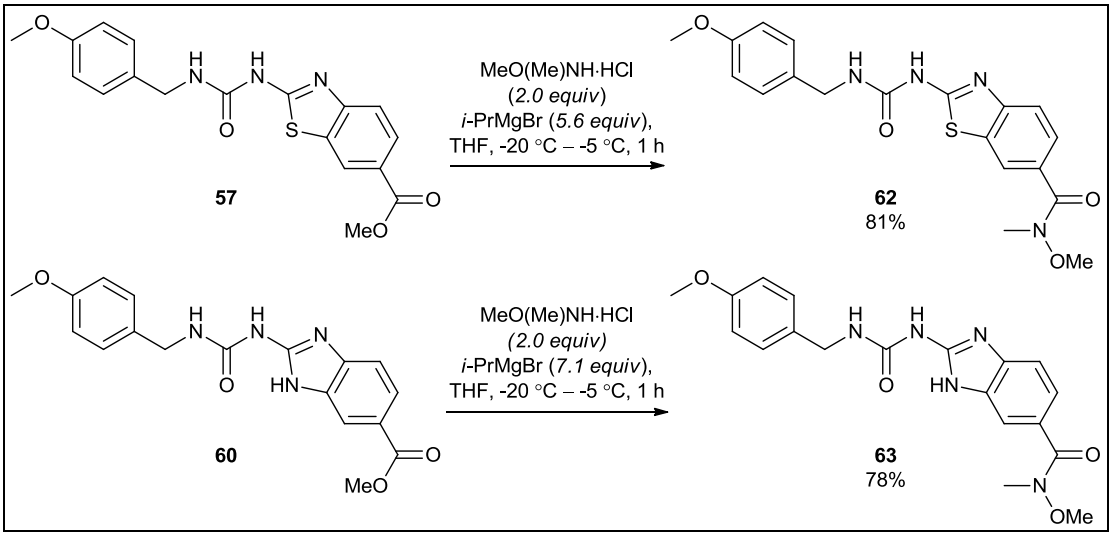

Scheme 5.7: The preparation of Weinreb amides 62 and 63

In the preparation of **62**, the ester **57** was initially treated with 1.6 equivalents of MeO(Me)NH·HCl and 3.0 equivalents of *i*-PrMgBr, for 30 min (Table 5.2). The reaction provided a relatively clean crude product, which only consisted of the Weinreb product and remaining starting material. Unfortunately, only 10% of Weinreb product had formed, while the rest of the starting material was left unreacted. It was found that once the *i*-PrMgBr had been added, a longer reaction time or a higher reaction temperature (0 °C) did not affect the conversion. Instead the equivalents of *i*-PrMgBr played a major role in the degree of ester conversion to the Weinreb product. The yield of **62** was increased to 81% when the reaction was treated with 5.6 equivalents of *i*-PrMgBr (entry 3, Table 5.2).

Table 5.2: The optimisation of the Weinreb reaction with ester 57

Entry	Reagents	Temp. (°C)	Time (h)	Yield (%)
1	MeO(Me)NH·HCl (*1.6 equiv*), THF, *i*-PrMgBr (***3.0 equiv***)	−20 to −10	0.5	10
2	MeO(Me)NH·HCl (*2.0 equiv*), THF, *i*-PrMgBr (***4.0 equiv***)	−20 to 0	3	38
3	MeO(Me)NH·HCl (*2.0 equiv*), THF, *i*-PrMgBr (***5.6 equiv***)	−20 to −5	1	**81**

It is suggested that several factors could have contributed to this large excess of *i*-PrMgBr consumed in this reaction. The two protons of MeO(Me)NH·HCl required a minimum of 2.0 equivalents of *i*-PrMgBr to form the active magnesium amide species. However, *i*-PrMgBr could also have been consumed in the removal of acidic protons on the ester starting material (**57**). For instance, the urea functionality of ester **57** has two acidic protons. When the acidic protons of the urea are removed, the charges can be stabilised by delocalisation into the carbonyl group and benzothiazole ring. Furthermore, the hygroscopic nature of MeO(Me)NH·HCl could have required the use of excess *i*-PrMgBr. The MeO(Me)NH·HCl salt was dried before the reaction, but still the salt could have introduced small quantities of moisture into the reaction, which would have decomposed some of the Grignard reagent.

In the reaction of the benzimidazole ester **60** (Scheme 5.7) with MeO(Me)NH·HCl and *i*-PrMgBr, 7.1 equivalents of *i*-PrMgBr afforded the Weinreb amide **63** in 78% yield. It is suggested that more equivalents of *i*-PrMgBr were required, since ester **60** had one additional acidic proton on the benzimidazole ring available for deprotonation.

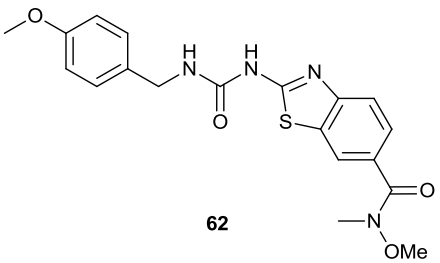

62

In the ^{1}H NMR spectrum of **62**, the aliphatic proton chemical shift region clearly confirmed formation of the Weinreb amide. The starting material (**57**)'s methyl ester protons (OCH_3) were no longer visible at 3.86 ppm. A signal at 3.56 ppm integrated for 3H and represented the NOCH_3 protons. A new signal at 3.27 ppm integrating for 3H, represented the NCH_3 protons. The signal of the methoxybenzyl protons (BnOCH_3) remained at 3.73 ppm. Similar changes were seen in the aliphatic proton chemical shift region of benzimidazole derivative **63**. The structures of **62** and **63** were further confirmed with ^{13}C NMR and IR spectroscopy, as well as HRMS.

5.2.2 Grignard reactions with the Weinreb amides to produce ketones

In four separate reactions, the Weinreb amides **62** and **63** were each treated with vinylmagnesium bromide in THF to form the vinyl ketones, whereas treatment with ethynylmagnesium bromide afforded the ethynyl ketones. Unfortunately, these reactions did not proceed well, irrespective of multiple attempts at optimisation.

The syntheses were commenced with the preparation of vinyl ketone **9** (Scheme 5.8). A suspension of Weinreb amide **62** in THF was treated dropwise with vinylmagnesium bromide (1 M in THF) at 0 °C. After 2 h, the reaction was allowed to reach room temperature. The reaction was monitored by TLC—a few drops would be collected from the reaction mixture and then quenched with sat. aq. NH_4Cl and extracted into EtOAc, before spotting on the TLC plate. After stirring for 20 h, the reaction was incomplete as starting material remained. It was found that the reaction was successfully moved to completion by the addition of more vinylmagnesium bromide and nearly all starting material reacted. Apart from driving the reaction forward, an excess of Grignard reagent was once again necessary to account for interaction with additional acidic protons on the Weinreb starting material. Unfortunately, when the reaction was quenched with sat. aq. NH_4Cl, a large amount of by-product formed, which was not UV-active at 254 nm and was only visible on TLC upon staining with *p*-anisaldehyde. The ketone product must have been consumed in this side-reaction, since only 9% of ketone **9** was isolated from the reaction (entry 1, Table 5.3).

In order to ensure that the tetrahedral intermediate was successfully quenched in the work-up procedure, the reaction was repeated (entry 2, Table 5.3) and quenched with a stronger aqueous acid mixture. The reaction mixture was therefore transferred dropwise into a stirred solution of 1 M HCl at 0 °C, and was left to stir 30 minutes before completing the work-up procedure. Nonetheless, the side-reaction took place and the product (**9**) was isolated in a 17% yield.

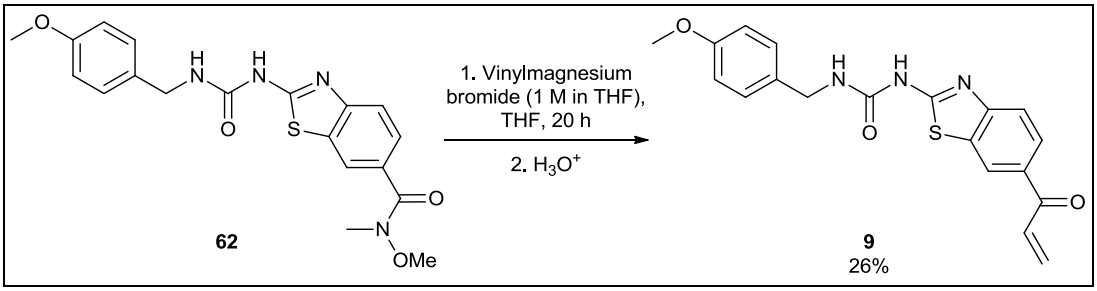

Scheme 5.8: The synthesis of vinyl ketone 9 from Weinreb amide 62

In the synthesis of ethynyl ketones, Pirc *et al.*[40] found that the nucleophilic *N,O*-dimethylhydroxylamine, which is expelled from the tetrahedral intermediate in the quenching

step, can add to the newly synthesised ethynyl ketone by Michael addition. They managed to avoid this Michael reaction, by quenching with 1 M aq. $NaHSO_4$, instead of aq. NH_4Cl. To ensure that Michael addition was not taking place as side-reaction in our reactions, 1 M aq. $NaHSO_4$ was thus used to quench the reaction. This improved the yield to 26%, but did not prevent the formation of the non-UV active by-product (entry 3, Table 5.3). In another attempt, this reaction was repeated at a lower temperature of −78 °C; however no significant differences were observed using this method (entry 4, Table 5.3).

Table 5.3: Attempts to synthesise vinyl ketone 9 from Weinreb amide 62 (Scheme 5.8)

Entry	Reagents	Temp. (°C)	Quench	% yield
1	Vinylmagnesium bromide (1 M in THF) (*6.4 equiv)*, THF	0 °C – r.t.	sat. aq. NH_4Cl, −10 °C	9
2	Vinylmagnesium bromide (1 M in THF) (*5.0 equiv)*, THF	0 °C – r.t.	1 M HCl, 0 °C	17
3	Vinylmagnesium bromide (1 M in THF) (*9.5 equiv)*, THF	−20 °C – 15 °C	1 M aq. $NaHSO_4$, 0 °C	**26**
4	Vinylmagnesium bromide (1 M in THF) (*12.0 equiv)*, THF	−78 °C – 15°C	1 M aq. $NaHSO_4$, 0 °C	23

Unfortunately, the nature of the side-reaction which hindered the formation of the product **9**, was not successfully determined in this project. The non-UV active by-product was isolated and inspected by ^{1}H NMR spectroscopy (Figure 5.3). The acquired ^{1}H NMR spectrum could not be fully deciphered, but the characteristic multiplets of two vinyl groups were visible at 5.85 – 5.74 ppm, 5.13 ppm and 4.98 ppm, and constituted a major part of the spectrum. Signals in the aromatic region of the spectrum were barely visible, which eliminated the common challenges associated with these reactions, such as diol formation (over-addition of Grignard reagent) and Michael addition to the ketone (due to OMe(Me)NH in solution).

From the ^{1}H NMR spectrum analysis was concluded that the large excess of vinylmagnesium bromide in solution may hinder the success of the reaction. In future studies, it is proposed that the equivalents of vinylmagnesium bromide are minimised, and that heating of the reaction mixture should be considered as an alternative to drive the reaction to completion.

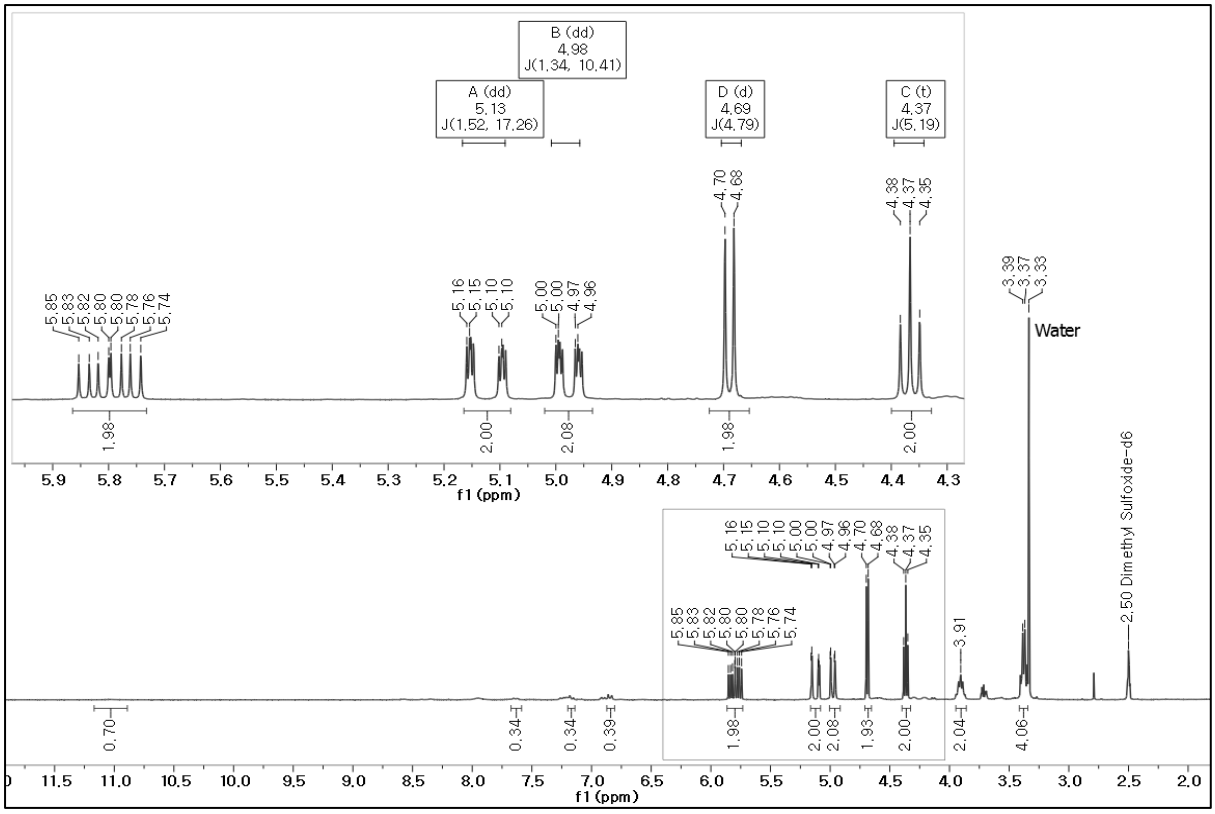

Figure 5.3: The ^{1}H NMR spectrum (DMSO-d_6) of the non-UV active by-product which forms upon quenching of the Grignard reaction with Weinreb amide 62

Using the same reaction temperatures and work-up procedure as in the highest yielding entry of Table 5.3 (entry 3), the synthesis of the vinyl and ethynyl ketones were completed. The results are summarised in Scheme 5.9.

The required equivalents of the Grignard reagent were monitored by TLC. It is of interest to note that the side-reactions in the quenching step only occurred in the reactions of the Weinreb amides with vinylmagnesium bromide, and not in the reactions with ethynylmagnesium bromide. Therefore a higher yield (76%) was observed for the ethynyl ketone **11**. The reaction to form ethynyl ketone **12** required heating overnight at 40 °C. Unfortunately, all of the starting material did not react and some by-products formed in the overnight heating process, yielding 15% of product. The ethynyl ketones were synthesised only once and their reaction- and purification procedures have not been optimised.

Although compounds **9**, **10** and **12** were obtained in very low yields, a few milligrams could be sent for biological testing, together with compound **11**.

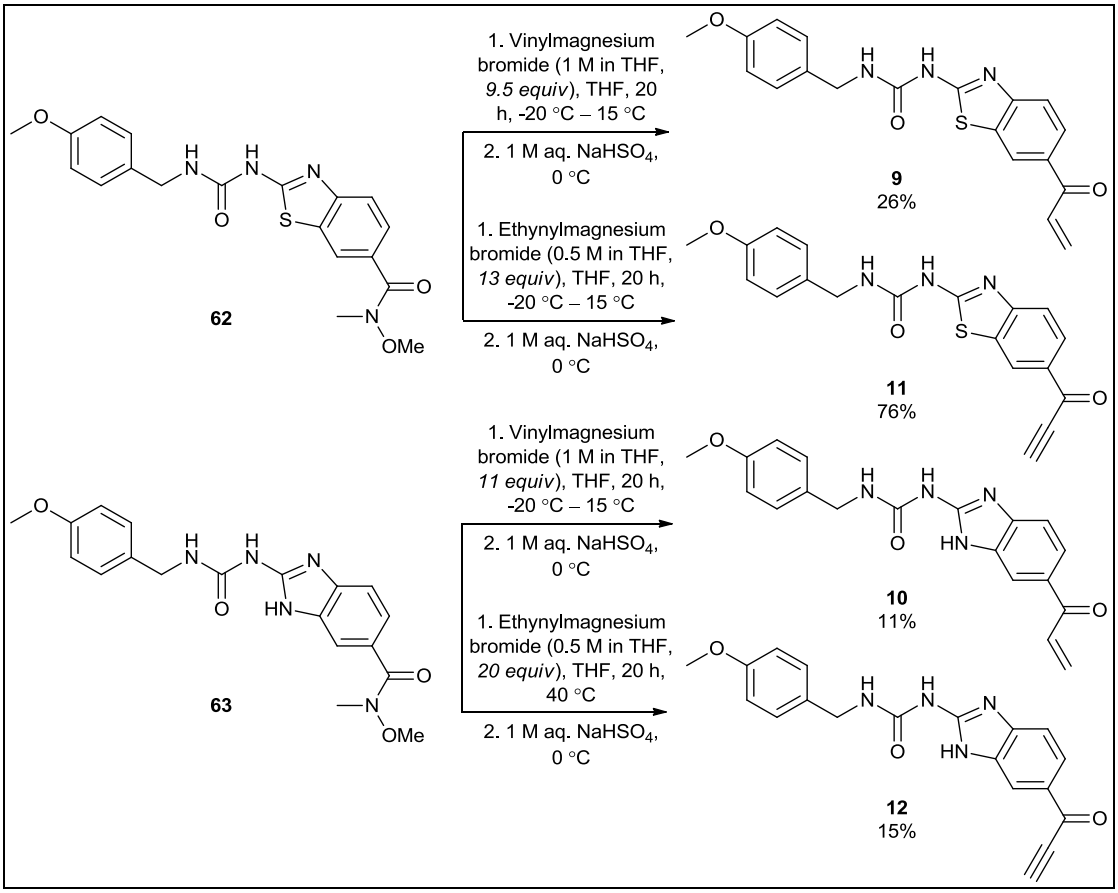

Scheme 5.9: A summary of the vinyl- and ethynyl ketone formation reactions

The structures of compounds **9** – **12** were best confirmed by ^{1}H NMR spectroscopy and HRMS. The ^{13}C NMR spectra of compounds **9**, **11** and **12** were also collected, whereas too small of an amount of compound **10** was available to acquire its ^{13}C NMR spectrum. The ^{1}H NMR spectrum of vinyl ketone **9**, clearly displayed the vinylic protons (see Figure 5.4 below). Vinylic proton H_9 resonated as a doublet of doublets at 7.50 ppm, due to the ^{3}J-coupling (16.9 Hz) to the H_{10} proton *trans* of H_9, and the ^{3}J-coupling (10.4 Hz) to the H_{10} proton *cis* of H_9. The H_{10} *trans* proton resonated at 6.36 ppm and displayed a doublet of doublets splitting pattern due to the *trans* ^{3}J-coupling with H_9 and the ^{2}J-coupling with the geminal H_{10} proton (1.7 Hz). The doublet of doublets peak of the H_{10} *cis* proton appeared at 5.96 ppm, as result of the *cis* ^{3}J-coupling with H_9 and the geminal ^{2}J-coupling. This vinylic splitting pattern was also visible in the ^{1}H NMR spectrum of the benzimidazole derivative **10**; however, the doublet of doublets due to H_9 was disguised by overlapping with the signals of $NH_{3''}$ and one benzimidazole aromatic proton.

In the ^{1}H NMR spectrum of ethynyl ketone **11**, the terminal proton of the ethynyl group resonated at 5.06 ppm as a singlet integrating for 1H. Similarly, the ethynyl proton of ketone **12** resonated as a singlet at 4.95 ppm, integrating for 1H. As mentioned and discussed before in similar cases in Section

4.5.7, Chapter 4, the signals of the benzimidazole ring protons appeared broadened in the ^{1}H NMR spectrum of **12**, most likely due to tautomerism.

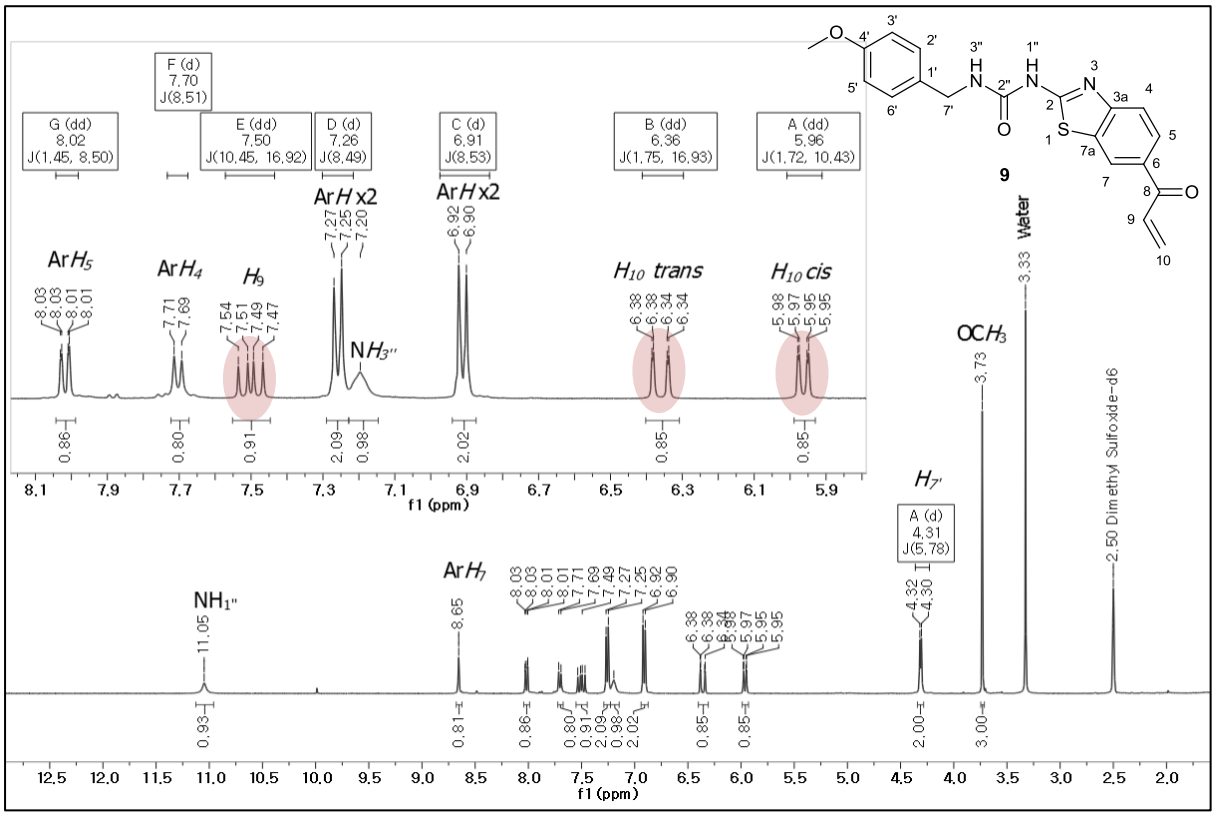

Figure 5.4: The vinylic protons are highlighted (red) in the ^{1}H NMR spectrum (DMSO-d_6) of ketone 9

In future work, there is ample opportunity for improvement in the Grignard reactions to form the vinyl- and ethynyl ketone compounds **9** – **12**. In the case where these proposed compounds display remarkable biological efficiency, the development of an efficient synthetic pathway will be necessary.

5.3 The synthesis of the acrylamides

The acrylamides were synthesised from the nitro-substituted benzazole ureas **58** and **61**. This procedure entailed two steps. In the first step the nitro-group was reduced to the amine, whereupon the amine was treated with acryloyl chloride to form the acrylamide moiety.

5.3.1 Reduction of the nitrobenzazole ureas

Nitrobenzothiazole urea **58** was utilised to develop the general reduction procedure.[41,42] Due to the polar nature of the substrate, DMF was required to dissolve the starting material, whereafter MeOH and 10% palladium on carbon were added to the mixture. Heating at 60 °C was necessary to promote the catalytic hydrogenation reaction under a hydrogen atmosphere. The aminobenzothiazole urea **64** was isolated in a 40% yield. The low yield was ascribed to a small quantity of unreacted starting

material which remained in solution, as well as minor by-products in the crude mixture which complicated the purification step. The product was easily detected on TLC, due to the product's bright yellow colour upon staining with *p*-anisaldehyde. The reduction of **58** was also attempted at 60 °C with a Fe(0) powder, NH_4Cl, dioxane, EtOH and H_2O system,[43] but this procedure produced two major products, as well as by-products. The hydrogenation procedure was thus adopted as the most efficient procedure.

The catalytic hydrogenation procedure was successfully applied to nitrobenzimidazole urea **61** to afford the aminobenzimidazole urea **65** in 85% yield. This reaction proceeded more cleanly, which accounted for the higher yield.

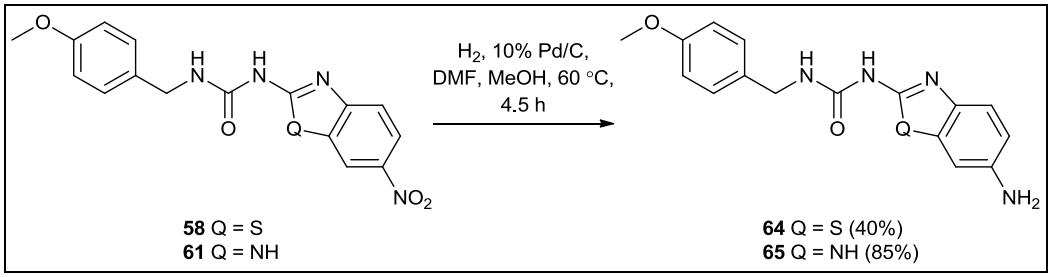

Scheme 5.10: The hydrogenation of the nitrobenzazole ureas 58 and 61

The structures of the ureas were confirmed by ^{1}H NMR, ^{13}C NMR and IR spectroscopy, as well as HRMS. In the ^{1}H NMR spectrum of 6-aminobenzothiazole urea **64**, the new amine signal was visible at 5.02 ppm, integrating for 2H. As for 6-aminobenzimidazole urea **65**, the new amine signal resonated at 5.01 – 4.32 ppm as a broadened singlet.

*5.3.1.1 The crystal structure of 1-(6-amino-1H-benzo[d]imidazol-2-yl)-3-(4-methoxybenzyl)urea (**65**)*

Throughout this project, it has been challenging to obtain the ^{13}C NMR spectra of the benzimidazole ureas. Often two to five signals were missing from the spectra or the appearance of the signals were very weak and broad. Nonetheless, the structures of the synthesised benzimidazole ureas were confirmed by ^{1}H NMR, IR, HRMS and R_f values. As final validation of these benzimidazole urea scaffolds, the crystallographic structure of 1-(6-amino-1*H*-benzo[*d*]imidazol-2-yl)-3-(4-methoxybenzyl)urea (**65**) was determined.

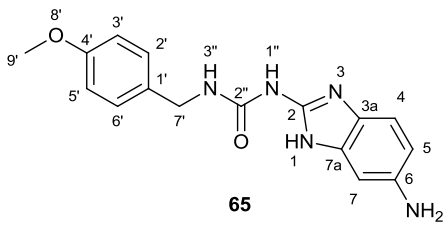

The single-crystal X-ray diffraction experiment was performed by Ms. Monica Clements in our research group. She also processed the data to solve and refine the crystal structure. The two molecules in the asymmetric unit are connected by

N-H…N hydrogen bonding, between the urea group and the nitrogen atom of the benzimidazole moiety (Figure 5.5). Intramolecular hydrogen bonding by N-H…O bonding was facilitated by the amine proton of the benzimidazole moiety and the urea carbonyl oxygen.

The primary amino group in position 6 of the benzimidazole ring is displayed without the two attached hydrogens in Figure 5.5. The location of these hydrogens could not be determined from the electron density map. The amine can rotate freely and the two hydrogens attached to the nitrogen atom can occupy different positions. This results in an averaged electron density around the nitrogen atom, and since each hydrogen atom only contributes one electron to the electron density map, the averaged electron density map did not allow for the placement of the hydrogens.

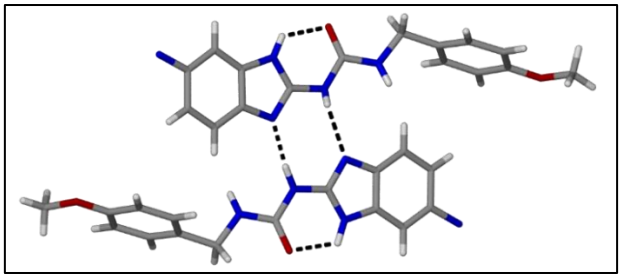

Figure 5.5: Two molecules of 65 are linked by hydrogen bonding to form the asymmetric unit of the crystal lattice. (Figure generated using POV-Ray).[44]

The dimers pack in columns to form the three-dimensional hydrogen-bonded network. The crystal packing viewed down the crystallographic *a* axis is displayed in Figure 5.6.

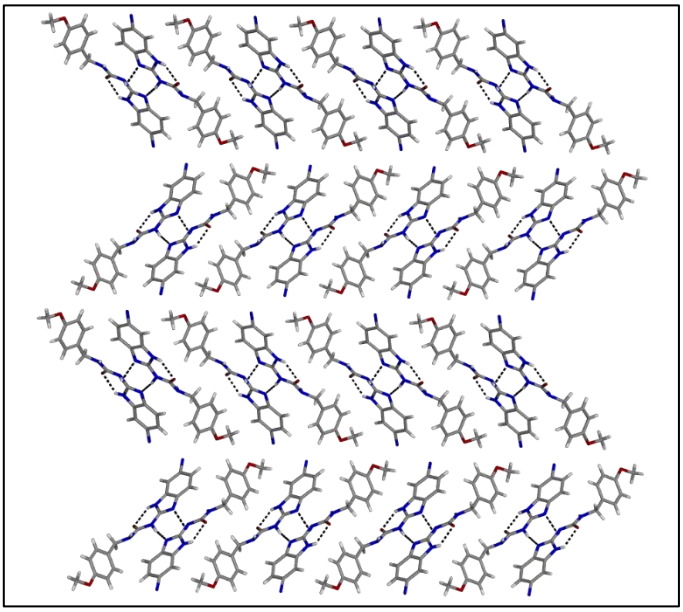

Figure 5.6: The packing of the molecules (65) viewed down the crystallographic a axis. (Figure generated using POV-Ray).[44]

The structure of compound **65** was successfully validated by crystallography and also supports the data of the rest of the benzimidazole urea range.

5.3.2 The synthesis of the acrylamides from the aminobenzazole ureas

The acrylamides were synthesised by treating the aminobenzazole urea dropwise with 1.1 equivalents of acryloyl chloride at 0 °C in a solvent mixture of DMF and THF, with 1.1 equivalents of NEt_3 base (Scheme 5.11). After work-up, **13** and **14** were obtained in yields of 54% and 40%, respectively. The reactions were not further optimised, but in future studies, it is suggested that lower temperatures are explored.

The structures of **13** and **14** were confirmed by ^{1}H NMR, ^{13}C NMR, 2D NMR and IR spectroscopy, as well as HRMS, and the compounds were sent for biological testing. The 2D NMR spectroscopic results (gHSQC and gHMBC) of benzothiazole acrylamide **13** allowed for the assignment of the signals in its ^{13}C NMR spectrum. In general, the ^{13}C NMR spectra of the benzothiazole urea range displayed similar signal patterns throughout this project, therefore the assignment of the ^{13}C NMR spectrum of **13** was insightful (Table 5.3). One quaternary carbon was not visible in the ^{13}C NMR spectrum of **13**, and from the 2D NMR results this carbon was suggested to be C_{7a}. The complete set of 2D NMR structural elucidation data is displayed in the experimental chapter (Chapter 9).

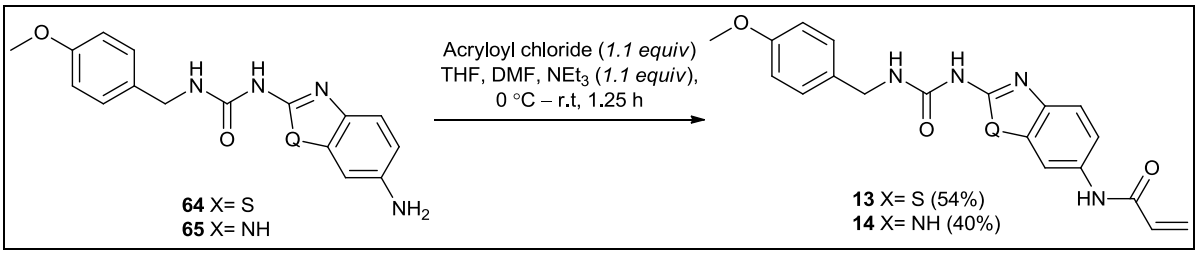

Scheme 5.11: The synthesis of acrylamides 13 and 14

Table 5.4: Assignments of the carbon signals in the ^{13}C NMR spectrum of acrylamide 13

^{13}C (δ ppm)	**Carbon assignment**
	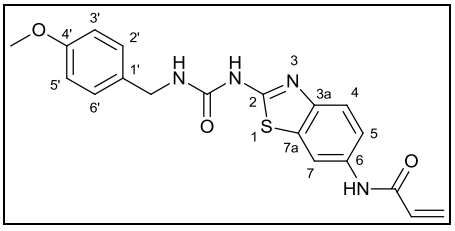
42.5	$HNCH_2$
55.1	OCH_3

111.7	Ar*C*$_7$H
113.8	Ar*C*$_{3'+5'}$H
118.3	Ar*C*$_5$H
119.6	Ar*C*$_4$H
126.7	NHCOCH*C*H$_2$
128.7	Ar*C*$_{2'+6'}$H
131.3	Ar*C*$_{1'}$
131.9	NHCO*C*HCH$_2$
134.3	Ar*C*$_6$
145.3	Ar*C*$_{3a}$
153.8	HN*C*ONH
158.4	Ar*C*$_{4'}$
159.0	ArC$_2$
163.0	NH*C*OCHCH$_2$

A 2D NMR spectral study was also performed on the benzimidazole acrylamide **14.** However, due to the missing signals in the ^{13}C NMR spectrum of the benzimidazole urea (a common occurrence), 2D NMR spectroscopy (gHSQC and gHMBC) did not allow for complete structural elucidation.

5.4 Chapter conclusion

In this chapter, 1-benzazole-3-(4-methoxybenzyl)ureas with modifiable substituents in the sixth position of their benzazole rings, were utilised to prepare the last compounds of the proposed irreversible GSK-3β inhibitor set. The halomethylketones were successfully prepared from their acetyl precursors. The benzothiazole acetyl was α-monobrominated with a PTAB/THF system, whereas the benzimidazole acetyl was α-monobrominated *via* a silyl enol ether intermediate. These methods afforded **7** and **8** in low to moderate yields. The vinyl- and the ethynyl ketones (**9 – 12**) were prepared from their ester precursors by converting the esters into their corresponding Weinreb amides in good yields and then performing Grignard reactions. The course of the Grignard reactions was troublesome, yet the vinyl- and the ethynyl ketones were synthesised in generally low yields. The acrylamide syntheses required the reduction of the 6-nitro substituents by catalytic hydrogenation, whereafter acryloyl chloride was used to finish the synthesis of **13** and **14**. These proposed GSK-3β inhibitors were sent for biological testing, which will be presented in Chapter 6.

5.5 References

1 R. H. Vekariya and H. D. Patel, *Tetrahedron*, 2014, **70**, 3949–3961.

2 X.-U. Guan, Z. Al-Misba'a and K. W. Huang, *Arab. J. Chem.*, 2015, **8**, 892–896.

3 J. C. Lee, Y. H. Bae and S.-K. Chang, *Bull. Korean Chem. Soc.*, 2003, **24**, 407–408.

4 Y. Tong, J. J. Bouska, P. A. Ellis, E. F. Johnson, J. Leverson, X. Liu, P. A. Marcotte, A. M. Olson, D. J. Osterling, M. Przytulinska, L. E. Rodriguez, Y. Shi, N. Soni, J. Stavropoulos, S. Thomas, C. K. Donawho, D. J. Frost, Y. Luo, V. L. Giranda and T. D. Penning, *J. Med. Chem.*, 2009, **52**, 6803–6813.

5 K. Tanemura, T. Suzuki, Y. Nishida, K. Satsumabayashi and T. Horaguchi, *Chem. Commun.*, 2004, 470–471.

6 R. B. Mohan and N. C. G. Reddy, *Synth. Commun.*, 2013, **43**, 2603–2614.

7 Y. J. Abul-Hajj, *J. Org. Chem.*, 1986, **51**, 3380–3382.

8 E. Vanotti, R. Amici, A. Bargiotti, J. Berthelsen, R. Bosotti, A. Ciavolella, A. Cirla, C. Cristiani, R. D. Alessio, B. Forte, A. Isacchi, K. Martina, M. Menichincheri, A. Molinari, A. Montagnoli, P. Orsini, A. Pillan, F. Roletto, A. Scolaro, M. Tibolla, B. Valsasina, M. Varasi, D. Volpi and C. Santocanale, *J. Med. Chem.*, 2008, **51**, 487–501.

9 T. Suzuki, N. Muto, M. Bando, Y. Itoh, A. Masaki, M. Ri, Y. Ota, H. Nakagawa, S. Iida, K. Shirahige and N. Miyata, *ChemMedChem*, 2014, **9**, 657–664.

10 A. Moghimi, S. Rahmani, R. Zare, M. Sadeghzadeha and S. Faraji, *Iran. J. Org. Chem.*, 2011, **3**, 707–711.

11 R. Mestres and J. Palenzuela, *Green Chem.*, 2002, **4**, 314–316.

12 L. C. King and G. K. Ostrum, *J. Org. Chem.*, 1964, **29**, 3459–3461.

13 H. Eshghi, M. Bakavoli, M. Ghasemzadeh and S. M. Seyedi, *Res. Chem. Intermed.*, 2015, **41**, 1673–1682.

14 G. K. S. Prakash, R. Ismail, J. Garcia, C. Panja, G. Rasul, T. Mathew and G. A. Olah, *Tetrahedron Lett.*, 2011, **52**, 1217–1221.

15 A. K. Macharla, R. Chozhiyath Nappunni, M. R. Marri, S. Peraka and N. Nama, *Tetrahedron Lett.*, 2012, **53**, 191–195.

16 K. Jakhar and J. K. Makrandi, *Green Chem. Lett. Rev.*, 2008, **1**, 219–221.

17 S. Kajigaeshi, T. Kakinami, T. Okamoto and S. Fujisaki, *Bull. Chem. Soc. Jpn*, 1987, 60, 1159–1160.

18 S. Visweswariah, G. Prakash, V. Bhushan and S. Chandrasekaran, *Synthesis*, 1982, **1982**, 309–310.

19 N. De Kimpe and R. Verhé, *The chemistry of α-haloketones, α-haloaldehydes and α-haloimines*,

John Wiley and Sons, Inc., Chichester, 1988.

20 R. V. Hoffman, W. S. Weiner and N. Maslouh, *J. Org. Chem.*, 2001, **66**, 5790–5795.

21 A. Marquet and J. Jacques, *Tetrahedron Lett.*, 1959, **1**, 24–26.

22 R. S. Givens, K. Stensrud, P. G. Conrad II, A. L. Yousef, C. Perera, S. N. Senadheera, D. Heger and J. Wirz, *Can. J. Chem.*, 2011, **89**, 364–384.

23 E. J. Catanzaro, T. J. Murphy, E. L. Garner and W. R. Shields, *J. Res. Natl. Bur. Stand. Phys. Chem.*, 1964, **68A**, 593–599.

24 J. Clayden, N. Greeves and S. Warren, *Organic Chemistry*, Oxford University Press, Oxford, 2nd edn., 2001.

25 K. Sun, C. Fang, W. Yang, Z. Xu, H. Wang, W. Sun, Y. Luo and Y. Xu, *J. Label. Compd. Radiopharm.*, 2016, **59**, 552–556.

26 R. H. Reuss and A. Hassner, *J. Org. Chem.*, 1974, **39**, 1785–1787.

27 J. M. Bartolomé-Nebreda, S. A. Alonso De Diego, M. Artola, F. Delgado, Ó. Delgado, M. L. Martín-Martín, C. M. Martínez-Viturro, M. Á. Pena, H. M. Tong, M. Van Gool, J. M. Alonso, A. Fontana, G. J. Macdonald, A. Megens, X. Langlois, M. Somers, G. Vanhoof and S. Conde-Ceide, *J. Med. Chem.*, 2015, **58**, 978–993.

28 S. Nahm and S. M. Weinreb, *Tetrahedron Lett.*, 1981, **22**, 3815–3818.

29 J. Singh, N. Satyamurthi and I. S. Aidhen, *J. für Prakt. Chemie*, 2000, **342**, 340–347.

30 S. Balasubramaniam and I. S. Aidhen, *Synthesis*, 2008, **2008**, 3707–3738.

31 L. L. Fellinger and L. F. Audrieth, *J. Am. Chem. Soc.*, 1938, **60**, 579–581.

32 E. T. Roe, J. T. Scanlan and D. Swern, *J. Am. Chem. Soc.*, 1949, **71**, 2215–2218.

33 A. Basha, M. Lipton and S. M. Weinreb, *Tetrahedron Lett.*, 1977, **18**, 4171–4174.

34 J. I. Levin, E. Turos and S. M. Weinreb, *Synth. Commun.*, 1982, **12**, 989–993.

35 M. Furber, M. E. Cooper and D. K. Donald, *Tetrahedron Lett.*, 1993, **34**, 1351–1354.

36 T. Shimizu, K. Osako and T. Nakata, *Tetrahedron Lett.*, 1997, **38**, 2685–2688.

37 J. M. Williams, R. B. Jobson, N. Yasuda, G. Marchesini, U. H. Dolling and E. J. J. Grabowski, *Tetrahedron Lett.*, 1995, **36**, 5461–5464.

38 T. Suto, Y. Yanagita, Y. Nagashima, S. Takikawa, Y. Kurosu, N. Matsuo, T. Sato and N. Chida, *J. Am. Chem. Soc.*, 2017, **139**, 2952–2955.

39 H.-S. Lin and L. A. Paquette, *Synth. Commun.*, 1994, **24**, 2503–2506.

40 S. Pirc, D. Bevk, A. Golobič, B. Stanovnik and J. Svete, *Helv. Chim. Acta*, 2006, **89**, 30–44.

41 H. Ma, C. Zhuang, X. Xu, J. Li, J. Wang, X. Min, W. Zhang, H. Zhang and Z. Miao, *Eur. J. Med. Chem.*, 2017, **133**, 174–183.

42 4SC AG, US2006142570 (A1), 2006.

43 K. Ramadas and N. Srinivasan, *Synth. Commun.*, 1992, **22**, 3189–3195.

44 *POV-RayTM for Windows*, version 3.6, Persistence of Vision Raytracer Pty. Ltd, Williamstown, Australia, 2004.

Chapter 6: Biological activity and reversibility studies

Upon completion of the synthesis of the proposed GSK-3β inhibitors (Chapters 4 and 5), the library of compounds was sent for biological evaluation to our collaborator, Prof. Ana Martínez at the Instituto de Química Medica-CSIC in Madrid, Spain. All of the synthesised compounds that were sent for biological testing, had a purity greater or equal to 95%, except for the benzothiazole-derived acrylamide **13**, which was 94% pure. To determine purity, analyses were performed on a UPLC-MS system, fitted with a C18 column (1.7 µm, 100 mm × 2.1 mm), photodiode array detector and a QTOF spectrometer.

The initial biological studies entailed the measurement of GSK-3β inhibitory activity. The compounds with the lowest IC_{50} values were then further subjected to GSK-3β reversibility studies to determine the type of enzymatic inhibition (reversible vs. irreversible). Finally, the biological results were compared to the predictive modelling studies which were performed in this project (Chapter 3).

6.1 Structure-activity relationships

Table 6.1 summarises the GSK-3β inhibitory activity results of the reference compound, AR-A014418 (**3**), and the final library of synthesised small-molecules. High inhibitory activity is highlighted in red in the table.

Table 6.1: The GSK-3β inhibitory activity (IC_{50}) of the library of synthesised compounds.

	Compound	IC_{50} (µM)	SD	Compound	IC_{50} (µM)	SD
Reference: AR-A014418	**3**	0.072	0.043			
Ring substituent	**Benzothiazoles**			**Benzimidazoles**		
Nitrile	**4**	0.11	0.04	**6**	**0.086**	0.023
Acetyl	**56**	2.26	0.41	**59**	0.26	0.03
HMK	**7**	0.77	0.04	**8**	0.13	0.06
Vinyl ketone	**9**	4.05	0.39	**10**	1.82	0.22
Ethynyl ketone	**11**	4.21	0.33	**12**	2.47	0.32
Acrylamide	**13**	>10		**14**	>10	

IC_{50}: The concentration of a substance that causes 50% inhibition of a given system[1]

SD: Standard deviation

High inhibitory activity is highlighted in red

In comparison to the reference compound (**3**), which displayed an IC_{50} value of 0.072 ± 0.043 µM in the assay, a good inhibitory activity score was observed for 1-(6-cyano-1*H*-benzo[*d*]imidazol-2-yl)-3-(4-methoxybenzyl)urea (**6**) with an IC_{50} value of 0.086 ± 0.023 µM, which was also the best IC_{50} value obtained in the library. The benzothiazole equivalent, nitrile **4**, also displayed good inhibitory activity (IC_{50} = 0.11 ± 0.04 µM), but it should be noted that **4** has been synthesised in the literature before, and was one of the compounds that inspired our small-molecule library.[2]

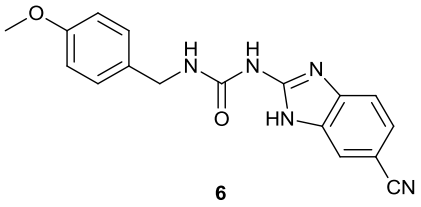

6

The results of Table 6.1 are further illustrated in Figure 6.1, to ease comparison. As already mentioned, the nitrile derivatives (**4**, **6**) displayed the best inhibitory activity. Furthermore, the HMK derivatives (bromoacetyl electrophilic warheads) displayed good inhibitory concentrations, with 1-[6-(2-bromoacetyl)-1*H*-benzo[*d*]imidazol-2-yl]-3-(4-methoxybenzyl)urea (**8**) having an IC_{50} value of 0.13 ± 0.06 µM. The benzothiazole-derivative **7** showed lower activity with an IC_{50} of 0.77 ± 0.04 µM. In fact, over the whole range of biological results (Figure 6.1), a clear trend existed in which the benzimidazole equivalents always displayed better inhibitory activity than the benzothiazole equivalents, within each electrophilic moiety group.

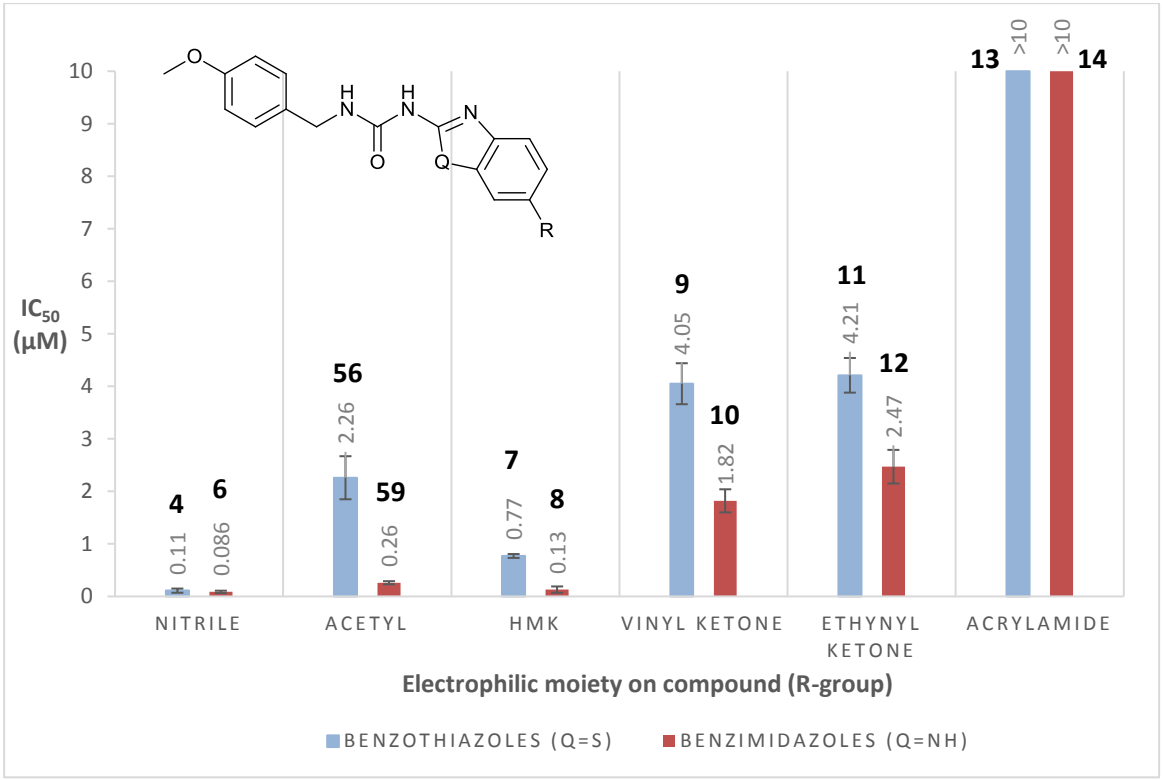

Figure 6.1: The variation in GSK-3β inhibitory activity (IC_{50}) over different electrophilic moieties in the benzothiazole- and benzimidazole urea compound sets.

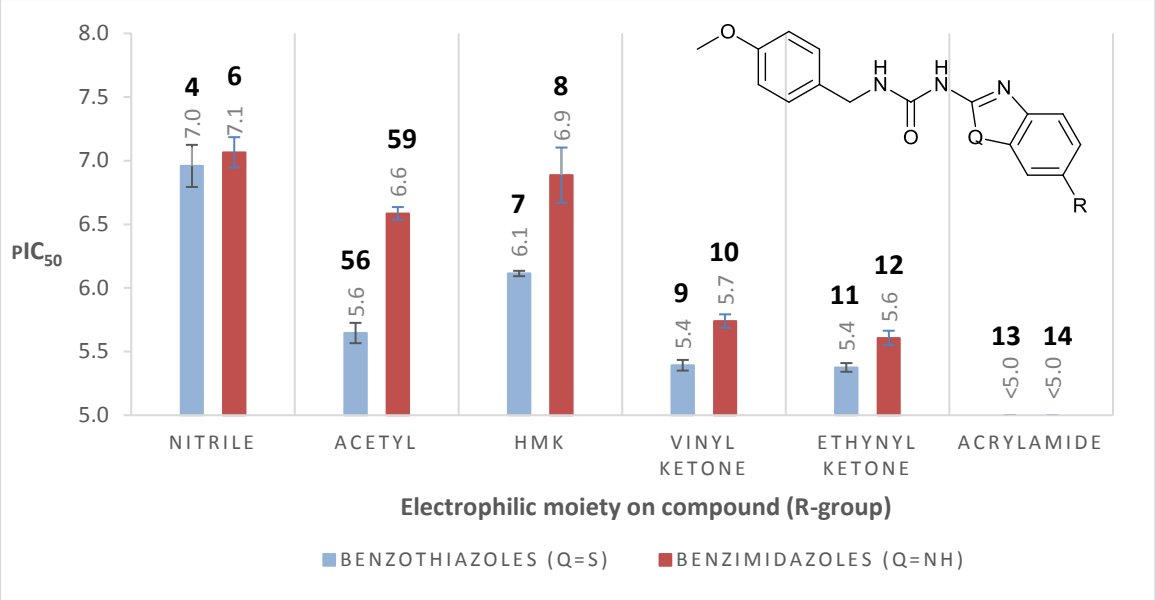

Figure 6.2: A comparison of pIC_{50} values over different electrophilic moieties in the benzothiazole- and benzimidazole urea compound sets (pIC_{50} = –log [IC_{50}])

To further compare the activities of the different electrophilic warhead groups, the pIC_{50} values of the compounds were calculated (Figure 6.2). pIC_{50} is the negative logarithmic value of the IC_{50} value (in molar concentration). Thus, a larger pIC_{50} value illustrates higher inhibitory activity.

The activity of bromoacetyl-derivative **7** (HMK) was higher in comparison to the acetyl-derivative **56**, which suggested the bromine atom to have a structure-activity influence in HMKs which can increase inhibitory activity. The same structure-activity influence may apply for bromoacetyl-derivative **8** (HMK) when compared to the benzimidazole-derived acetyl **59**, but in our data these two compounds displayed similar activities within error (standard deviation).

As further depicted in Figure 6.2, the inhibitory activities of the vinyl ketones (**9**, **10**) and the ethynyl ketones (**11**, **12**) were lower and in a pIC_{50} range of 5.3 – 5.8 (IC_{50} = 1.60 – 4.54 µM). The acrylamides did not show any significant inhibitory activity, with pIC_{50} values smaller than 5.0 (IC_{50} >10 µM). The larger size of the acrylamide warheads might complicate the entrance and positioning of the molecule in the ATP-binding site, and might no longer facilitate the binding of the electrophilic moiety in the deepest end of the GSK-3β ATP-binding pocket.

In general, large variations in GSK-3β inhibitory activity were observed across the different electrophilic warhead groups. These variations necessitated reversibility studies to evaluate whether the electrophilic warheads were reacting with Cys199 through an irreversible binding mechanism. Furthermore, compounds with smaller electrophilic moieties displayed better inhibitory activity,

which suggests that the size of electrophilic moieties might be a factor of consideration in the design of Cys199-targeted irreversible inhibitors for GSK-3β.

6.2 Reversibility studies

The reversibility studies entailed GSK-3β time-dependent studies, in which inhibition percentage was measured after different pre-incubation (GSK-3β enzyme + inhibitor) times. For irreversible inhibitors, a longer pre-incubation time with the enzyme is expected to increase the percentage of enzyme inhibition observed. Reversible inhibitors are not expected to increase the percentage of enzyme inhibition when longer pre-incubation times are applied. In the literature, these reversibility studies were applied by Martínez and co-workers[3] to evaluate whether their GSK-3β inhibitors act through reversible or irreversible inhibition.

Due to restricted funds, only the reference ligand (**3**) and two of the biologically potent, novel GSK-3 inhibitors, cyano-substituted benzimidazole urea **6** and HMK-substituted benzimidazole urea **8**, were subjected to reversibility studies. Results are displayed in Figure 6.3.

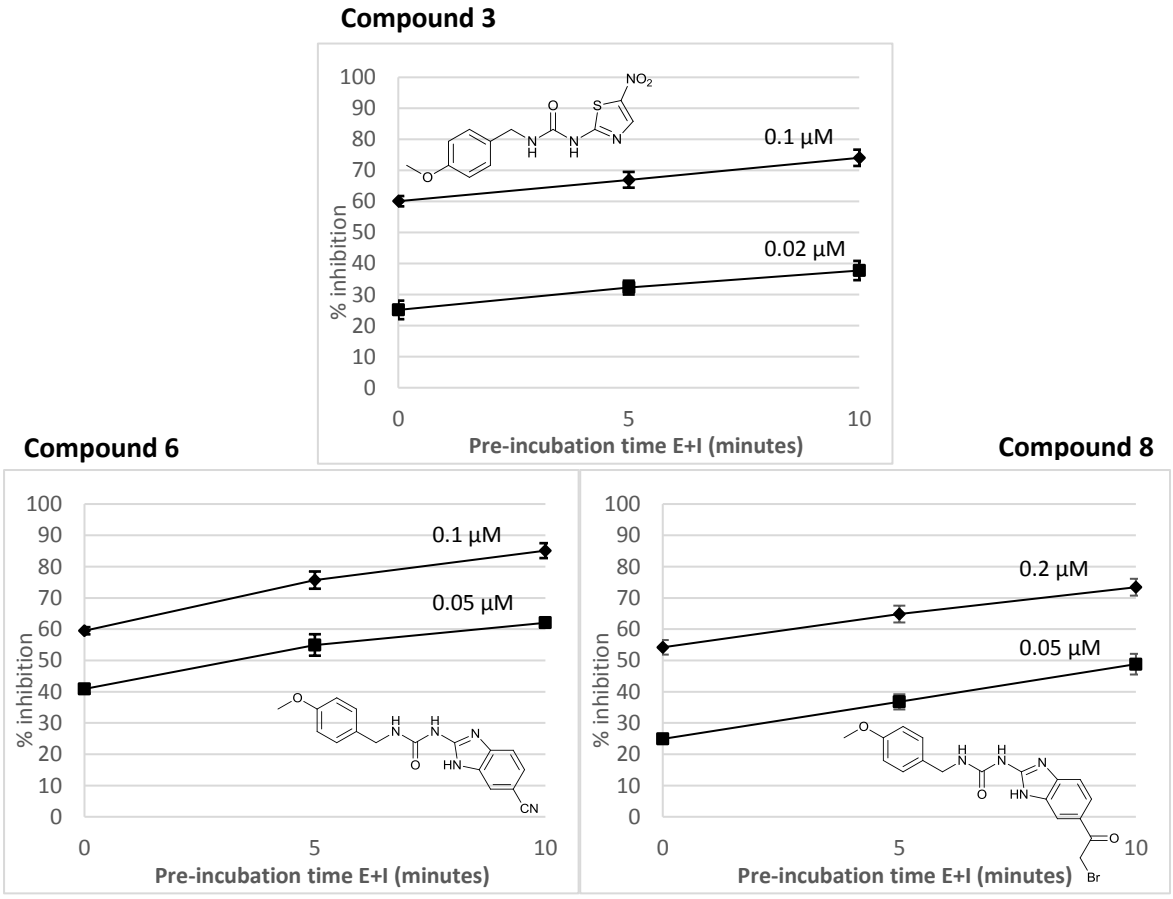

Figure 6.3: GSK-3β time-dependent studies with reference inhibitor, 3, and the newly synthesised GSK-3β inhibitors, 6 and 8. Inhibitory activity was monitored relative to pre-incubation time.

The results of newly synthesised GSK-3β inhibitors, **6** and **8**, appeared to indicate an irreversible binding mode with GSK-3β, facilitated by their electrophilic warheads. The increase in inhibition percentage with longer pre-incubation times, corresponded with the expected behaviour of an irreversible inhibitor. However, the result of the reference compound **3**, was not as expected, and therefore, in our opinion, the reversibility results are inconclusive.

The reference compound, AR-A014418 (**3**), is a well-known reversible GSK-3β inhibitor, as confirmed by X-ray crystallography. For a reversible binding mode, percentage GSK-3 inhibition is not expected to increase with longer pre-incubation times. The opposite was seen for **3** in Figure 6.3, and therefore the binding modes of the newly synthesised GSK-3 inhibitors are still unconfirmed.

In future studies, the reversibility studies should be repeated, and the reversible GSK-3 inhibitor, alsterpaullone, which is the reference compound in the studies of Martínez and co-workers, should be included.[3] It will also be of help to include the acetyl-substituted benzimidazole urea **59**, to compare its binding mode with HMK-substituted benzimidazole urea **8**. Additionally, covalent irreversible binding can be confirmed biophysically by MALDI-TOF MS analysis.[4] If the inhibitor binds the GSK-3 enzyme irreversibly, a mass peak corresponding to the combined mass of the enzyme and the inhibitor should be present in the mass spectrum.[3]

6.3 A comparison: Molecular modelling scores and activity

To evaluate the molecular modelling binding model which was used in Chapter 3, the biological activity results of the compound library were compared to the calculated irreversible and reversible docking scores recorded in the modelling study.

The increased biological inhibitory activity of the benzimidazole-derivatives relative to the benzothiazole-derivatives was successfully predicted in the molecular modelling studies and was ascribed to the ability of the imidazole ring system to accommodate one additional hydrogen bond to the hinge region. This can be seen in Figure 6.4 (a, b), in which the benzimidazoles continuously displayed lower affinity/docking scores, which implied more favourable binding interactions.

In Figure 6.4 it becomes clear that small differences in affinity scores (irreversible modelling) or docking scores (reversible modelling) did not correlate directly to increased or decreased IC_{50} values, i.e. there is no trend. However, in terms of the larger picture, all of the docked molecules displayed good affinity/docking scores (between −9.5 and −7.0 kcal/mol) which successfully predicted that these molecules have inhibitory ability, except for the acrylamides which did not display inhibitory activity.

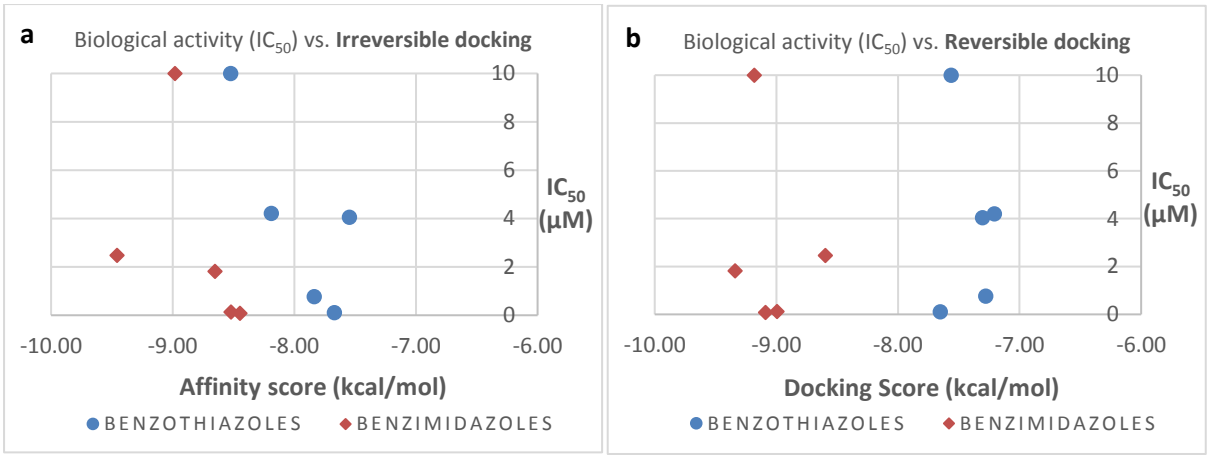

Figure 6.4: Molecular modelling affinity scores (irreversible docking) and docking scores (reversible docking) vs. actual biological inhibitory concentrations (IC_{50}).

A good correlation was observed when the Cys199 target distance (distance from the reactive atom of the electrophilic moiety to the sulfur atom of Cys199) obtained in the reversible docking stage was compared to the biological inhibitory activity (Figure 6.5). Compounds with a smaller Cys199 target distance displayed lower IC_{50} values, indicating higher inhibitory activity.

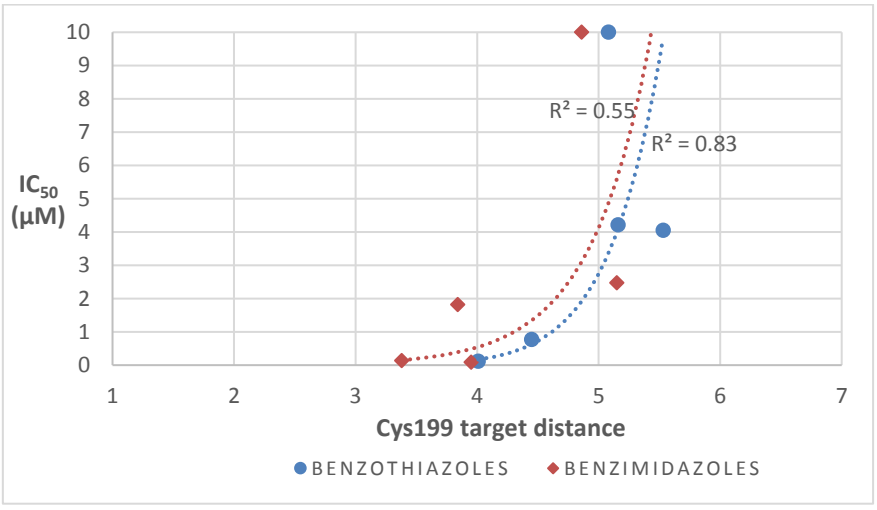

Figure 6.5: A comparison of the Cys199 target distance in the reversible docking stage with biological activity (IC_{50})

It can be concluded that the molecular docking model was sufficient to predict whether proposed compounds would have favourable binding interactions in the GSK-3β ATP-binding site, and to investigate possible binding modes. The model successfully predicted that the benzimidazole-derived ureas would display higher inhibitory activity than the benzothiazoles, and furthermore a direct correlation was visible between Cys199 target distance and inhibitory activity in the reversible docking stage.

6.4 Concluding remarks

To conclude, the GSK-3β inhibitory activity results were satisfying, with the nitrile derivatives (**4**, **6**) and the benzimidazole HMK derivative (**8**) displaying the best IC_{50} values. In comparison to the reference compound (**3**), which displayed an IC_{50} value of 0.072 ± 0.043 µM in our assay, the best IC_{50} value obtained in the library was 0.086 ± 0.023 µM, observed for 1-(6-cyano-1*H*-benzo[*d*]imidazol-2-yl)-3-(4-methoxybenzyl)urea (**6**). Over the whole range of biological results, the benzimidazole derivatives always displayed better inhibitory activity than their benzothiazole counterparts.

Reversibility studies were inconclusive, since the result of reference inhibitor **3** was not as expected in the pre-incubation time vs. inhibition percentage studies.

The molecular docking model was evaluated and was found sufficient to predict whether proposed compounds would display GSK-3β inhibitory activity, except in the case of the acrylamides. The model successfully predicted that the benzimidazole-derived ureas would display higher inhibitory activity than their benzothiazole counterparts. It is further suggested that Cys199 target distance and the size of the electrophilic moieties might influence inhibitory activity.

6.5 References

1 J. H. Duffus, *Pure Appl. Chem.*, 1993, **65**, 2003–2122.

2 F. Lo Monte, T. Kramer, A. Boländer, B. Plotkin, H. Eldar-Finkelman, A. Fuertes, J. Dominguez and B. Schmidt, *Bioorg. Med. Chem. Lett.*, 2011, **21**, 5610–5615.

3 D. I. Perez, V. Palomo, C. Pérez, C. Gil, P. D. Dans, F. J. Luque, S. Conde and A. Martínez, *J. Med. Chem.*, 2011, **54**, 4042–4056.

4 A. P. Kafka, T. Kleffmann, T. Rades and A. McDowell, *Int. J. Pharm.*, 2011, **417**, 70–82.

Chapter 7: Conclusion

The aim of this project was to design, synthesise, characterise and biologically test a proposed library of irreversible GSK-3 inhibitors as potential Alzheimer's drug candidates. Due to the multifactorial role of GSK-3 in AD pathogenesis, GSK-3 is a promising CNS target.

Our library included two sets of 1-aryl-3-(4-methoxybenzyl)ureas, wherein the incorporated aryl group was a benzimidazole or benzothiazole scaffold, respectively. These molecules contained different electrophilic warheads, with the potential to form a covalent, irreversible bond with nucleophilic Cys199 in the GSK-3 ATP binding pocket. The unique Cys199 residue was targeted covalently, with the hope of improving GSK-3 selectivity.

In the molecular modelling studies, the modelled binding interactions, Cys199 target distances and docking scores in both the non-covalent and covalent docking stages were very promising for the proposed 1-aryl-3-(4-methoxybenzyl)urea series. Thus, the final compound library for synthesis included the nitrile, HMK, vinyl- and ethynyl ketone and acrylamide electrophilic warheads.

The synthetic route commenced with the synthesis of the 6-substituted 2-aminobenzothiazole and 6-substituted 2-aminobenzimidazole scaffolds in good yields. The 6-substituted 2-aminobenzothiazoles (**20** – **23**) were synthesised from *para*-substituted anilines in a KSCN/AcOH/PTAB system, in which the first step entailed thiocyanation and the second step, cyclisation, when heated under reflux. The 6-substituted 2-aminobenzimidazoles (**39** – **42**) were synthesised from *para*-substituted anilines in a five-step procedure, in which the last step entailed cyclisation of the diamine using cyanogen bromide.

The urea formation step entailed a CDI-mediated coupling and could be applied to both the benzothiazole and the benzimidazole scaffolds. CDI was reacted with the ammonium hydrochloride salt of 4-methoxybenzylamine, to form the electrophile, *N*-(4-methoxybenzyl) carbamoylimidazole (**46**). Carbamoylimidazole **46** was reacted with the 6-substituted 2-aminobenzothiazoles (**20** – **23**) in a NaH/DMF system to afford the 1-(6-substituted benzothiazol-2-yl)-3-(4-methoxybenzyl)ureas (**4**, **56** – **58**) in high to quantitative yields. The similar synthesis of the 1-(6-substituted benzimidazol-2-yl)-3-(4-methoxybenzyl)ureas (**6**, **59** – **61**) proved more challenging and afforded moderate yields.

Ureas **56** – **58** and **59** – **61** were synthesised with modifiable substituents in the sixth position of their benzazole rings, which were further utilised to incorporate electrophilic warheads onto the compounds. Halomethylketones **7** and **8** were successfully prepared from their acetyl precursors, in low to moderate yields. The benzothiazole derivative required α-monobromination with a PTAB/THF

system, whereas the benzimidazole derivative was successfully α-monobrominated *via* a silyl enol ether intermediate. The vinyl- and the ethynyl ketones (**9** – **12**) were prepared from their ester precursors, which were converted into Weinreb amides in good yields and then reacted with Grignard reagents in low yields. Acrylamides **13** and **14** were synthesised in low to moderate yields by reduction of their 6-nitro precursors, and subsequent treatment of the amines with acryloyl chloride.

The biological GSK-3β inhibitory results were satisfactory, except in the case of the acrylamides. The nitrile derivatives (**4**, **6**) and the benzimidazole HMK derivative (**8**) displayed high inhibitory activity. The best IC_{50} value in the library was 0.086 ± 0.023 µM, observed for 1-(6-cyano-1*H*-benzo[*d*]imidazol-2-yl)-3-(4-methoxybenzyl)urea (**6**), and is excellent in comparison to the reference compound (**3**), with an IC_{50} value of 0.072 ± 0.043 µM in our assay. The benzimidazole derivatives were generally better inhibitors than their benzothiazole equivalents, supposedly due to their ability to form one additional hydrogen bond with the hinge region of the GSK-3β ATP pocket. Structure-activity studies further proposed that Cys199 target distance and electrophilic warhead size might influence inhibitory activity. Unfortunately, the binding mode of the GSK-3 inhibitors (reversible vs. irreversible) could not be confirmed in this study.

Highly active GSK-3β inhibitors, nitrile **6** and HMK **8**, were successfully developed and may potentially contribute to the AD drug development pipeline as disease-modifying therapeutics (DMTs). The AD drug pipeline is in an urgent need of DMTs which will target the underlying mechanisms of the disease.

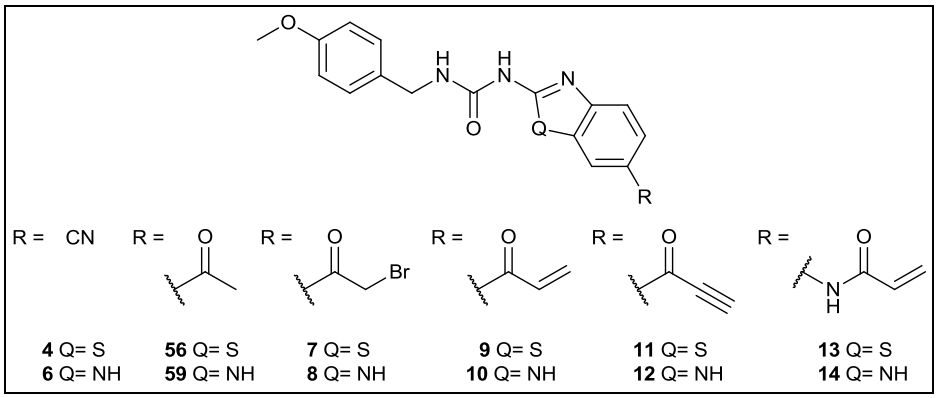

Figure 7.1: The final library of compounds which was sent for GSK-3β biological testing

Chapter 8: Future work

8.1 Future work: Chemistry

8.1.1 CDI-coupling with the 2-aminobenzimidazoles

In Chapter 4, the CDI-mediated urea formation step with the 2-aminobenzothiazoles and the 2-aminobenzimidazoles were discussed, respectively. When the 2-aminobenzothiazoles were reacted with carbamoylimidazole **46**, excellent yields were obtained. However, when the 2-aminobenzimidazoles were reacted with **46**, starting material remained in solution, which lowered the reaction yields. It was suggested that this might be due to 2-aminobenzimidazole's weaker nucleophilic nature, due to the involvement of the primary amine's electrons in tautomerism with the imidazole ring.

An increase in the electrophilicity of carbamoylimidazole **46** could be explored as an alternative to drive the reactions with the 2-aminobenzimidazoles to completion.[1] Methylation of the distal nitrogen in the imidazole ring of carbamoylimidazole **46** will form the resonance-stabilised carbamoylimidazolium salt **72** (Figure 8.1). Thus, compound **72** is activated at the carbonyl carbon centre and more susceptible to nucleophilic attack by 2-aminobenzimidazole (**39** – **42**).

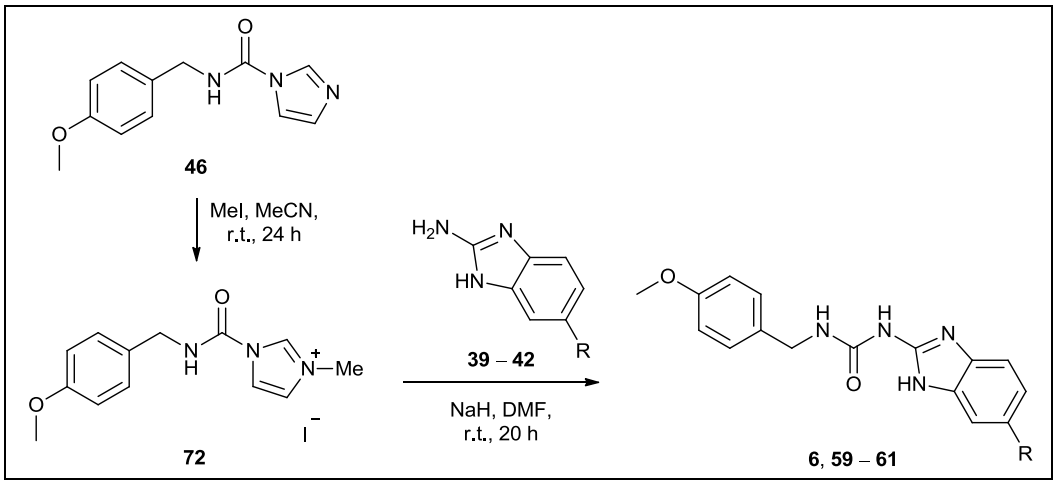

Figure 8.1: The proposed activation of carbamoylimidazole 46 with MeI, before the N-(4-methoxybenzyl)-N'-(6-substituted benzimidazolyl)ureas (6, 59 – 61) are synthesised.

8.1.2 α-Bromination *via* the silyl enol ether

In Chapter 5, 1-(6-acetyl-1*H*-benzo[*d*]imidazol-2-yl)-3-(4-methoxybenzyl)urea (**59**) was successfully α-brominated *via* a silyl enol ether intermediate, in order to obtain regioselectivity and to prevent over-bromination. In the synthesis, the first step involved the generation of the silyl enol ether from

the acetyl with TMSOTf and DIPEA at 0 °C. This reaction was found to be incomplete, even after increasing the reaction temperature to 30 °C and increasing the reagent equivalents (TMSOTf, 7.8 equiv, DIPEA, 10.4 equiv). TMSOTf is a powerful silylating agent which is usually used in stoichiometric quantities, and therefore a large excess of TMSOTf should not be necessary.[2,3] In future studies, a stronger base should be considered, to drive the enolization reaction forward. 1,8-Diazabicyclo[5.4.0]undec-7-ene (DBU, pK_a [BH^+]= 12.0) is a slightly stronger base than DIPEA (pK_a [BH^+] = 10.5) and might be worth exploring.[2,4] Otherwise, strong bases such as lithium diisopropyl amide (LDA) and lithium hexamethyldisilazide (LiHMDS) can be investigated. In the presence of a strong base, the acetyl will be deprotonated first to generate a highly reactive enolate, which is then trapped by a trimethylsilyl group. A powerful silylating reagent such as TMSOTf is no longer necessary and therefore trimethylsilyl chloride (TMSCl) can also be used as silylating reagent. The combination of strong bases with TMSCl is more common in the literature.[5]

8.1.3 Improving the Grignard reactions

In Chapter 5, the Weinreb amides **62** (81% yield) and **63** (78% yield) were successfully synthesised from their ester precursors. Next, the Weinreb amides were utilised in Grignard reactions to form the vinyl- and ethynyl ketones **9** – **12**. Unfortunately, these reactions did not proceed well, irrespective of optimisation attempts, and the yields of the products were very low. These Grignard reactions can be improved in future work. However, it should be noted that the vinyl- and ethynyl ketones **9** – **12** displayed low GSK-3β inhibitory activity in the biological studies, with IC_{50} values in the range of 1.60 – 4.54 µM. Thus, the vinyl- and ethynyl ketones **9** – **12** and their synthetic pathways will not be developed any further. However, from a chemistry perspective, it may be of value to improve these Grignard reactions.

The Grignard reactions required a large excess of the organomagnesium reagent to reach completion and it was suggested that these large quantities could have hindered the success of the reaction. It is therefore proposed that optimisation of the amount of organomagnesium reagent and higher reaction temperatures are explored as an alternative to drive reactions to completion. Nahm and Weinreb[6] applied temperatures of up to 65 °C in their Grignard reactions with Weinreb amides. Organolithiums can also be investigated as alternative, more reactive, organometallic reagents.

In the case of the vinyl ketones, a major by-product was formed during the quenching step, but the nature of the side-reaction could not be determined. The tetrahedral intermediate/product appears to be very sensitive to the quenching step, and alternative quenching solutions (e.g. 5% HCl in ethanol)[6] or quenching procedures can be considered. To apply very mild quenching conditions, one

might consider diluting the reaction mixture with EtOAc first. Then, immediately after adding 1 M aq. $NaHSO_4$ (quenching agent), the product will be able to partition into the organic layer.

8.2 Future work: Biological studies and exploration

8.2.1 Investigation of the binding mode: Irreversible vs. Reversible

The most important future work, in order to conclude the outcomes of this project, is to investigate the binding mode of the newly synthesised GSK-3β inhibitors in the GSK-3β ATP binding pocket. It is important to determine whether the proposed electrophilic warheads are targeting the Cys199 residue through an irreversible binding reaction.

The reversibility study results were deemed inconclusive, since the results of our reference compound, AR-A014418 (**3**), were not as expected. There was no significant difference in efficacy in the time period of the experiment between the non-covalent reference and the new compounds with the electrophilic warhead. In future studies, the reversibility studies should be repeated, and the reversible GSK-3 inhibitor, alsterpaullone, which was used as reference compound in the reversibility studies of Martínez and co-workers, should also be included.[7] Furthermore, covalent irreversible binding should be confirmed with MALDI-TOF MS analysis.[8] If the inhibitor binds the enzyme irreversibly, a combined mass peak will be present in the MS spectrum.

8.2.2 Investigation of alternative electrophilic warheads

In the biological activity results, the compounds with smaller electrophilic warheads displayed better IC_{50} values. As seen from the molecular modelling studies, the ligands are positioned with the electrophilic moiety in the deepest end of the GSK-3β ATP pocket. Therefore, larger electrophilic moieties may push the ligand out of the binding pocket, or compromise the entrance and positioning of the ligand in the pocket. In future studies, alternative small electrophilic warheads can be investigated, for example, sulfonyl fluorides and vinyl sulfones (Figure 8.2). Sulfonyl fluorides are privileged electrophilic warheads, which can covalently modify various reactive residues, including cysteine residues.[9] The potential of vinyl sulfones to mediate irreversible inhibition has also been

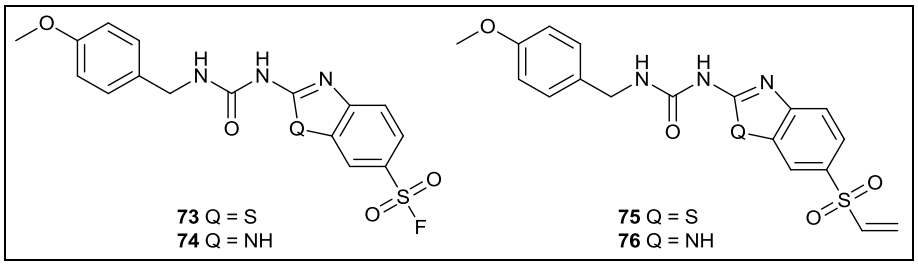

Figure 8.2: Alternative electrophilic moieties which can be explored

recorded in the literature.[10–12]

8.2.3 Investigation of alternative core structures

In this project, the inhibitors with benzimidazole core-structures displayed better docking scores and higher inhibitory activities than their benzothiazole counterparts. Therefore, the effect of other core-structures could be investigated in future studies. The benzoxazole core-structure (**77**) is the most obvious bioisostere to investigate (Figure 8.3). Smaller core-structures, such as imidazole (**78**) or triazole (**79**) are proposed to maintain the essential binding interactions with the GSK-3β hinge region, but additionally, these smaller structures may provide space for larger electrophilic warheads.

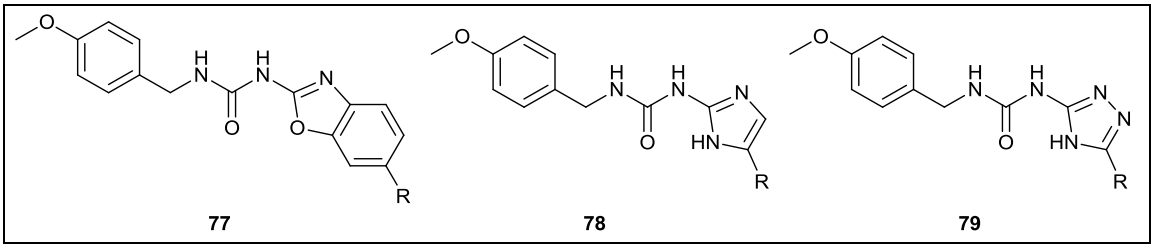

Figure 8.3: Possible core-structures modifications that can be investigated

It is important that compounds with new core-structures and electrophilic warheads are re-modelled in the GSK-3β ATP binding site, in order to investigate their feasibility, understand any potential binding interactions and to model the expected Cys199 target distances.

8.3 References

1 J. A. Grzyb, M. Shen, C. Yoshina-Ishii, W. Chi, R. S. Brown and R. A. Batey, *Tetrahedron*, 2005, **61**, 7153–7175.

2 R. Noyori, S. Murata and M. Suzuki, *Tetrahedron*, 1981, **37**, 3899–3910.

3 P. G. Gassman and S. J. Burns, *J. Org. Chem.*, 1988, **53**, 5574–5576.

4 C. Wiles and P. Watts, *Beilstein J. Org. Chem.*, 2011, **7**, 1360–1371.

5 H. O. House, L. J. Czuba, M. Gall and H. D. Olmstead, *J. Org. Chem.*, 1969, **34**, 2324–2336.

6 S. Nahm and S. M. Weinreb, *Tetrahedron Lett.*, 1981, **22**, 3815–3818.

7 D. I. Perez, V. Palomo, C. Pérez, C. Gil, P. D. Dans, F. J. Luque, S. Conde and A. Martínez, *J. Med. Chem.*, 2011, **54**, 4042–4056.

8 A. P. Kafka, T. Kleffmann, T. Rades and A. McDowell, *Int. J. Pharm.*, 2011, **417**, 70–82.

9 A. Narayanan and L. H. Jones, *Chem. Sci.*, 2015, **6**, 2650–2659.

10 E. Anscombe, E. Meschini, R. Mora-Vidal, M. P. Martin, D. Staunton, M. Geitmann, U. H.

Danielson, W. A. Stanley, L. Z. Wang, T. Reuillon, B. T. Golding, C. Cano, D. R. Newell, M. E. M. Noble, S. R. Wedge, J. A. Endicott and R. J. Griffin, *Chem. Biol.*, 2015, **22**, 1159–1164.

11 R. Vicik, M. Busemann, K. Baumann and T. Schirmeister, *Curr. Top. Med. Chem.*, 2006, **6**, 331–353.

12 W. R. Roush, S. L. Gwaltney, J. Cheng, K. A. Scheidt, J. H. McKerrow and E. Hansell, *J. Am. Chem. Soc.*, 1998, **120**, 10994–10995.

Chapter 9: Experimental Section

9.1 General practices

All reactions were performed in a fume hood. Unless carried out in water or if otherwise noted, all reactions were performed under a positive pressure of 5.0-grade nitrogen. Glassware was oven-dried (120 °C) and purged with nitrogen. Reagents were obtained from Sigma-Aldrich or Merck and were used without further purification, unless otherwise stated. Bulk solvents for chromatographic purposes were distilled by general distillation. Tetrahydrofuran was freshly distilled from sodium wire and benzophenone under nitrogen. Methanol and ethanol were freshly distilled from magnesium turnings and iodine. Dichloromethane was distilled from calcium hydride under nitrogen. Dimethylformamide was stirred over calcium hydride and filtered, whereafter it was distilled under nitrogen and stored over molecular sieves (4 Å). Any other reagents that required purification were purified according to standard protocol.[1]

9.1.1 Chromatography

Thin layer chromatography (TLC) was performed on Macherey Nagel aluminium TLC-plates, pre-coated with 0.20 mm silica gel and fluorescent indicator UV_{254}. Compounds were visualised with UV light (254 nm) and *p*-anisaldehyde stain. Stained TLC-plates required heating. Universal pH test paper strips were used to determine pH. Column chromatography was performed using 230 – 400 mesh silica (0.040 – 0.063 mm particle size). Automated flash column chromatography was carried out on the Teledyne ISCO Combiflash Rf 50, using 230 – 400 mesh silica. Mobile phase and R_f value solvent ratios are reported as v/v ratios. A rotary evaporator was used to remove solvents *in vacuo*. High vacuum (pressure less than 1 mm Hg) was used to dry products.

9.1.2 Spectroscopic and physical analysis

IR spectra were recorded on the Thermo Nicolet FT-IR, using an Attenuated Total Reflectance (ATR) attachment. OMNIC 7.0 software was used to analyse spectra. NMR spectra were recorded at 25 °C, on a 300 MHz Varian VNMRS (75 MHz for ^{13}C NMR spectra), 400 MHz Varian Unity Inova (101 MHz for ^{13}C NMR spectra) or 600 MHz Varian Unity Inova (151 MHz for ^{13}C NMR spectra) at the Central Analytical Facilities (CAF) of Stellenbosch University. Samples were dissolved in deuterated solvents. Chemical shifts (δ) are reported in ppm. Chemical shifts were referenced to the residual solvent signal in DMSO-d_6 (δ 2.50 ppm in ^1H NMR spectra; δ 39.5 ppm in ^{13}C NMR spectra) or $CDCl_3$ (δ 7.26 ppm in ^1H NMR spectra; δ 77.2 ppm in ^{13}C NMR spectra). Notwithstanding that DMSO-d_6 was dried over 4 Å molecular sieves, all ^1H NMR spectra in DMSO-d_6 displayed a water signal at δ 3.33 ppm. Spectra were

processed in MestreNova 6.0.2. Melting points were determined with Lasany Melting Point Apparatus. High-resolution mass spectrometry and purity analysis were conducted by CAF of Stellenbosch University, on a Waters Acquity UPLC system (fitted with a photodiode array detector) and a Waters SYNAPT G2 QTOF spectrometer, in ESI positive mode. A Waters BEH C18 column (1.7 μm, 100 mm × 2.1 mm) were used for UPLC purity testing.

9.1.3 Crystallography

A single crystal of diffraction quality was selected, mounted in oil, and analysed at 100 K using a Bruker DUO Apex III X-ray diffractometer. An Oxford Cryostream cryostat (700 series Cryostream Plus) attached to the diffractometer was used to cool the sample. Data reduction and unit cell determinations were performed using the Bruker diffraction software SAINT,[2] whereas absorption corrections were carried out in SADABS.[3,4] Crystal structures were solved and refined with SHELXT-14[5] and SHELXL-16,[6] using the X-Seed[7,8] graphical user interface. The positions of non-hydrogen atoms were refined anisotropically, and hydrogen atoms were placed on calculated positions. Electron density maps were used to locate the hydrogen atoms on nitrogen and oxygen atoms. POV-Ray was used to generate figures from the 3D crystal lattice.[9]

9.1.4 Biological testing

Inhibition of GSK-3 (Luminescent Assay):[10] Human recombinant GSK-3β and the prephosphorylated polypeptide substrate were purchased from Millipore Iberica S.A.U. and the Kinase-Glo Luminescent Kinase Assay from Promega Biotech Ibérica (SL). ATP and all other reagents were obtained from Sigma-Aldrich (St. Louis, MO). The assay buffer comprised of 50 mM HEPES (pH 7.5), 1 mM EDTA, 1 mM EGTA, and 15 mM magnesium acetate. The method of Baki *et al.*[11] was followed to determine GSK-3β inhibitory activity. In the assay, 10 µL (10 µM) of test compound (dissolved to 1 mM concentration in DMSO, and further diluted with assay buffer to the desired concentration) and 10 µL (20 ng) of enzyme were added to each well, followed by 20 µL of assay buffer containing 25 µM substrate and 1 µM ATP. The final DMSO concentration did not exceed 1%. After 30 min of incubation at 30 °C, 40 µL of Kinase-Glo reagent was added to stop the enzymatic reaction. After 10 min, the glow-type luminescence was recorded using a FLUOstar Optima multimode reader. Activity was determined from the difference in total ATP and ATP consumed. The inhibitory activity was then calculated by comparing with the maximal activity measured in the absence of an inhibitor. IC_{50} was defined as the concentration of compound that reduces the enzymatic activity by 50%.

GSK-3β reversibility study:[10] The enzyme was pre-incubated with the inhibitor for a certain pre-incubation time, before measuring the activity of the enzyme. GSK-3β inhibitory activities were

measured after several different pre-incubation times. A reversible inhibitor does not display increased levels of inhibition after longer pre-incubation times, whereas an irreversible inhibitor displays higher inhibition percentages with longer pre-incubation times.

9.2 Procedures

4-Amino-3-thiocyanatobenzonitrile (24)

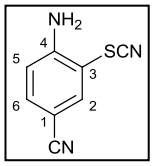

4-Aminobenzonitrile (**16**, 0.500 g, 4.23 mmol, 1.0 equiv), glacial acetic acid (10 mL) and KSCN (1.33 g, 13.7 mmol, 3.2 equiv) were added to a 2-neck flask and stirred at 5 °C for 10 min. Trimethylphenylammonium tribromide (2.15 g, 5.72 mmol, 1.4 eq.) was added to the reaction mixture in batches, at 5 °C, over 1 h. The reaction mixture was left to stir for 5 h at r.t. The yellow reaction mixture was quenched with H_2O (70 mL) and was left overnight at 0 – 4 °C. The yellow precipitate was collected by filtration. The product was extracted from the yellow precipitate with EtOAc (7 × 30 mL) and the combined organic layers were dried over $MgSO_4$, filtered and concentrated under reduced pressure. Column chromatography with 100% DCM afforded **24** as a white crystalline solid (0.553 g, 75% yield).

R_f = 0.49 (100% DCM); **^{1}H NMR** (300 MHz, DMSO-*d*$_6$) δ 7.95 (d, *J* = 2.0 Hz, 1H, Ar*H*$_2$), 7.57 (dd, *J* = 8.6, 2.0 Hz, 1H, Ar*H*$_6$), 6.93 (br.s, 2H, N*H*$_2$), 6.87 (d, *J* = 8.6 Hz, 1H, Ar*H*$_5$); **^{13}C NMR** (75 MHz, DMSO-*d*$_6$) δ 153.6, 140.8, 135.6, 118.9, 115.6, 110.9, 103.8, 97.3; **FT-IR** (ATR mode) 3443 (N-H stretch), 3343 (N-H stretch), 3243, 3219, 2220 (C≡N stretch), 2158 (S-C≡N stretch), 1633, 1598, 1506, 836 cm^{-1}; **HRMS (ESI)** *m/z* calcd for $C_8H_5N_3SNa$, $[M+Na]^+$: 198.0104, found 198.0104.

^{1}H NMR spectroscopic data correlated well with that in the literature.[12]

2-Aminobenzo[*d*]thiazole-6-carbonitrile (20)

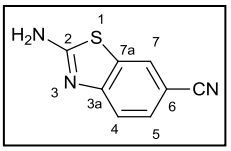

To a stirred solution of 4-amino-3-thiocyanatobenzonitrile (**24**, 0.110 g, 0.628 mmol, 1.0 equiv) in THF (5 mL) was added 60% NaH in mineral oil (0.035 g, 0.88 mmol, 1.4 equiv) at r.t. The reaction mixture was heated under reflux for 2 h and then concentrated under reduced pressure. The product was purified by column chromatography (50% Hexane/EtOAc) to afford **20** as a white powder (0.093 g, 85% yield).

R_f = 0.64 (50% DCM/EtOAc); **mp** = 198 – 202 °C (lit.[13] mp 203 – 204 °C); **^{1}H NMR** (400 MHz, DMSO-*d*$_6$) δ 8.17 (d, *J* = 1.7 Hz, 1H, Ar*H*$_7$), 8.03 (s, 2H, N*H*$_2$), 7.60 (dd, *J* = 8.4, 1.7 Hz, 1H, Ar*H*$_5$), 7.41 (d, *J* = 8.4 Hz, 1H, Ar*H*$_4$); **^{13}C NMR** (101 MHz, DMSO-*d*$_6$) δ 170.0 (Ar*C*$_2$), 156.5 (Ar*C*$_{3a}$), 131.7 (Ar*C*$_{7a}$), 129.6 (Ar*C*$_5$), 125.3 (Ar*C*$_7$), 119.7 (*C*N), 117.9 (Ar*C*$_4$), 102.0 (Ar*C*$_6$); **FT-IR** (ATR mode) 3412 (N-H stretch), 3288 (N-H stretch),

3064, 2935, 2215 (C≡N stretch), 1643, 1522, 1457, 1292, 1193, 809 cm^{-1}; **HRMS (ESI)** *m/z* calcd for $C_8H_6N_3S$, $[M+H]^+$: 176.0283, found 176.0278.

The signals in the ^{13}C NMR spectrum were assigned in accordance with the results obtained in a ^{13}C NMR spectroscopic study on benzothiazoles, which was performed by Sawhney and Boykin.[14] The ^{13}C NMR spectroscopic data correlated perfectly with their data.

1-(2-Aminobenzo[*d*]thiazol-6-yl)ethanone (21)

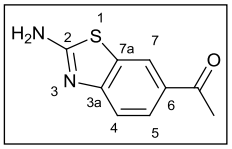

4-Aminoacetophenone (**17**, 0.300 g, 2.22 mmol, 1.0 equiv), glacial acetic acid (6 mL) and KSCN (0.669 g, 6.88 mmol, 3.1 equiv) were added to a 2-neck flask and stirred at 10 °C for 10 min. Trimethylphenylammonium tribromide (1.13 g, 3.01 mmol, 1.4 equiv) was added to the reaction mixture in batches, at 10 °C, over 1 h. The reaction mixture was left to stir for 5 h at r.t., whereafter it was heated under reflux for 10 min to drive the internal cyclisation step to completion. The reaction was quenched with H_2O (40 mL) and basified to pH = 10 with conc. NH_4OH. The mixture was left overnight at 0 – 4 °C to allow precipitation and then the orange precipitate was collected by filtration. The product was extracted from the precipitate with EtOAc (7 × 30 mL), followed by acetone (4 × 30 mL). The combined organic layers were dried over $MgSO_4$, filtered and concentrated under reduced pressure. Column chromatography with 50% DCM/EtOAc afforded **21** as a yellow solid (0.347 g, 81% yield).

R_f = 0.43 (50% DCM/EtOAc); **mp** = > 200 °C decomp (lit.[15] mp 257 – 258 °C); **^{1}H NMR** (300 MHz, DMSO-*d*$_6$) δ 8.32 (d, *J* = 1.8 Hz, 1H, Ar*H*$_7$), 7.91 (s, 2H, N*H*$_2$), 7.83 (dd, *J* = 8.4, 1.8 Hz, 1H, Ar*H*$_5$), 7.37 (d, *J* = 8.4 Hz, 1H, ArH$_4$), 2.54 (s, 3H, C*H*$_3$). **^{13}C NMR** (75 MHz, DMSO-*d*$_6$) δ 196.2 (*C*OCH$_3$), 169.8 (Ar*C*$_2$), 156.9 (Ar*C*$_{3a}$), 131.1 (Ar*C*), 129.9 (Ar*C*), 126.3 (Ar*C*), 122.0 (Ar*C*), 117.0 (Ar*C*$_4$), 26.5 (CO*C*H$_3$); **FT-IR** (ATR mode) 3351 (N-H stretch), 3322 (N-H stretch), 3042, 1644, 1586, 1513, 1417, 1354, 1293, 1276 (C-N stretch), 1231, 822 cm^{-1}; **HRMS (ESI)** *m/z* calcd for $C_9H_9N_2OS$, $[M+H]^+$: 193.0436, found 193.0428.

The NMR spectroscopic data of this compound compared well to literature data.[16] The signals in the ^{13}C NMR spectrum were assigned in accordance with the trends obtained in a ^{13}C NMR spectroscopic study on benzothiazoles, which was performed by Sawhney and Boykin.[14]

6-Nitrobenzo[*d*]thiazole-2-amine (23)

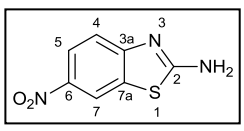

4-Nitroaniline (**19**, 0.500 g, 3.62 mmol, 1.0 equiv), glacial acetic acid (13 mL) and KSCN (1.09 g, 11.2 mmol, 3.1 equiv) were added to a 2-neck flask and cooled to 10 °C. Trimethylphenylammonium tribromide (1.84 g, 4.89 mmol, 1.4 equiv) was added to the reaction mixture in batches, at 10 °C, over 1 h. The reaction mixture was left to stir

for 5 h at r.t., whereafter it was heated under reflux for 10 min and then quenched with H_2O (40 mL). Conc. NH_4OH was then used to basify the reaction mixture to pH = 8. The mixture was extracted with EtOAc (3 × 50 mL) and the combined organic phase was washed with brine (20 mL), dried over $MgSO_4$, filtered and then concentrated *in vacuo.* The crude product was purified by column chromatography (5% MeOH/15% EtOAc/DCM) to afford **23** as a bright yellow solid (0.382 g, 54% yield).

R_f = 0.44 (5% MeOH/15% EtOAc/DCM); **^{1}H NMR** (300 MHz, DMSO-*d*$_6$) δ 8.68 (d, *J* = 2.5 Hz, 1H, Ar*H*$_7$), 8.24 (s, 2H, N*H*$_2$), 8.09 (dd, *J* = 8.9, 2.5 Hz, 1H, Ar*H*$_5$), 7.41 (d, *J* = 8.9 Hz, 1H, Ar*H*$_4$); **^{13}C NMR** (75 MHz, DMSO-*d*$_6$) δ 171.8 (Ar*C*$_2$), 158.6 (Ar*C*$_{3a}$), 140.7 (Ar*C*$_6$), 131.6 (Ar*C*$_{7a}$), 122.0 (Ar*C*$_5$), 117.7 (Ar*C*$_4$), 116.8 (Ar*C*$_7$); **FT-IR** (ATR mode) 3458 (N-H stretch), 3020, 2936, 1654, 1531, 1491 (N=O *asym* stretch), 1323 (N=O *sym* stretch), 1289, 1122, 753 cm^{-1}; **HRMS (ESI)** *m/z* calcd for $C_7H_6N_3O_2S$, $[M+H]^+$: 196.0181, found 196.0181**.**

The NMR spectroscopic data of this compound compared well to literature data.[14,17] The signals in the ^{13}C NMR spectrum were assigned in accordance with the results obtained by Sawhney and Boykin.[14]

Methyl 4-aminobenzoate (18)[18]

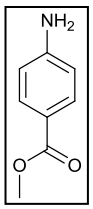

A solution of 4-aminobenzoic acid (**25**, 2.00 g, 14.6 mmol, 1.0 equiv) and MeOH (15 mL) was cooled to 0 °C. Thionyl chloride (2.6 mL, 36 mmol, 2.5 equiv) was added slowly by dropwise addition, which resulted in a white suspension. The reaction mixture was heated under reflux for 19 h to yield a yellow solution. After cooling, the solution was concentrated under reduced pressure. After the addition of sat. aq. $NaHCO_3$ (60 mL), the mixture was extracted with EtOAc (3 × 40 mL). The combined organic layers were dried over $MgSO_4$, filtered and concentrated under reduced pressure. Column chromatography with 40% EtOAc/Hexane afforded **18** as a cream-coloured solid (2.13 g, 97% yield).

R_f = 0.66 (50% EtOAc/Hexane); **^{1}H NMR** (300 MHz, $CDCl_3$) δ 7.84 (d, *J* = 8.6 Hz, 2H, 2 × Ar*H*), 6.63 (d, *J* = 8.6 Hz, 2H, 2 × Ar*H*), 4.06 (br.s., 2H, N*H*$_2$), 3.85 (s, 3H, C*H*$_3$); **^{13}C NMR** (75 MHz, $CDCl_3$) δ 167.3 (*C*O_2CH$_3$), 151.0, 131.7, 119.8, 113.9, 51.7 (*C*H$_3$).

The NMR spectroscopy data collected for this compound compared well to literature data.[18]

Methyl 2-aminobenzo[*d*]thiazole-6-carboxylate (22)

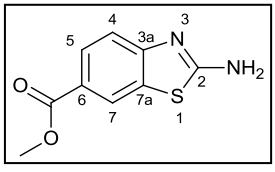

Methyl 4-aminobenzoate (**18**, 0.750 g, 4.96 mmol, 1.0 equiv), glacial acetic acid (12 mL) and KSCN (1.49 g, 15.3 mmol, 3.1 equiv) were added to a 2-neck flask and cooled to 10 °C. Trimethylphenylammonium tribromide (2.52 g, 6.70 mmol, 1.4 equiv) was added to the reaction mixture in batches, at 10 °C,

over 1 h. The reaction mixture was left to stir for 5 h at r.t., whereafter it was heated under reflux for 40 min and then quenched with H_2O (80 mL). Conc. NH_4OH was used to basify the reaction mixture to pH = 10. The reaction mixture was left overnight at 0 – 4 °C to allow precipitation. The precipitate was collected by filtration and the colourless mother liquid discarded. The precipitate and H_2O (50 mL) were transferred into a separatory funnel and the suspension was extracted with EtOAc (4 × 40 mL). The organic layers were combined and washed with brine (30 mL). The solvent was removed *in vacuo* and the crude product was purified by column chromatography (50% Hexane/EtOAc) to afford **22** as a yellow solid (0.761 g, 74% yield).

R_f = 0.32 (50% Hexane/EtOAc); **^{1}H NMR** (300 MHz, DMSO-d_6) δ 8.28 (d, *J* = 1.8 Hz, 1H, ArH_7), 7.90 (s, 2H, NH_2), 7.81 (dd, *J* = 8.4, 1.8 Hz, 1H, ArH_5), 7.37 (d, *J* = 8.4 Hz, 1H, ArH_4), 3.82 (s, 3H, CH_3); **^{13}C NMR** (75 MHz, DMSO-d_6) δ 169.8 (ArC_2), 166.1 (CO_2CH_3), 156.9 (ArC_{3a}), 131.2 (ArC_{7a}), 127.1 (ArC_5), 122.6 (Ar$C_{6/7}$), 121.7 (Ar$C_{6/7}$), 117.1 (ArC_4), 51.8 (CO_2CH_3); **FT-IR** (ATR mode) 3357 (N-H stretch), 3298 (N-H stretch), 3084, 2948, 1691 (C=O), 1645, 1523, 1463, 1430, 1330, 1279, 1236, 1111, 765 cm^{-1}; **HRMS (ESI)** *m/z* calcd for $C_9H_9N_2O_2S$, $[M+H]^+$: 209.0385, found 209.0386.

The signals in the ^{13}C NMR spectrum were assigned in accordance with the results obtained for ethyl 2-aminobenzo[*d*]thiazole-6-carboxylate in a ^{13}C NMR spectroscopic study on benzothiazoles, which was performed by Sawhney and Boykin.[14]

_N_-(4-methoxybenzyl)-1_H_-imidazole-1-carboxamide (46)[19]

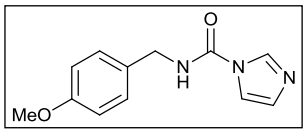

4-Methoxybenzylamine (**15**, 0.13 mL, 1.0 mmol, 1.0 equiv) was added to DCM (3 mL). The mixture was then treated with 4.0 M HCl in 1,4-dioxane (0.25 mL, 1.0 mmol, 1.0 equiv) while stirring at r.t. The resultant colour change from colourless to white, indicated the *in situ* formation of the ammonium hydrochloride salt. After stirring for 10 min, DMF (1.6 mL) was added and the reaction mixture was cooled to 0 °C. CDI (0.211 g, 1.30 mmol, 1.3 equiv) was added to the white suspension and the mixture was stirred for 7 min at 0 °C. The colourless solution was concentrated immediately under reduced pressure, while maintaining a temperature of 30 °C on the rotary evaporator. After addition of EtOAc (30 mL), the mixture was washed with a saturated aqueous solution of NH_4Cl (4 × 10 mL). The organic layer was dried over $MgSO_4$, filtered and concentrated under reduced pressure. The product was purified by column chromatography (5% MeOH/DCM) to give **46** as a crystalline white solid (0.231 g, quant. yield).

R_f = 0.31 (5% MeOH/DCM); **mp** = 115 – 118 °C (lit.[19] mp 113 – 114 °C); **^{1}H NMR** (300 MHz, $CDCl_3$) δ 8.06 (s, 1H, Ar*H*), 7.57 (br.t[†], 1H, N*H*), 7.41 (s, 1H, Ar*H*), 7.23 (d, *J* = 8.7 Hz, 2H, 2 × Ar*H*), 6.89 (s, 1H, Ar*H*), 6.85 (d, *J* = 8.7 Hz, 2H, 2 × Ar*H*), 4.47 (d, *J* = 5.6 Hz[†], 2H, CH_2), 3.78 (s, 3H, OCH_3); **^{13}C NMR** (75 MHz, $CDCl_3$) δ 159.4, 149.1, 135.9, 129.9, 129.5, 129.3, 116.5, 114.3, 55.4, 44.5; **FT-IR** (ATR mode) 3204 (N-H stretch), 3001, 1715 (C=O stretch), 1545, 1509, 1483, 1473, 1447, 1331, 1286, 1251, 1231, 1212, 1174, 1070, 1033 cm^{-1}; **HRMS (ESI)** *m/z* calcd for $C_{12}H_{14}N_3O_2$, $[M+H]^+$: 232.1086, found 232.1092.

The ^{13}C NMR spectroscopic data correlated well with that in the literature,[19] whereas slight deviations were present in the rest of the spectroscopic data.

1-(4-Methoxybenzyl)-3-(5-nitrothiazol-2-yl)urea (3)[19]

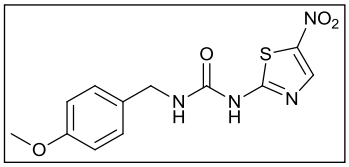

60% NaH in mineral oil (0.0580 g, 1.45 mmol, 1.4 equiv) was added portion-wise to a solution of 2-amino-5-nitrothiazole (**52**, 0.150 g, 1.03 mmol, 1.0 equiv) and *N*-(4-methoxybenzyl)-1*H*-imidazole-1-carboxamide (**46**, 0.239 g, 1.03 mmol, 1.0 equiv) in DMF (7 mL). The reaction mixture was stirred for 15 h, whereafter the mixture was diluted with EtOAc (100 mL) and extracted with sat. aq. NH_4Cl (3 × 35 mL). The organic layer was washed with brine (30 mL) and concentrated *in vacuo.* Purification of the crude product required two steps. First, column chromatography (3% MeOH, 97% DCM) was performed and the desired fractions were collected and concentrated *in vacuo*. Subsequently, trituration with DCM (3 × 7 mL) yielded the pure product **3** as a yellow solid (0.083 g, 26% yield).

R_f = 0.26 (3% MeOH, 97% DCM); **mp** = > 190 °C decomp (lit.[20] > 190 °C decomp); **^{1}H NMR** (300 MHz, DMSO-d_6) δ 11.63 (br.s, 1H, N*H*), 8.50 (s, 1H, Ar*H*), 7.25 – 7.22 (d imposed on a br.t. [app. d], *J* = 8.7 Hz, 3H, 2 × Ar*H*, N*H*), 6.90 (d, *J* = 8.7 Hz, 2H, 2 × Ar*H*), 4.29 (d, *J* = 5.9 Hz, 2H, CH_2), 3.73 (s, 3H, OCH_3); **^{13}C NMR** (75 MHz, DMSO-d_6) δ 164.3, 158.4, 153.3, 143.3, 140.9, 130.8, 128.7, 113.8, 55.1, 42.6; **FT-IR** (ATR mode) 3313 (N-H stretch), 1673 (C=O stretch), 1516, 1480, 1440, 1352 (N=O *sym* stretch), 1315, 1225, 1176, 1023, 821 cm^{-1}; **HRMS (ESI)** *m/z* calcd for $C_{12}H_{13}N_4O_4S$, $[M+H]^+$: 309.0658, found 309.0651; **UPLC**: Purity >95%, r.t = 6.02 min, acetonitrile/H_2O (0.1% formic acid) 5/95.

The spectroscopy data of this compound compared well to literature data.[19]

[†] The amide proton (*NH)* and the benzylic CH_2 protons couple with one another. The *J*-coupling value measured for the N*H* triplet peak was not precise, due to the broadness of the signal. Therefore, only the *J*-coupling constant of the sharper CH_2 signal is reported. This reporting method was applied throughout the experimental chapter, to all compounds displaying this particular N*H* to CH_2 coupling.

General procedure for the synthesis of *N*-(4-methoxybenzyl) ureas (4, 56 – 58) from 2-aminobenzothiazoles.[19]

The amine (1.0 equiv) and *N*-(4-methoxybenzyl)-1*H*-imidazole-1-carboxamide (**46**, 1.3 equiv) were dissolved in DMF (3 – 6 mL). 60% NaH in mineral oil (1.4 equiv) was added in portions over 20 min and the solution was left to stir at r.t. for 22 h. After the addition of EtOAc (70 mL), the mixture was washed with a saturated aqueous solution of NH_4Cl (4 × 20 mL) and then brine (1 × 20 mL). During the course of DMF removal, the organic layer changed from colourless to a white suspension. The organic layer was concentrated under reduced pressure. The crude product was purified by column chromatography to yield ureas **4**, **56 – 58**.

1-(6-Cyanobenzo[*d*]thiazol-2-yl)-3-(4-methoxybenzyl)urea (4)

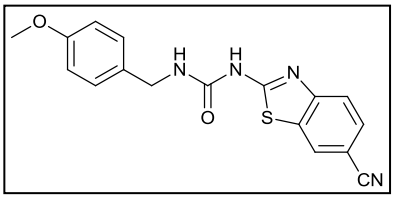

Prepared according to the general procedure, with the following amounts: 2-Aminobenzo[*d*]thiazole-6-carbonitrile (**20**, 0.086 g, 0.49 mmol), *N*-(4-methoxybenzyl)-1*H*-imidazole-1-carboxamide (**46**, 0.148 g, 0.640 mmol), 60% NaH in mineral oil (0.028 g, 0.70 mmol). Column chromatography (5% MeOH/15% EtOAc/DCM) yielded **4** as a white solid (0.165 g, 99% yield).

R_f = 0.53 (5% MeOH/DCM); **mp** = > 207 °C decomp; **^{1}H NMR** (300 MHz, DMSO-d_6) δ 11.11 (s, 1H, N*H*), 8.45 (s, 1H, Ar*H*), 7.75 – 7.74 (m, 2H, 2 × Ar*H*), 7.25 (d, *J* = 8.7 Hz, 2H, 2 × Ar*H*), 7.20 (br.t, 1H, N*H*), 6.91 (d, *J* = 8.7 Hz, 2H, 2 × Ar*H*), 4.31 (d, *J* = 5.8 Hz, 2H, CH_2), 3.73 (s, 3H, CH_3); **^{13}C NMR** (75 MHz, DMSO-d_6) δ 163.6, 158.4, 153.5, 152.5, 132.3, 131.0, 129.5, 128.7, 126.4, 120.2, 119.3, 113.8, 104.3, 55.1, 42.5; **FT-IR** (ATR mode) 3314 (N-H stretch), 2226 (C≡N stretch), 1667 (C=O stretch), 1557, 1547, 1514, 1446, 1274, 1257, 1227, 1174, 1033, 824 cm^{-1}; **HRMS (ESI)** *m/z* calcd for $C_{17}H_{15}N_4O_2S$, $[M+H]^+$: 339.0916, found 339.0915; **UPLC**: Purity 99%, r.t = 6.71 min, acetonitrile/H_2O (0.1% formic acid) 2/98.

The spectroscopy data of this compound compared well to literature data.[21]

1-(6-Acetylbenzo[*d*]thiazol-2-yl)-3-(4-methoxybenzyl)urea (56)

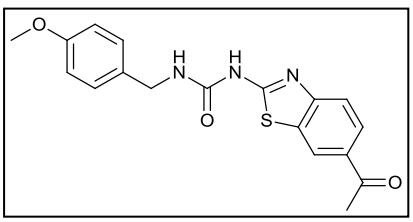

Prepared according to the general procedure, with the following amounts: 1-(2-Aminobenzo[*d*]thiazol-6-yl)ethanone (**21**, 0.150 g, 0.780 mmol), *N*-(4-methoxybenzyl)-1*H*-imidazole-1-carboxamide (**46**, 0.230 g, 0.995 mmol), 60% NaH in mineral oil (0.045 g, 1.1 mmol). Column chromatography (5% MeOH/25% EtOAc/DCM) yielded **56** as a light yellow solid (0.228 g, 82% yield).

R_f = 0.61 (5% MeOH/25% EtOAc/DCM); **mp** = > 214 °C decomp; **^{1}H NMR** (300 MHz, DMSO-*d*$_6$) δ 11.02 (s, 1H, N*H*), 8.57 (d, *J* = 1.5 Hz, 1H, Ar*H*$_7$), 7.95 (dd, *J* = 8.5, 1.5 Hz, 1H, Ar*H*$_5$), 7.67 (d, *J* = 8.5 Hz, 1H, Ar*H*$_4$), 7.26 (d, *J* = 8.6 Hz, 2H, 2 × Ar*H*), 7.20 (br.t, 1H, N*H*), 6.91 (d, *J* = 8.6 Hz, 2H, 2 × Ar*H*), 4.31 (d, *J* = 5.8 Hz, 2H, C*H*$_2$), 3.73 (s, 3H, OC*H*$_3$), 2.60 (s, 3H, COC*H*$_3$); **^{13}C NMR** (75 MHz, DMSO-*d*$_6$) δ 196.7 (*C*OCH$_3$), 163.2, 158.4, 153.6, 152.8, 131.7, 131.5, 131.1, 128.7, 126.0, 122.8, 119.3, 113.8, 55.1, 42.5, 26.7 (CO*C*H$_3$); **FT-IR** (ATR mode) 3312 (N-H stretch), 1685 (C=O stretch), 1673 (C=O stretch), 1557, 1527, 1510, 1268, 1233 cm^{-1}; **HRMS (ESI)** *m/z* calcd for $C_{18}H_{18}N_3O_3S$, $[M+H]^+$: 356.1070, found 356.1057; **UPLC**: Purity 95%, r.t = 5.88 min, acetonitrile/H_2O (0.1% formic acid) 5/95.

Methyl 2-[3-(4-methoxybenzyl)ureido]benzo[*d*]thiazole-6-carboxylate (57)

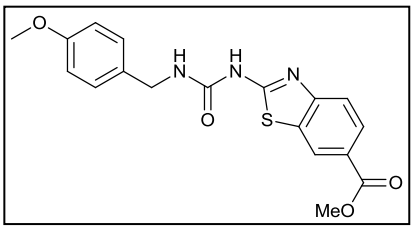

Prepared according to the general procedure, with the following amounts: Methyl 2-aminobenzo[*d*]thiazole-6-carboxylate (**22**, 0.200 g, 0.960 mmol), *N*-(4-methoxybenzyl)-1*H*-imidazole-1-carboxamide (**46**, 0.289 g, 1.25 mmol), 60% NaH in mineral oil (0.0540 g, 1.35 mmol). The crude product was purified by column chromatography (5% MeOH/25% EtOAc/DCM) to afford **57** as a white solid (0.265 g, 74%).

R_f = 0.69 (5% MeOH/25% EtOAc/DCM); **mp** = > 220 °C decomp; **^{1}H NMR** (300 MHz, DMSO-*d*$_6$) δ 11.04 (br.s, 1H, N*H*), 8.53 (d, *J* = 1.7 Hz, 1H, Ar*H*$_7$), 7.94 (dd, *J* = 8.5, 1.7 Hz, 1H, Ar*H*$_5$), 7.67 (d, *J* = 8.5 Hz, 1H, Ar*H*$_4$), 7.26 (d, *J* = 8.7 Hz, 2H, 2 × Ar*H*), 7.18 (br.t, 1H, N*H*) , 6.91 (d, *J* = 8.7 Hz, 2H, 2 × Ar*H*), 4.31 (d, *J* = 5.8 Hz, 2H, C*H*$_2$), 3.86 (s, 3H, CO_2CH_3), 3.73 (s, 3H, PhOC*H*$_3$); **^{13}C NMR** (75 MHz, DMSO-*d*$_6$) δ 166.1, 163.3, 158.4, 153.7, 152.9, 131.8, 131.1, 128.7, 126.9, 123.6, 123.3, 119.3, 113.8, 55.1, 52.1 (CO_2CH_3), 42.5; **FT-IR** (ATR mode) 3291 (N-H stretch), 1720 (C=O stretch), 1668 (C=O stretch), 1555, 1536, 1510, 1434, 1296, 1271, 1235, 1112, 1030, 770 cm^{-1}; **HRMS (ESI)** *m/z* calcd for $C_{18}H_{18}N_3O_4S$, $[M+H]^+$: 372.1019, found 372.1001.

1-(4-Methoxybenzyl)-3-(6-nitrobenzo[*d*]thiazol-2-yl)urea (58)

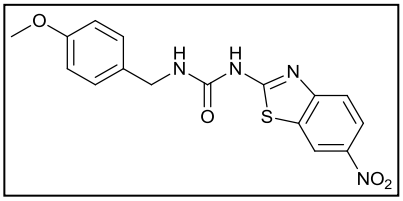

Prepared according to the general procedure, with the following amounts: 6-Nitrobenzo[*d*]thiazol-2-amine (**23**, 0.130 g, 0.666 mmol), *N*-(4-methoxybenzyl)-1*H*-imidazole-1-carboxamide (**46**, 0.200 g, 0.865 mmol), 60% NaH in mineral oil (0.037 g, 0.93 mmol). Column chromatography (5% MeOH/25% EtOAc/DCM) yielded **58** as a white solid (0.24 g, quant. yield).

R_f = 0.61 (5% MeOH/25% EtOAc/DCM); **^{1}H NMR** (300 MHz, DMSO-*d*$_6$) δ 11.25 (s, 1H, N*H*), 8.94 (d, *J* = 2.4 Hz, 1H, Ar*H*$_7$), 8.21 (dd, *J* = 8.9, 2.4 Hz, 1H, Ar*H*$_5$), 7.74 (d, *J* = 8.9 Hz, 1H, Ar*H*$_4$), 7.27 – 7.21 (m, 3H,

2 × Ar*H*, N*H*), 6.91 (d, *J* = 8.7 Hz, 2H, 2 × Ar*H*), 4.32 (d, *J* = 5.8 Hz, 2H, CH_2), 3.73 (s, 3H, OCH_3); **^{13}C NMR** (75 MHz, DMSO-d_6) δ 165.3, 158.4, 154.3, 153.6, 142.3, 132.2, 131.0, 128.7, 121.6, 119.5, 118.5, 113.8, 55.1, 42.6; **FT-IR** (ATR mode) 3290 (N-H stretch), 1668 (C=O stretch), 1551, 1508, 1445, 1332 (N=O *sym* stretch), 1276, 1257, 1231, 1179, 1129, 1025, 821 cm^{-1}; **HRMS (ESI)** *m/z* calcd for $C_{16}H_{15}N_4O_4S$, $[M+H]^+$: 359.0815, found 359.0805.

The spectroscopy data of this compound compared well to literature data.[21]

***N*-(4-cyanophenyl)acetamide (26)**[22]

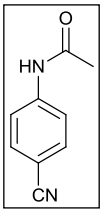

4-Aminobenzonitrile (**16**, 1.00 g, 8.46 mmol) was added portion-wise to acetic anhydride (12 mL) over 1 h, while stirring and maintaining the temperature at 35 – 45 °C. While keeping the flask on ice, ice water (20 mL) was added to the white suspension. The mixture was left at 0 – 4 °C for 1 h. The product was collected by filtration and was washed with cold H_2O (3 × 30 mL). The product was dried in the oven at 120 °C to give **26** as a white solid (1.13 g, 83% yield).

R_f = 0.07 (100% DCM); **^{1}H NMR** (300 MHz, $CDCl_3$) δ 7.67 – 7.59 (m, 4H, 4 × Ar*H*), 7.44 (br.s, 1H, N*H*), 2.22 (s, 3H, CH_3); **^{13}C NMR** (75 MHz, $CDCl_3$) δ 168.7, 142.0, 133.5, 119.6, 118.9, 107.3, 24.9. **FT-IR** (ATR mode) 3298, 3256, 3184, 3111, 2221 (C≡N stretch), 1666 (C=O stretch), 1596, 1538, 1531, 1505, 1403, 1360, 1320, 1264, 1175, 833 cm^{-1}.

The spectroscopic data correlated well with that in the literature.[23]

***N*-(4-acetylphenyl)acetamide (27)**[22]

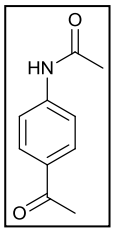

4-Aminoacetophenone (**17**, 2.00 g, 14.8 mmol) was added portion-wise, over 30 minutes, to an acetic anhydride (20 mL) and DCM (40 mL) mixture at 10 °C. The reaction mixture was left to stir at r.t. for 1.5 h, whereafter the DCM was removed *in vacuo*. While keeping the flask on ice, ice water (100 mL) was added to the mixture. The mixture was left at 0 – 4 °C overnight. The product, a white precipitate, was collected by filtration and washed with cold H_2O (3 × 30 mL). It became evident that the mother liquid still contained product, therefore it was neutralised with conc. NH_4OH and extracted with EtOAc (3 × 40 mL). The organic layers and the white precipitate were combined and washed with brine (20 mL). Column chromatography (60% EtOAc/Hexane → 80% EtOAc/Hexane) afforded **27** as a white solid (2.53 g, 97% yield).

R_f = 0.44 (80% EtOAc/Hexane); **^{1}H NMR** (400 MHz, DMSO-d_6) δ 10.30 (s, 1H, N*H*), 7.91 (d, *J* = 8.7 Hz, 2H, 2 × Ar*H*), 7.71 (d, *J* = 8.7 Hz, 2H, 2 × Ar*H*), 2.51 (s, 3H, CH_3), 2.08 (s, 3H, CH_3); **^{13}C NMR** (101 MHz,

DMSO-d_6) δ 196.4 (*C*OCH_3), 168.9 (HN*C*OCH_3), 143.6, 131.5, 129.4, 118.1, 26.4, 24.2; **FT-IR** (ATR mode) 3291, 3265, 1673 (C=O stretch), 1591, 1528, 1510, 1408, 1369, 1358, 1317, 1263, 1182, 853, 839 cm^{-1}.

The spectroscopy data collected for this compound compared well to literature data.[24,25]

Methyl 4-acetamidobenzoate (28)[22]

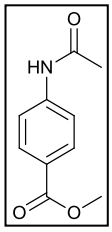

Methyl 4-aminobenzoate (**18**, 0.583 g, 3.86 mmol) was added portion-wise, over 30 minutes, to an acetic anhydride (6 mL) and DCM (10 mL) mixture at 10 °C. The reaction mixture was left to stir at r.t. for 1 h. The DCM was removed *in vacuo*, whereafter the orange solution was diluted with H_2O (40 mL) and extracted with EtOAc (3 × 30 mL). The combined organic layers were dried over $MgSO_4$, filtered and concentrated *in vacuo*. Automated column chromatography (20 – 60% EtOAc/Hexane) gave **28** as a white solid (0.704 g, 94% yield).

R_f = 0.44 (50% EtOAc/Hexane); **^{1}H NMR** (300 MHz, DMSO-d_6) δ 10.27 (s, 1H, N*H*), 7.90 (d, *J* = 8.7 Hz, 2H, 2 × Ar*H*), 7.71 (d, *J* = 8.7 Hz, 2H, 2 × Ar*H*), 3.81 (s, 3H, CO_2CH_3), 2.08 (s, 3H, HNCOCH_3); **^{13}C NMR** (75 MHz, DMSO-d_6) δ 168.9, 165.8, 143.7, 130.3, 123.7, 118.3, 51.8, 24.2;

The NMR spectroscopy data collected for this compound compared well to literature data.[26]

***N*-(4-cyano-2-nitrophenyl)acetamide (29)**[22]

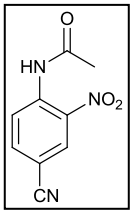

A solution of potassium nitrate (0.663 g, 6.56 mmol, 1.5 equiv) in conc. H_2SO_4 (4 mL) was cooled to −15 °C. *N*-(4-cyanophenyl)acetamide (**26**, 0.700 g, 4.37 mmol, 1.0 equiv) was added to the mixture in a slow, batch-wise manner, while maintaining the temperature below −15 °C. The temperature was kept below −10 °C, while the reaction mixture was stirred for 3.5 h. The reaction was quenched with ice water (35 mL) to form a bright yellow precipitate. The flask was left overnight at 0 – 4 °C and then the yellow product was collected by filtration. The product was purified by automated column chromatography (0-20% EtOAc/Hexane → 20% EtOAc/Hexane → 30% EtOAc/Hexane) to afford **29** as a bright yellow solid (0.615 g, 69% yield).

R_f = 0.63 (100% DCM); **mp** = 125 – 127 °C (lit.[27] mp 130 – 131 °C in MeOH); **^{1}H NMR** (300 MHz, $CDCl_3$) δ 10.54 (s, 1H, N*H*), 9.02 (d, *J* = 8.9 Hz, 1H, ArH_6), 8.55 (d, *J* = 2.0 Hz, 1H, ArH_3), 7.87 (dd, *J* = 8.9, 2.0 Hz, 1H, ArH_5), 2.34 (s, 3H, CH_3); **FT-IR** (ATR mode) 3341 (N-H stretch), 3139, 3099, 2231 (C≡N stretch), 1712 (C=O stretch), 1616, 1570, 1538, 1499 (N=O *asym* stretch), 1441, 1396, 1371, 1345 (N=O *sym* stretch), 1263, 1215, 1191, 1142, 858, 762 cm^{-1}.

The NMR spectroscopic data of this compound compared well to the literature.[28]

General nitration procedure to yield compounds 30 – 31.

A stirred mixture of 65% HNO_3 and the *N*-(4-substituted phenyl)acetamide were cooled to 0 °C and then treated, dropwise, with conc. H_2SO_4 (1:1 v/v; 65% HNO_3/ conc. H_2SO_4). While maintaining a temperature of 0 °C, the bright yellow solution was stirred for 1 h and then quenched with H_2O (40 mL). The mixture was basified with conc. NH_4OH to pH = 8 and extracted with EtOAc (4 × 30 mL). The combined organic layer was washed with brine (25 mL), dried over $MgSO_4$, filtered and concentrated *in vacuo*. The pure product was isolated by automated column chromatography (0 – 30% EtOAc/Hexane → 30% EtOAc/Hexane).

***N*-(4-acetyl-2-nitrophenyl)acetamide (30)**

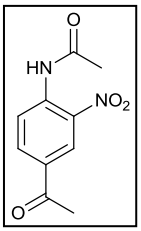

Prepared according to the general procedure with *N*-(4-acetylphenyl)acetamide (**27**, 0.150 g, 0.847 mmol), 65% HNO_3 (2 mL) and conc. H_2SO_4 (2 mL). **30** was obtained as a bright yellow solid (0.130 g, 69% yield).

R_f = 0.29 (30% EtOAc/Hexane); **^{1}H NMR** (400 MHz, $CDCl_3$) δ 10.54 (br.s, 1H, N*H*), 8.93 (d, *J* = 8.9 Hz, 1H, ArH_6), 8.79 (d, *J* = 2.1 Hz, 1H, ArH_3), 8.20 (dd, *J* = 8.9, 2.1 Hz, 1H, ArH_5), 2.63 (s, 3H, CH_3), 2.33 (s, 3H, CH_3); **^{13}C NMR** (101 MHz, $CDCl_3$) δ 194.8 (*C*OCH_3), 169.2 (HN*C*OCH_3), 138.5, 135.7, 135.3, 131.8, 126.4, 121.9, 26.5, 25.9; **FT-IR** (ATR mode) 3345 (N-H stretch), 1716 (C=O stretch), 1682 (C=O stretch), 1610, 1569, 1539, 1502 (N=O *asym* stretch), 1448, 1396, 1360, 1340 (N=O *sym* stretch), 1305, 1259, 1233, 1219, 1140, 853 cm^{-1}.

The NMR spectroscopy data collected for this compound compared well to literature data.[29]

Methyl 4-acetamido-3-nitrobenzoate (31)

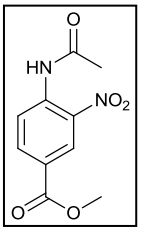

Prepared according to the general procedure with methyl 4-acetamidobenzoate (**28**, 0.681 g, 3.52 mmol), 65% HNO_3 (8 mL) and conc. H_2SO_4 (8 mL). **31** was obtained as a bright yellow solid (0.758 g, 90% yield).

R_f = 0.47 (30% EtOAc/Hexane); **^{1}H NMR** (300 MHz, DMSO-d_6) δ 10.55 (s, 1H, N*H*), 8.38 (d, *J* = 1.9 Hz, 1H, ArH_2), 8.20 (dd, *J* = 8.6, 1.9 Hz, 1H, ArH_6), 7.86 (d, *J* = 8.6 Hz, 1H, ArH_5), 3.88 (s, 3H, CO_2CH_3), 2.12 (s, 3H, HNCOCH_3); **^{13}C NMR** (75 MHz, DMSO-d_6) δ 168.8, 164.3, 141.1, 135.4, 134.1, 125.9, 125.4, 124.6, 52.6 (COO*C*H_3), 23.7 (HNCO*C*H_3); **FT-IR** (ATR mode) 3351 (N-H stretch), 1716 (C=O stretch), 1617, 1579, 1505 (N=O *asym* stretch), 1439, 1380, 1340 (N=O *sym* stretch), 1290, 1257, 1211, 1146, 1128, 1073, 1003, 984, 861, 751 cm^{-1}.

General deacetylation procedure (32 – 34).[27]

The acetamide and 1 M H_2SO_4 were heated under reflux for 2 h. The reaction mixture was left to cool, whereafter it was neutralised with sat. aq. $NaHCO_3$. The yellow product was extracted from the mixture with EtOAc (4 × 30 mL). The combined organic layers were dried over $MgSO_4$, filtered and concentrated under reduced pressure. Column chromatography was used to isolate the pure compound.

4-Amino-3-nitrobenzonitrile (32)

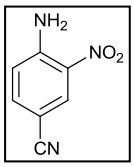

Prepared according to the general procedure with *N*-(4-cyano-2-nitrophenyl)acetamide (**29**, 0.746 g, 3.64 mmol) and 1 M H_2SO_4 (45 mL). Column chromatography with 100% DCM afforded **32** as a bright yellow powder (0.567 g, 95% yield).

$\mathbf{R_f}$ = 0.54 (100% DCM); **^{1}H NMR** (300 MHz, $CDCl_3$) δ 8.48 (d, *J* = 1.9 Hz, 1H, ArH_2), 7.54 (dd, *J* = 8.8, 1.9 Hz, 1H, ArH_6), 6.89 (d, *J* = 8.8 Hz, 1H, ArH_5), 6.54 (br.s, 2H, NH_2); **^{13}C NMR** (75 MHz, $CDCl_3$) δ 147.1, 137.3, 132.0, 119.8, 117.8, 100.1, one quaternary carbon missing; **FT-IR** (ATR mode) 3494, 3468, 3381, 3338, 2227 (C≡N stretch), 1630, 1597, 1555, 1519 (N=O *asym* stretch), 1482, 1423, 1355 (N=O *sym* stretch), 1286, 1271, 1203, 1174, 1086, 918, 829, 822 cm^{-1}.

The spectroscopy data collected for this compound compared well to literature data.[27,28,30]

1-(4-Amino-3-nitrophenyl)ethanone (33)

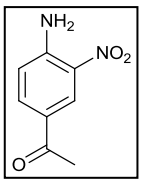

Prepared according to the general procedure with *N*-(4-acetyl-2-nitrophenyl)acetamide (**30**, 0.124 g, 0.558 mmol) and 1 M H_2SO_4 (9 mL). Column chromatography with 5% EtOAc/DCM afforded **33** as a dark yellow solid (0.097 g, 96% yield).

$\mathbf{R_f}$ = 0.56 (5% EtOAc/DCM); **^{1}H NMR** (400 MHz, $CDCl_3$) δ 8.74 (d, *J* = 2.0 Hz, 1H, ArH_2), 8.00 (dd, *J* = 8.8, 2.0 Hz, 1H, ArH_6), 6.86 (d, *J* = 8.8 Hz, 1H, ArH_5), 6.52 (br.s, 2H, NH_2), 2.57 (s, 3H, CH_3); **^{13}C NMR** (101 MHz, $CDCl_3$) δ 195.1 (*C*OCH_3), 147.7, 134.7, 131.1, 128.5, 126.9, 119.0, 26.2 (CO*C*H_3); **FT-IR** (ATR mode) 3444 (N-H stretch), 3325 (N-H stretch), 1665, 1626, 1555, 1475, 1358, 1346, 1297, 1248, 1156, 1091, 1071, 1022, 952, 900, 831 cm^{-1};

The NMR spectroscopy data collected for this compound compared well to literature data.[31]

Methyl 4-amino-3-nitrobenzoate (34)

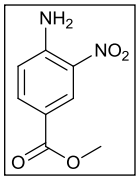

Prepared according to the general procedure with methyl 4-acetamido-3-nitrobenzoate (**31**, 0.729 g, 3.06 mmol) and 1 M H_2SO_4 (24 mL). Automated column chromatography with 30% EtOAc/Hexane afforded **34** as a yellow solid (0.491 g, 82% yield).

R_f = 0.40 (30% EtOAc/Hexane); **^{1}H NMR** (300 MHz, DMSO-*d*$_6$) δ 8.54 (d, *J* = 1.9 Hz, 1H, Ar*H*$_2$), 7.98 (br.s, 2H, N*H*$_2$), 7.85 (dd, *J* = 8.9, 1.9 Hz, 1H, Ar*H*$_6$), 7.06 (d, *J* = 8.9 Hz, 1H, Ar*H*$_5$), 3.81 (s, 3H, OC*H*$_3$); **^{13}C NMR** (75 MHz, DMSO-*d*$_6$) δ 164.9 (*C*OOCH$_3$), 148.9, 134.8, 129.6, 128.0, 119.4, 116.1, 51.9 (O*C*H$_3$).

The NMR spectroscopy data collected for this compound compared well to literature data.[32]

General hydrogenation procedure to form the diamines 35 – 37.[33]

The 4-amino-3-nitro compound was dissolved in EtOAc and MeOH. The solution was treated with 10% palladium on carbon (10% w/w) and hydrogenated with a H_2 balloon at r.t. The reaction mixture was monitored by TLC and by a complete colour change from bright yellow to a transparent orange or red. When judged to be complete, the reaction mixture was filtered through a bed of celite and concentrated *in vacuo*. The product was purified by column chromatography.

3,4-Diaminobenzonitrile (35)

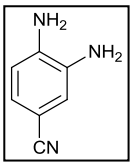

Prepared according to the general procedure with 4-amino-3-nitrobenzonitrile (**32**, 0.150 g, 0.920 mmol) dissolved in a 4:1 mixture of EtOAc (6.4 mL) and MeOH (1.6 mL). The product was purified by column chromatography (50% EtOAc/Hexane) to give **35** as an orange-cream coloured solid (0.121 g, 99% yield).

R_f = 0.12 (100% DCM); **^{1}H NMR** (400 MHz, $CDCl_3$) δ 7.04 (dd, *J* = 8.1, 1.8 Hz, 1H, Ar*H*$_6$), 6.94 (d, *J* = 1.8 Hz, 1H, Ar*H*$_2$), 6.68 (d, *J* = 8.1 Hz, 1H, Ar*H*$_5$), 3.81 (br.s, 2H, N*H*$_2$), 3.39 (br.s, 2H, N*H*$_2$); **^{13}C NMR** (101 MHz, $CDCl_3$) δ 140.1, 134.0, 125.8, 120.1, 119.9, 115.7, 102.0; **FT-IR** (ATR mode) 3436, 3360, 3186, 2211 (C≡N stretch), 1625, 1593, 1578, 1509, 1440, 1307, 1270, 1149, 863, 810 cm^{-1}.

The spectroscopy data collected for this compound compared well to literature data.[34]

1-(3,4-Diaminophenyl)ethanone (36)

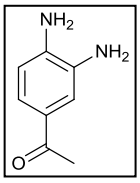

Prepared according to the general procedure with 1-(4-amino-3-nitrophenyl)ethanone (**33**, 0.076 g, 0.42 mmol) dissolved in a 2:1 mixture of EtOAc (4 mL) and MeOH (2 mL). The product was purified by column chromatography (70% EtOAc/DCM) to yield **36** as an orange solid (0.057 g, 90% yield).

R_f = 0.42 (70% EtOAc/DCM); **^{1}H NMR** (300 MHz, DMSO-*d*$_6$) δ 7.13 – 7.10 (m, 2H, Ar$H_{2,6}$), 6.50 (d, *J* = 8.7 Hz, 1H, ArH_5), 5.36 (s, 2H, NH_2), 4.63 (s, 2H, NH_2), 2.35 (s, 3H, CH_3); **^{13}C NMR** (75 MHz, DMSO-*d*$_6$) δ 195.4 (*C*OCH$_3$), 141.0, 133.7, 126.2, 120.4, 113.6, 112.3, 25.9 (*C*H$_3$); **FT-IR** (ATR mode) 3437 (N-H stretch), 3395 (N-H stretch), 3360 (N-H stretch), 3286 (N-H stretch), 1665, 1637, 1621, 1567, 1432, 1363, 1324, 1291, 1228, 1150, 1054, 965, 930, 878, 832 cm^{-1}; **HRMS (ESI)** *m/z* calcd for $C_8H_{11}N_2O$, $[M+H]^+$: 151.0871, found 151.0864.

Methyl 3,4-diaminobenzoate (37)

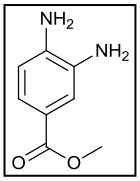

Prepared according to the general procedure with methyl 4-amino-3-nitrobenzoate (**34**, 0.485 g, 2.47 mmol) dissolved in a 2:1 mixture of EtOAc (24 mL) and MeOH (12 mL). The product was purified by column chromatography (50% EtOAc/Hexane) to yield **37** as a red-orange solid (0.374 g, 91% yield).

R_f = 0.35 (50% EtOAc/Hexane); **^{1}H NMR** (400 MHz, DMSO-*d*$_6$) δ 7.15 (d, *J* = 1.8 Hz, 1H, ArH_2), 7.09 (dd, *J* = 8.1, 1.8 Hz, 1H, ArH_6), 6.50 (d, *J* = 8.1 Hz, 1H, ArH_5), 5.27 (s, 2H, NH_2), 4.65 (s, 2H, NH_2), 3.71 (s, 3H, OCH_3); **^{13}C NMR** (101 MHz, DMSO-*d*$_6$) δ 166.8 (*C*O$_2$CH$_3$), 140.5, 133.8, 120.2, 117.2, 114.9, 112.6, 51.0 (OCH$_3$).

The NMR spectroscopy data collected for this compound compared well to literature data.[35]

General cyclisation procedure to form 2-aminobenzimidazoles 39 – 42.[36]

Cyanogen bromide (1.3 equiv) in CH_3CN was added to a solution of diamine (1.0 equiv) in H_2O/MeOH (1:1). The reaction mixture was stirred at r.t. for 18 h. Conc. NH_4OH was used to basify the reaction mixture to pH = 8, whereafter MeOH and CH_3CH were removed under reduced pressure. H_2O was added to the residual mixture and the mixture was extracted with EtOAc. The combined organic layers were dried over $MgSO_4$, filtered and concentrated under reduced pressure. Column chromatography afforded a pure product.

2-Amino-1*H*-benzo[*d*]imidazole-6-carbonitrile (39)

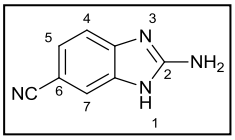

Prepared according to the general procedure, with the following amounts: Cyanogen bromide (0.665 g, 6.28 mmol), CH_3CN (0.8 mL), 3,4-diaminobenzonitrile (**35**, 0.643 g, 4.83 mmol), H_2O (8.5 mL) and MeOH (8.5 mL). H_2O (10 mL) and EtOAc (3 × 25 mL) were used in the work-up procedure. Column chromatography (2% MeOH/EtOAc → 3% MeOH/EtOAc) afforded **39** as a cream-coloured solid (0.682 g, 89% yield).

R_f = 0.21 (100% EtOAc); **mp** = 215 – 218 °C (lit.[36] mp 213 – 215 °C); **^{1}H NMR** (300 MHz, DMSO-*d*$_6$) δ 11.14 (br.s, 1H, N*H*), 7.46 (d, *J* = 1.6 Hz, 1H, Ar*H*$_7$), 7.26 (dd, *J* = 8.1, 1.6 Hz, 1H, Ar*H*$_5$), 7.20 (d, *J* = 8.1 Hz, 1H, *ArH*$_4$), 6.65 (s, 2H, N*H*$_2$); **^{13}C NMR** (101 MHz, DMSO-*d*$_6$) δ 157.7 (ArC_2), 144.0 (weak br.s), 138.0 (weak br.s), 123.9, 120.9, 114.4 (weak br.s), 112.4 (weak br.s), 100.0; **FT-IR** (ATR mode) 3421 (N-H stretch), 3324 (N-H stretch), 2213 (C≡N stretch), 1643, 1618, 1548, 1469, 1441, 1284, 823 cm^{-1}; **HRMS (ESI)** *m/z* calcd for $C_8H_7N_4$, $[M+H]^+$: 159.0671, found 159.0666.

The ^{1}H NMR spectroscopic data correlated with the literature data,[36] however small chemical shift differences were seen since the literature values were internally referenced to tetramethylsilane.

1-(2-Amino-1*H*-benzo[*d*]imidazol-6-yl)ethanone (40)

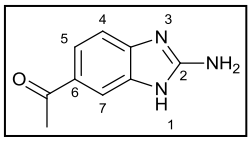

Prepared according to the general procedure, with the following amounts: Cyanogen bromide (0.347 g, 3.28 mmol), CH_3CN (0.7 mL), 1-(3,4-diaminophenyl)ethanone (**36**, 0.379 g, 2.52 mmol), H_2O (5 mL) and MeOH (5 mL). H_2O (60 mL) and EtOAc (6 × 40 mL) were used in the work-up procedure. Column chromatography (10% MeOH/DCM) afforded **40** as a yellow solid (0.383 g, 87% yield).

R_f = 0.28 (10% MeOH/DCM); **mp** = > 198 °C decomp, mp 205 – 207 °C; **^{1}H NMR** (400 MHz, DMSO-*d*$_6$) δ 7.71 (d, *J* = 1.6 Hz, 1H, Ar*H*$_7$), 7.60 (dd, *J* = 8.3, 1.6 Hz, 1H, Ar*H*$_5$), 7.14 (d, *J* = 8.3 Hz, 1H, Ar*H*$_4$), 6.61 (s, 2H, N*H*$_2$), 2.52 (s, 3H, C*H*$_3$), N*H* signal not visible due to tautomerism; **^{13}C NMR** (101 MHz, DMSO-*d*$_6$) δ 196.8 (*C*OCH_3), 157.6 (ArC_2), 145.1, 137.1, 128.5, 121.4, 111.6, 110.7, 26.5 (*C*H$_3$); **FT-IR** (ATR mode) 3328 (N-H stretch), 3139 (N-H stretch), 1649, 1621, 1558, 1453, 1358, 1280, 1233, 1194, 1099, 1020, 812 cm^{-1}; **HRMS (ESI)** *m/z* calcd for $C_9H_{10}N_3O$, $[M+H]^+$: 176.0824, found 176.0816.

6-Nitro-1*H*-benzo[*d*]imidazol-2-amine (42)

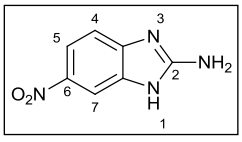

Prepared according to the general procedure, with the following amounts: Cyanogen bromide (0.225 g, 2.12 mmol, 1.6 equiv), CH_3CN (0.4 mL), 4-nitrobenzene-1,2-diamine (**38**, 0.200 g, 1.31 mmol), H_2O (3.5 mL) and MeOH (3.5 mL). The reaction mixture was stirred one additional day. H_2O (30 mL) and EtOAc (4 × 30 mL) were used in the work-up procedure. Automated column chromatography (EtOAc → 5% MeOH/EtOAc) afforded **42** as a bright yellow solid (0.24 g, quant. yield).

R_f = 0.12 (100% EtOAc); **^{1}H NMR** (300 MHz, DMSO-*d*$_6$) δ 11.25 (br.s, 1H, N*H*), 7.95 (d, *J* = 2.3 Hz, 1H, Ar*H*$_7$), 7.87 (dd, *J* = 8.7, 2.3 Hz, 1H, Ar*H*$_5$), 7.18 (d, *J* = 8.7 Hz, 1H, Ar*H*$_4$), 6.93 (br.s, 2H, N*H*$_2$); **^{13}C NMR** (75 MHz, DMSO-*d*$_6$) 159.1 (ArC_2), 150.3 (weak br.s), 139.5, 133.9 (weak br.s), 116.8, 112.2 (weak br.s), 105.4 (weak br.s); **HRMS (ESI)** *m/z* calcd for $C_7H_7N_4O_2$, $[M+H]^+$: 179.0569, found 179.0569. The carbon

signals were barely visible and were seen as very weak and broad signals, even after running the ^{13}C NMR spectroscopic analysis overnight.

The ^{1}H NMR spectroscopy data collected for this compound fitted the literature perfectly. The ^{13}C NMR data corresponded well to the literature, but small deviations were seen due to the broadness of some signals.[37]

Methyl 2-amino-1*H*-benzo[*d*]imidazole-6-carboxylate (41)

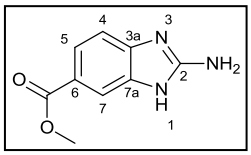

Prepared according to the general procedure, with the following amounts: Cyanogen bromide (0.307 g, 2.90 mmol), CH_3CN (0.7 mL), methyl 3,4-diaminobenzoate (**37**, 0.370 g, 2.23 mmol), H_2O (6 mL) and MeOH (6 mL). H_2O (15 mL) and EtOAc (6 × 30 mL) were used in the work-up procedure. Column chromatography (10% MeOH/DCM) afforded **41** as an orange-cream coloured solid (0.400 g, 94% yield).

R$_f$ = 0.32 (10% MeOH/DCM); **mp** = 184 – 186 °C; **^{1}H NMR** (600 MHz, DMSO-*d*$_6$) δ 7.71 (d, *J* = 1.6 Hz, 1H, Ar*H*$_7$), 7.58 (dd, *J* = 8.2, 1.6 Hz, 1H, Ar*H*$_5$), 7.14 (d, *J* = 8.2 Hz, 1H, Ar*H*$_4$), 6.55 (s, 2H, N*H*$_2$), 3.80 (s, 3H, OC*H*$_3$), N*H* signal not visible due to tautomerism; **^{13}C NMR** (151 MHz, DMSO-*d*$_6$) δ 167.2 (*C*O$_2$CH$_3$), 157.4 (Ar*C*$_2$), 144.9 (weak br.s, Ar*C*$_{3a}$), 137.2 (weak br.s, Ar*C*$_{7a}$*), 121.6 (Ar*C*$_5$H), 119.8 (Ar*C*$_6$*), 111.7 (Ar*C*$_{4+7}$H), 51.5 (O*C*H$_3$); **FT-IR** (ATR mode) 3101 (N-H stretch), 1667 (C=O stretch), 1624, 1566, 1433, 1293, 1235, 1207, 1119, 1092, 771, 744 cm^{-1}; **HRMS (ESI)** *m/z* calcd for $C_9H_{10}N_3O_2$, $[M+H]^+$: 192.0773, found 192.0779.

^{1}H,^{13}C gHSQC NMR (600/600 MHz, DMSO-*d*$_6$) δ ^{1}H/ δ ^{13}C 7.71/111.7 (Ar*H*$_7$/Ar*C*$_7$H), 7.58/121.6 (Ar*H*$_5$/Ar*C*$_5$H), 7.14/111.7 (Ar*H*$_4$/Ar*C*$_4$H), 3.80/51.5 (OC*H*$_3$/O*C*H$_3$); **^{1}H,^{13}C gHMBC NMR** (600/600 MHz, DMSO-*d*$_6$) δ ^{1}H/ δ ^{13}C **7.71**/ 167.2, 144.9, 121.6 (Ar*H*$_7$/ *C*O$_2$CH$_3$, Ar*C*$_{3a}$, Ar*C*$_5$H), **7.58**/ 167.2, 144.9, 111.7 (Ar*H*$_5$/*C*O$_2$CH$_3$, Ar*C*$_{3a}$, Ar*C*$_7$H), **7.14**/ 137.2, 119.8 (Ar*H*$_4$/ Ar*C*$_{7a+6}$), **3.80**/167.2 (OC*H*$_3$/ *C*O$_2$CH$_3$).

*Ar*C*$_{7a}$ and Ar*C*$_6$ may be reversed. The signals were assigned based on the assumption that Ar*C*$_{7a}$ and Ar*C*$_{3a}$ have a similar chemical environment.

The ^{1}H NMR spectroscopy data collected for this compound corresponded well to the available literature.[38]

Table 9.1: The 2D NMR spectra assignments (gHSQC and gHMBC) for methyl 2-amino-1H-benzo[d]imidazole-6-carboxylate (41)

^{13}C (δ ppm)	gHSQC (δ ppm)	gHMBC (δ ppm)	Carbon assignment
51.5	3.80		O*C*H$_3$
111.7	7.14, 7.71	7.58	Ar*C*$_{4+7}$H
119.8	–	7.14	Ar*C*$_{7a/6}$
121.6	7.58 (dd)	7.71	Ar*C*$_5$H
137.2	–	7.14	Ar*C*$_{7a/6}$
144.9	–	7.71, 7.58	Ar*C*$_{3a}$
157.4	–	–	Ar*C*$_2$
167.2	–	7.71, 7.58, 3.80	*C*O$_2$CH$_3$

General procedure for the synthesis of *N*-(4-methoxybenzyl) ureas (6, 59 – 61) from 2-aminobenzimidazoles.[19]

To a solution of the amine (1.0 equiv) and *N*-(4-methoxybenzyl)-1*H*-imidazole-1-carboxamide (**46**, 1.3 equiv) in DMF (3.5 – 9 mL) were added 60% NaH in mineral oil (1.4 equiv) in portions over 20 min. The reaction mixture was left to stir for 20 h at r.t. Thereafter, another portion of 60% NaH in mineral oil (0.4 equiv) was added to the reaction mixture to ensure that all *N*-(4-methoxybenzyl)-1*H*-imidazole-1-carboxamide react and the reaction mixture was left to stir for 1 h. After the addition of EtOAc (35 – 100 mL), the reaction mixture was washed with a sat. aq. NH_4Cl (4 × 30 mL). The organic layer was then washed with 1 M HCl (30 mL) to remove the remaining starting material and was kept aside. The combined aqueous layers were extracted with EtOAc (2 × 30 mL) and the resultant organic portion (60 mL) was washed with sat. aq. NH_4Cl (2 × 30 mL). All of the organic layers were combined and dried over $MgSO_4$, filtered and concentrated *in vacuo*. The crude product was purified by column chromatography to yield ureas **6, 59 – 61**.

1-(6-Cyano-1*H*-benzo[*d*]imidazol-2-yl)-3-(4-methoxybenzyl)urea (6)

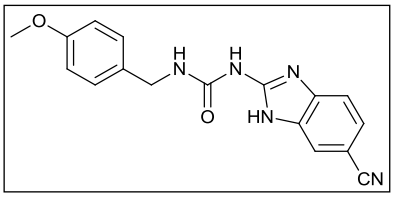

Prepared according to the general procedure, with the following amounts: 2-Amino-1*H*-benzo[*d*]imidazole-6-carbonitrile (**39**, 0.060 g, 0.38 mmol), *N*-(4-methoxybenzyl)-1*H*-imidazole-1-carboxamide (**46**, 0.13 g, 0.56 mmol, 1.5 equiv), 60% NaH in mineral oil (0.022 g + 0.020 g, 1.1 mmol, 2.9 equiv). The product was purified by column chromatography (5% MeOH/15% EtOAc/DCM) to yield **6** as a white solid (0.060 g, 49% yield).

R_f = 0.30 (5% MeOH/15% EtOAc/DCM); **mp** = > 230 °C decomp; **^{1}H NMR** (400 MHz, DMSO-*d*$_6$) δ 12.09 (br.s, 1H, N*H*), 10.21 (br.s, 1H, N*H*), 7.76 (s, 1H, ArH_7), 7.48 (br.t, 1H, NH), 7.44 – 7.41 (m, 2H, 2 × Ar*H*), 7.26 (d, *J* = 8.7 Hz, 2H, 2 × ArH), 6.91 (d, *J* = 8.7 Hz, 2H, 2 × ArH), 4.32 (d, *J* = 5.8 Hz, 2H, CH_2), 3.73 (s, 3H, OCH_3); **^{13}C NMR** (101 MHz, DMSO-*d*$_6$) δ 158.3, 153.9, 150.5, 131.3, 128.6, 124.6, 120.4, 113.8, 55.1, 42.4; five carbon signals were not visible in the spectrum; **FT-IR** (ATR mode) 3398 (N-H stretch), 3309 (N-H stretch), 2219 (C≡N stretch), 1668, 1649, 1588, 1506, 1463, 1249, 1223, 1174, 1027, 827, 812, 741 cm^{-1}; **HRMS (ESI)** *m/z* calcd for $C_{17}H_{16}N_5O_2$, $[M+H]^+$: 322.1304, found 322.1309; **UPLC**: Purity 99%, r.t = 5.77 min, acetonitrile/H_2O (0.1% formic acid) 2/98.

1-(6-Acetyl-1*H*-benzo[*d*]imidazol-2-yl)-3-(4-methoxybenzyl)urea (59)

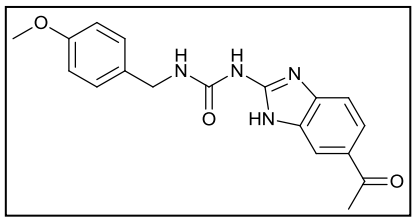

Prepared according to the general procedure, with the following amounts: 1-(2-Amino-1*H*-benzo[*d*]imidazol-6-yl)ethanone (**40**, 0.383 g, 2.19 mmol), *N*-(4-methoxybenzyl)-1*H*-imidazole-1-carboxamide (**46**, 0.650 g, 2.81 mmol), 60% NaH in mineral oil (0.123 g + 0.0350 g, 3.95 mmol). The product was purified by column chromatography (3% MeOH/15% EtOAc/DCM) to yield **59** as a yellow solid (0.554 g, 75% yield).

R_f = 0.25 (3% MeOH/15% EtOAc/DCM); **mp** = > 200 °C decomp; **^{1}H NMR** (300 MHz, DMSO-*d*$_6$) δ 11.91 (br.s, 1H, N*H*), 10.18 (br.s, 1H, N*H*), 8.00 (s, 1H, ArH_7), 7.72 (dd, *J* = 8.3, 1.5 Hz, 1H, ArH_5), 7.55 (br.t, 1H, N*H*), 7.42 (d, *J* = 8.3 Hz, 1H, ArH_4), 7.27 (d, *J* = 8.6 Hz, 2H, 2 × Ar*H*), 6.91 (d, *J* = 8.6 Hz, 2H, 2 × Ar*H*), 4.34 (d, *J* = 5.8 Hz, 2H, CH_2), 3.73 (s, 3H, OCH_3), 2.56 (s, 3H, COCH_3); **^{13}C NMR** (75 MHz, DMSO-*d*$_6$) δ 197.1 (*C*OCH$_3$), 158.4, 154.1, 150.4, 131.5, 130.1, 128.6, 121.8, 113.8, 55.1, 42.4, 26.7 (CO*C*H$_3$); four carbon signals were not visible in the spectrum; **FT-IR** (ATR mode) 3305 (N-H stretch), 1666, 1651, 1579, 1501, 1461, 1304, 1244, 1180, 1110, 818, 806, 743 cm^{-1}; **HRMS (ESI)** *m/z* calcd for $C_{18}H_{19}N_4O_3$, $[M+H]^+$: 339.1457, found 339.1443; **UPLC**: Purity 99%, r.t = 4.43 min, acetonitrile/H_2O (0.1% formic acid) 5/95.

Methyl 2-[3-(4-methoxybenzyl)ureido]-1*H*-benzo[*d*]imidazole-6-carboxylate (60)

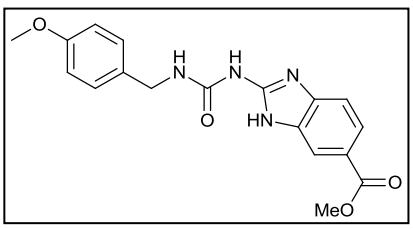

Prepared according to the general procedure, with the following amounts: Methyl 2-amino-1*H*-benzo[*d*]imidazole-6-carboxylate (**41**, 0.400 g, 2.09 mmol), *N*-(4-methoxybenzyl)-1*H*-imidazole-1-carboxamide (**46**, 0.629 g, 2.72 mmol), 60% NaH in mineral oil (0.117 g + 0.033 g, 3.75 mmol). The product was purified by column chromatography (2% MeOH/15% EtOAc/DCM) to afford **60** as a white solid (0.450 g, 61% yield).

R_f = 0.18 (3% MeOH/15% EtOAc/DCM); **mp** = > 260 °C decomp; **^{1}H NMR** (300 MHz, DMSO-*d_6*) δ 11.94 (br.s, 1H, N*H*), 10.17 (br.s, 1H, N*H*), 8.00 (br.s, 1H, Ar*H_7*), 7.70 (dd, *J* = 8.3, 1.6 Hz, 1H, Ar*H_5*), 7.50 (br.t, 1H, N*H*), 7.41 (d, *J* = 8.3 Hz, 1H, Ar*H_4*), 7.27 (d, *J* = 8.6 Hz, 2H, 2 × Ar*H*), 6.91 (d, *J* = 8.6 Hz, 2H, 2 × Ar*H*), 4.33 (d, *J* = 5.8 Hz, 2H, C*H_2*), 3.83 (s, 3H, CO_2C*H_3*), 3.73 (s, 3H, PhOC*H_3*); **^{13}C NMR** (75 MHz, DMSO-*d_6*) δ 166.9 (*C*O_2CH_3), 158.3, 154.0, 150.2, 131.4, 128.6, 122.3, 113.8, 55.1, 51.8 (CO_2*C*H_3), 42.4; five carbon signals were not visible in the spectrum; **FT-IR** (ATR mode) 3374 (N-H stretch), 3325 (N-H stretch), 1710 (C=O stretch), 1668, 1653, 1598, 1581, 1501, 1466, 1300, 1246, 1225, 1197, 1180, 1115, 1036, 817, 769, 742 cm^{-1}; **HRMS (ESI)** *m/z* calcd for $C_{18}H_{19}N_4O_4$, $[M+H]^+$: 355.1406, found 355.1406.

1-(4-Methoxybenzyl)-3-(6-nitro-1*H*-benzo[*d*]imidazol-2-yl)urea (61)

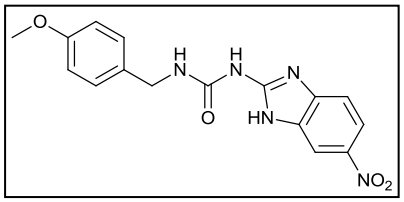

Prepared according to the general procedure, with the following amounts: 6-Nitro-1*H*-benzo[*d*]imidazol-2-amine (**42**, 0.400 g, 2.25 mmol), *N*-(4-methoxybenzyl)-1*H*-imidazole-1-carboxamide (**46**, 0.670 g, 2.90 mmol), 60% NaH in mineral oil (0.126 g + 0.036 g, 4.05 mmol). The product was purified by column chromatography (2.5% MeOH/25% EtOAc/DCM) to yield **61** as a yellow solid (0.438 g, 57% yield).

R_f = 0.22 (2.5% MeOH/25% EtOAc/DCM); **mp** = > 280 °C decomp; **^{1}H NMR** (300 MHz, DMSO-*d_6*) δ 12.28 (br.s, 1H, N*H*), 10.37 (br.s, 1H, N*H*), 8.25 (br.s, 1H, Ar*H*), 7.99 (dd, *J* = 8.8, 2.3 Hz, 1H, Ar*H_5*), 7.49 (br.s, 1H, Ar*H*), 7.39 (br.t, 1H, N*H*), 7.27 (d, *J* = 8.6 Hz, 2H, 2 × Ar*H*), 6.90 (d, *J* = 8.6 Hz, 2H, 2 × Ar*H*), 4.33 (d, *J* = 5.8 Hz, 2H, C*H_2*), 3.73 (s, 3H, OC*H_3*); **^{13}C NMR** (75 MHz, DMSO-*d_6*) δ 158.4, 153.8, 131.3, 128.7, 113.8, 55.1, 42.4; seven carbon signals were not visible in the spectrum; **FT-IR** (ATR mode) 3344 (N-H stretch), 3300 (N-H stretch), 1673, 1658, 1588, 1493, 1464, 1327 (N=O *sym* stretch), 1293, 1242, 1223, 1175, 1056, 1027, 817, 740 cm^{-1}; **HRMS (ESI)** *m/z* calcd for $C_{16}H_{16}N_5O_4$, $[M+H]^+$: 342.1202, found 342.1189.

Very weak, broad signals were present on the baseline of the ^{13}C NMR spectra, which could represent some quaternary carbons. Due to the low S/N ratio, these signals could not be selected unambiguously, and are not listed in the ^{13}C NMR spectroscopic data.

1-[6-(2-Bromoacetyl)benzo[*d*]thiazol-2-yl]-3-(4-methoxybenzyl)urea (7)[39]

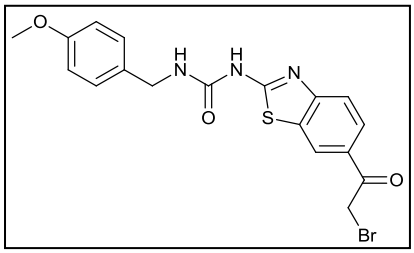

Trimethylphenylammonium tribromide (0.098 g, 0.26 mmol, 1.1 equiv) was added to a stirred suspension of 1-(6-acetylbenzo[*d*]thiazol-2-yl)-3-(4-methoxybenzyl)urea (**56**, 0.084 g, 0.24, 1.0 equiv) in THF (4 mL), over 20 minutes. The reaction mixture was stirred at 30 °C for 64 h, whereafter the solvent was removed *in vacuo*, at 30 °C. The crude product was resuspended into EtOAc (60 mL) and washed with sat. aq. $NaHCO_3$ (20 mL) and brine (20 mL). The organic layer was concentrated *in vacuo.* Column chromatography (20% EtOAc/DCM) was used to obtain the pure product **7** as an off-white solid (0.036 g, 35% yield).

R_f = 0.41 (20% EtOAc/DCM); **mp** = > 182 °C decomp; **^{1}H NMR** (300 MHz, DMSO-d_6) δ 11.08 (br.s, 1H, N*H*), 8.62 (d, *J* = 1.7 Hz, 1H, ArH_7), 7.99 (dd, *J* = 8.5, 1.7 Hz, 1H, ArH_5), 7.70 (d, *J* = 8.5 Hz, 1H, ArH_4), 7.26 (d, *J* = 8.7 Hz, 2H, 2 × Ar*H*), 7.21 (br.t, 1H, N*H*), 6.91 (d, *J* = 8.7 Hz, 2H, 2 × Ar*H*), 4.93 (s, 2H, CH_2Br), 4.31 (d, *J* = 5.8 Hz, 2H, NHCH_2), 3.73 (s, 3H, OCH_3); **^{13}C NMR** (75 MHz, DMSO-d_6) δ 190.5 (*C*OCH_2Br), 163.7, 158.4, 153.7, 153.2, 131.8, 131.0, 128.7, 128.4, 126.7, 123.3, 119.4, 113.8, 55.1, 42.5, 34.0 (*C*H_2Br); **FT-IR** (ATR mode) 3282 (N-H stretch), 1678 (C=O stretch), 1667 (C=O stretch), 1551, 1531, 1513, 1274, 1251, 1236 cm^{-1}; **HRMS (ESI)** *m/z* calcd for $C_{18}H_{17}N_3O_3S^{79}Br$, $[M+H]^+$: 434.0174, found 434.0178, *m/z* calcd for $C_{18}H_{17}N_3O_3S^{81}Br$, $[M+H]^+$: 436.0174, found 436.0162; **UPLC**: Purity >95%, r.t = 6.77 min, acetonitrile/H_2O (0.1% formic acid) 5/95.

1-[6-(2-Bromoacetyl)-1*H*-benzo[*d*]imidazol-2-yl]-3-(4-methoxybenzyl)urea (8)[40]

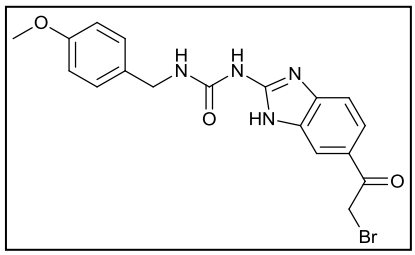

Trimethylsilyl trifluoromethanesulfonate (0.28 mL, 1.5 mmol, 3.9 equiv) and *N*,*N*-diisopropylethylamine (0.35 mL, 2.0 mmol, 5,2 equiv) were added to a suspension of 1-(6-acetyl-1*H*-benzo[*d*]imidazol-2-yl)-3-(4-methoxybenzyl)urea (**59**, 0.130 g, 0.384 mmol, 1.0 equiv) in DCM (4 mL) at 0 °C. The reaction mixture was stirred at 0 °C for 1.5 h, whereafter it was stirred at r.t. for 40 min and then at 30 °C for 40 min. The reaction was monitored by TLC and was judged to be incomplete. The solution was treated with additional equivalents of trimethylsilyl trifluoromethanesulfonate (0.28 mL, 1.5 mmol, 3.9 equiv) and *N*,*N*-diisopropylethylamine (0.35 mL, 2.0 mmol, 5,2 equiv) at 0 °C and was left to stir at r.t. for 20 h.[‡] The orange solution was diluted with DCM (35 mL) and washed with cold sat. aq. $NaHCO_3$

[‡] After increasing the equivalents and stirring overnight, the reaction was still incomplete, as judged by the presence of remaining starting material on the TLC plate. However a significant amount of silyl enol ether was present in the reaction mixture and the crude mixture could be utilised further to perform the bromination step.

(25 mL). The organic layer was dried over $MgSO_4$, filtered and concentrated *in vacuo* to yield the crude silyl enol ether intermediate; $\mathbf{R_f}$ = 0.74 (100% EtOAc). The crude intermediate was dissolved in THF (4 mL) and treated with *N*-bromosuccinimide (0.051 g, 0.29 mmol, 0.76 equiv) and $NaHCO_3$ powder (0.048 g, 0.57 mmol, 1.5 equiv) at −78 °C. The reaction was stirred at −78°C for 1.5 h, after which TLC indicated that the majority of silyl enol ether had been consumed. The solution was partitioned between EtOAc (25 mL) and cold sat. aq. $NaHCO_3$ (25 mL). The organic layer was dried over $MgSO_4$, filtered and concentrated *in vacuo*. The product was purified by column chromatography (50 – 70% EtOAc/DCM) to yield **8** as a light yellow solid (0.077 g, 48% yield).

$\mathbf{R_f}$ = 0.50 (100% EtOAc); **mp** = > 200 °C decomp; **^{1}H NMR** (400 MHz, DMSO-*d*$_6$) δ 8.05 (s, 1H, Ar*H*$_7$), 7.77 (dd, *J* = 8.4, 1.1 Hz, 1H, Ar*H*$_5$), 7.54 (br.t, 1H, N*H*), 7.45 (d, *J* = 8.4 Hz, 1H, Ar*H*$_4$), 7.27 (d, *J* = 8.6 Hz, 2H, 2 × Ar*H*), 6.91 (d, *J* = 8.6 Hz, 2H, 2 × Ar*H*), 4.88 (s, 2H, BrC*H*$_2$), 4.34 (d, *J* = 5.7 Hz, 2H, HNC*H*$_2$), 3.73 (s, 3H, OC*H*$_3$), two NH signals not visible due to tautomerism; **^{13}C NMR** (101 MHz, DMSO-*d*$_6$) δ 191.0 (*C*OCH$_2$Br), 158.4, 153.8, 150.3, 131.4, 128.6, 127.1, 122.5, 113.8, 55.1, 42.4, 34.0 (Br-*C*H$_2$), four carbon signals were not visible in the spectrum; **FT-IR** (ATR mode) 3356 (N-H stretch), 3307 (N-H stretch), 1647, 1571, 1504, 1463, 1300, 1246, 1224, 1176, 1097, 1037, 812, 743 cm^{-1}; **HRMS (ESI)** *m/z* calcd for $C_{18}H_{18}N_4O_3{}^{79}Br$, $[M+H]^+$: 417.0562, found 417.0565, *m/z* calcd for $C_{18}H_{18}N_4O_3{}^{81}Br$, $[M+H]^+$: 419.0562, found 419.0545; **UPLC**: Purity 98%, r.t = 3.81 min, acetonitrile/H_2O (0.1% formic acid) 5/95.

General reduction procedure to synthesise the aminobenzazole ureas 64 – 65.[41,42]

The nitrobenzazole urea was dissolved in DMF (5 mL), whereafter MeOH (15 mL) and 10% palladium on carbon (10% w/w) were added to the stirred solution. The mixture was hydrogenated at 60 °C for 4.5 h, by employing a H_2 balloon. The mixture was filtered through a bed consisting of celite and cotton wool and concentrated under reduced pressure. The crude product was diluted with EtOAc (80 mL) and washed with H_2O (4 × 20 mL). The organic layer was dried over $MgSO_4$, filtered and concentrated *in vacuo*. The pure product was isolated by column chromatography.

1-(6-Aminobenzo[*d*]thiazol-2-yl)-3-(4-methoxybenzyl)urea (64)

Prepared according to the general procedure with 1-(4-methoxybenzyl)-3-(6-nitrobenzo[*d*]thiazol-2-yl)urea (**58**, 0.150 g, 0.419 mmol). Column chromatography (5% MeOH/15% EtOAc/DCM) yielded a light yellow solid (**64**, 0.055 g, 40% yield).

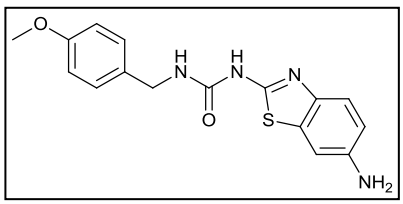

$\mathbf{R_f}$ = 0.34 (5% MeOH/15% EtOAc/DCM); **mp** = 190 – 191 °C; **^{1}H NMR** (300 MHz, DMSO-*d*$_6$) δ 10.36 (s, 1H, N*H*), 7.29 (d, *J* = 8.5 Hz, 1H, Ar*H*$_4$), 7.24 (d, *J* = 8.5 Hz, 2H, 2 × Ar*H*), 7.11 (br.t, 1H, N*H*), 6.95 (d, *J* = 1.9 Hz, 1H, Ar*H*$_7$), 6.90 (d, *J* = 8.5 Hz, 2H, 2 × Ar*H*), 6.64 (dd, *J* = 8.5, 1.9 Hz, 1H, Ar*H*$_5$), 5.02 (s, 2H, N*H*$_2$),

4.28 (d, *J* = 5.7 Hz, 2H, C*H*$_2$), 3.73 (s, 3H, OC*H*$_3$); **^{13}C NMR** (75 MHz, DMSO-*d*$_6$) δ 158.3, 155.2, 153.9, 145.0, 140.2, 132.6, 131.4, 128.6, 120.0, 113.9, 113.8, 104.4, 55.1, 42.4; **FT-IR** (ATR mode) 3319 (N-H stretch), 1666 (C=O stretch), 1579, 1562, 1512, 1456, 1269, 1228, 1177, 1029, 823, 803, 718 cm^{-1}; **HRMS (ESI)** *m/z* calcd for $C_{16}H_{17}N_4O_2S$, $[M+H]^+$: 329.1072, found 329.1065.

1-(6-Amino-1*H*-benzo[*d*]imidazol-2-yl)-3-(4-methoxybenzyl)urea (65)

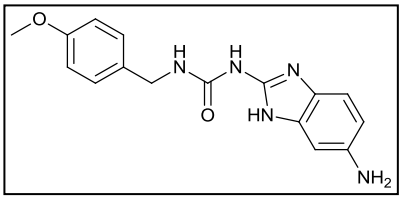

Prepared according to the general procedure with 1-(4-methoxybenzyl)-3-(6-nitro-1*H*-benzo[*d*]imidazol-2-yl)urea (**61**, 0.120 g, 0.352 mmol). Column chromatography (5 – 7 % MeOH/DCM) yielded a pink-white solid (**65**, 0.094 g, 85% yield).

R$_f$ = 0.33 (5% MeOH/DCM); **mp** = 184 – 186 °C; **^{1}H NMR** (300 MHz, DMSO-*d*$_6$) δ 11.69 – 8.81 (br.s, 2H, 2 × N*H*), 7.91 (br.s, 1H, N*H*), 7.25 (d, *J* = 8.6 Hz, 2H, 2 × Ar*H*), 7.00 (d, *J* = 8.3 Hz, 1H, Ar*H*$_4$), 6.90 (d, *J* = 8.6 Hz, 2H, 2 × Ar*H*), 6.57 (d, *J* = 2.0 Hz, 1H, Ar*H*$_7$), 6.35 (dd, *J* = 8.3, 2.0 Hz, 1H, Ar*H*$_5$), 5.01 – 4.32 (br.s, 2H, N*H*$_2$), 4.32 (d, *J* = 5.8 Hz, 2H, C*H*$_2$), 3.73 (s, 3H, OC*H*$_3$); **^{13}C NMR** (101 MHz, DMSO-*d*$_6$) δ 158.3, 154.7, 147.1, 143.2, 136.2 (weak br.s), 131.8, 128.5, 113.8, 109.3, 97.8, 55.1, 42.3; two carbon signals were not visible in the spectrum; **FT-IR** (ATR mode) 3388 (N-H stretch), 3338 (N-H stretch), 1647, 1604, 1506, 1483, 1242, 1221, 1175, 1030, 830, 816, 736 cm^{-1}; **HRMS (ESI)** *m/z* calcd for $C_{16}H_{18}N_5O_2$, $[M+H]^+$: 312.1460, found 312.1457.

X-ray crystal structure determination (**65**)

Table 9.2: Selected crystallographic data of compound 65

Molecular formula (dimer)	$C_{32}H_{30}N_{10}O_4$ [§]
***Mr*/ g.mol^{-1}**	618.66 [§]
Temperature/ K	100
Crystal system	Monoclinic
Space group	*P*21
***a*/ ♦**	4.9564(1)
***b*/ ♦**	26.216(5)
***c*/ ♦**	11.040(2)
Σ/∀	90.00
T/∀	96.004(3)

[§] Four hydrogens are absent in the molecular formula and molar mass of the dimer in the asymmetric unit, since the location of the primary amine protons could not be located in the electron density map.

Υ/∀	90.00
***V* / ◆^{3}**	1426.7(5)
Z	2
}/mm^{-1}	0.10
R_1 [I > 2′(I)]	0.037
wR_2 (F^2)	0.183

Table 9.3: Hydrogen-bond geometry (Å, °) for 65

D*—H···*A	***D*—H**	**H···*A***	***D*···*A***	***D*—H···*A***
N6—H6···O3^{i}	0.87	2.32	3.125	154
N1—H1···O1^{ii}	0.93	2.21	3.137	174
N2—H2···N8	0.91	1.96	2.862	170
N3—H3···O1	0.95	2.09	2.715	122
C25—H25A···N10^{iii}	0.96	2.53	3.471	165.6
N4—H10···N7	1.15	1.70	2.837	170

Symmetry codes: (i) *x*+1, *y*, *z*; (ii) *x*−1, *y*, *z*; (iii) −*x*+1, *y*−1/2, −*z*.

General procedure for the synthesis of acrylamides 13 – 14 from their amine precursors.

THF and NEt_3 (1.1 equiv) were added to a stirred solution of the aminobenzazole urea (1.0 equiv) in DMF. The mixture was cooled to 0 °C before the dropwise addition of acryloyl chloride (1.1 equiv). The reaction mixture was left to stir at 0 °C for 30 min and then at r.t. for 45 min. The mixture was quenched with H_2O (10 mL) and concentrated *in vacuo*. The crude product was diluted with EtOAc (60 mL) and washed with H_2O (4 × 20 mL). A small amount of product remained in the aqueous layer, therefore the combined aqueous layer was extracted with EtOAc (3 × 30 mL) and the newly formed organic layer (90 mL) was washed with H_2O (3 × 20 mL). All organic layers were combined, dried over $MgSO_4$, filtered and concentrated *in vacuo*. The pure product was isolated by column chromatography.

***N*-{2-[3-(4-methoxybenzyl)ureido]benzo[*d*]thiazol-6-yl}acrylamide (13)**

Prepared according to the general procedure, utilising THF (2 mL), DMF (1 mL), 1-(6-aminobenzo[*d*]thiazol-2-yl)-3-(4-methoxybenzyl)urea (**64**, 0.100 g, 0.305 mmol), NEt_3 (0.05 mL, 0.34 mmol) and acryloyl chloride (0.030 g, 0.33 mmol).

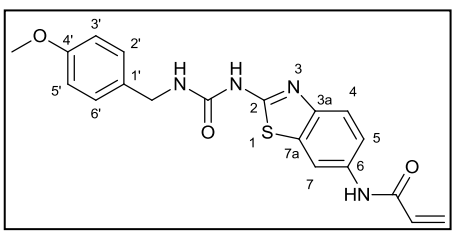

Column chromatography (5% MeOH/DCM) afforded **13** as a white solid (0.063 g, 54% yield).

R_f = 0.22 (5% MeOH/DCM); **mp** = 192 – 195 °C; **^{1}H NMR** (300 MHz, DMSO-*d*$_6$) δ 10.67 (br.s, 1H, N*H*), 10.23 (s, 1H, N*H*COCHCH$_2$), 8.30 (d, *J* = 1.8 Hz, 1H, Ar*H*$_7$), 7.56 (d, *J* = 8.7 Hz, 1H, Ar*H*$_4$), 7.51 (dd, *J* = 8.7, 1.8 Hz, 1H, Ar*H*$_5$), 7.25 (d, *J* = 8.7 Hz, 2H, Ar*H*$_{2'+6'}$), 7.13 (br.t, 1H, *H*NCH$_2$), 6.91 (d, *J* = 8.7 Hz, 2H, Ar*H*$_{3'+5'}$), 6.45 (dd, $^3J_{trans}$ = 17.0, $^3J_{cis}$ = 10.0 Hz, 1H, NHCOC*H*CH$_2$), 6.26 (dd, $^3J_{trans}$ = 17.0, $^2J_{gem}$ = 2.2 Hz, 1H, NHCOCHC*H*$_2$), 5.75 (dd, $^3J_{cis}$ = 10.0, $^2J_{gem}$ = 2.2 Hz, 1H, NHCOCHC*H*$_2$), 4.30 (d, *J* = 5.8 Hz, 2H, HNC*H*$_2$), 3.73 (s, 3H, OC*H*$_3$); **^{13}C NMR** (75 MHz, DMSO-*d*$_6$) δ 163.0 (NH*C*OCHCH$_2$), 159.0 (ArC$_2$), 158.4 (Ar*C*$_{4'}$), 153.8 (HN*C*ONH), 145.3 (Ar*C*$_{3a}$), 134.3 (Ar*C*$_6$), 131.9 (NHCO*C*HCH$_2$), 131.3 (Ar*C*$_{1'}$), 128.7 (Ar*C*$_{2'+6'}$H), 126.7 (NHCOCH*C*H$_2$), 119.6 (Ar*C*$_4$H), 118.3 (Ar*C*$_5$H), 113.8 (Ar*C*$_{3'+5'}$H), 111.7 (Ar*C*$_7$H), 55.1 (O*C*H$_3$), 42.5 (HN*C*H$_2$), one quaternary carbon signal was not visible in the spectrum; **FT-IR** (ATR mode) 3267 (N-H stretch), 1678 (C=O stretch), 1656 (C=O stretch), 1612, 1536, 1513, 1455, 1408, 1269, 1240, 1225, 1196, 1176, 826 cm^{-1}; **HRMS (ESI)** *m/z* calcd for $C_{19}H_{19}N_4O_3S$, $[M+H]^+$: 383.1178, found 383.1180; **UPLC**: Purity 94%, r.t = 5.43 min, acetonitrile/H_2O (0.1% formic acid) 5/95.

^{1}H,^{13}C gHSQC NMR (300/300 MHz, DMSO-*d*$_6$) δ ^{1}H/ δ ^{13}C 8.30/111.7 (Ar*H*$_7$/ Ar*C*$_7$H), 7.56/119.6 (Ar*H*$_4$/ Ar*C*$_4$H), 7.51/118.3 (Ar*H*$_5$/ Ar*C*$_5$H), 7.25/128.7 (Ar*H*$_{2'+6'}$/Ar*C*$_{2'+6'}$H), 6.91/113.8 (Ar*H*$_{3'+5'}$/Ar*C*$_{3'+5'}$H), 6.45/131.9 (NHCOC*H*CH$_2$/NHCO*C*HCH$_2$), 6.26/126.7 (NHCOCHC*H*$_{trans}$/NHCOCH*C*H$_2$), 5.75/126.7 (NHCOCHC*H*$_{cis}$/NHCOCH*C*H$_2$), 4.30/42.5 (HNC*H*$_2$/ HN*C*H$_2$), 3.73/55.1 (OC*H*$_3$/O*C*H$_3$);

^{1}H,^{13}C gHMBC NMR (300/300 MHz, DMSO-*d*$_6$) δ ^{1}H/ δ ^{13}C **10.23**/ 163.0, 134.3, 118.3, 111.7 (N*H*COCHCH$_2$/ NH*C*OCHCH$_2$, Ar*C*$_6$, Ar*C*$_5$H, Ar*C*$_7$H), **8.30**/ 145.3, 134.3, 118.3 (Ar*H*$_7$/ Ar*C*$_{3a}$, Ar*C*$_6$, Ar*C*$_5$H), **7.56**/ 134.3, (Ar*H*$_4$/ Ar*C*$_6$), **7.51**/ 145.3, 111.7 (Ar*H*$_5$/ Ar*C*$_{3a}$, Ar*C*$_7$H), **7.25**/ 158.4, 128.7, 113.8, 42.5 (Ar*H*$_{2'+6'}$/ Ar*C*$_{4'}$, Ar*C*$_{2'+6'}$H, Ar*C*$_{3'+5'}$H, HNCH$_2$), **7.13**/ 153.8 (*H*NCH$_2$/ HN*C*ONH), **6.91**/ 158.4, 131.3, 113.8 (Ar*H*$_{3'+5'}$/ Ar*C*$_{4'}$, Ar*C*$_{1'}$, Ar*C*$_{3'+5'}$H), **6.45**/ 163.0, 126.7 (NHCOC*H*CH$_2$/ NH*C*OCHCH$_2$, NHCOCH*C*H$_2$), **6.26**/ 163.0, 131.9 (NHCOCHC*H*$_{trans}$/ NH*C*OCHCH$_2$, NHCO*C*HCH$_2$), **5.75**/ 163.0 (NHCOCHC*H*$_{cis}$/ NH*C*OCHCH$_2$), **4.30**/ 153.8, 131.3, 128.7 (HNC*H*$_2$/ HN*C*ONH, Ar*C*$_{1'}$, Ar*C*$_{2'+6'}$H), **3.73**/ 158.4 (OC*H*$_3$/ Ar*C*$_{4'}$).

The 2D NMR spectra assignments (gHSQC and gHMBC) for *N*-{2-[3-(4-methoxybenzyl)ureido]benzo[*d*]thiazol-6-yl}acrylamide (13)

^{13}C (δ ppm)	**gHSQC (δ ppm)**	**gHMBC (δ ppm)**	**Carbon assignment**
42.5	4.30	7.25	HNC*H*$_2$
55.1	3.73	–	OC*H*$_3$
111.7	8.30	10.23, 7.51	Ar*C*$_7$H
113.8	6.91	7.25, 6.91	Ar*C*$_{3'+5'}$H

118.3	7.51 (dd)	10.23, 8.30	Ar*C*$_5$H
119.6	7.56	–	Ar*C*$_4$H
126.7	6.26, 5.75	6.45	NHCOCH*C*H$_2$
128.7	7.25	7.25, 4.30	Ar*C*$_{2'+6'}$H
131.3	–	6.91, 4.30	Ar*C*$_{1'}$
131.9	6.45	6.26	NHCO*C*HCH$_2$
134.3	–	10.23, 8.30, 7.56	Ar*C*$_6$
145.3	–	8.30, 7.51	Ar*C*$_{3a}$
153.8	–	7.13, 4.30	HN*C*ONH
158.4	–	7.25, 6.91, 3.73	Ar*C*$_{4'}$
159.0	–	–	Ar*C*$_2$
163.0	–	10.23, 6.45, 6.26, 5.75	NH*C*OCHCH$_2$

_N_-{2-[3-(4-methoxybenzyl)ureido]-1_H_-benzo[_d_]imidazol-6-yl}acrylamide (14)

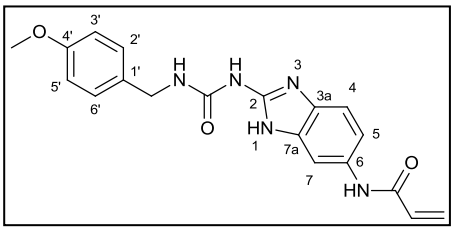

Prepared according to the general procedure, utilising THF (4 mL), DMF (2 mL), 1-(6-amino-1*H*-benzo[*d*]imidazol-2-yl)-3-(4-methoxybenzyl)urea (**65**, 0.230 g, 0.739 mmol), NEt$_3$ (0.11 mL, 0.79 mmol) and acryloyl chloride (0.070 g, 0.77 mmol). Column chromatography (7% MeOH/30% EtOAc/DCM) afforded **14** as a white solid (0.109 g, 40% yield).

R$_f$ = 0.24 (7% MeOH/30% EtOAc/DCM); **mp** = 188 – 192 °C; **^{1}H NMR** (400 MHz, DMSO-*d*$_6$) δ 11.49 (br.s, 1H, N*H*), 10.01 (s, 1H, N*H*COCHCH$_2$), 9.92 (br.s, 1H, N*H*), 7.86 (s, 1H, Ar*H*$_7$), 7.72 (br.s, 1H, N*H*), 7.27 – 7.25 (m, 3H, Ar*H*$_{2'+6'}$, Ar*H*$_4$), 7.22 (dd, *J* = 8.6, 1.2 Hz, 1H, Ar*H*$_5$), 6.91 (d, *J* = 8.7 Hz, 2H, Ar*H*$_{3'+5'}$), 6.45 (dd, $^3J_{trans}$ = 17.0, $^3J_{cis}$ = 10.1 Hz, 1H, NHCOC*H*CH$_2$), 6.23 (dd, $^3J_{trans}$ = 17.0, $^2J_{gem}$ = 2.1 Hz, 1H, NHCOCHC*H*$_2$), 5.70 (dd, $^3J_{cis}$ = 10.1, $^2J_{gem}$ = 2.1 Hz, 1H, NHCOCHC*H*$_2$), 4.33 (d, *J* = 5.8 Hz, 2H, HNC*H*$_2$), 3.73 (s, 3H, OC*H*$_3$); **^{13}C NMR** (101 MHz, DMSO-*d*$_6$) δ 162.7 (NH*C*OCHCH$_2$), 158.3 (Ar*C*$_{4'}$), 154.3 (HN*C*ONH), 148.6, 132.7 (Ar*C*$_{3a/6/7a}$), 132.3 (NHCO*C*HCH$_2$), 131.6 (Ar*C*$_{1'}$), 128.6 (Ar*C*$_{2'+6'}$H), 126.0 (NHCOCH*C*H$_2$), 113.8 (Ar*C*$_{3'+5'}$H), 113.4 (Ar*C*$_5$H), 104.3 (weak br.s), 55.1 (O*C*H$_3$), 42.3 (HN*C*H$_2$); three carbon signals were not visible in the spectrum; **FT-IR** (ATR mode) 3281 (N-H stretch), 1653, 1548, 1510, 1483, 1218, 1176, 803, 741 cm^{-1}; **HRMS (ESI)** *m/z* calcd for $C_{19}H_{20}N_5O_3$, $[M+H]^+$: 366.1566, found 366.1569; **UPLC**: Purity 95%, r.t = 3.73 min, acetonitrile/H_2O (0.1% formic acid) 5/95.

^{1}H,^{13}C gHSQC NMR (400/400 MHz, DMSO-*d*$_6$) δ ^{1}H/ δ ^{13}C 7.27 – 7.25 (m)/128.6 (Ar*H*$_{2'+6'}$/ Ar*C*$_{2'+6'}$H), 7.22/113.4 (Ar*CH*$_5$/Ar*C*$_5$H), 6.91/113.8 (ArC$_{3'+5'}$*H*/ Ar*C*$_{3'+5'}$H), 6.45/132.3 (NHCOC*H*CH$_2$/ NHCO*C*HCH$_2$), 6.23/126.0 (NHCOCHC*H*$_{trans}$/ NHCOCH*C*H$_2$), 5.70/126.0 (NHCOCHC*H*$_{cis}$/ NHCOCH*C*H$_2$), 4.33/42.3 (HNC*H*$_2$/ HN*C*H$_2$), 3.73/55.1 (OC*H*$_3$/O*C*H$_3$);

^{1}H,^{13}C gHMBC NMR (400/400 MHz, DMSO-*d*$_6$) δ ^{1}H/ δ ^{13}C **10.01**/ 162.7, 132.3, 113.4 (N*H*COCHCH$_2$/ NH*C*OCHCH$_2$, NHCO*C*HCH$_2$, Ar*C*$_5$H), **7.86**/ 132.7, 113.4 (Ar*H*$_7$/ Ar*C*$_{3a/6/7a}$, Ar*C*$_5$H), **7.27 – 7.25**/ 158.3, 132.7, 128.6, 113.8, 42.3 (Ar*H*$_{2'+6'}$, Ar*H*$_4$ / Ar*C*$_{4'}$, Ar*C*$_{3a/6/7a}$, Ar*C*$_{2'+6'}$H, Ar*C*$_{3'+5'}$H, HN*C*H$_2$), **6.91**/ 158.3, 131.6, 128.6, 113.8 (Ar*H*$_{3'+5'}$/ Ar*C*$_{4'}$, Ar*C*$_{1'}$, Ar*C*$_{2'+6'}$H, Ar*C*$_{3'+5'}$H), **6.45**/ 162.7, 126.0 (NHCOC*H*CH$_2$/ NH*C*OCHCH$_2$, NHCOCH*C*H$_2$), **6.23**/ 162.7, 132.3 (NHCOCHC*H*$_2$/ NH*C*OCHCH$_2$, NHCO*C*HCH$_2$), **5.70**/ 162.7, 132.3 (NHCOCHC*H*$_2$/ NH*C*OCHCH$_2$, NHCO*C*HCH$_2$), **4.33**/154.3, 131.6, 128.6 (HNC*H*$_2$/ HN*C*ONH, Ar*C*$_{1'}$, Ar*C*$_{2'+6'}$H), **3.73**/158.3 (OC*H*$_3$/Ar*C*$_{4'}$).

Table 9.4: The 2D NMR spectra assignments (gHSQC and gHMBC) for N-{2-[3-(4-methoxybenzyl)ureido]-1H-benzo[d]imidazol-6-yl}acrylamide (14)

^{13}C (δ ppm)	gHSQC (δ ppm)	gHMBC (δ ppm)	Carbon assignment
42.3	4.33	7.27 – 7.25 (2 × ArH)	HN*C*H$_2$
55.1	3.73	–	O*C*H$_3$
104.3	–	–	unknown
113.4	7.22	10.01, 7.86	Ar*C*$_5$H
113.8	6.91	7.27 – 7.25, 6.91	Ar*C*$_{3'+5'}$H
126.0	5.70, 6.23	6.45	NHCOCH*C*H$_2$
128.6	7.27 – 7.25 (m)	7.27 – 7.25, 6.91, 4.33	Ar*C*$_{2'+6'}$H
131.6	–	6.91, 4.33	Ar*C*$_{1'}$
132.3	6.45	10.01, 6.23, 5.70	NHCO*C*HCH$_2$
132.7	–	7.86, 7.27 – 7.25 (Ar*H*$_4$)	Ar*C*$_{3a/6/7a}$
148.6	–	–	unknown
154.3	–	4.33	HN*C*ONH
158.3	–	7.27 – 7.25, 6.91, 3.73	Ar*C*$_{4'}$
162.7	–	10.01, 6.45, 6.23, 5.70	NH*C*OCHCH$_2$

Ar*C*$_5$H is the only carbon in the benzimidazole ring that could be assigned. The other carbons (*C*$_2$, *C*$_{3a}$, *C*$_4$, *C*$_6$, *C*$_7$, *C*$_{7a}$) were either absent from the ^{13}C NMR spectrum or could not be assigned with the use of

the available 2D NMR results. A total of three carbon signals were missing from the ^{13}C NMR spectrum, and three carbon signals (δ 104.3, 132.7, 148.6 ppm) could not be assigned.

General procedure for the synthesis of the Weinreb amides (62 – 63).[43–45]

Reactions were performed under argon, using glassware that was oven-dried overnight. 2-Bromopropane was freshly distilled from calcium hydride under argon. *N,O*-Dimethylhydroxylamine hydrochloride was dried overnight under vacuum, in a 40 °C oil bath. Mg turnings were dried in the oven (120 °C) overnight.

Preparation of the Grignard reagent, isopropylmagnesium bromide

Mg turnings (1.50 g, 61.7 mmol, 1.5 equiv) and THF (20 mL) were placed in a 2-neck flask with a rubber septum. In order to initiate the reaction, a small allocate (1 mL) of the required 2-bromopropane (3.8 mL, 40 mmol, 1.0 equiv) was added to the stirred solution at r.t. and then the reaction flask was warmed by hand. When the reaction mixture started to dissipate heat, the rest of the 2-bromopropane was added by slow dropwise addition. The mixture was left to stir for 30 min or until the reaction mixture had cooled down.

The Grignard reagent was titrated at r.t., by the dropwise addition of isopropylmagnesium bromide to a stirred solution of menthol (0.239 g, 1.53 mmol, 1.0 equiv) and 1,10 phenanthroline (5 mg, 0.03 mmol, 0.02 equiv) in THF (10 mL). The end-point was characterised by a distinct pink colour that persisted for longer than a minute.

Conversion of the ester to the Weinreb amide

The ester (1.0 equiv) and *N,O*-Dimethylhydroxylamine hydrochloride (2.0 equiv) were suspended in THF. The suspension was cooled to −20 °C with an acetonitrile/dry ice bath, before the dropwise addition of isopropylmagnesium bromide solution. The reaction mixture was left to stir for 1 h, allowing it to reach −5 °C. The bright yellow solution was quenched with sat. aq. NH_4Cl (15 mL), extracted with a mixture of 10% MeOH/DCM (3 × 35 mL) and washed with brine (30 mL). The organic layer was dried over $MgSO_4$, filtered and concentrated under reduced pressure. The crude product was purified by column chromatography to yield the Weinreb amides **62 – 63**.

_N_-methoxy-2-[3-(4-methoxybenzyl)ureido]-_N_-methylbenzo[_d_]thiazole-6-carboxamide (62)

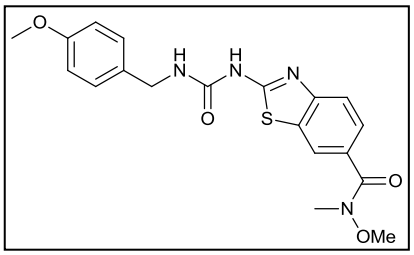

Prepared according to the general procedure, with the following amounts: Methyl 2-[3-(4-methoxybenzyl)ureido]benzo[*d*]thiazole-6-carboxylate (**57**, 0.988 g, 2.66 mmol), *N,O*-dimethylhydroxylamine hydrochloride (0.519 g, 5.32 mmol), THF (26 mL) and isopropylmagnesium bromide (1.3 M in THF, 11.8 mL, 15 mmol, 5.6 equiv). The crude product was purified by column chromatography (2% MeOH/30% EtOAc/DCM) to afford **62** as a white solid (0.863 g, 81% yield).

R_f = 0.25 (40% EtOAc/DCM); **mp** = 190 – 193 °C; **^{1}H NMR** (400 MHz, DMSO-d_6) δ 10.90 (br.s, 1H, N*H*), 8.18 (s, 1H, ArH_7) 7.65 – 7.60 (m, 2H, Ar$H_{4,5}$), 7.26 (d, *J* = 8.7 Hz, 2H, 2 × Ar*H*), 7.17 (br.t, 1H, N*H*), 6.91 (d, *J* = 8.7 Hz, 2H, 2 × Ar*H*), 4.31 (d, *J* = 5.8 Hz, 2H, CH_2), 3.73 (s, 3H, Ph-OCH_3), 3.56 (s, 3H, NOCH_3), 3.27 (s, 3H, NCH_3); **^{13}C NMR** (101 MHz, DMSO-d_6) δ 168.8, 161.9, 158.4, 153.7, 150.7, 131.1, 128.7, 128.3, 125.9, 121.7, 118.8, 113.8, 60.6, 55.1, 42.5, 33.6, one quaternary carbon missing in the spectrum; **FT-IR** (ATR mode) 3311 (N-H stretch), 1668 (C=O stretch), 1604, 1560, 1513, 1447, 1271, 1236, 1177, 1035, 832, 806, 753, 716 cm^{-1}; **HRMS (ESI)** *m/z* calcd for $C_{19}H_{21}N_4O_4S$, $[M+H]^+$: 401.1284, found 401.1284.

_N_-methoxy-2-[3-(4-methoxybenzyl)ureido]-_N_-methyl-1_H_-benzo[_d_]imidazole-6-carboxamide (63)

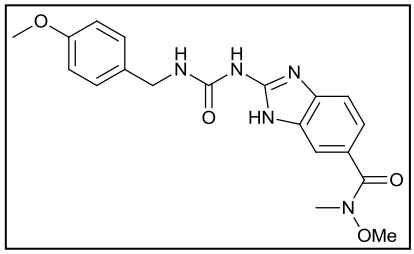

Prepared according to the general procedure, with the following amounts: Methyl 2-[3-(4-methoxybenzyl)ureido]-1*H*-benzo[*d*]imidazole-6-carboxylate (**60**, 0.450 g, 1.27 mmol), *N,O*-dimethylhydroxylamine hydrochloride (0.248 g, 2.54 mmol), THF (15 mL) and isopropylmagnesium bromide (1.4 M in THF, 6.4 mL, 9.0 mmol, 7.1 equiv). The pure product was isolated by column chromatography (2% MeOH/60% EtOAc/DCM) to yield a white solid (**63**, 0.381 g, 78% yield).

R_f = 0.14 (60% EtOAc/DCM), **mp** = 158 – 160 °C; **^{1}H NMR** (300 MHz, DMSO-d_6) δ 11.79 (br.s, 1H, N*H*), 10.07 (br.s, 1H, N*H*), 7.68 (s, 1H, ArH_7), 7.58 (br.t, 1H, N*H*), 7.39 – 7.32 (m, 2H, Ar$H_{4,5}$), 7.27 (d, *J* = 8.7 Hz, 2H, 2 × Ar*H*), 6.91 (d, *J* = 8.7 Hz, 2H, 2 × Ar*H*), 4.33 (d, *J* = 5.8 Hz, 2H, CH_2), 3.73 (s, 3H, Ph-OCH_3), 3.55 (s, 3H, NOCH_3), 3.25 (s, 3H, NCH_3); **^{13}C NMR** (75 MHz, DMSO-d_6) δ 169.9, 158.3, 154.1, 149.6, 131.5, 128.6, 126.0, 121.2, 113.1, 60.4, 55.1, 42.3, 33.8, four carbon signals missing in the spectrum; **FT-IR** (ATR mode) 3392 (N-H stretch), 3319 (N-H stretch), 1672 (C=O stretch), 1650, 1628, 1594, 1509, 1245, 1223, 1174, 1030, 993, 835, 816 cm^{-1}; **HRMS (ESI)** *m/z* calcd for $C_{19}H_{22}N_5O_4$, $[M+H]^+$: 384.1672, found 384.1671.

General Grignard reaction procedure to synthesise ketones 9 – 12.[46]

The Weinreb amide (1.0 equiv) was suspended in THF (4 mL) and was cooled to −20 °C with an acetonitrile/dry ice bath, before the dropwise addition of the Grignard reagent. The reaction mixture was monitored by TLC to determine the amount of Grignard reagent to be added. The reaction mixture was left to stir 45 min in between portions of Grignard reagent. Finally, the reaction mixture was stirred for 20 h, wherein the mixture was allowed to reach 15 °C. The transparent yellow solution was transferred dropwise into a stirred solution of 1 M aq. $NaHSO_4$ (30 mL) at 0 °C and was left to stir for 1 h at 0 °C. The mixture was allowed to reach r.t. and was extracted with EtOAc (3 × 25 mL). The organic layer was washed with brine (20 mL), dried over $MgSO_4$, filtered and concentrated in vacuo. The pure product was obtained by column chromatography.

1-(6-Acryloylbenzo[*d*]thiazol-2-yl)-3-(4-methoxybenzyl)urea (9)

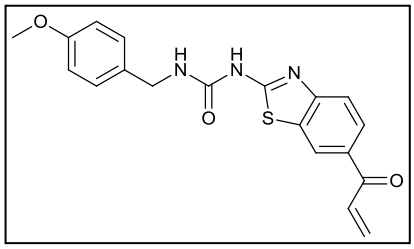

Prepared according to the general procedure with Weinreb amide **62** (0.110 g, 0.275 mmol) and vinylmagnesium bromide (1 M in THF, 2.6 mL, 2.6 mmol, 9.5 equiv). A major by-product formed which was only visible when the TLC plate was stained with *p*-anisaldehyde stain. The product was purified by column chromatography (1% MeOH/10% Hexane/30% EtOAc/DCM) to yield **9** as a white solid (0.026 g, 26% yield).

R_f = 0.47 (40% EtOAc/DCM); **mp** = > 150 °C decomp; **^{1}H NMR** (400 MHz, DMSO-d_6) δ 11.05 (br.s, 1H, N*H*), 8.65 (s, 1H, ArH_7), 8.02 (dd, *J* = 8.5, 1.5 Hz, 1H, ArH_5), 7.70 (d, *J* = 8.5 Hz, 1H, ArH_4), 7.50 (dd, $^3J_{trans}$ = 16.9, $^3J_{cis}$ = 10.4 Hz, 1H, COC*H*CH_2), 7.26 (d, *J* = 8.5 Hz, 2H, 2 × Ar*H*), 7.20 (br.s, 1H, N*H*), 6.91 (d, *J* = 8.5 Hz, 2H, 2 × Ar*H*), 6.36 (dd, $^3J_{trans}$ = 16.9, $^2J_{gem}$ = 1.7 Hz, 1H, COCHCH_2), 5.96 (dd, $^3J_{cis}$ = 10.4, $^2J_{gem}$ = 1.7 Hz, 1H, COCHCH_2), 4.31 (d, *J* = 5.8 Hz, 2H, HNCH_2), 3.73 (s, 3H, OCH_3); **^{13}C NMR** (101 MHz, DMSO-d_6) δ 188.4 (*C*OCHCH_2), 163.5, 158.4, 153.6, 153.0, 132.3, 131.9, 131.3, 131.1, 129.7, 128.7, 126.6, 123.1, 119.5, 113.8, 55.1, 42.5; **FT-IR** (ATR mode) 3295 (N-H stretch), 1672 (C=O stretch), 1608, 1555, 1512, 1454, 1275, 1229, 1177, 1032, 785 cm^{-1}; **HRMS (ESI)** *m/z* calcd for $C_{19}H_{18}N_3O_3S$, $[M+H]^+$: 368.1069, found 368.1069; **UPLC**: Purity 96%, r.t = 4.12 min, acetonitrile/H_2O (0.1% formic acid) 5/95.

1-(4-Methoxybenzyl)-3-(6-propioloylbenzo[*d*]thiazol-2-yl)urea (11)

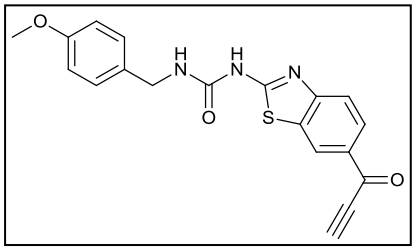

Prepared according to the general procedure with Weinreb amide **62** (0.100 g, 0.250 mmol) and ethynylmagnesium bromide (0.5 M in THF, 6.5 mL, 3.3 mmol, 13 equiv). Column chromatography (1% MeOH/10% Hexane/30% EtOAc/DCM) afforded **11** as a light yellow solid (0.069 g, 76% yield).

R$_f$ = 0.62 (40% EtOAc/DCM); **mp** = > 185 °C decomp; **^{1}H NMR** (300 MHz, DMSO-*d*$_6$) δ 11.15 (br.s, 1H, N*H*), 8.69 (d, *J* = 1.7 Hz, 1H, Ar*H*$_7$), 8.06 (dd, *J* = 8.5, 1.7 Hz, 1H, Ar*H*$_5$), 7.73 (d, *J* = 8.5 Hz, 1H, Ar*H*$_4$), 7.27 – 7.21 (m, 3H, 2 × Ar*H*, N*H*), 6.91 (d, *J* = 8.7 Hz, 2H, 2 × Ar*H*), 5.06 (s, 1H, COCC*H*), 4.31 (d, *J* = 5.8 Hz, 2H, HNC*H*$_2$), 3.73 (s, 3H, OC*H*$_3$); **^{13}C NMR** (75 MHz, DMSO-*d*$_6$) δ 175.8 (*C*OCCH), 164.5, 158.4, 154.3, 153.6, 132.2, 131.0, 130.5, 128.7, 127.1, 124.1, 119.6, 113.9, 84.9 (C≡C), 80.5 (C≡C), 55.1, 42.6; **FT-IR** (ATR mode) 3291 (N-H stretch), 3252 (N-H stretch), 2096 (C≡C stretch), 1672 (C=O stretch), 1642, 1603, 1554, 1535, 1511, 1450, 1269, 1242, 1225, 1028, 757 cm^{-1}; **HRMS (ESI)** *m/z* calcd for $C_{19}H_{16}N_3O_3S$, $[M+H]^+$: 366.0912, found 366.0910; **UPLC**: Purity 96%, r.t = 5.59 min, acetonitrile/H_2O (0.1% formic acid) 0/100.

1-(6-Acryloyl-1*H*-benzo[*d*]imidazol-2-yl)-3-(4-methoxybenzyl)urea (10)

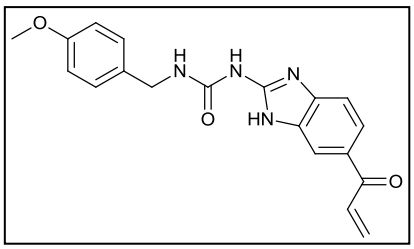

Prepared according to the general procedure with Weinreb amide **63** (0.100 g, 0.261 mmol) and vinylmagnesium bromide (1 M in THF, 2.9 mL, 2.9 mmol, 11 equiv). A major by-product formed which was only visible when the TLC plate was stained with *p*-anisaldehyde stain. The product was purified by column chromatography (1% MeOH/20% DCM/60% EtOAc/Hexane) to yield **10** as a light yellow solid (0.010 g, 11% yield).

R$_f$ = 0.38 (60% EtOAc/DCM), **^{1}H NMR** (400 MHz, DMSO-*d*$_6$) δ 11.95 (br.s, 1H, N*H*), 10.17 (br.s, 1H, N*H*), 8.05 (s, 1H, Ar*H*$_7$), 7.78 (d, *J* = 8.0 Hz, 1H, Ar*H*), 7.51 – 7.44 (m, 3H, COC*H*CH$_2$, N*H*, Ar*H*), 7.27 (d, *J* = 8.5 Hz, 2H, 2 × Ar*H*), 6.91 (d, *J* = 8.5 Hz, 2H, 2 × Ar*H*), 6.31 (dd, $^3J_{trans}$ = 16.9, $^2J_{gem}$ = 1.8 Hz, 1H, COCHC*H*$_2$), 5.91 (d, $^3J_{cis}$ = 11.3 Hz, 1H, COCHC*H*$_2$), 4.33 (d, *J* = 5.7 Hz, 2H, HNCH$_2$), 3.73 (s, 3H, OC*H*$_3$); **HRMS (ESI)** *m/z* calcd for $C_{19}H_{19}N_4O_3$, $[M+H]^+$: 351.1457, found 351.1451.

1-(4-Methoxybenzyl)-3-(6-propioloyl-1*H*-benzo[*d*]imidazol-2-yl)urea (12)

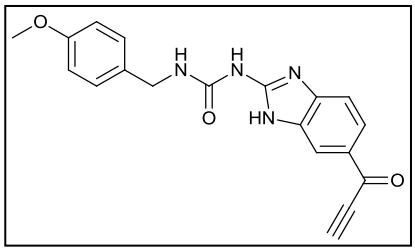

Prepared according to the general procedure with Weinreb amide **63** (0.100 g, 0.261 mmol) and ethynylmagnesium bromide (0.5 M in THF, 10.4 mL, 5.20 mmol, 20 equiv). The reaction mixture was stirred at 40 °C during the 20 h period in the general procedure. Column chromatography (1% MeOH/10% Hexane/50% EtOAc/DCM) afforded **12** as a light yellow solid (0.014 g, 15% yield).

R$_f$ = 0.50 (60% EtOAc/DCM), **mp** = > 160 °C decomp, mp 208 – 210 °C; **^{1}H NMR** (400 MHz, DMSO-d_6) δ 12.08 (br.s, 1H, N*H*), 10.28 (br.s, 1H, N*H*), 8.18 (br.s, 1H, Ar*H*), 7.85 (d, *J* = 8.2 Hz, 1H, Ar*H*), 7.33 – 7.60 (br.s, 2H, Ar*H,* N*H*), 7.27 (d, *J* = 8.6 Hz, 2H, 2 × Ar*H*), 6.91 (d, *J* = 8.6 Hz, 2H, 2 × Ar*H*), 4.95 (s, 1H, COCC*H*), 4.33 (d, *J* = 5.8 Hz, 2H, HNCH_2), 3.73 (s, 3H, OCH_3); **^{13}C NMR** (101 MHz, DMSO-d_6) δ 176.3 (*C*OCCH), 158.3, 153.9, 151.5, 131.4, 128.6, 123.4, 115.9, 113.8, 112.9, 83.8 (C≡C), 80.9 (C≡C), 55.1, 42.4; three carbon signals were not visible in the spectrum; **HRMS (ESI)** *m/z* calcd for $C_{19}H_{17}N_4O_3$, $[M+H]^+$: 349.1301, found 349.1303; **UPLC**: Purity 97%, r.t = 4.76 min, acetonitrile/H_2O (0.1% formic acid) 0/100.

9.3 References

1 W. L. F. Armarego and C. L. L. Chai, *Purification of Laboratory Chemicals*, Butterworth-Heinemann, Burlington, 6th edn., 2009.

2 *SAINT Data Collection Software*, version V7.99A, Bruker AXS Inc., Madison, WI, 2012.

3 *SADABS*, version 2012/1, Bruker AXS Inc., Madison, WI, 2012.

4 R. H. Blessing, *Acta Crystallogr., Sect. A*, 1995, **51**, 33–38.

5 G. M. Sheldrick, *Acta Crystallogr., Sect. A*, 2015, **71**, 3–8.

6 G. M. Sheldrick, *Acta Crystallogr., Sect. C*, 2015, **71**, 3–8.

7 J. L. Atwood and L. J. Barbour, *Cryst. Growth Des.*, 2003, **3**, 3–8.

8 L. J. Barbour, *J. Supramol. Chem.*, 2001, **1**, 189–191.

9 *POV-RayTM for Windows*, version 3.6, Persistence of Vision Raytracer Pty. Ltd, Williamstown, Australia, 2004.

10 D. I. Perez, V. Palomo, C. Pérez, C. Gil, P. D. Dans, F. J. Luque, S. Conde and A. Martínez, *J. Med. Chem.*, 2011, **54**, 4042–4056.

11 A. Baki, A. Bielik, L. Molnár, G. Szendrei and G. M. Keserü, *Assay Drug Dev. Technol.*, 2007, **5**, 75–83.

12 Institute Of Pharmacology And Toxicology, Academy Of Military Medical Sciences, EP2354136 (A1), 2011.

13 A. Tsuruoka, Y. Kaku, H. Kakinuma, I. Tsukada, M. Yanagisawa, N. Kazumasa and T. Naito, *Chem. Pharm. Bull.*, 1998, **46**, 623–630.

14 S. N. Sawhney and D. W. Boykin, *J. Org. Chem.*, 1979, **44**, 1136–1142.

15 C. Ricci, *Ann. Chim.*, 1955, **45**, 172–175.

16 Takeda Pharmaceuticals Company Limited, EP3225618 (A1), 2017.

17 W. Hirose, K. Sato and A. Matsuda, *Eur. J. Org. Chem.*, 2011, **2011**, 6206–6217.

18 S. Hinsberger, J. C. De Jong, M. Groh, J. Haupenthal and R. W. Hartmann, *Eur. J. Med. Chem.*, 2014, **76**, 343–351.

19 P. A. Duspara, M. Sadequl Islam, A. J. Lough and R. A. Batey, *J. Org. Chem.*, 2012, **77**, 10362–10368.

20 R. Bhat, Y. Xue, S. Berg, S. Hellberg, M. Ormö, Y. Nilsson, A. C. Radesäter, E. Jerning, P. O. Markgren, T. Borgegård, M. Nylöf, A. Giménez-Cassina, F. Hernández, J. J. Lucas, J. Díaz-Nido and J. Avila, *J. Biol. Chem.*, 2003, **278**, 45937–45945.

21 F. Lo Monte, T. Kramer, A. Boländer, B. Plotkin, H. Eldar-Finkelman, A. Fuertes, J. Dominguez and B. Schmidt, *Bioorg. Med. Chem. Lett.*, 2011, **21**, 5610–5615.

22 T. Fairley, R. Tidwell, I. Donkor, N. Naiman, K. Ohemeng, R. Lombardy, J. Bentley and M. Cory, *J. Med. Chem.*, 1993, **36**, 1746–1753.

23 W. Yin, C. Wang and Y. Huang, *Org. Lett.*, 2013, **15**, 1850–1853.

24 C.-H. Park and R. S. Givens, *J. Am. Chem. Soc.*, 1997, **119**, 2453–2463.

25 H. Sharghi, M. Jokar, M. M. Doroodmand and R. Khalifeh, *Adv. Synth. Catal.*, 2010, **352**, 3031–3044.

26 S. S. Thakkar, P. Thakor, H. Doshi and A. Ray, *Bioorg. Med. Chem.*, 2017, **25**, 4064–4075.

27 B. Maji, K. Kumar, M. Kaulage, K. Muniyappa and S. Bhattacharya, *J. Med. Chem.*, 2014, **57**, 6973–6988.

28 D. Kelly, S. Bateman, R. Martin, M. Reum, M. Rose and A. Whittaker, *Aust. J. Chem.*, 1994, **47**, 247–262.

29 Y. Lu, Y. Li, R. Zhang, K. Jin and C. Duan, *Tetrahedron*, 2013, **69**, 9422–9427.

30 Y. Zhu, M. Zhao, W. Lu, L. Li and Z. Shen, *Org. Lett.*, 2015, **17**, 2602–2605.

31 C. J. Reinhardt, E. Y. Zhou, M. D. Jorgensen, G. Partipilo and J. Chan, *J. Am. Chem. Soc.*, 2018, **140**, 1011–1018.

32 N. Charrier, E. Demont, R. Dunsdon, G. Maile, A. Naylor, A. O'Brien, S. Redshaw, P. Theobald, D. Vesey and D. Walter, *Synthesis*, 2006, **2006**, 3467–3477.

33 U. Tawar, A. K. Jain, B. S. Dwarakanath, R. Chandra, Y. Singh, N. K. Chaudhury, D. Khaitan and V. Tandon, *J. Med. Chem.*, 2003, **46**, 3785–3792.

34 J. Sun Kim, B. Gatto, C. Yu, A. Liu, L. F. Liu and E. J. LaVoie, *J. Med. Chem.*, 1996, **39**, 992–998.

35 University of Sunderland, WO2014096864 (A1), 2014.

36 K. Starcevic, I. Caleta, D. Cincic, B. Kaitner, M. Kralj, K. Ester and G. M. Karminski-Zamola, *Heterocycles*, 2006, **68**, 2285–2299.

37 K. Kikuchi, R. B. Hannak, M. J. Guo, A. J. Kirby and D. Hilvert, *Bioorg. Med. Chem.*, 2006, **14**, 6189–6196.

38 K. Sagi, K. Fujita, M. Sugiki, M. Takahashi, S. Takehana, K. Tashiro, T. Kayahara, M. Yamanashi, Y. Fukuda, S. Oono, A. Okajima, S. Iwata, M. Shoji and K. Sakurai, *Bioorg. Med. Chem.*, 2005, **13**, 1487–1496.

39 S. Visweswariah, G. Prakash, V. Bhushan and S. Chandrasekaran, *Synthesis*, 1982, **1982**, 309–310.

40 J. M. Bartolomé-Nebreda, S. A. Alonso De Diego, M. Artola, F. Delgado, Ó. Delgado, M. L. Martín-Martín, C. M. Martínez-Viturro, M. Á. Pena, H. M. Tong, M. Van Gool, J. M. Alonso, A. Fontana, G. J. Macdonald, A. Megens, X. Langlois, M. Somers, G. Vanhoof and S. Conde-Ceide, *J. Med. Chem.*, 2015, **58**, 978–993.

41 4SC AG, US2006142570 (A1), 2006.

42 H. Ma, C. Zhuang, X. Xu, J. Li, J. Wang, X. Min, W. Zhang, H. Zhang and Z. Miao, *Eur. J. Med. Chem.*, 2017, **133**, 174–183.

43 J. M. Williams, R. B. Jobson, N. Yasuda, G. Marchesini, U. H. Dolling and E. J. J. Grabowski, *Tetrahedron Lett.*, 1995, **36**, 5461–5464.

44 H.-S. Lin and L. A. Paquette, *Synth. Commun.*, 1994, **24**, 2503–2506.

45 T. Suto, Y. Yanagita, Y. Nagashima, S. Takikawa, Y. Kurosu, N. Matsuo, T. Sato and N. Chida, *J. Am. Chem. Soc.*, 2017, **139**, 2952–2955.

46 S. Pirc, D. Bevk, A. Golobič, B. Stanovnik and J. Svete, *Helv. Chim. Acta*, 2006, **89**, 30–44.